
High-performance shape memory composites with intrinsic heating capabilities

Dissertation submitted by,

Gokul Ganesh Murali

in partial fulfilment of the requirements for the degree of

Doctor of Philosophy (PhD)

in Aerospace Engineering

at Imperial College London

June 2023

Department of Aeronautics

Imperial College London

South Kensington Campus

London, SW7 2AZ

An electronic version of this thesis will be available at <https://spiral.imperial.ac.uk/>.



This project has received funding from the European Union's Horizon 2020 research and innovation programme under the Marie Skłodowska-Curie grant agreement No 765881. Within H2020-EU.1.3.1 the goal is to train a new generation of creative and innovative researchers, able to convert knowledge and ideas into products and services for economic and social benefit in the Union.

This page is intentionally left blank.

Declaration of originality

The studies described in this dissertation are the original research works of the author. The research was performed partially at Imperial College London under the supervision of Professor Paul Robinson, and partially at the University of Vienna under the supervision of Professor Alexander Bismarck. No part of this dissertation has been submitted for consideration for another degree at this or any other institution.

Gokul Ganesh Murali

June 2023

This page is intentionally left blank.

Copyright declaration

The copyright of this thesis rests with the author. Unless otherwise indicated, its contents are licensed under a Creative Commons Attribution-NonCommercial 4.0 International Licence (CC BY-NC).

Under this licence, you may copy and redistribute the material in any medium or format. You may also create and distribute modified versions of the work. This is on the condition that: you credit the author and do not use it, or any derivative works, for a commercial purpose.

When reusing or sharing this work, ensure you make the licence terms clear to others by naming the licence and linking to the licence text. Where a work has been adapted, you should indicate that the work has been changed and describe those changes.

Please seek permission from the copyright holder for uses of this work that are not included in this licence or permitted under UK Copyright Law.

Gokul Ganesh Murali

June 2023

This page is intentionally left blank.

Abstract

Shape morphing structures have played a significant role within the field of aerospace for more than a century. While the shape morphing aerostructures of the past and present have depended on hinges and motors to achieve morphing, their future is expected to rely on smart materials and structures that have intrinsic shape morphing capabilities.

One such smart material, that has previously been developed at Imperial College London, is the carbon fibre reinforced epoxy polymer (CFRP) composite with thermoplastic (TP) interleaves. These interleaved composites exhibit controllable stiffness (CS) and shape memory (SM) capabilities under suitable thermal conditions. While these interleaved composites showed excellent shape morphing capabilities, they had several drawbacks. These composites showed poor flexural modulus and through-thickness shear strength compared to the epoxy-based non-interleaved CFRP. These composites also used an oven to achieve the high temperatures required to exhibit the CS and SM capabilities.

This thesis describes studies conducted to mitigate these drawbacks. In the first study described in this thesis, the source of the premature through-thickness shear failure in TP interleaved CFRP composites was discovered to be the low shear strength of the polystyrene (PS) interleaves used in previous works. It was then demonstrated that replacing PS with Poly(styrene-co-acrylonitrile) (SAN) could improve the through-thickness shear strength of the interleaved composites to be almost as high as that of pristine CFRP. Furthermore, the SAN-interleaved CFRP laminates also exhibited excellent CS and SM capabilities.

In the next study described in this thesis, it was demonstrated that the flexural modulus of TP interleaved CFRP composites can be substantially improved by two different methods- (i) reducing the thickness of the TP interleaves, and (ii) introducing reinforcements within the TP interleaves.

The following study describes how intrinsic heating capability was achieved in TP interleaved CFRP composites, through resistive heating of heater elements such as stainless steel (SS)

meshes and woven carbon fabric (WCF) embedded within the layup of the composite. This intrinsic heating strategy was used to supply the temperature necessary for the corresponding composites to exhibit CS and SM capabilities. As a result, these intrinsically heated TP interleaved CFRP composites exhibited successful out-of-oven morphing capabilities.

In the final study described in this thesis, composite structures that were initially flat in their as-cured state, but were capable of deployment into planar and curved meshes were designed. Finite element numerical models were used to predict the deployment capabilities of these composite structures. Finally, the deployable composite mesh structures were manufactured and characterised.

Acknowledgements

I would like to thank my supervisors Prof Paul Robinson from Imperial College London and Prof Alexander Bismarck from the University of Vienna for their support and motivation throughout the duration of this research project. I thank them for helping me identify my strengths and weaknesses and helping me become a successful researcher. I hope that their monumental guidance will greatly aid me in my career for years to come.

I would like to thank Dr Frank Gommer, Mr Keith Wolstenholme, Mr Gary Senior, Mr Joseph Meggyesi, Mr Jonathan Cole and Mr Franco Giammaria for their help with the experimental activities in this research. I also thank Dr Omar Bacarreza Nogales for his help with the numerical studies described in this thesis. The administrative assistance provided by Ms Lisa Kelly, Ms Susan Avery and Ms Ela Sapinska also supported me in completing my thesis. The help provided to me by Dr Andreas Mautner and Dr Florian Meyer during my visits to the University of Vienna also played a significant role in this project.

I would also like to thank the entire pan-European HyFiSyn team for all their help and motivation throughout the duration of this project. I will always remember the time I spent with this team as a ray of sunshine. I thank Dr Yentl Swolfs for bringing together such a vibrant and talented team. Additionally, I would like to thank my friends and colleagues for all their support.

I would also love to thank my family for all their help and sacrifice to help me reach such great heights. Finally, I would love to especially thank my wife Kirubashini, for being a pillar of support over all the ups and downs I faced over these years. Without her care and support, the completion of this research work would have not been possible.

Gokul Ganesh Murali

June 2023

This page is intentionally left blank.

Table of contents

Declaration of originality	3
Copyright declaration	5
Abstract	7
Acknowledgements	9
Table of contents	11
List of publications and conference presentations	19
List of figures	20
List of tables.....	31
List of equations.....	37
List of abbreviations	39
List of nomenclatures	41
List of units	45
Chapter 1. Introduction.....	47
1.1. Aim and objective.....	49
1.2. Structure of the thesis	49
Chapter 2. Literature study	51
2.1. Need for morphing structures	51
2.2. Morphing composites	57
2.2.1. Morphing of conventional composites using shape memory alloys	58
2.2.2. Morphing of multistable composites.....	60
2.2.3. Morphing of anisotropic composites.....	65

2.2.4.	Morphing of shape memory polymer composites.....	67
2.2.5.	Morphing of controllable (variable) stiffness composites	69
2.3.	Controllable stiffness and shape memory characteristics of interleaved composites	73
2.4.	Generation of residual stresses in interleaved composites during manufacture to allow deployment directly from as-cured state	75
2.5.	Deployable structures made with interleaved composites.....	77
2.6.	Mechanical performance of interleaved composites	79
2.7.	Reinforcement of thermoplastic matrices.....	81
2.8.	Intrinsic heating of composites	83
2.9.	Propositions based on the literature study	85
Chapter 3. Improvement of the through-thickness shear strength of thermoplastic interleaved carbon-epoxy composites.....		
3.1.	Identification of the location of premature through-thickness shear failure in PS-interleaved CFRP composites	88
3.1.1.	Materials and laminates.....	88
3.1.2.	Experimental methodology	89
3.1.2.1.	<i>3-point bending (3PB) tests</i>	89
3.1.2.2.	<i>Optical microscopy of composites</i>	90
3.1.2.3.	<i>XPS analysis</i>	90
3.1.3.	Results and discussion.....	90
3.1.3.1.	<i>3PB test results</i>	90
3.1.3.2.	<i>XPS results</i>	93
3.1.4.	Conclusion.....	97

3.2.	Investigation of alternative interleaf materials to improve the through-thickness shear strength of thermoplastic interleaved carbon-epoxy composites.....	98
3.2.1.	Materials and laminates.....	98
3.2.2.	Experimental methodology	99
3.2.2.1.	<i>3PB and SBS tests</i>	99
3.2.2.2.	<i>Optical microscopy of composites</i>	100
3.2.3.	Results and discussions	102
3.2.3.1.	<i>3PB test results</i>	102
3.2.3.2.	<i>SBS test results</i>	105
3.2.4.	Conclusion.....	107
3.3.	Investigation of the controllable stiffness and shape memory capabilities of SAN-interleaved CFRP composites.....	107
3.3.1.	Materials, laminates and sample preparation.....	107
3.3.2.	Experimental methodology	111
3.3.2.1.	<i>Controllable stiffness (CS) tests</i>	111
3.3.2.2.	<i>3PB tests</i>	112
3.3.2.3.	<i>Shape memory (SM) tests</i>	112
3.3.2.4.	<i>Optical microscopy of composites</i>	114
3.3.3.	Results and discussions	114
3.3.3.1.	<i>CS test results</i>	114
3.3.3.2.	<i>3PB test results</i>	117
3.3.3.3.	<i>SM test results</i>	120
3.3.3.4.	Void formation within the thermoplastic interleaves	122

3.3.4.	Conclusion.....	128
3.4.	Chapter summary.....	128
Chapter 4. Improvement of the flexural modulus of thermoplastic interleaved carbon-epoxy composites 129		
4.1.	Investigation of improvement of the flexural modulus of interleaved composites by reducing the thickness of the interleaves 129	
4.1.1.	Materials, laminates and sample preparation.....	129
4.1.2.	Experimental methodology	132
4.1.2.1.	CS tests	132
4.1.2.2.	SM tests.....	132
4.1.2.3.	3PB tests	132
4.1.2.4.	Optical microscopy of composites	133
4.1.3.	Results and discussion	133
4.1.3.1.	CS test results.....	133
4.1.3.2.	SM test results	138
4.1.3.3.	3PB test results	142
4.1.4.	Conclusion.....	146
4.2.	Investigation of improvement of the flexural modulus of interleaved composites by reinforcing the interleaves..... 146	
4.2.1.	Materials and laminates.....	146
4.2.2.	Experimental methodology	147
4.2.2.1.	Prediction of moduli of RTPs.....	147
4.2.2.2.	CS tests	150
4.2.2.3.	SM tests.....	150

4.2.2.4.	3PB tests	150
4.2.2.5.	Optical microscopy of composites	152
4.2.3.	Results and discussion	152
4.2.3.1.	CS test results.....	152
4.2.3.2.	Quantifying the increase in apparent flexural modulus of interleaved composites due to introducing WCF reinforcement in the interleaves	154
4.2.3.3.	SM test results	156
4.2.3.4.	3PB test results	158
4.2.4.	Conclusion.....	160
4.3.	Chapter summary.....	161
Chapter 5. Achieving intrinsic heating capability in thermoplastic interleaved carbon-epoxy composites		
		162
5.1.	Materials, laminates, and specimens.....	162
5.2.	Experimental methodology	169
5.2.1.	Modified test setup used in 3PB loading of intrinsically heated interleaved composite specimens	169
5.2.2.	Investigation of intrinsic heating capabilities of the interleaved composites with embedded heaters.....	171
5.2.3.	CS tests.....	171
5.2.4.	SM tests	172
5.2.5.	Optical microscopy	172
5.3.	Results and discussion.....	172

5.3.1.	Analysing the quality of the 3-step modular manufacturing process.....	172
5.3.2.	Flexural tests on intrinsically heated composite specimens	174
5.3.3.	CS test results	177
5.3.4.	SM test results.....	182
5.4.	Conclusion and chapter summary	187
Chapter 6.	Developing deployable meshes with intrinsic heating capabilities	188
6.1.	Concept development of deployable composite meshes	189
6.1.1.	Planar deployable mesh layup and working principle.....	189
6.1.2.	Layup proposal for a non-planar deployable mesh	191
6.1.3.	Parameters proposed to quantify the deployment of the meshes... ..	192
6.2.	Numerical study of deployable composite meshes	194
6.2.1.	Mesh convergence study of CFRP sub-laminates	194
6.2.1.1.	<i>Materials</i>	194
6.2.1.2.	<i>Details of modelling</i>	195
6.2.1.3.	<i>Analysing the mesh convergence of CFRP plies</i>	197
6.2.2.	Mesh convergence study of PS interleaves in the proposed layup.....	198
6.2.2.1.	<i>Materials</i>	199
6.2.2.2.	<i>Details of modelling</i>	199
6.2.2.3.	<i>Analysing the mesh convergence of PS interleaves</i>	201
6.2.3.	Modelling a segment of a deployable mesh with different layups... ..	203
6.2.3.1.	<i>Details of modelling</i>	204

6.2.3.2.	<i>Comparison of deployment parameters of meshes with different layups.....</i>	205
6.2.4.	Conclusion.....	208
6.3.	Manufacture and characterisation of deployable composite meshes	209
6.3.1.	Materials, laminates, and specimens	209
6.3.1.1.	<i>Manufacturing composite meshes capable of deployment only using an external heating source</i>	209
6.3.1.2.	<i>Manufacturing composite meshes capable of deployment using an external heating source and also through intrinsic heating</i>	212
6.3.2.	Experiment methodology	216
6.3.2.1.	<i>Deployment of composite meshes using a convection oven.....</i>	216
6.3.2.2.	<i>Deployment of composite meshes through intrinsic heating.....</i>	217
6.3.2.3.	<i>Optical microscopy of composites</i>	217
6.3.3.	Results and discussions	219
6.3.4.	Conclusion.....	229
6.4.	Chapter summary.....	230
Chapter 7.	Discussion, conclusions and suggestions for future work.....	232
7.1.	Discussion.....	232
7.2.	Conclusions.....	236
7.3.	Suggestions for future work.....	237
References	240

Appendices	266
A.1. Measuring dimensions of composite specimens.....	266
A.1.1. Samples cut with a circular dry saw	266
A.1.2. Samples cut with a waterjet cutter	266
A.2. Methodology to extract load associated with the initiation of failure (L_f) from the force-displacement plots obtained from the 3PB and SBS tests of composite specimens	270
A.3. Repairability of CFRP-PS composites	273
A.4. Differential scanning calorimetry (DSC) of thermoplastic materials.....	275
A.5. SBS study of CFRP-PS composites with different layup sequences.....	277
A.6. Behaviour of the 3PB setup while it cools down during the SM tests	280
A.7. Comparing the shapes of cross-plyed laminates predicted using analytical and numerical approaches	283
A.7.1. Using Timoshenko bimetal curvature equation to predict the shape of a cross-plyed laminate	283
A.7.2. Using classical laminate theory (CLT) to predict the shape of a cross-plyed laminate.....	284
A.7.3. Using numerical modelling to predict the shape of a cross-plyed laminate	284
A.7.4. Results and discussions	286

List of publications and conference presentations

1. Murali, G. G., Robinson, P., Bismarck, A., and Burgstaller, C., (2021). Improving flexural modulus of interleaved composites using reinforced thermoplastic interleaves, SAMPE Europe 21 Conference, September 2021.
2. Murali, G. G., Robinson, P., Bismarck, A., and Burgstaller, C., (2021). Design of a deployable composite mesh to form a segment of a circular cylindrical surface, HyFiSyn school and conference, September 2021.
3. Murali, G. G., Robinson, P., Bismarck, A., and Burgstaller, C., (2021). Development of intrinsically heated, interleaved composites with controllable flexural stiffness and shape memory capability, MECHCOMP7, September 2021.
4. Murali, G. G., Robinson, P., Bismarck, A., and Burgstaller, C., (2021). Deployable composite meshes – modelling, manufacture and characterisation, ECCM20, June 2022.
5. Jones, M. P., Murali, G. G., Laurin, F., Robinson, P., & Bismarck, A. (2022). Functional flexibility: The potential of morphing composites. *Composites Science and Technology*, 230, 109792. <https://doi.org/10.1016/J.COMPSCITECH.2022.109792>

This page is intentionally left blank.

List of figures

Figure 2.1. Wright flyer showing warping wings.....	53
Figure 2.2. Ideal wing profiles of an aircraft for various manoeuvres	53
Figure 2.3. Morphing aircraft structures showing (a) variable wing sweep, and (b) variable nose shape.....	54
Figure 2.4. Variable geometry control surface installed on a Gulfstream GIII	55
Figure 2.5. Deployment sequence of James Webb Space Telescope.....	56
Figure 2.6. Futuristic morphing aircraft concept designs by (a) NASA, and (b) Lockheed Martin.....	57
Figure 2.7. Morphing of flexible composites using SMA actuators	59
Figure 2.8. Boeing's shape morphing chevron that uses SMA actuators.....	60
Figure 2.9. Shape morphing of multistable composite by shifting between different low potential energy states.....	61
Figure 2.10. Transition of a cross-ply $[0_3/90_3]$ bistable composite from one stable shape to another using thermal actuation.....	61
Figure 2.11. Different shapes of bistable composites based on their layup	62
Figure 2.12. Bistable composite with mechanically prestressed elastomeric layers mounted on a stress-free core.....	63
Figure 2.13. Shape change in NACA 0012 wing profile induced by the embedded bistable composites	63
Figure 2.14. (a) The schematic of the deployable boom structure, (b) stable deployed and unstable stored states of composite tape and (c) deployable boom structure at various stages of deployment	65
Figure 2.15. Corrugated composite with structural anisotropy	66
Figure 2.16. Corrugated composite with improved stiffness (due to CFRP rods), and smoother profile (due to flexible rubber)	67
Figure 2.17. Schematic showing the shape memory behaviour of SMPs	68

Figure 2.18. Deployable hinge constructed with SMP constituents recovering from 120° bent shape to its initial shape.....	69
Figure 2.19. Interleaved composite with variable stiffness caused by ply slippage	71
Figure 2.20. Controllable stiffness composite made of segmented stiff plates and a deformable polymer	72
Figure 2.21. Schematic of the shape memory process in interleaved composites	75
Figure 2.22. Morphing of (a) cross-plyed, and (b) TP interleaved cross-plyed composite using residual stress approach	76
Figure 2.23. Deployable box section made using conventional and TP interleaved CFRP composite specimens	77
Figure 2.24. Composite mesh with shape contraction capability	78
Figure 2.25. Composite mesh with shape expansion capability.....	79
Figure 2.26. Flexural modulus of various interleaved composites at different temperatures.	80
Figure 2.27. Film stacking process used in the manufacture of reinforced thermoplastic composites	83
Figure 2.28. Experimental setup for heating interleaved composites by resistive heating of outermost CFRP plies	85
Figure 3.1. Typical load-displacement curves of the composites in the 3PB tests described in Section 3.1.2.1	91
Figure 3.2. Micrographs of polished longitudinal cross-sections of the composite specimens tested until failure in the 3PB tests described in Section 3.1.2.1 ...	93
Figure 3.3. Photographs of the fracture surfaces of CFRP-PS specimens	94
Figure 3.4. Typical wide range XPS survey of (a) pristine PS film, (b) control composite, and (c) the fracture surfaces CFRP-PS composite	95
Figure 3.5. Typical deconvoluted carbon (C1s) peaks of the XP-spectra of (a) pristine PS film, (b) control composite, and (c) the fracture surfaces of CFRP-PS composite	96

Figure 3.6. Polished longitudinal microsection and the associated force-displacement curves obtained from the 3PB tests of (a) control, (b) CFRP-PS, (c) CFRP-SAN, (d) CFRP-MABS, (e) CFRP-ASA+PC composites	104
Figure 3.7. Typical load-displacement curves of the composites in the SBS tests described in Section 3.2.2.1	105
Figure 3.8. Polished microsection of the edges of PS-interleaved CFRP composites cut using waterjet cutter, showing damages to the regions near the cuts made using waterjet	109
Figure 3.9. (a) A typical high-contrast pattern on a composite specimen, and (b) the associated shape profile	114
Figure 3.10. Typical force-displacement curves of composite specimens at (a) RT1, (b) HT1 and (c) RT2 test conditions in the CS tests described in Section 3.3.2.2	116
Figure 3.11. Typical load-displacement curves of the composites in the 3PB tests described in Section 3.3.2.2	119
Figure 3.12. Micrographs of polished longitudinal cross-sections of the composite specimens tested until failure in the 3PB tests described in Section 3.3.2.2	119
Figure 3.13. Typical shapes of CFRP-PS _{174μ} specimens at (a) initial, (b) deformed, (c) springback, (d) recovery (2 minutes) and (e) recovery (5 minutes) stages of SM tests	121
Figure 3.14. Distance (ζ) between the mid-span and the ends of the specimens in the direction of loading, after deformation in SM tests	122
Figure 3.15. Polished longitudinal microsection of the mid-span of CFRP-PS _{110μ} composites (a) after heating to 120°C, (b) after deformation, cooldown, and removal of deformation load, and (c) after 10 minutes of shape recovery at 120°C	124

Figure 3.16. Polished longitudinal microsection of the free end of CFRP-PS _{110μ} composites (a) after heating to 120°C, (b) after deformation, cooldown, and removal of deformation load, and (c) after 10 minutes of shape recovery at 120°C	125
Figure 3.17. Polished longitudinal microsection of the mid-span of CFRP-SAN _{118μ} composites (a) after heating to 120°C, (b) after deformation, cooldown, and removal of deformation load, and (c) after 10 minutes of shape recovery at 120°C	126
Figure 3.18. . Polished longitudinal microsection of the free end of CFRP-SAN _{118μ} composites (a) after heating to 120°C, (b) after deformation, cooldown, and removal of deformation load, and (c) after 10 minutes of shape recovery at 120°C	127
Figure 4.1 Typical force-displacement curves of composite specimens at (a) RT1 and (b) HT1 test conditions in the CS tests described in Section 4.1.2.1	134
Figure 4.2 E_{RT1} , E_{HT1} , and E_{RT2} (see Table 4.5) of composites plotted against their interleaf thickness.....	136
Figure 4.3 Polished longitudinal microsection of pristine CFRP-PS _{33μ} and CFRP-SAN _{37μ} , showing bridging of CFRP	137
Figure 4.4 Free ends of (a) CFRP-PS _{174μ} , (b) CFRP-PS _{33μ} , and (c) CFRP-SAN _{37μ} specimens after deformation in SM study, where the specimen edges are highlighted using green dotted lines, and poor CFRP ply slippages are circled.....	139
Figure 4.5 Polished longitudinal microsection of (a) CFRP-PS _{33μ} , (b) CFRP-PS _{110μ} , (c) CFRP-PS _{174μ} , (d) CFRP-SAN _{37μ} and (e) CFRP-SAN _{151μ} composites after SM tests	141
Figure 4.6 Typical load-displacement curves of the composites in the 3PB tests described in Section 4.1.2.3.....	143

Figure 4.7 Polished longitudinal microsection of (a) CFRP-PS _{33μ} , (b) CFRP-PS _{110μ} , (c) CFRP-PS _{174μ} , (d) CFRP-SAN _{37μ} and (e) CFRP-SAN _{151μ} specimens after failure in 3PB tests.....	145
Figure 4.8 Typical force-displacement curves of composite specimens at (a) RT1 and (b) HT1 test conditions in the CS tests described in Section 4.2.2.2	153
Figure 4.9 Polished longitudinal microsection of (a) CFRP-PS-WCF, and (b) CFRP-SAN-WCF after SM study.....	157
Figure 4.10 Typical load-displacement curves of the composites in the 3PB tests described in Section 4.2.2.4	159
Figure 4.11 Polished longitudinal microsection of (a) CFRP-PS-WCF and (b) CFRP-SAN-WCF specimens after failure in 3PB tests	160
Figure 5.1 (a) Layup of the laminate during the first step of the manufacturing process, (b) top-view of the heater layer during the second step, and (c) the layup of the laminate during the third step described in Section 5.1	164
Figure 5.2 (a) CFRP-SAN-SS _{heater} and (b) CFRP-SAN-WCF _{heater} composites at the start of the step-3 of the production process.....	165
Figure 5.3 (a) CFRP-SAN-SS _{heater} and (b) CFRP-SAN-WCF _{heater} specimens showing the dry heaters and copper connectors	167
Figure 5.4 Positions where conductive copper tape and silver loaded adhesive were used to facilitate a good electrical connection in each CFRP-SAN-SS _{heater} and CFRP-SAN-WCF _{heater} specimen	168
Figure 5.5 Modified 3PB setup used in the characterisation of intrinsically heated interleaved composite specimens.....	170
Figure 5.6 Polished longitudinal microsection of the mid-span (a) CFRP-SAN-SS _{heater} and (b) CFRP-SAN-WCF _{heater} in their as-cured state	173
Figure 5.7 Polished longitudinal microsection of the free end (a) CFRP-SAN-SS _{heater} and (b) CFRP-SAN-WCF _{heater} in their as-cured state	174

Figure 5.8 Typical normalised applied force and surface temperature of the	
(a) CFRP-SAN-SS _{heater} and (b) CFRP-SAN-WCF _{heater} specimens in the	
fixed displacement 3PB tests described in Section 5.2.2	176
Figure 5.9 Typical force-displacement curves of intrinsically heated composite specimens	
at (a) RT1 and (b) HT1* test conditions in CS tests. (*i _{DC} used to achieve HT1	
test conditions are provided in the legend).....	178
Figure 5.10 Polished longitudinal microsection of the mid-span of CFRP-SAN-SS _{heater} and	
CFRP-SAN-WCF _{heater} specimens showing void formation within the	
interleaves after CS tests where i _{DC} of (a) 2.0 A, (b) 2.5 A, (c) 1.1 A, and	
(d) 1.4 A were used	180
Figure 5.11 Polished longitudinal microsection of the free end of CFRP-SAN-SS _{heater} and	
CFRP-SAN-WCF _{heater} specimens showing void formation within the	
interleaves after CS tests where i _{DC} of (a) 2.0 A, (b) 2.5 A, (c) 1.1 A, and	
(d) 1.4 A were used	181
Figure 5.12 Polished longitudinal microsection of the mid-span of CFRP-SAN-SS _{heater}	
and CFRP-SAN-WCF _{heater} specimens showing void formation within the	
interleaves after SM tests where i _{DC} of (a) 2.0 A, (b) 2.5 A, (c) 1.1 A, and	
(d) 1.4 A were used	184
Figure 5.13 Polished longitudinal microsection of the free end of CFRP-SAN-SS _{heater} and	
CFRP-SAN-WCF _{heater} specimens showing void formation within the	
interleaves after SM tests where i _{DC} of (a) 2.0 A, (b) 2.5 A, (c) 1.1 A, and	
(d) 1.4 A were used	185
Figure 6.1. (a) Schematic of a mesh made of several repeating segments, and (b) layup	
of the repeating segment.....	190
Figure 6.2. (a) Proposed layup of the repeating segment of a mesh and (b) a schematic	
showing how the layup should be mirrored to achieve a full mesh cell.....	192
Figure 6.3. Schematic showing a deployed curved mesh with a segment of it	
highlighted.	193

Figure 6.4. Layup of the model used in the mesh convergence study of CFRP	
sub-laminates used in the proposed layup.....	194
Figure 6.5. A schematic of the layup in the FE model to study the mesh convergence of	
CFRP sub-laminates.	196
Figure 6.6. Shape of the FE model used to study the mesh convergence of CFRP	
sub-laminates in its initial flat and final deployed shapes	197
Figure 6.7. Layup of the model used in the convergence study of PS interleaves used	
in the proposed layup	199
Figure 6.8. A schematic of the layup in the FE model to study the mesh convergence of	
PS interleaves.	200
Figure 6.9. The predicted expansion ratio of the FE model (shown in Figure 6.8) for a	
range of elastic moduli of PS	202
Figure 6.10. Layup of the model used to study the effect of different layups on the	
deployment capabilities of a mesh.....	203
Figure 6.11. A schematic of the layup in the FE model used to study the effect of	
different layups on the deployment capabilities of a mesh	205
Figure 6.12. FE model of a repeating segment of a deployable mesh with $\theta=45^\circ$ in its	
layup, after cooling to 25°C	207
Figure 6.13. Layup of the composite panels prepared using the method described in	
Section 6.3.1.1	211
Figure 6.14. Schematic of a deployed mesh with layup shown in Figure 6.13,	
with $\theta=90^\circ$	212
Figure 6.15. Names and layups of the composite sublaminates prepared during the first	
step of the manufacturing process described in Section 6.3.1.2	214
Figure 6.16. Layup of the Mesh _{0/90-SS} laminate prepared during the third step of the	
manufacturing process described in Section 6.3.1.2.....	215
Figure 6.17. Mesh _{0/90-SS} panel at the start of the third step of the manufacturing process	
described in Section 6.3.1.2	216

Figure 6.18. Mesh _{0/90-SS} specimens showing the dry SS heaters and copper connectors.....	216
Figure 6.19. Positions in a composite mesh cell where optical microscopy was performed.....	218
Figure 6.20. Mesh _{0/90} and Mesh _{0/45} specimens in their as-cured and deployed states	219
Figure 6.21. Mesh _{0/90-SS} specimen in its as-cured and deployed states	220
Figure 6.22. Comparison of numerically predicted (from Section 6.2.3.2) and experimentally observed expansion ratio and deployment angle	221
Figure 6.23. Mesh _{0/90-SS} specimens deployed (a) using an oven and (b) through intrinsic heating	222
Figure 6.24. Longitudinal microsection of (a) Mesh _{0/90} , (b) Mesh _{0/45} and (c) Mesh _{0/90-SS} specimens in their pristine as-cured state	224
Figure 6.25. Longitudinal microsection of (a) Mesh _{0/90} , (b) Mesh _{0/45} and (c) Mesh _{0/90-SS} specimens after deployment inside an oven	227
Figure 6.26. Longitudinal microsection of Mesh _{0/90-SS} specimen after intrinsically heated deployment.....	228
Figure A.1. Positions where measurements of dimensions of composite specimens were made for composites cut using a circular dry saw.....	266
Figure A.2. Polished transverse microsection of the edges of PS-interleaved CFRP composites cut using (a) waterjet cutter and (b) circular dry saw.	267
Figure A.3. Dimensions of the composite specimens cut using a waterjet.....	269
Figure A.4. Representation of a force-displacement plot obtained from 3PB and SBS tests	271
Figure A.5. $\Delta F/\Delta d$ curve and identification of the plateau region of the curve shown in Figure A.4.....	271
Figure A.6. Mathematical operations performed on a representative force-displacement plot to obtain the load associated with the initiation of failure (L_f).....	272

Figure A.7. Load associated with the initiation of failure (L_f) where a load-displacement curve has a higher load before its intercept with the $C_{5\%}$ line	272
Figure A.8. Typical 3PB load-displacement curves of CFRP-PS specimens in 3PB tests at different damage-repair cycles.....	274
Figure A.9. The heat flow vs. temperature curves of (a) PS, (b) SAN, (c) MABS and (d) ASA+PC obtained from DSC studies.....	276
Figure A.10. Typical load-displacement curves of the composites with layup having (a) one thermoplastic interleaf and (b) multiple thermoplastic interleaves in the SBS tests described in Section A.5.....	278
Figure A.11. Experiment setup used for SM tests	280
Figure A.12. Load-displacement of a PS-interleaved CFRP composite being deformed in a 3PB setup in an SM test	281
Figure A.13. Applied force of the composite during the cooling process in an SM test	282
Figure A.14. Change in effective mid-span displacement of the 3PB setup during the cooling process in an SM test.....	282
Figure A.15. A schematic of the layup in the FE model to study the shape change of a cross-ply laminate, with its dimensions highlighted	285
Figure A.16. FE model of a cross-ply laminate after cooling to 88°C	285
Figure A.17. The shape of the deformed cross-ply laminate obtained through the FE model, and the fitted second-order polynomial curve	286

This page is intentionally left blank.

List of tables

Table 2.1. Advantages and disadvantages of the various approaches used to achieve shape morphing in composites, as discussed in Section 2.2	72
Table 2.2. Flexural strength of interleaved composites.....	81
Table 3.1. Names and layups of the composite panels prepared for the studies shown in Section 3.1	88
Table 3.2. Dimensions of composite specimens used in the 3PB tests described in Section 3.1.2.1	89
Table 3.3. Maximum bending (σ^{max}) and shear (τ^{max}) stresses (at L_f) of composites in the 3PB tests described in Section 3.1.2.1	92
Table 3.4. Atomic composition of specimens, as observed using XPS.....	95
Table 3.5. Bond composition within the C1s peaks of specimens, as observed using XPS.....	96
Table 3.6. Alternative thermoplastic interleaf materials explored in this study	101
Table 3.7. Names and layups of the composite panels prepared for the studies shown in Section 3.2	100
Table 3.8. Dimensions of composite specimens used in the SBS and 3PB tests described in Section 3.2.2.1	102
Table 3.9. σ^{max} and τ^{max} of composite specimens in the 3PB tests described in Section 3.2.2.1	103
Table 3.10. Maximum shear stress ($\tau^{max(SBS)}$) of composite specimens in the SBS tests described in Section 3.2.2.1	106
Table 3.11. Names and layups of the composite panels prepared for the studies shown in Section 3.3.....	108
Table 3.12. Dimensions of composite specimens used in the CS tests described in Section 3.3.2.1	110

Table 3.13. Dimensions of composite specimens used in the 3PB tests described in Section 3.3.2.2.....	110
Table 3.14. Dimensions of composite specimens used in the SM studies described in Section 3.3.2.3.....	110
Table 3.15. The apparent flexural modulus of composites at RT1, HT1 and RT2 test conditions in the CS tests described in Section 3.3.2.2.....	117
Table 3.16. τ^{max} , σ^{max} and $\sigma^{maxCFRP}$ of the CFRP-PS _{174μ} and CFRP-SAN _{151μ} specimens in the 3PB tests described in Section 3.3.2.2.....	118
Table 3.17. Distance (ζ) between the mid-span and the ends of composite specimens in the direction of loading at different stages of the SM study	121
Table 3.18. Specimen thickness (t) and apparent flexural moduli (E_{RT}) moduli of the composites before and after the SM tests described in Section 3.3.2.3.....	127
Table 4.1 Names and layups of the composite panels prepared for the studies shown in Section 4.1	130
Table 4.2 Dimensions of composite specimens used in CS tests described in Section 4.1.2.1.....	131
Table 4.3 Dimensions of composite specimens used in SM tests described in Section 4.1.2.2.....	131
Table 4.4 Dimensions of composite specimens used in 3PB tests described in Section 4.1.2.3.....	132
Table 4.5. The apparent flexural modulus of composites at RT1, HT1 and RT2 test conditions in the CS tests described in Section 4.1.2.1	135
Table 4.6. Distance (ζ) between the mid-span and the ends of composite specimens in the direction of loading at different stages of the SM tests described in Section 4.1.2.2.....	140
Table 4.7. Specimen thickness (t) and apparent flexural moduli (E_{RT}) moduli of the composites before and after the SM tests described in Section 4.1.2.2.....	142

Table 4.8. τ^{max} , σ^{max} , and $\sigma^{maxCFRP}$, and E_{RT-3PB} of interleaved composite specimens in the 3PB tests described in Section 4.1.2.3	144
Table 4.9 Names and layups of the composite panels prepared for the studies shown in Section 4.2.....	147
Table 4.10. E_{RTP} prediction based on mosaic model.....	148
Table 4.11. Parameters used to model the RTP layer in Wisetex and Texcomp software	148
Table 4.12. E_{RTP} prediction based on the method of inclusions	149
Table 4.13 Dimensions of composite specimens used in the CS tests described in Section 4.2.2.2.....	151
Table 4.14 Dimensions of composite specimens used in the SM tests described in Section 4.2.2.3.....	151
Table 4.15 Dimensions of composite specimens used in the 3PB tests described in Section 4.2.2.4.....	152
Table 4.16. The apparent flexural modulus of composites at RT1, HT1 and RT2 test conditions in the CS tests described in Section 4.2.2.2.....	154
Table 4.17. Experimentally measured and theoretically predicted apparent flexural modulus of composites with reinforced interleaves in high stiffness state	155
Table 4.18. Distance (ζ) between the mid-span and the ends of composite specimens in the direction of loading at different stages of the SM tests described in Section 4.2.2.3.....	157
Table 4.19. Specimen thickness (t) and apparent flexural moduli (E_{RT}) moduli of the composites before and after the SM tests described in Section 4.2.2.3.....	158
Table 4.20. τ^{max} , σ^{max} , $\sigma^{maxCFRP}$ and σ^{maxRTP} of interleaved composite specimens in the 3PB tests described in Section 4.2.2.4	159
Table 5.1. Names and layups of the composite panels prepared for the studies shown in Chapter 5	166

Table 5.2. Dimensions of composite specimens prepared for the studies shown in Chapter 5.....	166
Table 5.3. Current applied to composite specimens in the fixed displacement 3PB tests described in Section 5.2.2	171
Table 5.4. Time taken for specimens to lose 99% of their applied force, and the surface temperature of specimens in the fixed displacement 3PB tests described in Section 5.2.2.....	177
Table 5.5. Thickness of the composite specimens before and after the CS studies described in Section 5.2.3.....	178
Table 5.6. The apparent flexural modulus of composites at RT1, HT1 and RT2 test conditions in the CS studies described in Section 5.2.3	179
Table 5.7. Distance (ζ) between the mid-span and the ends of composite specimens in the direction of loading at different stages of the SM tests described in Section 5.2.4.....	183
Table 5.8. Specimen thickness (t) and apparent flexural moduli (E_{RT}) moduli of the composites before and after the SM tests described in Section 5.2.4	186
Table 6.1. Thermal and mechanical properties of CFRP in FE modelling.....	194
Table 6.2. Results of convergence studies performed on the CFRP sub-laminates in Section 6.2.1.....	198
Table 6.3. Thermal and mechanical properties of PS in FE modelling.....	199
Table 6.4. Results of convergence studies performed on the PS interleaves in Section 6.2.2.....	202
Table 6.5. Predicted expansion ratio and deployment angle obtained from the FE models with different θ in the proposed layup at 25°C.....	208
Table 6.6. Experimental parameters used and measured while deploying Mesh _{0/90-SS} specimens through intrinsic heating	218
Table 6.7. Expansion ratio and deployment angle of composite meshes after deployment.....	220

Table A.1. Shear stresses (τ^{max}) and repair efficacy of CFRP-PS specimens in 3PB tests at different damage-repair cycles.....	274
Table A.2. Names and layups of the composite panels prepared for the studies shown in Section A.5	277
Table A.3. Shear yield strength of interleaved composites, obtained through SBS tests described in Section A.5	279
Table A.4. Curvature of cross-ply laminates obtained through various analytical and numerical methods.....	287

This page is intentionally left blank.

List of equations

Eq 3-1	91
Eq 3-2	91
Eq 3-3	106
Eq 3-4	115
Eq 3-5	115
Eq 3-6	115
Eq 3-7	118
Eq 3-8	118
Eq 3-9	121
Eq 4-1	148
Eq 4-2	154
Eq 4-3	155
Eq 4-4	158
Eq A-1	268
Eq A-2	283
Eq A-3	284
Eq A-4	286

This page is intentionally left blank.

List of abbreviations

3PB	3-point bending
ASA+PC	Poly(acrylonitrile-co-styrene-co-acrylate) + Polycarbonate
ASTM	American Society for Testing and Materials
BC	Boundary condition
CFRP	Carbon fibre reinforced epoxy polymer
CPU	Central processing unit
CS	Controllable stiffness
CTE	Coefficient of thermal expansion
DC	Direct current
E	Flexural (or Young's) modulus
FE	Finite element
ILSS	Interlaminar shear strength
MABS	Poly(methyl methacrylate-co-acrylonitrile-co-butadiene-co-styrene)
NACA	National Advisory Committee for Aeronautics
NASA	National Aeronautics and Space Administration
PS	Polystyrene
PTFE	Polytetrafluoroethylene
RTP	Reinforced thermoplastic
SAN	Poly(styrene-co-acrylonitrile)
SBS	Short beam shear

SM	Shape memory
SMA	Shape memory alloy
SMP	Shape memory polymer
SS	Stainless steel
T_g	Glass transition temperature
TP	Thermoplastic
WCF	Woven carbon fibre
XPS	X-ray photoelectron spectroscopy

List of nomenclatures

C1s	1s orbital of carbon
C-C	carbon-carbon single bond
C=C	carbon-carbon double bond
C-O	carbon-oxygen single bond
C=O	carbon-oxygen double bond
E_c	Flexural modulus of CFRP
E_f	Flexural modulus of fibre
E_{HT}	Flexural modulus of composite, at elevated (or high) temperature
E_{HT1}	Experimentally measured flexural modulus of composite, at elevated (or high) temperature
E_{HT-Reinf}	Flexural modulus of composite with reinforced thermoplastic interleaves, at elevated (or high) temperature
E_m	Flexural modulus of matrix
E_{RT}	Flexural modulus of composite, at room temperature
E_{RT1}	Experimentally measured flexural modulus of pristine as-cured composite, at room temperature
E_{RT2}	Experimentally measured flexural modulus of composite at the end of CS tests, at room temperature
E_{RTafterSM}	Experimentally measured flexural modulus of composite at the end of SM tests, at room temperature
E_{RTP}	Flexural modulus of RTP

$E_{RT-reinf}$	Flexural modulus of composite with reinforced thermoplastic interleaves, at room temperature
$E_{RT-unreinf}$	Flexural modulus of composite with unreinforced interleaves, at room temperature
h	Predicted thickness of the composite used for analytical predictions
HT1	Elevated (or high) temperature test condition used in CS tests
i_{DC}	Applied direct current
l	Measured length of a specimen
L_f	Load associated with the initiation of failure
N1s	1s orbital of Nitrogen
O1s	1s orbital of Oxygen
RT1	Room temperature test condition used in CS tests before HT1
RT2	Room temperature test condition used in CS tests after HT1
span	In 3PB tests, span is the distance between the supports. In deployable composites, span is the length of the undeployed as-cured repeating segment of a mesh cell.
t	Measured thickness of a specimen
T_{g-PS}	Glass transition temperature of PS
T_{g-SAN}	Glass transition temperature of SAN
T_{g-TP}	Glass transition temperature of TP
t_i	Thickness of CFRP ply
t_j	Thickness of RTP ply

V_f	Fibre volume fraction
w	Measured width of a specimen
z_i	Distance from the neutral axis to mid-thickness of a CFRP ply
z_j	Distance from the neutral axis to mid-thickness of an RTP ply
$\pi=\pi$	Pi bonds of carbon
σ^{max}	Maximum flexural stress in a specimen in 3PB tests
$\sigma^{maxCFRP}$	True maximum bending stress experienced by the outmost CFRP ply in 3PB tests
σ^{maxRTP}	Maximum bending stress experienced by the outmost RTP ply in 3PB tests
τ^{max}	Maximum shear stress in a specimen in 3PB tests
$\tau^{max(SBS)}$	Maximum shear stress in a specimen in SBS tests

This page is intentionally left blank.

List of units

%	percentage
/cm	per centimetre
°	degree
°C	degree Celcius
A	ampere
bar	10^5 pascal (= 10^5 N/m ²)
c/s	counts of electrons per second
g/m²	grams per square metre
GPa	gigapascal (= 10^9 Pascal = 10^9 N/m ²)
kg/m³	kilogram per cubic metre
kN	kilonewton (= 10^3 N)
min	minute
mm	millimetre
mm/min	millimetre per minute
MPa	megapascal (= 10^6 Pascal = 10^6 N/m ²)
N	newton
psi	pounds per square inch
s	second
V	volt
µm	micrometre

This page is intentionally left blank.

Chapter 1. Introduction

Polymeric composites have higher specific volume, specific stiffness, specific strength, and fatigue resistance compared to metals and metallic alloys (Jones, 1999; Matthews and Rawlings, 1999; Yi, 2018). Due to these advantages, an aircraft with a structure made with composites can have improved efficiency and lower cost-of-running than a similar aircraft that has a structure made of aluminium. As a result, composites are gaining an ever-increasing presence in the aerospace industry as alternatives to aluminium alloys for structural applications (Nedelcu and Redon, 2012; Mrazova, 2013; Atique, Probha and Nafi, 2014; Soutis, 2015; Kesarwani, 2017).

Some composites also have additional advantages such as controllable stiffness and shape memory capabilities, that could potentially be exploited to create aircraft with shape morphing structures (Thill *et al.*, 2008; James *et al.*, 2009; McKnight and Henry, 2010; Sofla *et al.*, 2010; Barvosa-Carter and McKnight, 2011; Tridech *et al.*, 2013; Maples, 2014; Zhang, 2020). The application of composites in the development of morphing aerospace structures is of particular relevance to the research presented in this thesis.

Some of the common approaches to achieving morphing capabilities in composites are,

- by embedding shape memory alloys (SMA) in soft matrices (Barrett and Gross, 1996; Han *et al.*, 2016)
- by embedding SMAs in conventional composites (Harrison *et al.*, 1998; Wang, Rodrigue and Ahn, 2015)
- by using shape memory polymer (SMP) matrices in composites (Arzberger *et al.*, 2005; Leng *et al.*, 2011; Meng and Li, 2013; Rodriguez *et al.*, 2016)
- through multistable layups (Asanuma, Haga and Imori, 2006)
- through bimorph construction (Eckstein, Halbig and Weaver, 2016), and

- through controllable (variable) stiffness construction (Kuder *et al.*, 2013; Maples, 2014).

For application within the aerospace industry, it is expected that the morphing structures have desirable qualities such as, 1) use of simple construction materials and techniques, 2) repeatable morphing capabilities, and 3) need for no (or minimal) external actuation mechanism such as motors. Most of these techniques mentioned above require the morphing composites to have an external actuating mechanism or expensive construction materials to change their shape. These drawbacks can make morphable structures financially unviable and/or have complex construction techniques that make large-scale production impractical. Due to disadvantages like these, morphing composites are not used extensively in the aerospace industry.

The controllable stiffness approach, however, enables the production of morphing composites (and morphing structures) using simple and off-the-shelf construction materials and construction techniques. In this technique, the structure is temporarily induced to be in a low stiffness state when changing shape, thereby reducing or eliminating the need for external actuation. Morphing capability in a composite using the controlled stiffness approach can be achieved by the introduction of thermoplastic interleaves between conventional structural plies (Gandhi and Kang, 2007; Gordon and Clark, 2007; Robinson *et al.*, 2013, 2017; Tridech *et al.*, 2013; Maples, 2014; Maples *et al.*, 2014, 2016; Zhang *et al.*, 2018; Kanzleiter, 2018; Murali *et al.*, 2021). Furthermore, the morphing mechanism of interleaved composites also (theoretically) allows them to exhibit repeatable morphing capabilities, if additional actuation mechanism is provided to reset the shape of the composites.

However, interleaved composites have several challenges that limit their current use. The lower strength and stiffness of the interleaf material cause the interleaved composites to have lower strength and stiffness compared to non-interleaved composites (Maples, 2014). Furthermore, controllable stiffness and shape memory characteristics of these interleaved composites have only been achieved inside an environmental chamber.

The novel studies presented in this thesis were undertaken to address these drawbacks by improving the through-thickness shear strength and apparent flexural moduli of interleaved composites. Furthermore, to enable out-of-oven morphing capabilities, interleaved composites with intrinsic heating capabilities were also developed. Finally, composite mesh structures capable of deployment directly from an as-cured state were also designed, manufactured and deployed to serve as a proof-of-concept of out-of-oven deployment.

1.1. Aim and objective

This research activity aimed to further develop interleaved composite materials so that they are suitable for potential applications in morphing and deployable structures. This aim was accomplished by realising the following objectives –

1. To improve the flexural strength of the interleaved composites while retaining their shape morphing capabilities.
2. To improve the flexural modulus of the interleaved composites while retaining their shape morphing capabilities.
3. To incorporate intrinsic heating capabilities in the interleaved composites to provide out-of-oven thermal energy necessary for shape morphing.
4. To design, model, manufacture and characterise a deployable structure to serve as proof of the morphing capability of oven-heated and intrinsically heated interleaved shape memory composites.

1.2. Structure of the thesis

The literature corresponding to the state-of-the-art of various morphing composites is discussed in [Chapter 2](#). This chapter includes a discussion on the controllable stiffness and shape memory capabilities of interleaved composites. The reinforcement of the thermoplastic interleaf materials and various intrinsic heating strategies in composites are also discussed in this chapter.

Research into the improvement of flexural strength of the interleaved composites is presented in [Chapter 3](#). The first part of this chapter explores the research done on identifying the location and mechanism of premature through-thickness shear failure of the interleaved composites that has been observed in previous studies. In the second part of this chapter, the approach taken to improve the through-thickness failure strength of the interleaved composites is described in detail. The final part of this chapter explores the morphing capabilities of the composites that have higher through-thickness failure strength.

Two approaches to improve the flexural modulus of the interleaved composites are presented in [Chapter 4](#). The first approach was to reduce the volume fraction of interleaf material in the interleaved CFRP composites. The second approach was to improve the intrinsic elastic modulus of the interleaves by introducing reinforcements in these layers.

Research on the development of an intrinsic heating capability within interleaved composites is described in [Chapter 5](#). In this chapter, a study on the use of different heating elements is described and a study on the out-of-oven morphing capability of the intrinsically heated interleaved composites is also presented.

The numerical and experimental studies conducted to develop a deployable structure made of oven-heated and intrinsically heated interleaved composites are presented in [Chapter 6](#). Here, the design and numerical modelling of composite mesh structures which achieve planar and curved deployment are initially described. Furthermore, the manufacture and experimental characterisation of deployable composite structures are described.

Finally, [Chapter 7](#) summarises the activities, results, and discussions of this research project. In this chapter, the important observations and results from the various studies are provided. Based on critical consideration of the achievements of this research activity, some suggestions are also made for future work.

Chapter 2. Literature study

In this chapter, the need for morphing structures in the field of aerospace is first explored. The state-of-the-art of shape morphing of composites is then explored and their applicability in morphable structures is discussed. In particular, detailed insights are provided into the morphing and mechanical behaviour of composites interleaved with thermoplastics, which are the subject of this thesis. Reinforcement of thermoplastics and intrinsic heating of composites are also reviewed in this literature study since these aspects are explored in the research presented in this thesis.

2.1. Need for morphing structures

One of the earliest known shape morphing aerostructures is the twisting wings used in the Wright Flyer in 1903 (see [Figure 2.1](#)), where wires were used to change the shape of the wings ([Humphreys, 1910](#)). Over a century of research and innovation has shown us that ideal wing shapes of aircraft largely depend on their mission profiles, as shown in [Figure 2.2](#).

For high speed and quick manoeuvrability, the wings of the aircraft must ideally have low aspect ratio and large sweep. For high lift-to-drag ratio and long-endurance flights, the wings of the aircraft must have high aspect ratio and low sweep. Thus, based on the required dominant manoeuvres, a variety of aircraft with specific wing profiles are manufactured. However, if the wing profiles of aircraft can be changed, just one type of aircraft can be used for multiple mission profiles, potentially making their manufacture and maintenance more economical ([Kudva, 2004](#); [Thill *et al.*, 2008](#); [Baier and Datashvili, 2011](#); [Murugan *et al.*, 2012](#); [Rodriguez, 2013](#); [Weisshaar, 2013](#); [Ajaj *et al.*, 2014, 2016](#); [Donadon and Iannucci, 2014](#); [Friswell, 2014](#)). Based on this idea, aircraft such as General Dynamics F-111, and Dassault Mirage G have previously been designed with a variable wing sweep (see [Figure 2.3 \(a\)](#)). Similarly, variable nose shape was also used in aircraft such as Aérospatiale/BAC Concorde and Tupolev Tu-144, as seen in [Figure 2.3 \(b\)](#).

To achieve morphing in shape-changing structures, hinges and motors have conventionally been used in the past. More recent advances in morphing aero-structures have moved away from relying on conventional morphing structures to more integrated morphing structures (Ajaj, Beaverstock and Friswell, 2016c). Morphing of different aspects of an aerofoil such as its span (Ajaj, Bouchak and Friswell, 2014; Bishay *et al.*, 2019) and camber (Woods, Bilgen and Friswell, 2014; Cumming *et al.*, 2016; Kota, Flick and Collier, 2016; Muhammed, Ajaj and Khan, 2020; Rivero *et al.*, 2022; Khani Aminjan *et al.*, 2023) has been an interest of several research groups worldwide. Most of these novel aerofoil structures (see Figure 2.4) rely on significantly complex construction techniques and actuation systems for their morphing capabilities. Such features make the manufacture of the morphing structures complex and expensive while simultaneously increasing their weight, thereby potentially making them undesirable for widespread application (Barbarino *et al.*, 2011).

Morphing structures are even more common in the space sector. Many satellites and other spacecraft have deployable structures such as solar panels and antennas. Having such deployable shape-changing structures enables large satellites and other spacecraft to be fitted inside comparatively small launch vehicles. An example of a shape-changing space structure is the recently launched and deployed James Webb Space Telescope (see Figure 2.5).

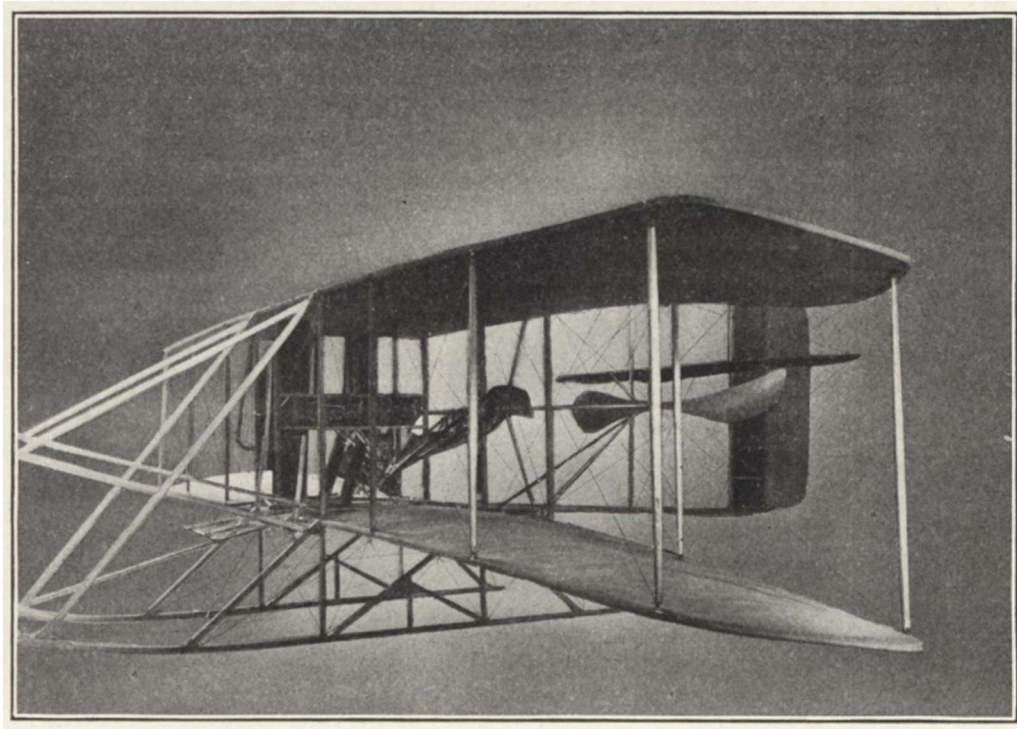


Figure 2.1. Wright flyer showing warping wings (Humphreys, 1910)

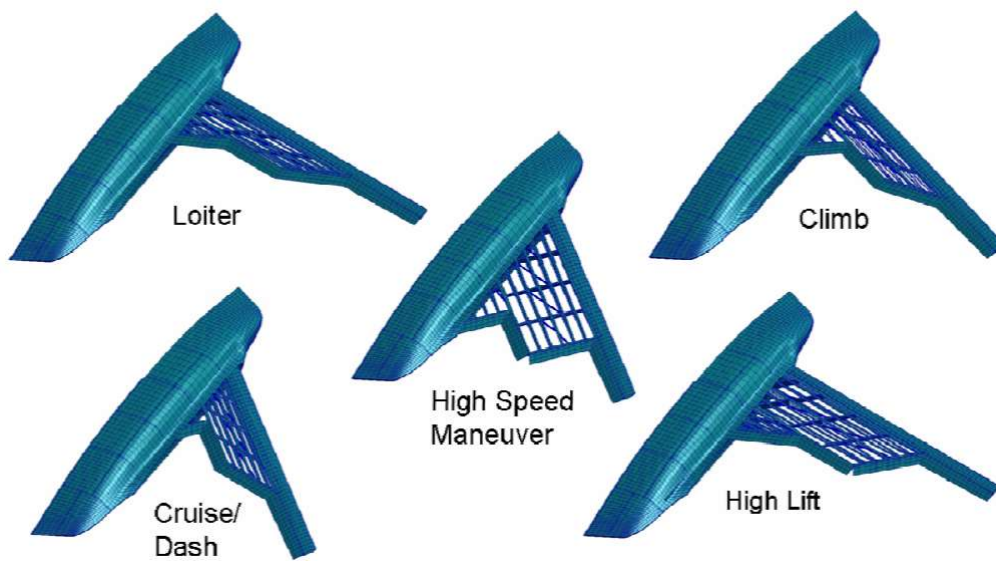
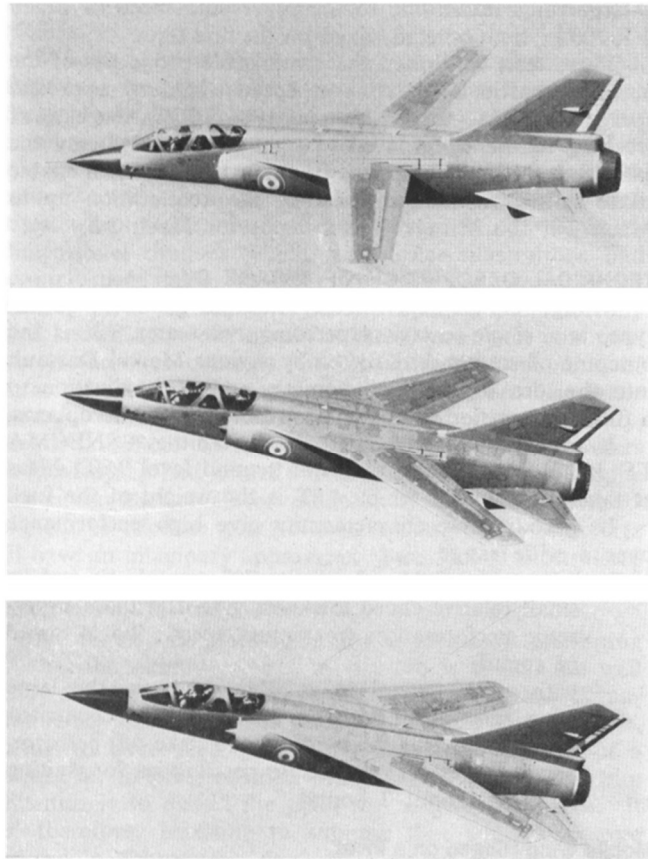


Figure 2.2. Ideal wing profiles of an aircraft for various manoeuvres
(Andersen, Cowan and Piatak, 2007)

(a)



Variable wing sweep of Dassault mirage G

(b)



Figure 2.3. Morphing aircraft structures showing (a) variable wing sweep, and (b) variable nose shape (Deplante, 1969; Morrison, 2019)

While there is no clear definition for morphing structures within the field of aerospace, it is a common consensus that a structure capable of non-localised continuous change in its shape can be considered to having morphing capabilities (Weisshaar, 2006, 2013; Rodriguez, 2007; Ajaj, Beaverstock and Friswell, 2016a, 2016b; Ajaj *et al.*, 2021; Chu *et al.*, 2022). Hence, within this thesis, any structure capable of changing its overall shape and maintaining the new shape is considered to have morphing capabilities.



Figure 2.4. Variable geometry control surface installed on a Gulfstream GIII (Kota, Flick and Collier, 2016)

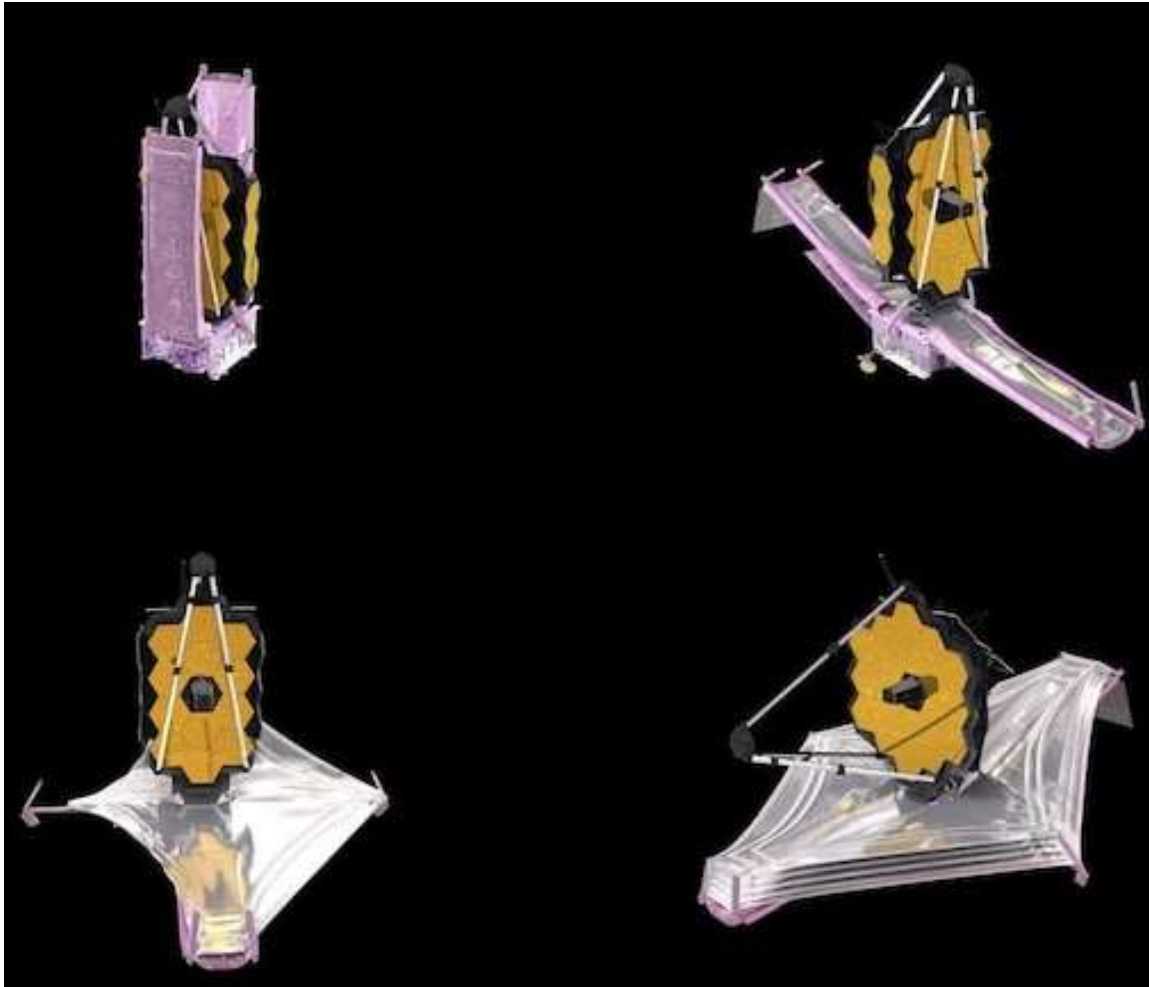


Figure 2.5. Deployment sequence of James Webb Space Telescope

(Roulette and Overbye, 2022)

Currently, research is being conducted into the development of next-generation aircraft that can more closely mimic the flight of a bird. It is possible that aircraft in the future might be influenced by the designs originating from such research activities. Examples of such an aircraft are the concept aircraft designed by NASA that incorporates seamless wings (see [Figure 2.6 \(a\)](#)), or the 'Z-wing' concept aircraft designed by Lockheed Martin that has foldable wings (see [Figure 2.6 \(b\)](#)). However, current limitations in materials technology, manufacturing methods, and avionics have to be overcome to produce such futuristic aircraft. One key area of materials technology concerns morphing materials which could reduce the need for complex actuation systems and thereby decrease the overall cost, complexity, and weight of a

morphing structure. The focus of this thesis is on morphing composite materials, and the state-of-the-art of these materials is explored in detail in the next section.

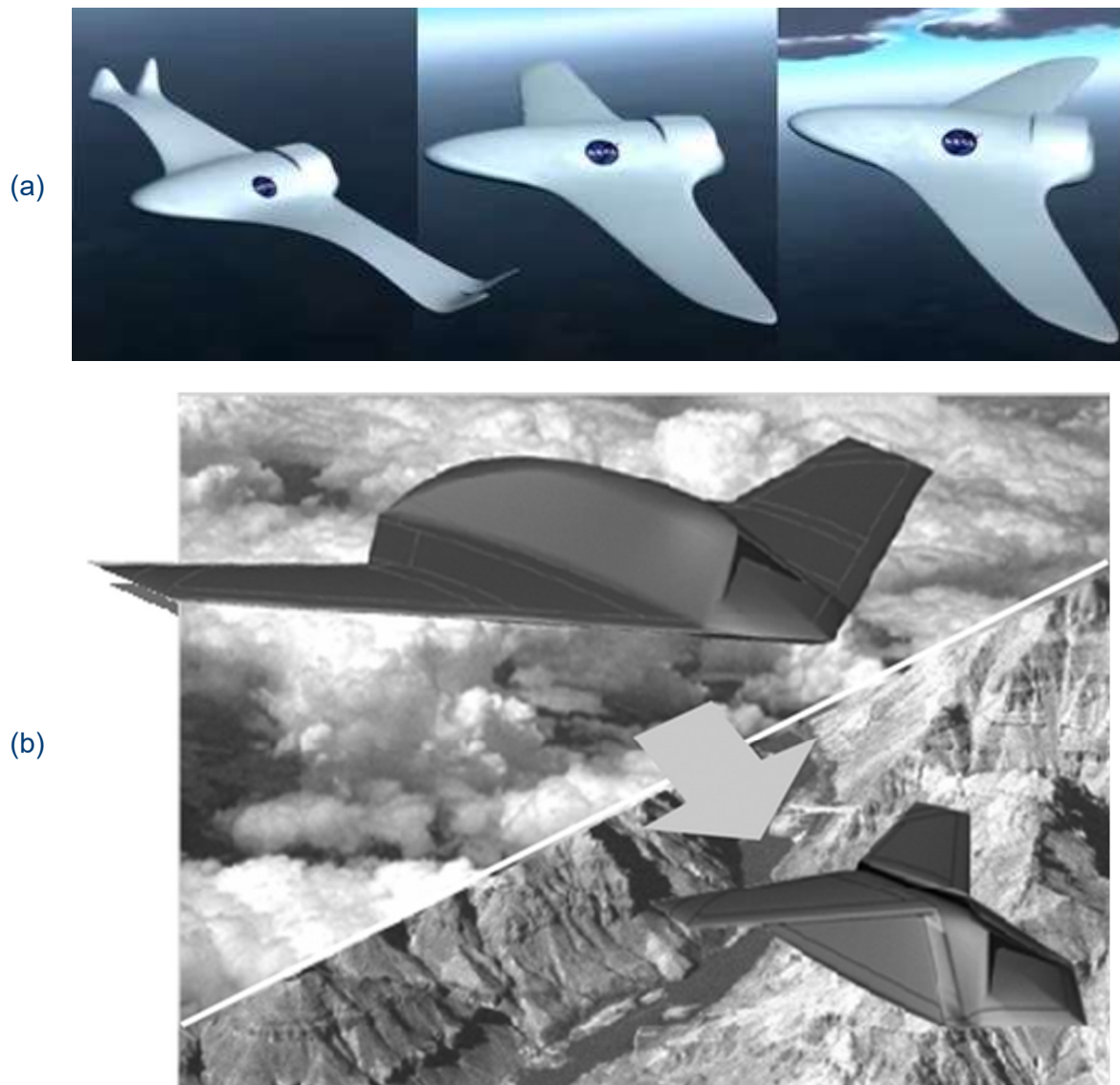


Figure 2.6. Futuristic morphing aircraft concept designs by (a) NASA (Read, 2021), and (b) Lockheed Martin (Weisshaar, 2013)

2.2. Morphing composites

Several approaches have been used to create shape morphing composites. Some of the interesting approaches among them involve the morphing of,

- (i) conventional composites using shape memory alloys as external actuation
- (ii) multistable composites using external actuation

- (iii) anisotropic composite structures using external actuation
- (iv) composites made of shape memory polymers
- (v) controllable (variable) stiffness composites

2.2.1. Morphing of conventional composites using shape memory alloys

An actuation mechanism can be used along with conventional composites to impart morphing capabilities to them. Shape memory alloys (SMA) have commonly been used as an actuation system in flexible composites (Harrison *et al.*, 1998; Psarras, Parthenios and Galiotis, 2001; Cho and Kim, 2005; Kim *et al.*, 2011; Wang, Rodrigue and Ahn, 2015; Yang, Han and Lee, 2018). To effectively deform conventional composites using SMAs, the composites are commonly designed to have high flexibility (i.e., low stiffness), thereby limiting their use in structural applications (Diaconu, Weaver and Mattioni, 2008).

In the research by (Wang, Rodrigue and Ahn, 2015), a flexible composite (with morphing capabilities) made of polydimethylsiloxane matrix embedded with Flexinol SMA wire was produced (see Figure 2.7). In this work, the stiffness of the material was also controlled by temporarily melting the embedded alloys by resistive heating of embedded Ni-Cr wires. In this composite, the actuation of the SMA wires was achieved by heating them using 0.55 A current, and the stiffness change of the composite was achieved by heating the Ni-Cr wires using 1.0 A current to temporarily melt the embedded alloys.

Some studies have shown that SMAs can be used to morph even the highly stiff composite structures that are commonly used in the aircraft industry. A recent work by Boeing explores the use of SMAs to achieve a variable geometry composite chevron shown in Figure 2.8, for noise reduction in jet engines. Research by (Mabe, 2008) shows that a significant reduction in noise levels of jet engines at transonic Mach numbers can be achieved by expanding the area of the jet nozzles by 20%.

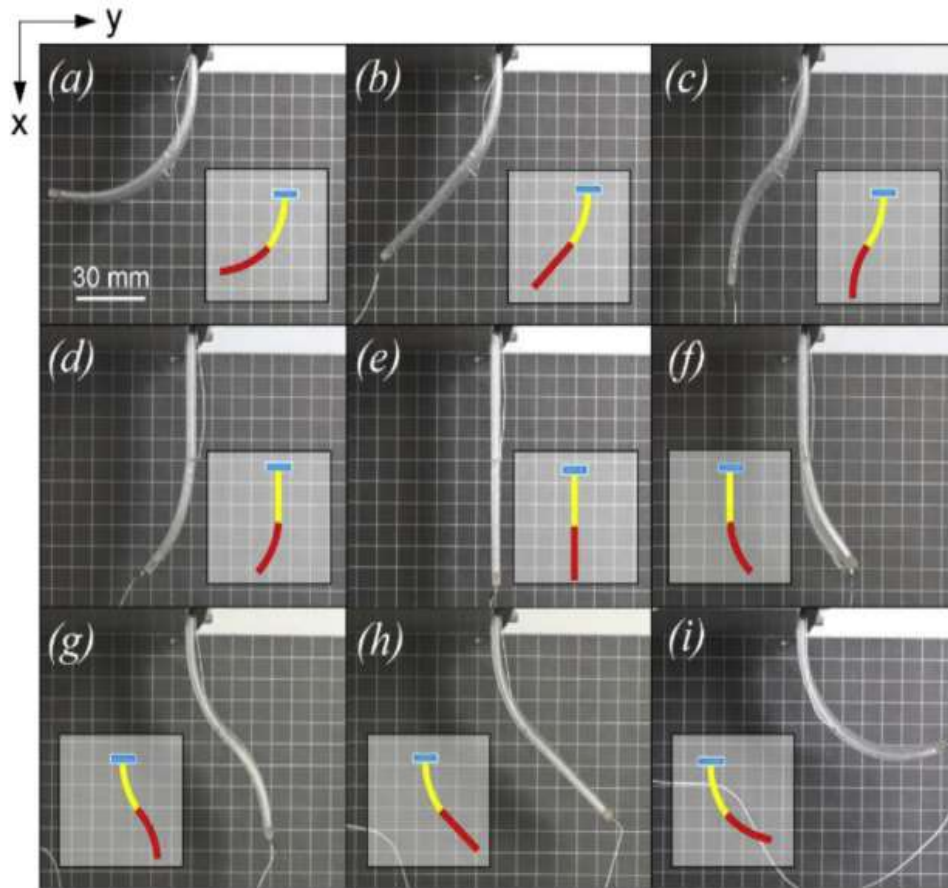


Figure 2.7. Morphing of flexible composites using SMA actuators

(Wang, Rodrigue and Ahn, 2015)

These studies demonstrate the morphing capabilities of composites using shape memory alloys. However, shape morphing structures made using this technique have several issues. While morphable flexible composites (see Figure 2.7) can be used for non-structural applications, they do not possess sufficiently high specific stiffness to be used for structural applications. On the other hand, in morphable stiff structural components that are actuated by SMAs (see Figure 2.8), the quantity of the actuator material needed could significantly increase the weight of the structure. The range of shapes achievable in such morphing structures will also be limited by their stiffness. Additionally, SMAs are highly specialised materials that may be considered too expensive to be used extensively in large-scale manufacturing processes. These drawbacks make this shape morphing approach undesirable for structural applications.



Figure 2.8. Boeing's shape morphing chevron that uses SMA actuators (Liu *et al.*, 2018)

2.2.2. Morphing of multistable composites

A simple and effective way to achieve morphing capabilities in composites is by manufacturing structures with multiple stable shapes and switching between them. Composites with such a property are commonly referred to as bistable or multistable composites.

The functioning of multistable composites relies on the residual stresses developed in the composites (Hyer, 1981; Dano and Hyer, 2003; Bowen *et al.*, 2007; Daynes *et al.*, 2010; Tawfik, Stefan Dancila and Armanios, 2011; Gude, Hufenbach and Kirvel, 2011; Arrieta *et al.*, 2012; Daynes and Weaver, 2013; Eckstein, Pirrera and Weaver, 2014). The residual stresses in multistable composites are commonly achieved through an unsymmetrical layup of laminae. In composite laminates, the ratio of thermal expansion coefficient (CTE) between fibre longitudinal direction and transverse direction tends to be in the order of 10^2 (Mattioni *et al.*, 2008a). Therefore, joining composite plies in different orientations at high curing temperatures and bringing them down to a lower ambient temperature will result in the generation of residual stresses, leading to the deformation of the composite (Li, Dai and Du, 2012).

The residual stress in the bistable/multistable composites leads them to have multiple low potential energy states with each state corresponding to a different shape of the structure (Filippo Mattioni, Paul M Weaver, Kevin Potter, 2005; Zhang *et al.*, 2019). By shifting from one stable low potential energy state to another, shape morphing is achieved, as shown in Figure 2.9.

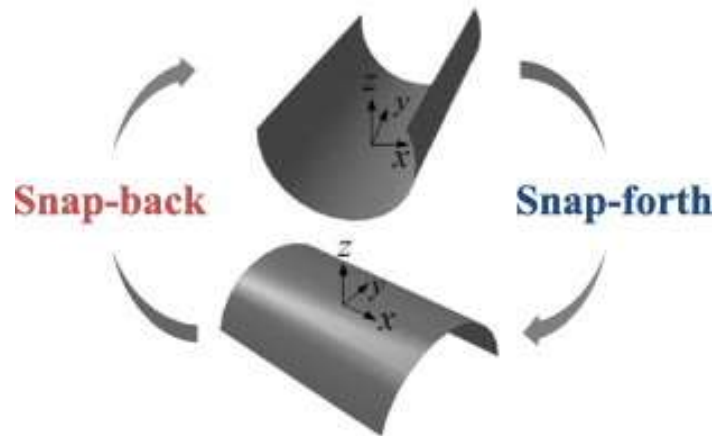


Figure 2.9. Shape morphing of multistable composite by shifting between different low potential energy states (Lee *et al.*, 2015)

Multistable composite structures require external energy, commonly known as ‘snap-through force’, to transfer from one stable shape to another. This can be achieved, for example, using piezoelectric actuation, thermal actuation (see Figure 2.10), SMA actuation, or magnetic actuation systems (Mattioni *et al.*, 2008a; Zhang *et al.*, 2019).

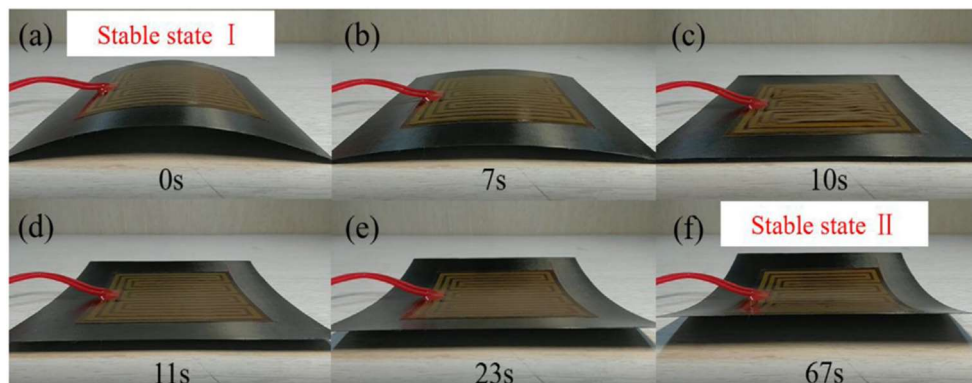


Figure 2.10. Transition of a cross-ply $[0_3/90_3]$ bistable composite from one stable shape to another using thermal actuation (Zhang *et al.*, 2017)

Furthermore, using this approach, different multistable shapes can be achieved by controlling the fibre direction in different laminae, as shown in Figure 2.11 (Portela *et al.*, 2008; Schultz, 2008; Panesar and Weaver, 2012). The work by (Portela *et al.*, 2008) shows that composites with $[0^\circ/90^\circ]$ laminates have multistable shapes with a curvature along the longitudinal direction, while the composites with $[0^\circ/-45^\circ]$ and $[45^\circ/-45^\circ]$ laminates have multistable shapes with curvature oriented at an angle away from longitudinal direction (i.e., in between the longitudinal and transverse directions).



Figure 2.11. Different shapes of bistable composites based on their layup
(Portela *et al.*, 2008)

Another way to achieve residual stress in the composites is by pre-tensioning the fibres. When the prestressed fibres and their matrix are cured into a composite, the stored energy in the fibres imparts the necessary residual stress for the composite to exhibit multistable behaviour. The work by (Daynes *et al.*, 2010) demonstrated that by mechanically loading the fibres of a symmetric layup before and during the curing process, bistable structures can be produced. This work also demonstrated that the bistable composites with prestressed fibres can require up to 72.7% higher load to transition from one stable state to another. Similar work by (Wang and Fancey, 2015) demonstrates that the composites made with viscoelastically prestressed polymeric fibres can also be used to achieve bistable composite structures.

Recent studies by (Chillara and Dapino, 2017, 2019) have also shown that mounting pre-stressed anisotropic elastomeric polymer composites on a stress-free isotropic material can result in the generation of residual stress within them, leading to a structure with bistable configuration (see Figure 2.12).

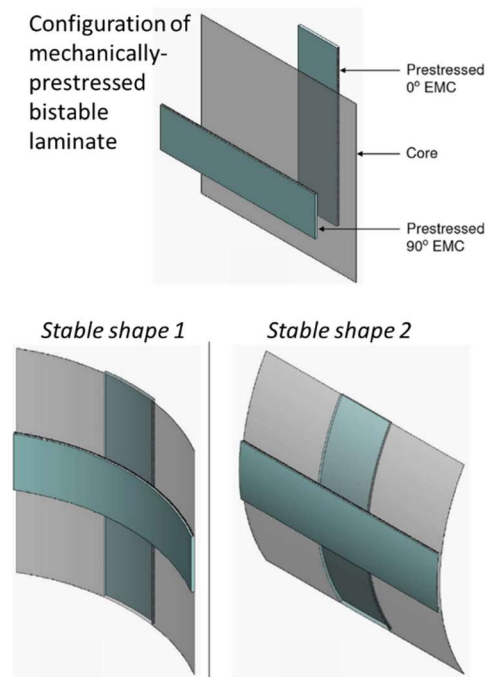


Figure 2.12. Bistable composite with mechanically prestressed elastomeric layers mounted on a stress-free core (Chillara and Dapino, 2017)

Although multistable composites have not been used for structural composites on their own, numerical models have indicated that the shapes of aircraft components can be changed by embedding multistable composites in them. The research by (Kuder *et al.*, 2016) demonstrates the use of bistable composites to change the shape of a compliant NACA 0012 airfoil profile, as shown in Figure 2.13.

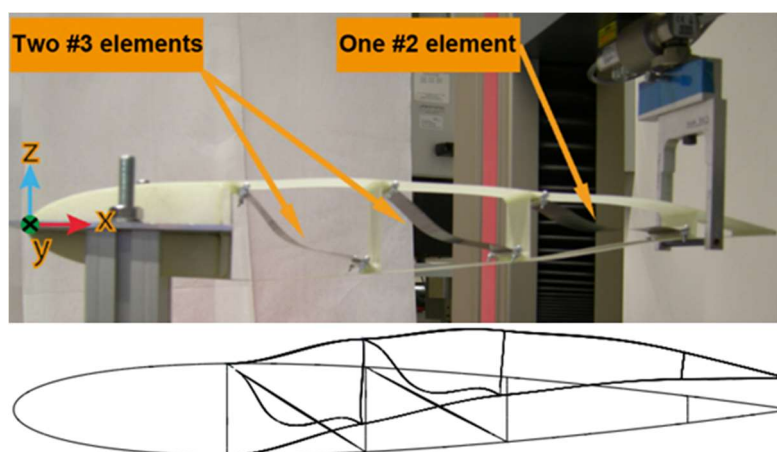
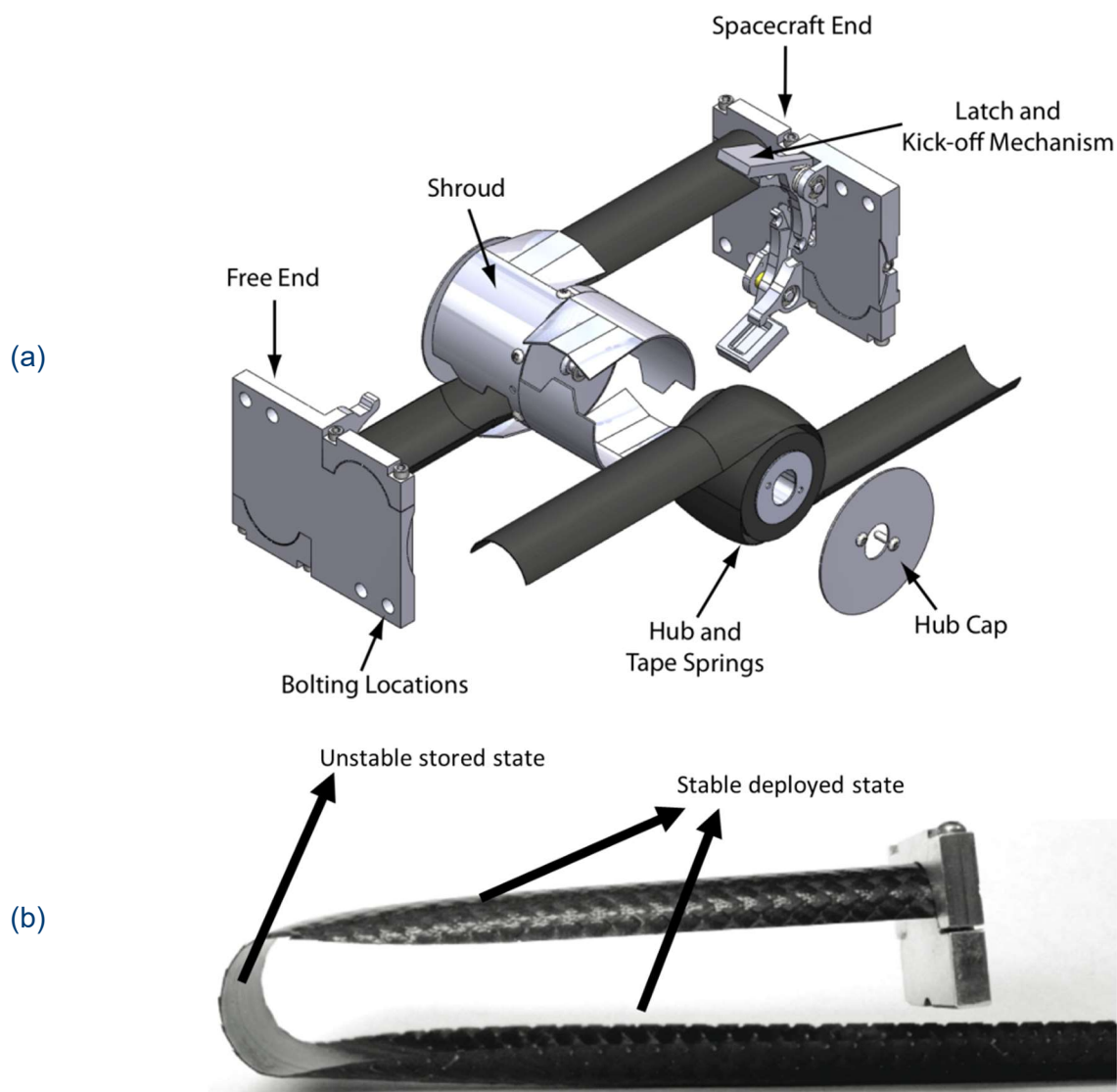


Figure 2.13. Shape change in NACA 0012 wing profile induced by the embedded bistable composites (Kuder *et al.*, 2016)

Studies have also shown that the bistable structures can be used in the deployment of booms in satellites. In the deployable boom structure (see Figure 2.14 (a)) produced by (Jeon and Murphey, 2011), the bistable composite tapes (made using 6k tow T300 carbon fibre plain weave fabric with PMT-7 toughened epoxy) are stored as rolls in their unstable configuration (see Figure 2.14 (b)). Using the stored energy of the tapes, a motor-less deployment was achieved (see Figure 2.14 (c)). Furthermore, the deployment causes the tape to achieve its stable state, therefore preventing the reversal of the deployment.



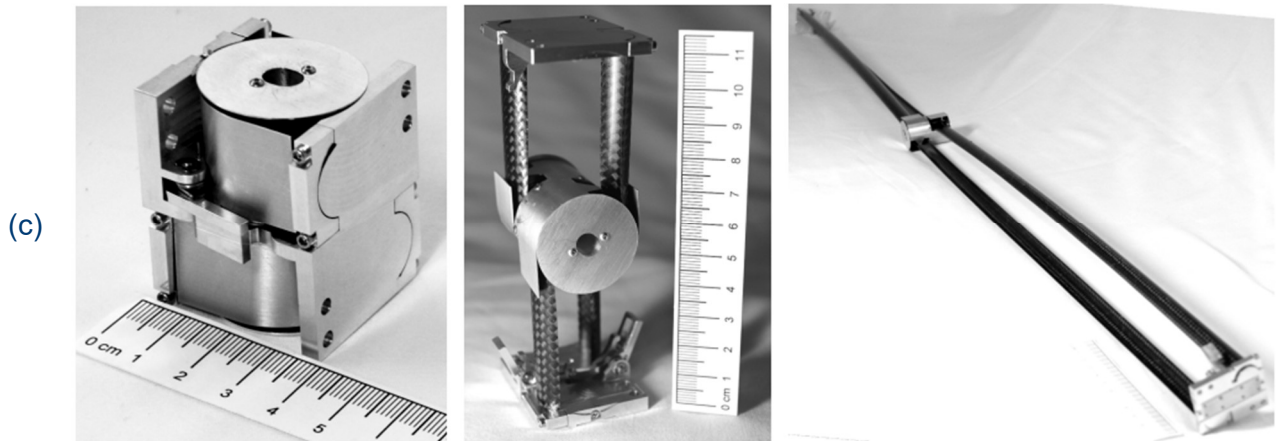


Figure 2.14. (a) The schematic of the deployable boom structure, (b) stable deployed and unstable stored states of composite tape and (c) deployable boom structure at various stages of deployment (Jeon and Murphey, 2011)

While the multistable composites can change their shape with low input energy, they can achieve only a discrete number of shapes as they cannot hold any shape that is in between the different low-energy shape states. This might limit the use of these composites in situations such as flight control surfaces on an aircraft wing as they require continuous and controllable shape changes.

While a simple cross-ply can be used to achieve basic multistable shapes, more complex deformation shapes require careful designing, advanced computation modelling, and sophisticated manufacturing tools. Due to these limitations, the scope of application of these composites to be used in the manufacture of deployable composite structures is limited.

2.2.3. Morphing of anisotropic composites

One way to morph composites is to have lower stiffness in one plane and higher stiffness in the other so that the composite can bear load in one direction while deforming in another direction (Murugan and Friswell, 2013).

Such structural anisotropy in composite structures can be achieved using corrugated profiles (see Figure 2.15). In such composites, the second moment of area along one direction will be much lower than that in the other directions. Hence, these composites tend to be flexible in one direction and rigid in others (Thill *et al.*, 2008; C. Thill, Downsborough, *et al.*, 2010; C.

Thill, Etches, *et al.*, 2010; Christophe Thill *et al.*, 2010; Barvosa-Carter and McKnight, 2011; Dayyani *et al.*, 2015; Shaw, Dayyani and Friswell, 2015; Airoidi *et al.*, 2017; Ermakova and Dayyani, 2017). For example, the corrugated composite structure developed by (Yokozeki *et al.*, 2006) showed that its flexural modulus along the stiff direction was more than 6800 times higher than that in its flexible direction.

Studies have also explored the use of CFRP as additional reinforcements to further increase the stiffness in the direction perpendicular to corrugation, while not affecting the flexibility in the corrugation direction, as shown in Figure 2.16.

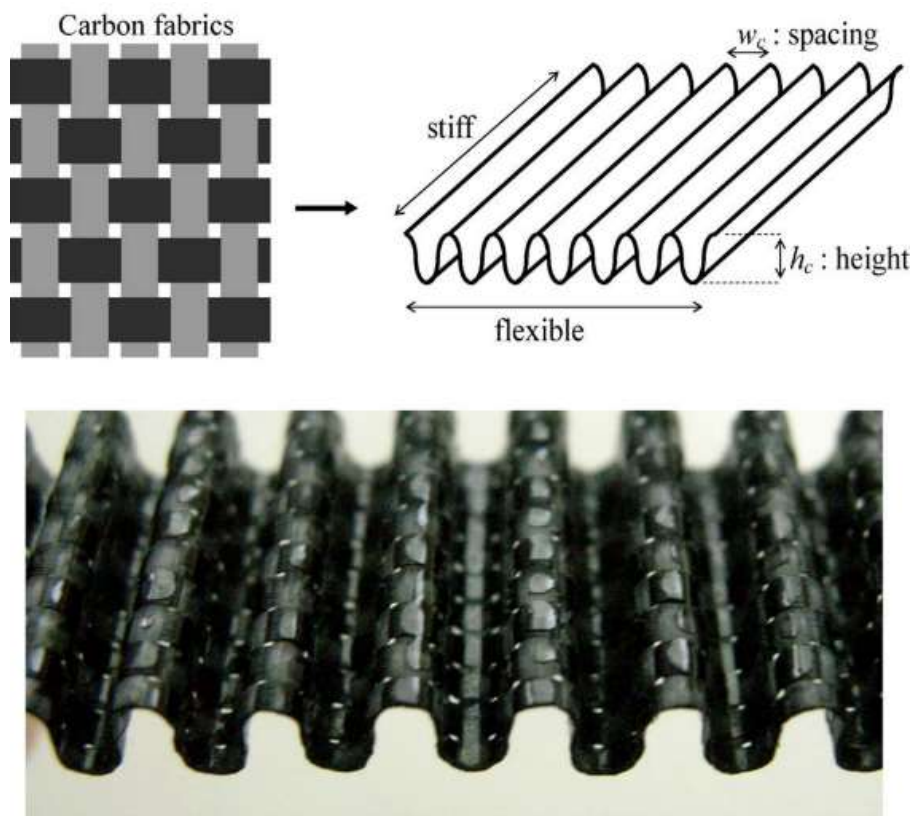


Figure 2.15. Corrugated composite with structural anisotropy (Yokozeki *et al.*, 2006)

Aerodynamic studies have shown that aerofoils that use corrugated composites as skins tend to have higher drag (C. Thill, Downsborough, *et al.*, 2010; Daynes and Weaver, 2013). However, this increase in drag can be avoided by providing corrugated composites with smooth skin. A smooth surface can be achieved by filling or covering the corrugation with flexible/elastomeric material or stiff composite strips (Yokozeki *et al.*, 2006; Daynes and

Weaver, 2013; Dayyani *et al.*, 2015). Thus, by using an anisotropic corrugated core with smooth skin, a flexible sandwich structure can be created (see Figure 2.16).

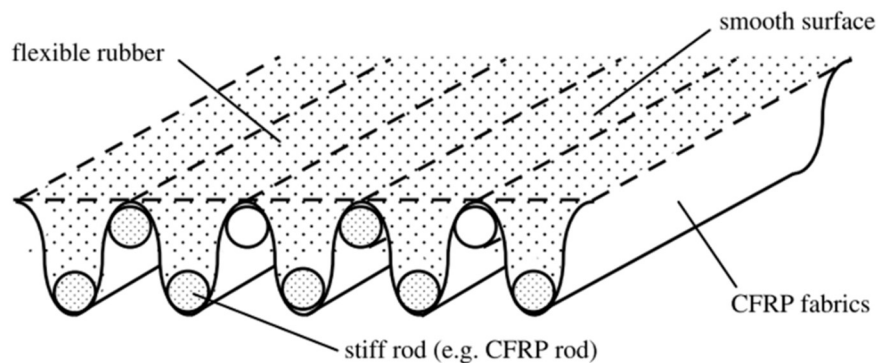


Figure 2.16. Corrugated composite with improved stiffness (due to CFRP rods), and smoother profile (due to flexible rubber) (Yokozeki *et al.*, 2006)

Due to their flexibility in one direction, these anisotropic composites cannot be used to produce morphing structural components in aircraft on their own. The manufacture of corrugated structures is also quite difficult as it requires highly skilled manual labour and/or complex manufacturing tools.

2.2.4. Morphing of shape memory polymer composites

Certain types of polymers, known as shape memory polymers (SMP), show controllable and reversible morphing characteristics (Meng and Li, 2013). The SMPs are an interlinked network of polymer chains whose backbone structure can change shape and orientation without any damage to interlinks. By controlling the applied thermal energy to these polymers, the mobility of the backbone chains can be controlled. When SMPs are heated, deformed, and then cooled down, they tend to stay in the deformed state. When the SMPs are then reheated, they return to their original shape. This phenomenon, shown schematically in Figure 2.17, is called shape memory behaviour.

The reversible shape change property of SMPs can be imparted to composites made with SMP matrices (Gall *et al.*, 2000; McKnight and Henry, 2005; Zhang and Ni, 2007; Lan, Liu, *et al.*, 2009; Yu *et al.*, 2009; Chen *et al.*, 2012; Rodriguez, 2013; Tolley *et al.*, 2014; Jeon, Hauser and Hayward, 2017). Similarly, a combination of SMP and SMA can be used to create flexible

composites with large shape recovery loads (i.e., the force exerted by the composite while it recovers shape) and strains (Tobushi *et al.*, 2009, 2010).

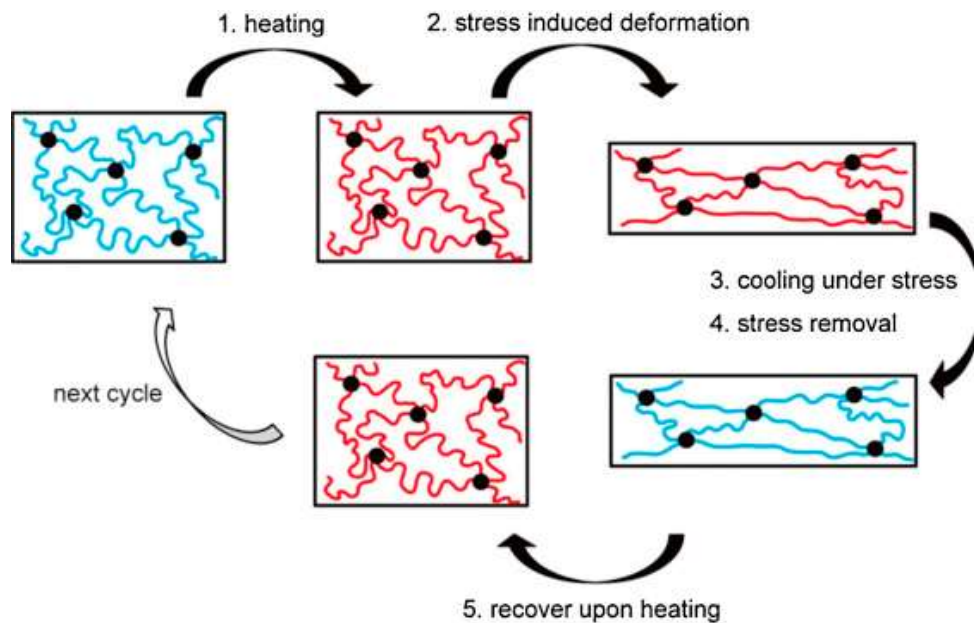


Figure 2.17. Schematic showing the shape memory behaviour of SMPs (Zhao, Qi and Xie, 2015)

SMP-based composites have previously been useful in making deployable structures such as hinges and booms (Arzberger *et al.*, 2005; Lan, Liu, *et al.*, 2009; Puig, Barton and Rando, 2010; Rodriguez, 2013; Liu *et al.*, 2014). A recent work (Le, Le and Goo, 2019) has demonstrated the potential of SMP-based composites in the production of a deployable hinge Figure 2.18. In this work, a deployable hinge structure was made using a composite with both SMP-based and conventional CFRP laminates. As shown in (Figure 2.18), upon heating using a surface-mounted heater, these hinges were able to be bent up to 120°, store the deformed shape upon cooling, and then recover their initial shape upon further heating. In addition to surface-mounted heating, embedded heating systems have also been previously explored to provide SMP-composites with the thermal energy needed for its morphing capabilities (Quadrini *et al.*, 2021).

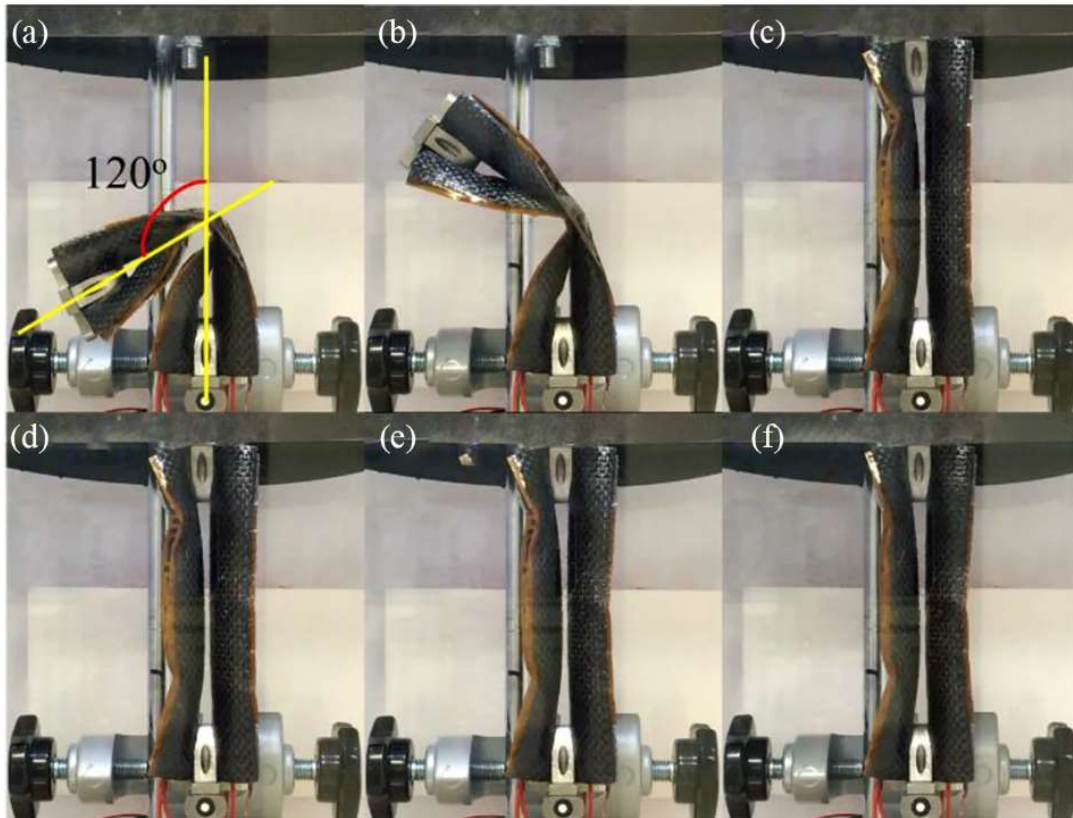


Figure 2.18. Deployable hinge constructed with SMP constituents recovering from 120° bent shape to its initial shape (Le, Le and Goo, 2019)

The SMPs and their composites, however, are mechanically weaker than conventional CFRP composites (Sun, Liu and Leng, 2014; Herath *et al.*, 2018). Furthermore, the SMPs are also specialised materials that are more expensive than conventional polymers (American Chemical Society, 2021). Such drawbacks limit their appeal economically.

2.2.5. Morphing of controllable (variable) stiffness composites

It has been discussed in Section 2.2.3 that morphing of composites is possible when they are flexible (i.e., low stiffness). However, for structural applications, high stiffness is required. Therefore, by maintaining the composite at a high stiffness state in its ambient and loaded state, and then temporarily reducing the stiffness in its unloaded state and when there is a need to change its shape, such shape morphing composites can also be used for structural applications with limited need for additional support structures.

The stiffness of a composite in bending is a product of its flexural modulus and second moment of area. Hence, a composite can be made flexible by either decreasing its flexural modulus or the second moment of area. Research by (Maples *et al.*, 2014) has demonstrated that by temporarily permitting a slip between different plies of a composite, the effective second moment of area of the composite cross-section can be decreased without changing the geometry of the cross-section of the composite, thereby making it more flexible. This ply slip decouples the plies from one another and decreases the shear transfer between them, essentially decreasing the flexural stiffness (and the apparent flexural modulus) of the composite.

Such interply slips can be either passive or active. An interply slip can be considered passive when composite plies that undergo relative slip in ambient conditions can be coupled together under an external stimulus. An interply slip can be considered active when composite plies that are coupled together in ambient conditions can undergo relative slip under an external stimulus.

Passive interply slip has been achieved previously in composites with plies coated with materials such as PVDF (Polyvinylidene fluoride) or PTFE (Polytetrafluoroethylene) that are capable of electrostatic attraction under applied electric potential (Tabata *et al.*, 2001; Bergamini, Christen and Motavalli, 2005, 2007; Bergamini *et al.*, 2006; Di Lillo *et al.*, 2011). The electrostatic attraction that arises from the applied electric potential imparts normal force between the plies. This normal force along with the frictional coefficient between the plies results in their coupling. Therefore, by controlling electric potential, the electrostatic bonding between these plies can be controlled. Here, the coupling of the plies depends on parameters such as dielectric coefficient of the plies, thickness of dielectric layer, applied electric potential, and frictional coefficient between plies.

In a composite that has thermoplastic (TP) layers used as interleaves between composite plies, ply slip can be induced by heating the laminate beyond the glass transition temperature

(T_g) of the TP (see Figure 2.19). Such an active interply slip on a simple layup consisting of balsa wood plies interleaved with hot glue (TP) layer has previously been demonstrated by (Gordon and Clark, 2007). By heating the TP layer with an embedded nichrome wire heating element, the glue layer was made soft, and interply slip was induced. A similar work done by (Gandhi and Kang, 2007) resulted in the production of a variable stiffness composite made of aluminium plies, interleaved with TP polymers that were embedded with electric heating blankets. Extensive studies were also done on CFRP plies interleaved with polystyrene (PS) or poly(styrene-co-maleic anhydride) as the TP interleaves (Robinson *et al.*, 2013, 2017; Maples, 2014; Maples *et al.*, 2014, 2016). In these studies, over 98% reversible loss in the apparent flexural modulus of the composites was achieved.

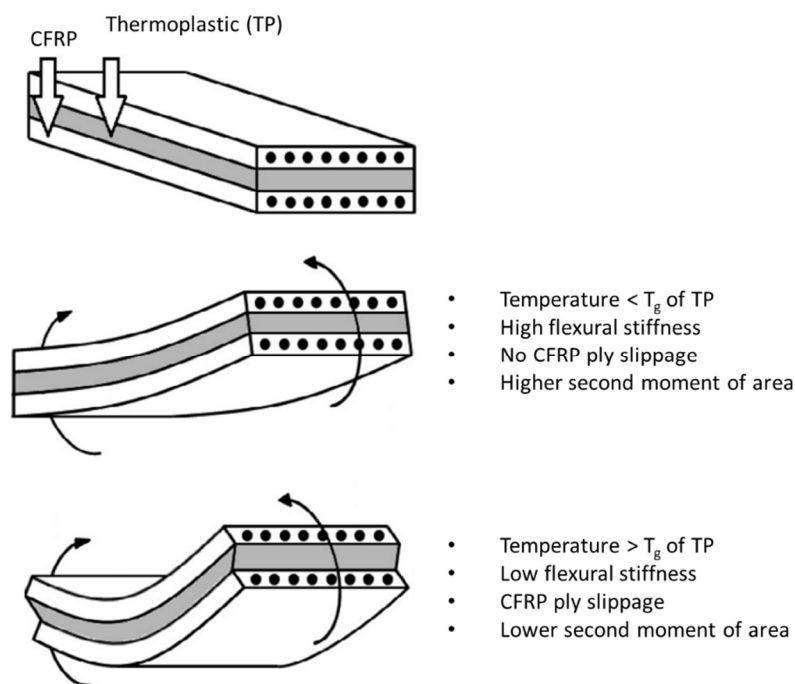


Figure 2.19. Interleaved composite with variable stiffness caused by ply slippage

Similar studies on composites made of discontinuous steel segments connected with a commercially available polyurethane thermoplastic shape memory polymer (MHI Diaplex 5510 by Mitsubishi Heavy Industries) (Figure 2.20) have also shown variable stiffness capabilities that are controlled by their temperature (McKnight and Henry, 2005; McKnight *et al.*, 2007; McKnight *et al.*, 2010). In these composites, the stiffness dropped upon heating, with the ratio

of stiffness of the composite at its high stiffness state to its low stiffness state reaching as high as 77. Furthermore, reversible axial strains of 2-10% were also achieved in these composites.

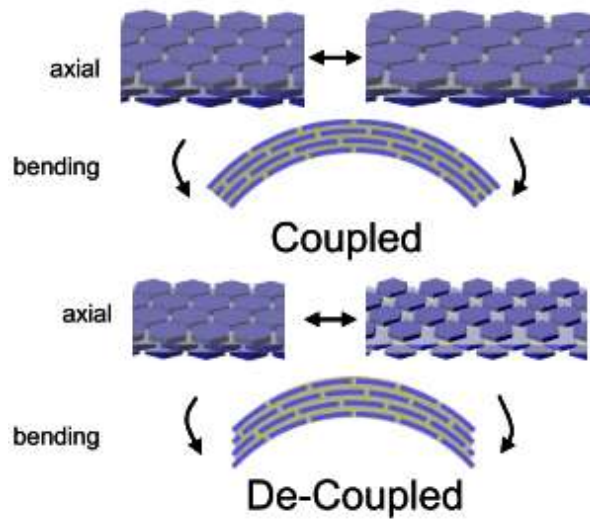


Figure 2.20. Controllable stiffness composite made of segmented stiff plates and a deformable polymer (McKnight *et al.*, 2007)

Each of the discussed approaches used to achieve shape morphing in composites has its list of advantages and disadvantages (see Table 2.1). Among them, it can be seen that the various controllable (variable) stiffness composites made of composite plies with TP interleaves using conventional materials can have a simple manufacturing process and can undergo deployment without the need for an external actuator (Robinson *et al.*, 2017). The further investigation and development of these interleaved composites is the focus of the research presented in this thesis. A detailed insight into the controllable stiffness and shape memory (morphing) capabilities of interleaved composites is provided in Sections 2.3, 2.4, and 2.5.

Table 2.1. Advantages and disadvantages of the various approaches used to achieve shape morphing in composites, as discussed in Section 2.2.

S.No.	Morphing approach	Advantages	Disadvantages
1	Morphing of conventional composites using SMAs	<ul style="list-style-type: none"> • Technology maturity of SMA 	<ul style="list-style-type: none"> • Relatively heavy construction

		<ul style="list-style-type: none"> • Previous in-field testing of the concept 	<ul style="list-style-type: none"> • Limited range of shapes • Expensive constituent materials
2	Multistable composites morphed using external actuation	<ul style="list-style-type: none"> • Technology maturity of concept at lab-scale 	<ul style="list-style-type: none"> • Complex layup design for complex deformations • Discrete number of stable shapes • Complex manufacturing process
3	Anisotropic composites morphed using external actuation	<ul style="list-style-type: none"> • Need for low actuation forces 	<ul style="list-style-type: none"> • Complex manufacturing process
4	Morphing of composites made of SMPs	<ul style="list-style-type: none"> • Technology maturity of SMPs • Previous lab-scale testing of the concept 	<ul style="list-style-type: none"> • Mechanically weaker than conventional composites • Expensive constituent materials
5	Morphing of controllable (variable) stiffness composites	<ul style="list-style-type: none"> • Capable of self-actuation • Need for no (or simple) actuation mechanism • Technology maturity of concept at lab-scale • Simple manufacturing process • Conventional materials 	<ul style="list-style-type: none"> • One-time self-actuation capability • Mechanically weaker than conventional composites • Need for shape control during shape transition

2.3. Controllable stiffness and shape memory characteristics of interleaved composites

Conventionally, laminated composites are made of multiple layers of plies or laminae that are bound together through interlaminar chemical bonds. As discussed in [Section 2.2.5](#), by allowing a slip between the plies of a composite, the stiffness of an interleaved composite can be greatly reduced. When composites are made of CFRP layers interleaved with TP layers, a

slip between the CFRP layers can be enabled by heating the composite from a temperature T^R to T^H ($T^R < T_{g-TP} < T^H < T_{g-CFRP}$, where T_{g-TP} - glass transition temperature of TP and T_{g-CFRP} - glass transition temperature of epoxy in CFRP). Hence, these composites show a loss in flexural stiffness when heated to a temperature T^H , as seen in [Figure 2.19](#), and when the temperature is then reduced to T^R , the initial stiffness is fully restored ([Maples, 2014](#); [Maples et al., 2014](#)).

Due to ply slippage, the CFRP layers can undergo large curvature change without failure when an interleaved composite is in its low stiffness state (i.e., at a temperature of T^H). The interleaved composites are therefore capable of large deformations with relatively low applied forces.

When the composite is brought back to a temperature T^R in the deformed state, the composite returns to its full flexural stiffness and so, upon removal of the deformation force, the deformed shape is almost fully retained. In this state, the stresses are 'locked' inside the CFRP plies. When the unconstrained deformed composite is heated again to temperature T^H , the stored energy (stored stress) is released since the CFRP plies are now free to slide again, and the composite returns to its original shape, thus making the composite exhibit shape memory behaviour (see [Figure 2.21](#)). The above-mentioned loading cycle can be repeated to achieve multiple shape memory morphing cycles. However, previous research have revealed development of significant degradation within the thermoplastic region of the interleaved composites when subjected to shape memory deformation ([Robinson et al., 2017](#)). This degradation indicates the presence of a limitation on the number of shape memory morphing cycles that the previously developed interleaved composites are capable of exhibiting. Some deployable structures made using such TP-interleaved composites are discussed in [Section 2.5](#).

Another significant challenge that can be identified in the morphing (i.e., shape memory) capability of such composites is the need to control their shape at T^H . During the morphing process, when the composite is in its low-stiffness state (at T^H), any unplanned forces acting

on the structure can cause undesirable changes to its shape. Hence, to control the shape of the composite as desired, it is necessary to either morph the composite (or structure) in its unloaded state or use a support structure that can prevent undesirable shape changes.

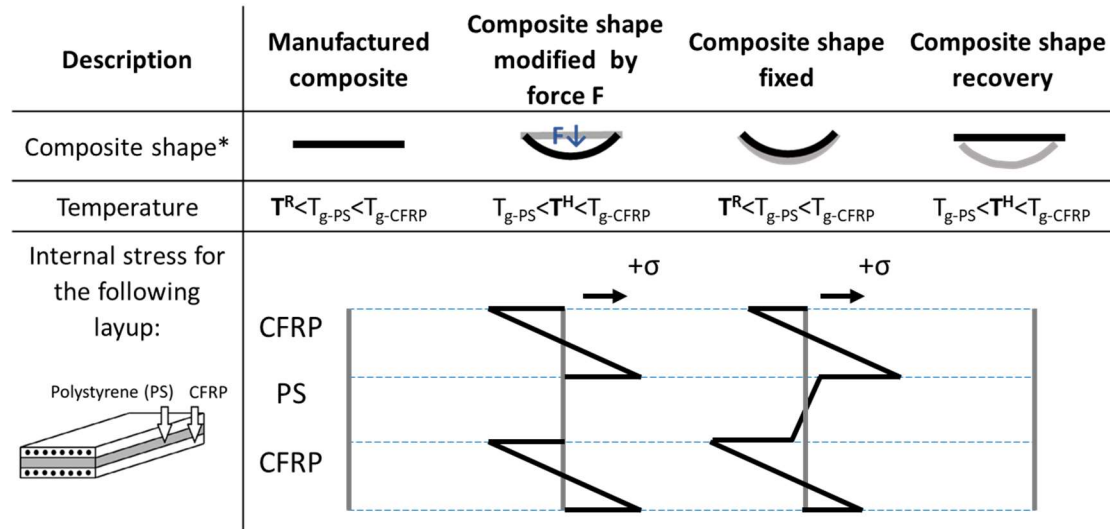


Figure 2.21. Schematic of the shape memory process in interleaved composites

(Robinson *et al.*, 2017).

* Grey line – Initial shape, Black line – Final shape

2.4. Generation of residual stresses in interleaved composites during manufacture to allow deployment directly from as-cured state

In the shape memory process described in Section 2.3, it can be seen that to achieve morphing of an interleaved composite from a shape A to a shape B (in the example presented in Section 2.3, shape A was curved and shape B was straight), the interleaved composite has to be initially cured in shape B, then deformed into shape A at T^H and then cooled to T^R . After this, the interleaved composite can be deployed to shape B by reheating it to T^H . Consequently, two drawbacks can be identified in the manufacturing of interleaved composites that may be capable of morphing. The first drawback is that if the deployed shape is complex, then there may be a significant production cost to manufacture the composite in that shape. The second drawback is the need to deform the composite at T^H before deployment to the ‘non-deployed’ shape, adding further to the production cost.

Some preliminary research has been done to overcome this drawback by manufacturing the composite directly in the non-deployed shape (i.e., shape B) in such a way that it can then be deployed to a different shape (i.e., shape A) just by heating, thereby removing the ‘deformation step’. The strain energy necessary for the morphing of the composite was achieved through the generation of residual stresses within the composites as it was cured (Zhang *et al.*, 2018; Zhang, 2020).

When a composite is made of unsymmetric pairs of CFRP plies, the difference between curing and ambient temperatures will result in the development of residual stresses within the CFRP plies and deform them (see Figure 2.22 (a)). A composite made of a number of such unsymmetric sublaminae interleaved with thermoplastic laminae and held flat during the curing process (e.g., in an autoclave) will have smaller curvature in its cured state than a single unsymmetric sublaminate. As the number of unsymmetric sublaminae in a composite is increased, its curvature will reduce and become ‘almost flat’ (see Figure 2.22 (b)). When the composite is then heated to T^H , the TP layers will soften and allow the unsymmetric CFRP sub-laminates to slip relative to one another, dissipate the stored residual stresses, and change their shape, as shown in Figure 2.22 (b). Upon cooling the composite back to T^R , the deformed shape of the composite will be retained. Hence, using this approach, deployment of a composite can be achieved by directly heating the composite from its as-cured state.

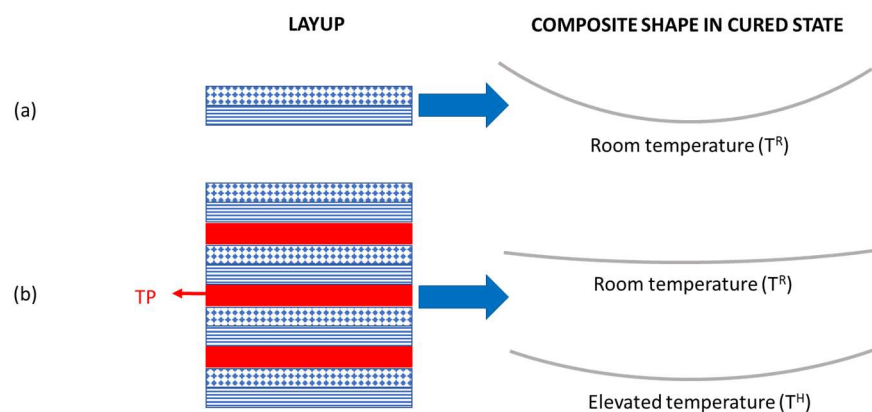


Figure 2.22. Morphing of (a) cross-ply, and (b) TP interleaved cross-ply composite using residual stress approach

2.5. Deployable structures made with interleaved composites

Interleaved composites have been used to produce deployable composites of various shapes. In the research work done by (Robinson *et al.*, 2017), 'L' shaped composite specimens were reshaped into 'U' and 'I' shapes, and the 'L' shape was then recovered upon heating. By combining a number of such deployable specimens and conventional composites, a deployable box section was developed, as shown in Figure 2.23.

In the work by (Zhang, 2020), meshes made of composite materials were produced as initially flat structures. Upon heating, reshaping, and cooling down, an expanded mesh was produced. When the unconstrained mesh was then reheated, the initial as-cured shape was recovered, as shown in Figure 2.24. Some preliminary investigations into the production of composite meshes (with cross-ply sub-laminates) that are flat in the as-cured state, and can deploy into mesh upon heating (see Figure 2.25) were also conducted by (Zhang *et al.*, 2018) using the methodology discussed in Section 2.4.

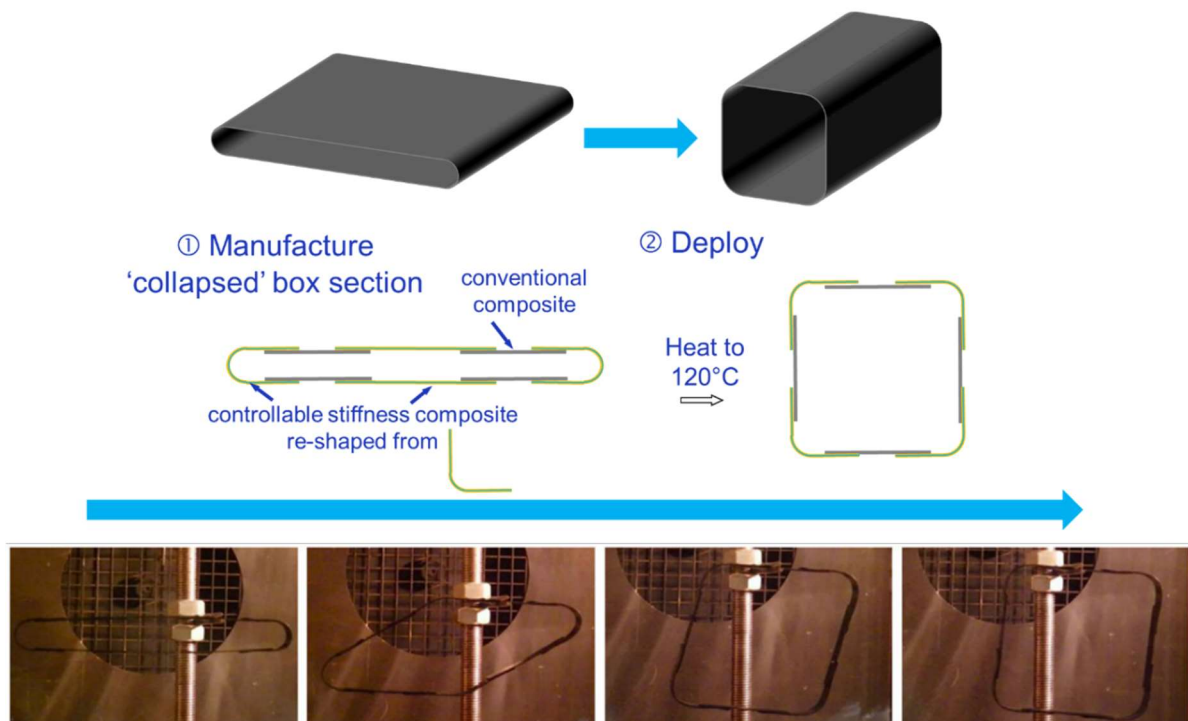


Figure 2.23. Deployable box section made using conventional and TP interleaved CFRP composite specimens (Robinson *et al.*, 2017; Zhang *et al.*, 2018)

Expanded mesh returning to as-cured flat state upon heating

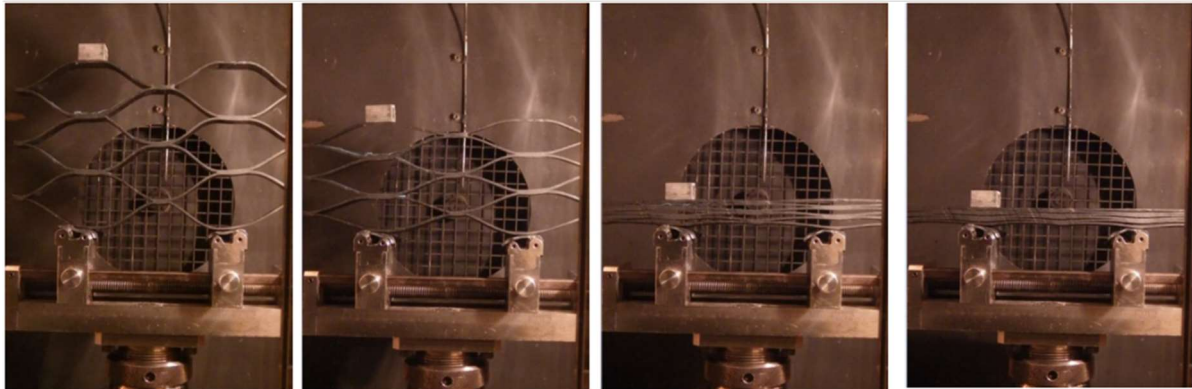


Figure 2.24. Composite mesh with shape contraction capability (Zhang, 2020)

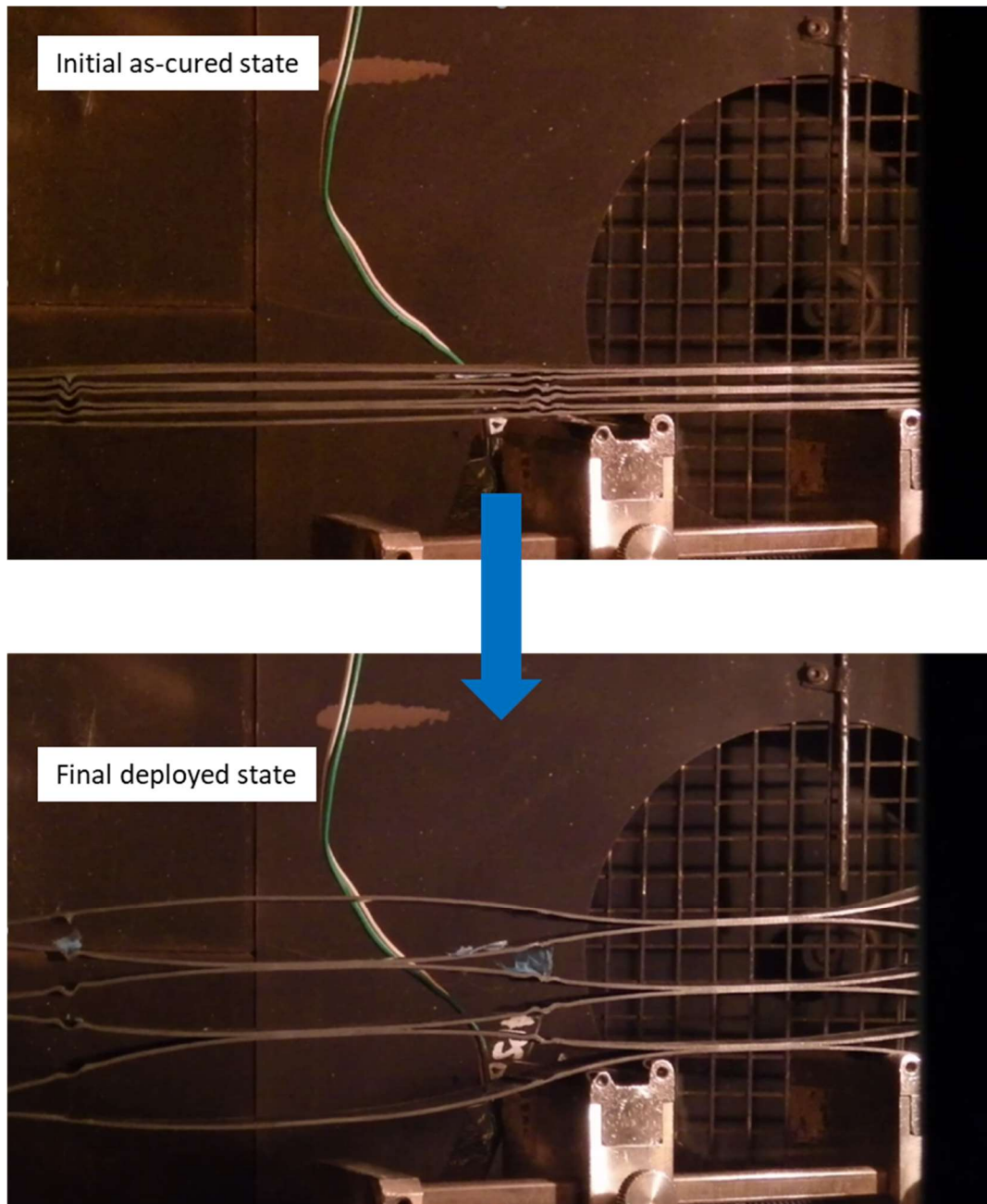


Figure 2.25. Composite mesh with shape expansion capability (Zhang *et al.*, 2018)

2.6. Mechanical performance of interleaved composites

In conventional CFRP composites, carbon fibre reinforcements play a major role in their load-bearing capabilities. With the introduction of unreinforced TP interleaves, the fraction of carbon fibres in the composite cross-section decreases, and the flexural stiffness of the interleaved composites can reduce significantly. It can be seen from [Figure 2.26](#) that for several CFRP-PS interleaved composite layups having different distributions of thermoplastic PS interleaves

(dark region in the layup sequence), the apparent flexural modulus at room temperature is much lower than that of the 0° control samples. The reduced flexural modulus at a temperature of 120 °C ($T_{g-PS} < T^H < T_{g-CFRP}$) is also shown in Figure 2.26.

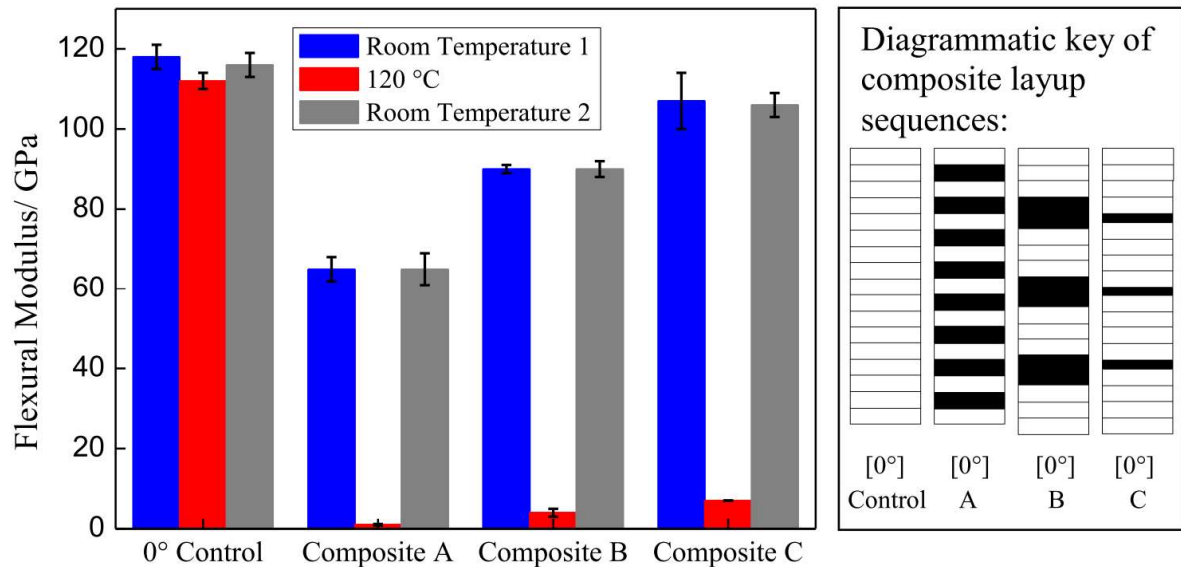


Figure 2.26. Flexural modulus of various interleaved composites at different temperatures (Maples, 2014).

(Here, tests were performed on composite specimens according to ASTM 2344 standards.

All layups had a thickness of ~2 mm and each CFRP layer had a thickness of ~0.125 mm.)

Based on the data presented in the previous research, it is clear that one strategy for improving the flexural modulus of the thermoplastic interleaved CFRP is to decrease the thickness of the interleaves.

Another strategy for improving the flexural modulus of the thermoplastic interleaved CFRP could be to reinforce the thermoplastic layers. The state-of-the-art of reinforcement of TP matrices, therefore, is briefly explored in Section 2.7.

The research presented in this thesis examines both of these strategies to improve the flexural modulus of thermoplastic interleaved CFRP composites while retaining their CS and SM properties.

Furthermore, when compared to CFRP composites, interleaved composites exhibit lower flexural strength, as shown in Table 2.2 (Maples, 2014; Maples *et al.*, 2016; Zhang *et al.*, 2018). The failure during flexural tests of CFRP-PS composites was observed to be a premature shear failure at the TP interlaminar region and can be attributed to either the poor interfacial shear strength between the CFRP and the PS layer, or the low shear strength of PS. However, the exact location of the premature failure was not identified.

Table 2.2. Flexural strength of interleaved composites (Maples, 2014).

Composite	Flexural tests			SBS tests [†]	
	Apparent Flexural Strength/ MPa			τ_{\max} at Failure/ MPa	ILSS/ MPa
	RT [†]	120 °C	% loss	RT	RT
0° control	1550 ± 11	636 ± 25	59	24 ± 0.2	111 ± 2
A	966 ± 18 (936) [‡]	- [*] (23)	- (98)	15 ± 0.3	71 ± 6
B	894 ± 12 (1280)	- [*] (81)	- (93)	14 ± 0.2	79 ± 4
C	987 ± 20 (1474)	- [*] (132)	- (91)	15 ± 0.3	52 ± 2

[†] RT: Room temperature, SBS: Short beam shear

(Theoretically predicted values are provided in brackets.)

The composite layups are shown in Figure 2.26)

2.7. Reinforcement of thermoplastic matrices

To improve the mechanical properties of interleaved composites reinforcements can be introduced in the thermoplastic interleaves, as suggested in Section 2.6.

Carbon fibre reinforced thermoplastics have been an interest of research since the 1980s (Chang and Lees, 1988). A variety of thermoplastic materials (such as PEEK (Mallon, O'Brádaigh and Pipes, 1989; Yuan, Shyu and Lai, 1991), PPS (Kishi *et al.*, 2017), ABS (Liang *et al.*, 2000), PS (Suzhu and Hing, 2008), PA (Sugahara *et al.*, 2014; Zopp *et al.*, 2019), MMA (Kishi *et al.*, 2017), and PEKK (Schuster *et al.*, 2018)) have been used as matrices in such composites (Yao *et al.*, 2018).

Various forms of carbon reinforcements that have been considered include unidirectional long fibres (Sugahara *et al.*, 2014), short fibres (Liang *et al.*, 2000; Rezaei *et al.*, 2008), recycled carbon fibres (Wong *et al.*, 2012; Yao *et al.*, 2018; Khurshid *et al.*, 2019), or even carbon nanotubes (CNT) in some cases (Peters, Papavassiliou and Grady, 2008; Li and Chen, 2012).

However, unlike thermoset CFRP which commonly has an epoxy-based matrix, the carbon fibres do not interact well with the TP matrix materials due to limited reactivity between the surface of pristine CFRP and the polymer backbone of conventional TPs. This poor bond detrimentally affects the mechanical properties of the carbon fibre reinforced thermoplastics. To promote these bonds, surface treatment of carbon fibres using plasma (Yuan, Shyu and Lai, 1991; Li and Zhou, 2010) or nitric acid treatment (Liang *et al.*, 2000; Li and Sun, 2009b, 2009a; Li and Cai, 2011) is commonly undertaken. Surface treatment allows the addition of reactive groups to the surface of the carbon fibres. Similarly, the addition of reactive groups to standard thermoplastics through grafting or blending can also be used to promote their interaction with the reinforcements (Li and Sun, 2009a, 2009b; Li and Cai, 2011).

Reinforced thermoplastic composites can be manufactured using several approaches (Gibson and Manson, 1992; Lustiger and Jang, 1992; De Almeida, Bessard and Bernhart, 2012) such as melt impregnation (Bigg *et al.*, 1988), using comingled fabric (Wang, Mayer and Neitzel, 1997; Bernet *et al.*, 1999), solvent impregnation, and film stacking (Grouve and Akkerman, 2010; Zal *et al.*, 2016). Among these manufacturing methods, melt impregnation or solvent impregnation are used extensively in industry for large-scale production of thermoplastic prepregs.

However, for the small-scale production used in the research presented in this thesis, the film stacking process (see Figure 2.27) is sufficient.

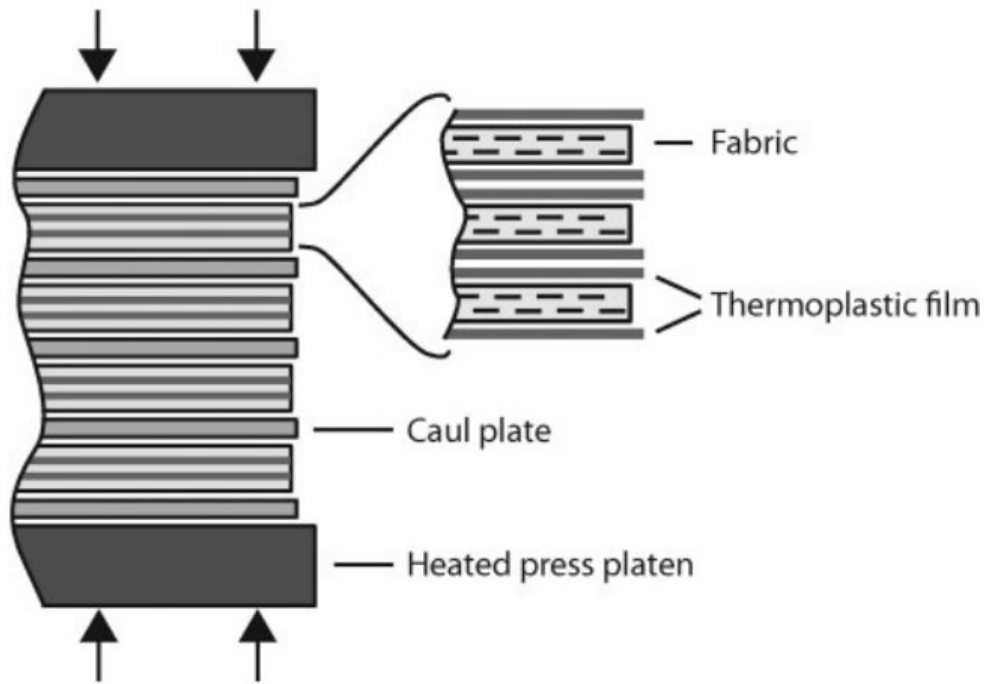


Figure 2.27. Film stacking process used in the manufacture of reinforced thermoplastic composites (Grouve and Akkerman, 2010)

2.8. Intrinsic heating of composites

It can be seen in [Section 2.3](#) that controllable stiffness and shape memory behaviours of thermoplastic interleaved composite are governed by temperature. The necessary temperature for controllable stiffness and shape memory (morphing) capabilities of the interleaved composites in previous studies has usually been achieved by using an environmental chamber or a convection oven ([Robinson *et al.*, 2013, 2017](#); [Tridech *et al.*, 2013](#); [Maples, 2014](#); [Maples *et al.*, 2014, 2016](#)). However, to achieve out-of-laboratory controllable stiffness and shape memory capabilities, it is necessary to produce interleaved composites with intrinsic heating capabilities.

Intrinsic heating of composites has been previously explored for their applications in the welding of TP composites ([Ageorges, Ye and Hou, 2000a](#); [Stavrov and Bersee, 2005](#); [Dubé *et al.*, 2011](#); [Villegas and Bersee, 2015](#); [O'Shaughnessey, Dubé and Villegas, 2016](#); [Brassard, Dubé and Tavares, 2019](#); [Russello *et al.*, 2020](#)), shape-memory morphing ([Choi and Lee, 1998](#); [Francis *et al.*, 2003](#); [Lan, Liu, *et al.*, 2009](#); [Lan, Wang, *et al.*, 2009](#); [Brampton *et al.*,](#)

2014; Wang, Lee and Liu, 2017), self-healing (Wang *et al.*, 2012), and anti-icing (Buschhorn *et al.*, 2013). In these applications, the heating of composites was achieved by either joule heating of embedded heating systems/elements or by inductive heating. The study by (Villegas and Bersee, 2015) explores a simple but effective way of heating the composites by Joule heating of embedded stainless steel meshes. In this work, temperatures close to 400°C were reached to achieve resistive welding of thermoplastic composites.

Some preliminary investigations by (Maples, 2014) have also looked into heating interleaved composites by resistive heating of the carbon fibres in the CFRP laminae, as shown in Figure 2.28. The electrical connection to the carbon fibres was achieved through copper tapes bonded to the specimen using silver-loaded adhesive. Although controllable stiffness and shape memory capabilities were achieved in these laboratory-based tests, it is unlikely that this approach would be suitable for practical applications.

The drawbacks include the robustness of the electrical connection to the carbon fibres, and the requirement to have enough continuous longitudinal reinforcing fibres to achieve the required heating.

Another major challenge associated with heating of thermoplastics is the generation of voids within them (Xiao, 1993; Ageorges, Ye and Hou, 2000b; Lu, Ye and Mai, 2004; Wolfrath, Michaud and Manson, 2005; Shi, Villegas and Bersee, 2016; Robinson *et al.*, 2017; Zhang, 2020; Totla *et al.*, 2023; Zhao *et al.*, 2023). The reason behind the formation of voids, especially during resistance or induction welding of thermoplastics, have been found to be either, a) phase change of trapped moisture, b) coalescence of trapped air, or c) thermal degradation. Hence, to prevent formation of voids within the thermoplastic region of the interleaved composites, avoiding these void-inducing aspects is crucial.

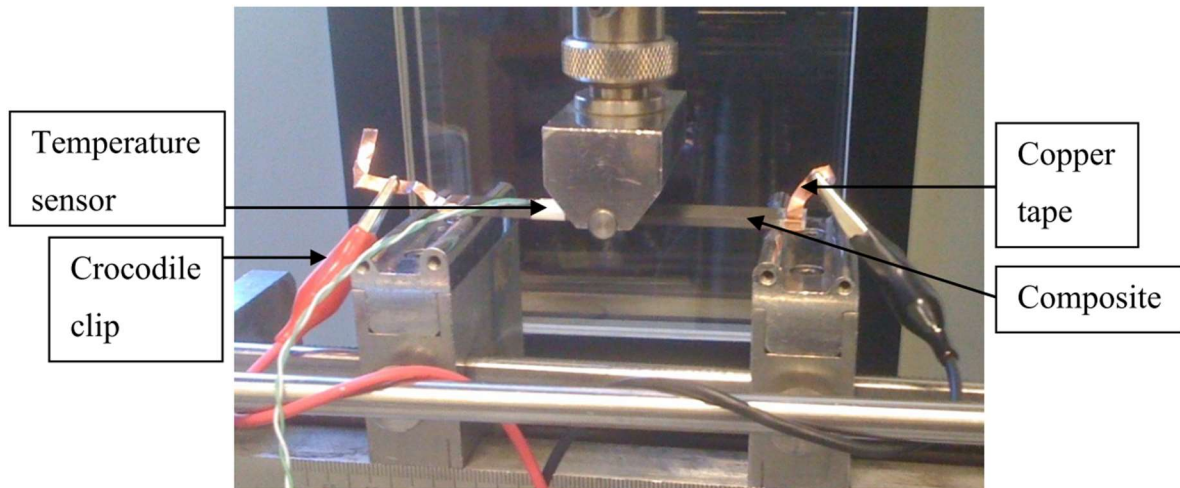


Figure 2.28. Experimental setup for heating interleaved composites by resistive heating of outermost CFRP plies (Maples, 2014)

2.9. Propositions based on the literature study

From the literature study, the following propositions related to the aims of the research can be identified:

- By understanding the location and mechanism of the premature through-thickness shear failure of the CFRP-PS interleaved composites loaded in flexure, the steps required to improve the apparent flexural strength can be determined (using a stronger interleaf material and/or by improving the interfacial properties between CFRP and the TP interleaves).
- The flexural stiffness of the interleaved composites can be improved by reducing the quantity of the unreinforced TP interleaves within the layup. One of the simplest ways in which the reduction of the quantity of the unreinforced TP interleaves within the layup can be achieved is by reducing the thickness of the interleaves.
- The flexural stiffness of the interleaved composites can also be improved by replacing the unreinforced TP layers with reinforced TP layers. To reinforce the TP interleaves, a film stacking approach can be used while the composite is laid up.
- Intrinsic heating of composites can be achieved by introducing resistive heating layers inside the layup sequence. These resistive heaters can also be embedded into the

thermoplastic interleaves of the composite using the film stacking approach.

- By generating residual stresses within the CFRP laminae of an interleaved composite during the curing process, it is possible to develop a composite structure that is initially almost flat but can then deploy into a complex shape on a subsequent heating-cooling cycle.

Chapter 3. Improvement of the through-thickness shear strength of thermoplastic interleaved carbon-epoxy composites

As shown in [Section 2.6](#), PS-interleaved CFRP composites loaded in a 3-point bending test setup underwent premature through-thickness shear failure associated with the PS interleaf ([Maples, 2014](#); [Maples *et al.*, 2016](#); [Zhang *et al.*, 2018](#)). This chapter describes studies to overcome the shear weakness observed in the PS-interleaved CFRP composites.

The first section of this chapter reports on an investigation to establish whether the shear failure occurred within the PS interleaf or at the interface between CFRP laminae and PS interleaves. If the failure had occurred within the PS interleaf, then the through-thickness shear strength of the thermoplastic interleaved CFRP composites can be improved by improving the intrinsic shear strength of the interleaves. If the failure had occurred at the interface between CFRP laminae and PS interleaves, then the improvement of through-thickness shear strength of the thermoplastic interleaved CFRP composites will require an investigation into the surface treatment of the interleaves.

The second section of this chapter describes a study to identify alternative thermoplastic interleaves that could help in improving the through-thickness shear strength of thermoplastic interleaved CFRP composites. The final section of this chapter includes an investigation to confirm that the interleaved composites containing the thermoplastic interleaf material that is selected as a replacement for PS showed good controllable stiffness and shape memory capabilities.

3.1. Identification of the location of premature through-thickness shear failure in PS-interleaved CFRP composites

To identify the through-thickness shear failure location in PS-interleaved CFRP composites, 3-point bending (3PB) tests of composite specimens of suitable dimensions were performed to induce a through-thickness shear failure. After the through-thickness shear failure, the elemental composition of the fracture surfaces was analysed and compared to the elemental composition of pristine CFRP and PS.

3.1.1. Materials and laminates

Unidirectional TS300/914 carbon epoxy prepreg (Hexcel, UK), which has a cured thickness of 125 μm (Ciba-Geigy Plastics, 1989), was selected for the CFRP part of the interleaved composite. The interleaf material selected to be a part of the interleaved composite was Styrolution 124N (INEOS Styrolution GmbH, Germany) polystyrene film, produced at Transfercenter für Kunststofftechnik (TCKT) by film extrusion method, with a thickness of 70 μm .

Composite panels (175 mm x 220 mm) were prepared with layups shown in Table 3.1. These panels were cured at 175°C and 7 bar pressure in an autoclave for 1 hour according to the cure schedule recommended by the manufacturer of the CFRP.

Table 3.1. Names and layups of the composite panels
prepared for the studies shown in Section 3.1

Composite name	Layup	Nominal thickness of interleaf films used in layup (μm)
Control	$[0^\circ]_{25}$	-
CFRP-PS	$[0^\circ_{12}/\text{PS}/0^\circ_{12}]$	70

3.1.2. Experimental methodology

3.1.2.1. 3-point bending (3PB) tests

Specimens having the dimensions shown in Table 3.2 were cut from the cured composite panels using a circular dry saw (Startrite, UK).

The flexural tests were performed in a three-point bending (3PB) fixture broadly according to the ASTM D7264M standard. A support span of 70 mm was used. The diameter of the support and loading rollers was 6 mm (whereas the test standard specifies 5 mm). Each specimen was loaded in a universal test machine (Instron 5960 series, USA) equipped with a 50 kN load cell. Flexural tests were conducted at a constant crosshead speed of 1 mm/min at room temperature until a sharp drop in the applied force is observed.

Table 3.2. Dimensions of composite specimens used in the
3PB tests described in Section 3.1.2.1

(here, l , w , t – length, width and thickness of the specimens)

Composite name	Dimensions ^{*†‡§}		
	l (mm)	w (mm)	t (mm)
Control	80.30 ± 0.74	10.15 ± 0.19	2.92 ± 0.01
CFRP-PS	80.80 ± 0.16	9.97 ± 0.10	2.90 ± 0.03

* Any data provided in this thesis in the ' $X \pm Y$ ' format represents the 'Average \pm Standard deviation' of the datapoints in its dataset.

† Unless mentioned otherwise, any data provided in this thesis in the ' $X \pm Y$ ' format consists of a minimum of 5 datapoints in its dataset.

‡ All the specimen dimensions (i.e., length (l), width (w), and thickness (t)) provided in this thesis were measured as specified in Appendix A.1.

§ Unless mentioned otherwise, the 0° fibre direction in the CFRP laminae of all the specimens in this thesis was parallel to their longer edge.

3.1.2.2. *Optical microscopy of composites*

After the failure in flexural tests, the central 20 mm section (i.e., mid-span) of selected specimens was mounted in polyester potting resin (KLEER-SET TYPE FF, MetPrep Ltd., UK) and cured at room temperature. The mounted specimens were then polished in a grinder-polishing machine (Saphir 550, ATM GmbH, Germany) using P600 silicon carbide grinding paper followed by polishing using dispersions of diamond (9 μm), alumina (0.3 μm) and silica (0.06 μm) before being inspected using an optical microscope (ZEISS Axio Imager 2, Carl Zeiss AG, Germany).

3.1.2.3. *XPS analysis*

After the CFRP-PS composite specimens underwent premature through-thickness shear failure as a result of the flexural tests described in [Section 3.1.2.1](#), their fracture surfaces were analysed using X-ray photoelectron spectroscopy (XPS) to identify their elemental composition. To serve as a baseline for comparison, the surface of the pristine PS films and control composite specimens were also analysed using XPS.

The XPS analysis was performed using a Nexsa XPS analyser (Thermo Fisher Scientific Inc., USA). The analysed surfaces were initially cleaned with an argon ion etch with an energy of 6000 eV for 60 seconds using an Argon cluster of 1000 atoms to remove surface impurities deposited on the surfaces as a result of exposure to the atmosphere. Using Al-K α X-rays on a 400 μm diameter spot, wide-scan XPS spectra were recorded with 1 eV resolution and high-resolution XPS spectra of carbon (C1s) peaks with a resolution of 0.1 eV.

3.1.3. *Results and discussion*

3.1.3.1. *3PB test results*

Typical load-displacement curves of the control and CFRP-PS composites in flexural tests are shown in [Figure 3.1](#). Conventionally, the load at which the failure of a specimen initiates is considered the load at which its load-displacement (or stress-strain) curve diverges from its

initial linearity (Lee and Waas, 1999; Blackman and Kinloch, 2001; Huang *et al.*, 2020; Kadiyala *et al.*, 2022). Hence, for consistency, in the flexural tests performed in this research, the load associated with the initiation of failure in flexure tests is considered as the load at which the non-linearity in the load-displacement curves begins. The methodology to select the load associated with the initiation of failure (L_f) is explained in detail in [Appendix A.2](#).

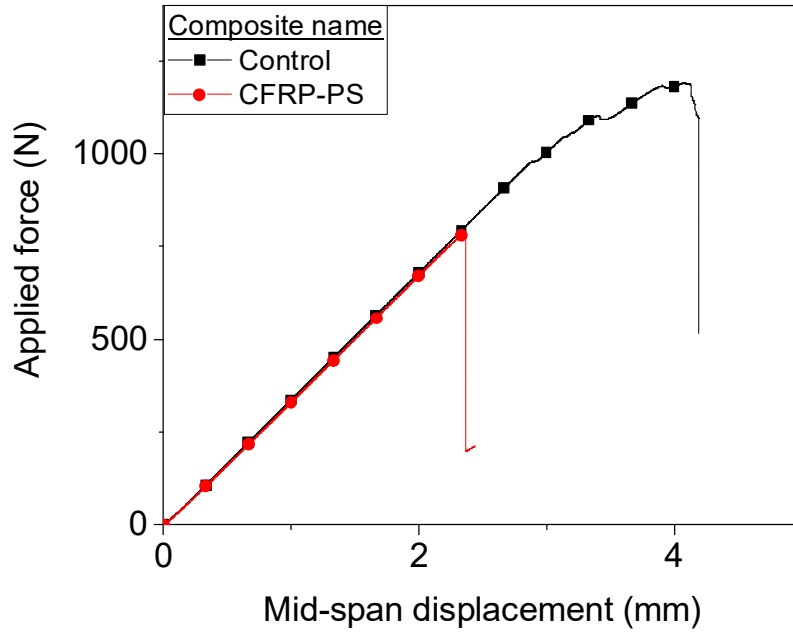


Figure 3.1. Typical load-displacement curves of the composites in the 3PB tests described in Section 3.1.2.1

The maximum bending (σ^{\max}) and shear (τ^{\max}) stresses associated with the load associated with the initiation of failure (L_f) were calculated using equations [Eq 3-1](#) and [Eq 3-2](#) and are listed in [Table 3.3](#).

$$\sigma^{\max} = \frac{3 L_f s}{2 w t^2} \quad \text{Eq 3-1}$$

where, s , w , t – span, width, and thickness of each specimen

$$\tau^{\max} = \frac{3 L_f}{4 t w} \quad \text{Eq 3-2}$$

Table 3.3. Maximum bending (σ^{\max}) and shear (τ^{\max}) stresses (at L_f) of composites in the 3PB tests described in Section 3.1.2.1

Composite name	σ^{\max} (GPa)	τ^{\max} (MPa)
Control	1.37 ± 0.04	28.69 ± 0.83
CFRP-PS	0.97 ± 0.04	20.17 ± 1.09

Micrographs of polished longitudinal cross-sections of the composite specimens tested until failure in 3PB tests are shown in Figure 3.2. The failure in the control composite is due to flexural failure of the CFRP, with evidence of compressive and tensile failures seen at the upper and lower surfaces respectively. This observation is further supported by the agreement between σ^{\max} of the control composite and the 0° compressive strength of the CFRP (1.35 GPa (Ciba-Geigy Plastics, 1989)). Furthermore, this observation also adds credibility to the failure load selection criteria used in this experiment.

As observed in previous work, the failure in CFRP-PS composite is due to premature through-thickness shear failure either due to shear failure of the PS interleaf or due to an interfacial failure between the CFRP plies and the PS interleaf. The micrographs (see Figure 3.2) also indicate that the PS interleaf is attached to only one of the fracture surfaces and completely detached from the other fracture surface, thereby indicating the presence of an interfacial failure. However, visual inspection of the fracture surfaces (see Figure 3.3) shows the presence of lighter-coloured PS regions on both the fracture surfaces, thereby indicating the probable presence PS on both the fracture surfaces. Hence, to validate the presence (or absence) of PS on both the fracture surfaces, XPS was performed on them.

3.1.3.2. XPS results

The typical wide range XPS survey* of the pristine PS film, control composite, and the fracture surfaces of CFRP-PS composites are shown in Figure 3.4, where the y-axes show the counts of electrons detected per second (c/s) by the XPS setup, corresponding to a particular binding energy. The atomic composition of different specimens obtained from the wide range XPS survey is provided in Table 3.4. Similarly, the typical deconvoluted high-resolution C1s spectra of the pristine PS film, control composite, and the fracture surfaces of CFRP-PS composites are shown in Figure 3.5, and the associated composition is provided in Table 3.5.

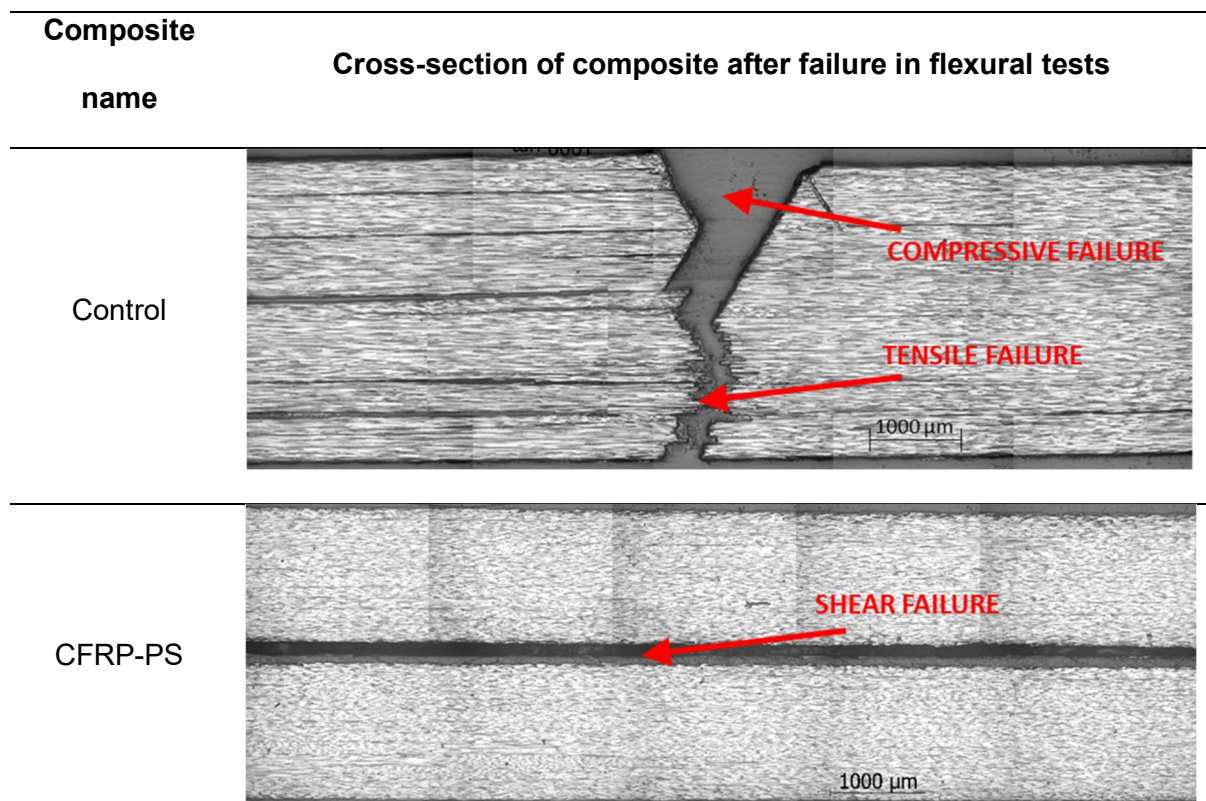


Figure 3.2. Micrographs of polished longitudinal cross-sections of the composite specimens tested until failure in the 3PB tests described in Section 3.1.2.1

* Using the technique mentioned in Section 3.1.2.3, XPS analysis was performed on random spots on the fracture surfaces spread out randomly across visually lighter and darker coloured regions.

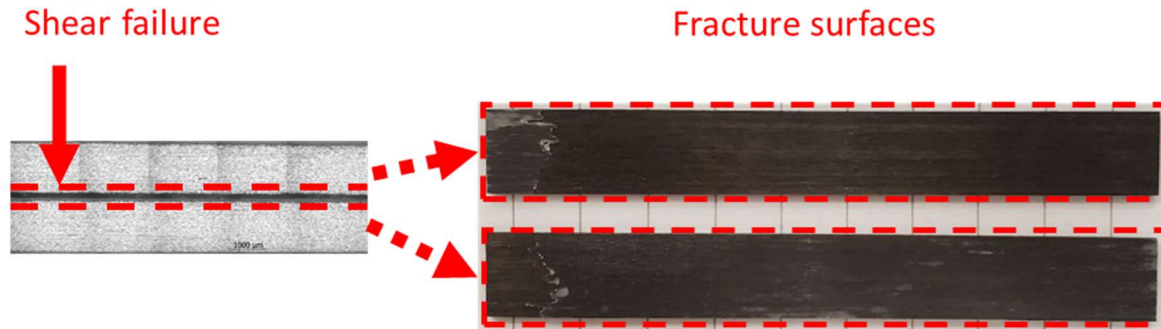
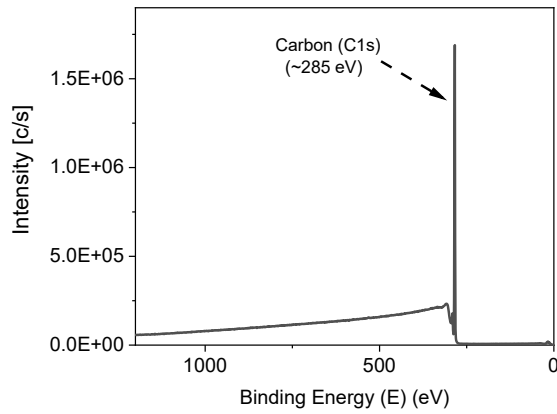


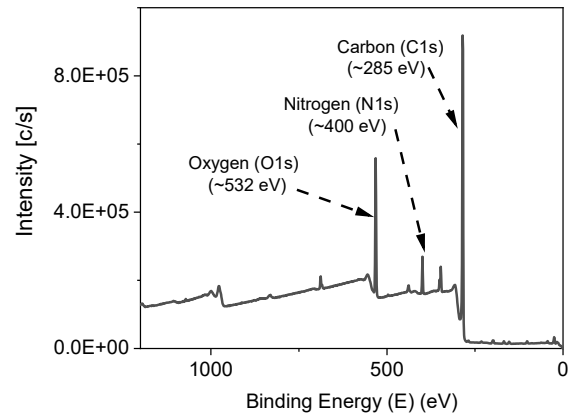
Figure 3.3. Photographs of the fracture surfaces of CFRP-PS specimens

The wide range XPS analysis of the pristine PS films predominantly showed the presence of carbon (C1s) peaks (see Figure 3.4). The deconvoluted C1s spectra of the pristine PS films (see Figure 3.5) also indicated the presence of C-C/C=C and $\pi=\pi$ peaks, as expected for the PS polymer (Beamson and Briggs, 1993).

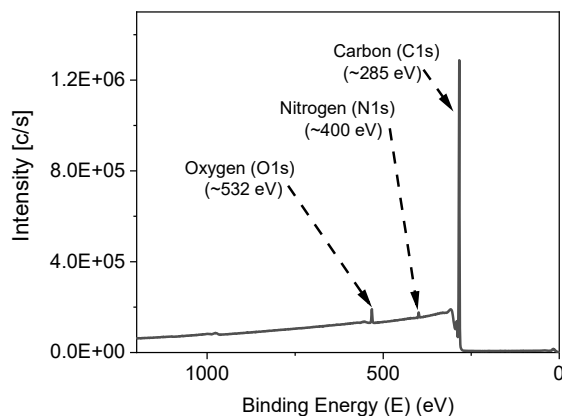
The wide range XPS analysis of the control composites showed that the carbon (C1s), oxygen (O1s) and nitrogen (N1s) peaks were dominant while the peaks corresponding to other elements were not present or were negligible (see Figure 3.4). Furthermore, the deconvoluted C1s spectra of the control composites (see Figure 3.5) also indicated the presence of C-C/C=C and C-O/C=O peaks, as expected for an epoxy matrix. Furthermore, a small fraction of $\pi=\pi$ peaks, much lower than that of PS, were also observed here.



(a) Pristine PS film



(b) Control composite

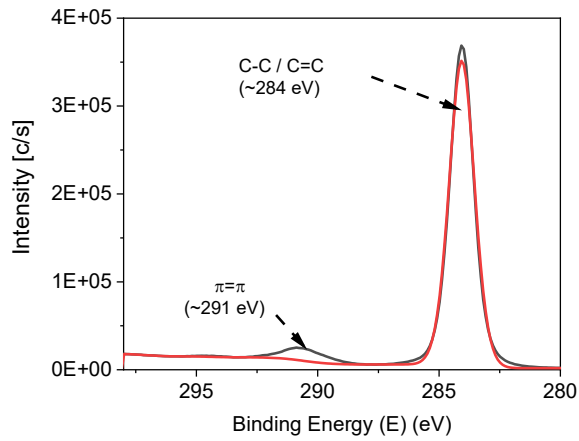


(c) fracture surfaces CFRP-PS composite

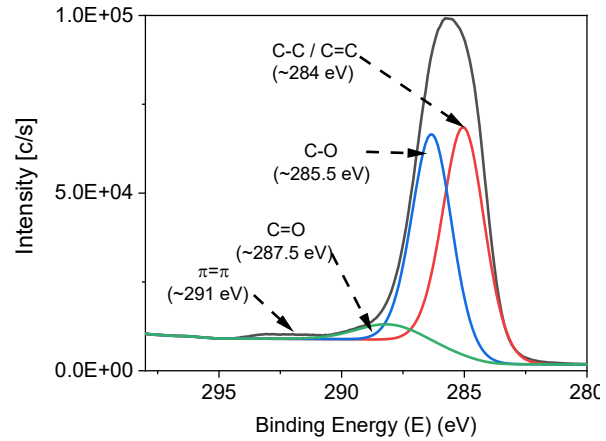
Figure 3.4. Typical wide range XPS survey of (a) pristine PS film, (b) control composite, and (c) the fracture surfaces CFRP-PS composite

Table 3.4. Atomic composition of specimens, as observed using XPS

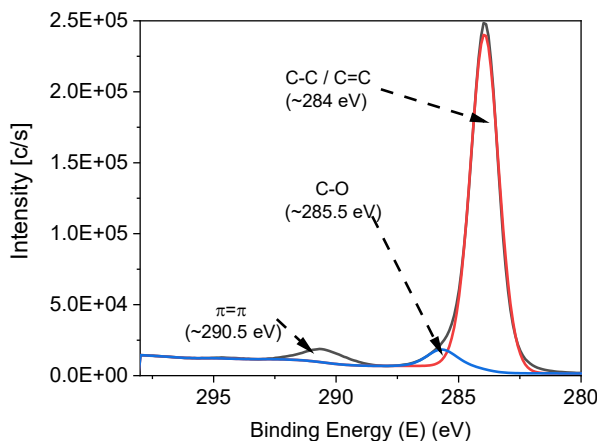
Specimen	C1s	O1s	N1s
	Carbon (%)	Oxygen (%)	Nitrogen (%)
PS film	99.89 ± 0.12	0.11 ± 0.12	0
Control composite	76.03 ± 0.26	16.22 ± 0.20	7.75 ± 0.26
Fracture surfaces of CFRP-PS composite	91.07 ± 6.51	5.39 ± 3.92	3.51 ± 2.63



(a) pristine PS film



(b) control composite



(c) fracture surfaces of CFRP-PS composite

Figure 3.5. Typical deconvoluted carbon (C1s) peaks of the XP-spectra of (a) pristine PS film, (b) control composite, and (c) the fracture surfaces of CFRP-PS composite

Table 3.5. Bond composition within the C1s peaks of specimens, as observed using XPS

Specimen	C-C/C=C bonds (%)	C-O bonds (%)	C=O bonds (%)	π=π bonds (%)
PS film	93.08 ± 3.54	-	-	6.92 ± 3.54
Control composite	54.13 ± 8.45	40.50 ± 7.83	4.08 ± 1.82	1.28 ± 0.20
Fracture surfaces of CFRP-PS composite	81.49 ± 11.92	14.64 ± 12.75	-	3.87 ± 1.26

When the fracture surfaces of the CFRP-PS composites were analysed using a wide range XPS, carbon (C1s), oxygen (O1s) and nitrogen (N1s) peaks were seen (see Figure 3.4).

However, as shown in Table 3.4, the concentration of oxygen and nitrogen on the fracture surfaces was higher than that of pristine PS, but less than that of the control composite. Furthermore, the deconvoluted C1s spectra of the fracture surfaces revealed a strong presence of both $\pi=\pi$ and C-O peaks, which are characteristic of pristine PS and control composite respectively. The composition of these bonds (see Table 3.5) shows that these fracture surfaces have less C-O bonds than the control composites and less $\pi=\pi$ bonds than the pristine PS films. Furthermore, the fracture surfaces did not show any C=O bonds, unlike the control composite.

Such an XPS observation can be seen if the Al-K α X-rays used in XPS interact with a thin PS layer on the fracture surface, and then breaches through it to interact with the CFRP substrates lying underneath the PS. This observation, therefore, indicates the probable presence of a thin residue of the PS film on the fracture surfaces.

The residue of PS can be found on both the fracture surfaces indicating that the premature through-thickness shear failure in CFRP-PS composites had occurred within the PS interleaf due to its shear failure. Although the presence of residual PS on the fracture surfaces is evident, the large standard deviations seen in Table 3.5 indicate a large variation in the C1s bonds (i.e., C-C/C=C, C-O and $\pi=\pi$) on the fracture surfaces probably due to the variation of the thickness of the residual PS layers.

3.1.4. Conclusion

When a CFRP-PS interleaved composite of a suitable dimension is subjected to 3PB tests at suitable test conditions, a premature through-thickness shear failure is seen. XPS analysis of both the fracture surfaces indicates the presence of residues of PS interleaves. This

observation indicates that the through-thickness shear failure in the CFRP-PS composites had occurred inside the PS interleaf rather than at the interface between CFRP and PS*.

3.2. Investigation of alternative interleaf materials to improve the through-thickness shear strength of thermoplastic interleaved carbon-epoxy composites

The results from the study described in [Section 3.1](#) indicate that an increase in through-thickness shear strength of thermoplastic interleaved carbon-epoxy composites is possible by replacing the PS interleaves with a stronger alternative TP material. In addition, the alternative interleaf material must also form a sufficiently strong bond with the adjacent CFRP plies to avoid interfacial failure between the CFRP laminae and TP interleaves.

For comparison to the study described in [Section 3.1](#), 3PB tests were on composites with alternative TP interleaves to assess the failure mode of the interleaved composites. For sufficiently strong interleaves, through-thickness shear failure was not seen in the 3PB tests. Therefore, SBS tests were also performed on these interleaved composites to identify their shear failure strength.

3.2.1. Materials and laminates

To identify materials that could replace PS as interleaf materials, the following criteria were used – 1) The selected polymer should have their higher (or comparable) bulk tensile yield strength than PS, due to the reason mentioned at the start of this chapter, 2) The selected polymer should have higher (or comparable) quantity of nucleophilic groups in them to facilitate formation of a strong bond with CFRP, 3) The selected polymer should not degrade when the interleaved composite is cured or when it undergoes high-temperature morphing, 4) The selected polymer should possess higher (or comparable) Young's modulus than PS so

* Exploitation of this failure mechanism to repair the CFRP-PS composites is shown in [Appendix A.3](#).

that the interleaved composites made with these interleaves have their plane sections remain plane when loaded in flexure at room temperature so that simple analytical and experimental calculation tools can be used to predict/calculate the mechanical properties of the composites, and 5) The selected polymer should be easy to manufacture as thin films.

The interleaf materials selected to be a part of the interleaved composite are listed in [Table 3.7](#). Among these materials, PS was selected to serve as a comparison with previous works ([Zhang, 2020](#)). Upon recommendation by experts from University of Vienna (Prof Alexander Bismarck), and Transfercenter für Kunststofftechnik (FH-Prof. Dr. Christoph Burgstaller), SAN, MABS and ASA+PC were selected as possible replacements for PS, as they were identified to comply with the criteria mentioned above (see [Table 3.7](#)).

The interleaf materials were supplied by Transfercenter für Kunststofftechnik (TCKT) as rolls of films. As in the previous study ([Section 3.1](#)), unidirectional TS300/914 carbon epoxy prepreg was selected as the CFRP component of the interleaved composite.

Composite panels (175 mm x 220 mm) were prepared with layups shown in [Table 3.6](#). These panels were cured at 175°C and 7 bar pressure in an autoclave for 1 hour according to the cure schedule recommended by the manufacturer of the CFRP.

3.2.2. Experimental methodology

3.2.2.1. 3PB and SBS tests

For 3PB and SBS tests, specimens having the dimensions shown in [Table 3.8](#) were cut from the cured composite panels using a circular dry saw (Startrite, UK). The 3PB tests were performed as described in [Section 3.1.2.1](#).

The SBS tests were performed in an SBS fixture broadly according to the ASTM D2344M standard. A support span of 12 mm was used. The diameter of the support and loading rollers was 6.3 mm (whereas the test standard specifies 5 mm). Each specimen was loaded in a universal test machine (Instron 5960 series, USA) equipped with a 50 kN load cell. SBS tests

were conducted at a constant crosshead speed of 1 mm/min at room temperature until a sharp drop in the applied force is observed.

3.2.2.2. Optical microscopy of composites

After 3PB tests, the central 20 mm section (i.e., mid-span) of selected specimens was inspected by optical microscopy by following the methodology described in [Section 3.1.2.2](#).

Table 3.6. Names and layups of the composite panels
prepared for the studies shown in [Section 3.2](#)

Composite name	Layup	Nominal thickness of interleaf films used in layup (μm)
Control ¹	$[0^\circ]_{25}$	-
CFRP-PS ¹	$[0^\circ_{12}/\text{PS}/0^\circ_{12}]$	70
CFRP-SAN	$[0^\circ_{12}/\text{SAN}/0^\circ_{12}]$	100
CFRP-MABS	$[0^\circ_{12}/\text{MABS}/0^\circ_{12}]$	100
CFRP-ASA+PC	$[0^\circ_{12}/\text{ASA+PC}/0^\circ_{12}]$	100

¹ Some/all data obtained from the characterisation of this composite has previously been shown in [Section 3.1](#).

Table 3.7. Alternative thermoplastic interleaf materials explored in this study

TP polymer	Trade name	Manufacturer of polymer	Glass transition temperature ¹ T _g [°C]	Melt temperature [°C]	Tensile yield strength ² (MPa); <i>Test standard</i>	Tensile modulus ² (GPa); <i>Test standard</i>
Polystyrene (PS)	Styrolution 124N	INEOS (Germany)	88	180-280	50; <i>ISO 527-2</i>	3.2; <i>ISO 527-1</i>
Poly(styrene-co-acrylonitrile) (SAN)	Luran 368R	INEOS (Germany)	102	220-260	75; <i>ISO 527-2</i>	3.7; <i>ISO 527-1</i>
Poly(methyl methacrylate-co-acrylonitrile-co-butadiene-co-styrene) (MABS)	LG MABS TR557	LG Chem Ltd. (South Korea)	99	190-220	48; <i>ASTM D638</i>	2.0; <i>ASTM D638</i>
Poly(acrylonitrile-co-styrene-co-acrylate) Polycarbonate blend (ASA+PC)	Luran S KR2863C	INEOS (Germany)	109, 142 ³	260-300	62; <i>ISO 527-2</i>	2.5; <i>ISO 527-1</i>

¹ Obtained from DSC tests (see [Appendix A.4](#)), where no degradation of polymers was observed for a temperature range of 25°C to 210°C; ²

Obtained from ([UL Prospector, 2000b, 2000a, 2012, 2013](#)); ³ 109°C is the T_g of the ASA part and 142°C is the T_g of the PC part of the blend

Table 3.8. Dimensions of composite specimens used in the
SBS and 3PB tests described in Section 3.2.2.1

(here, l , w , t – length, width and thickness of the specimens)

Composite name	SBS tests			3PB tests		
	l (mm)	w (mm)	t (mm)	l (mm)	w (mm)	t (mm)
Control	$15.18 \pm$	$6.17 \pm$	$2.90 \pm$	$80.30 \pm$	$10.15 \pm$	$2.92 \pm$
	0.13	0.06	0.02	0.74	0.19	0.01
CFRP-PS	$15.79 \pm$	$5.84 \pm$	$2.97 \pm$	$80.80 \pm$	$9.97 \pm$	$2.90 \pm$
	0.11	0.12	0.03	0.16	0.10	0.03
CFRP-SAN	$15.83 \pm$	$5.82 \pm$	$2.71 \pm$	$80.78 \pm$	$9.94 \pm$	$2.80 \pm$
	0.08	0.17	0.04	0.21	0.14	0.04
CFRP-MABS	$15.74 \pm$	$5.69 \pm$	$2.56 \pm$	$80.68 \pm$	$9.95 \pm$	$2.37 \pm$
	0.08	0.20	0.01	0.36	0.10	0.06
CFRP-ASA+PC	$15.82 \pm$	$5.88 \pm$	$2.95 \pm$	$80.75 \pm$	$9.93 \pm$	$2.85 \pm$
	0.04	0.08	0.04	0.07	0.18	0.06

3.2.3. Results and discussions

3.2.3.1. 3PB test results

Typical load-displacement curves of different composite specimens in 3PB tests are shown in Figure 3.6, where the corresponding micrographs of polished longitudinal cross-sections are also provided. As described in Section 3.1.3.1, the load associated with the initiation of failure (L_f) of each composite specimen was determined and the associated bending (σ^{max}) and shear (τ^{max}) stresses are shown in Table 3.9.

Table 3.9. σ^{max} and τ^{max} of composite specimens in the
3PB tests described in Section 3.2.2.1

Composite name	σ^{max} (GPa)	τ^{max} (MPa)
Control	1.37 ± 0.04	28.69 ± 0.91
CFRP-PS	0.97 ± 0.04	20.17 ± 1.09
CFRP-SAN	1.38 ± 0.04	27.58 ± 0.72
CFRP-MABS	1.20 ± 0.16	20.37 ± 3.01
CFRP-ASA+PC	1.30 ± 0.05	26.41 ± 1.43

The magnitude of σ^{max} and the associated microsection indicates flexural failure of CFRP in the control (as expected) and in CFRP-SAN and CFRP-ASA+PC composites, with failure stresses close to the 0° compressive strength of the CFRP (1.35 GPa ([Ciba-Geigy Plastics, 1989](#))). However, the CFRP-PS and CFRP-MABS composites showed through-thickness shear failure during these tests.

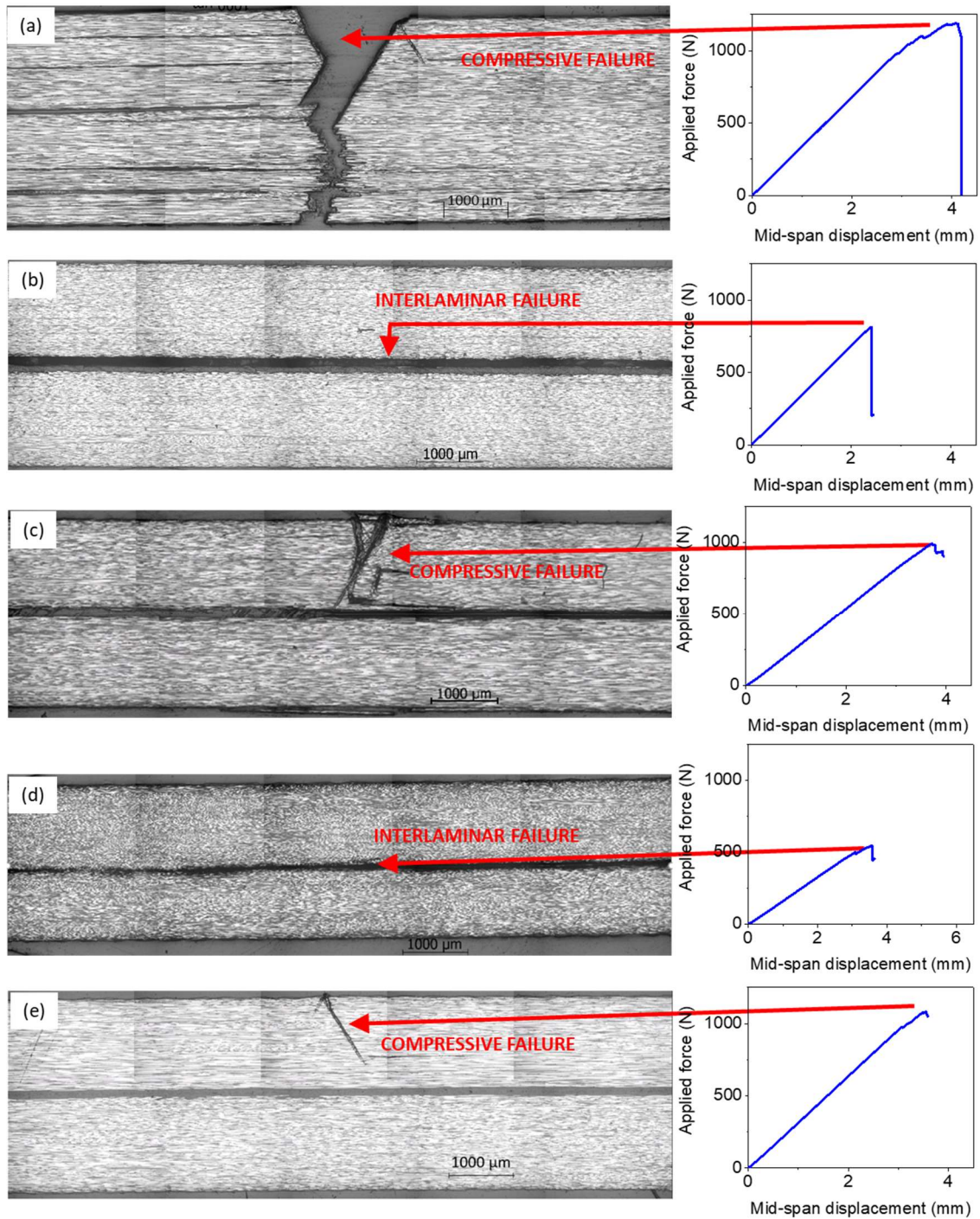


Figure 3.6. Polished longitudinal microsection and the associated force-displacement curves obtained from the 3PB tests of (a) control, (b) CFRP-PS, (c) CFRP-SAN, (d) CFRP-MABS, (e) CFRP-ASA+PC composites

3.2.3.2. SBS test results

Typical load-displacement curves of different composite specimens in SBS tests are shown in Figure 3.7. The load-displacement curves of the SBS tests of CFRP-PS, CFRP-SAN, CFRP-MABS and CFRP-ASA+PC composites diverge from their initial linearity at around 0.2-0.3 mm midspan displacement, followed by a total loss of load-bearing capabilities at around 0.55 mm midspan displacement. These characteristics are most likely due to the onset of yielding of the TP interleaf, followed by a failure in the CFRP laminae.

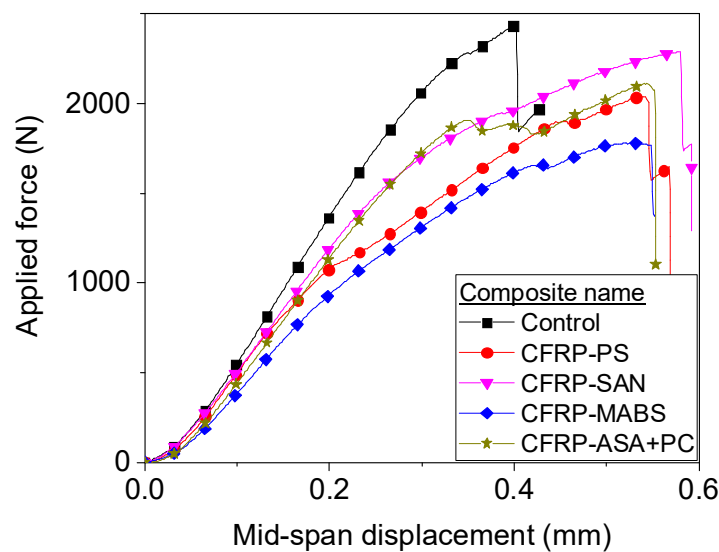


Figure 3.7. Typical load-displacement curves of the composites in the SBS tests described in Section 3.2.2.1

As shown previously in Section 3.1.3.1, the load (L_f) associated with the initiation of failure in the SBS tests was determined as the load at which the load-displacement curve diverges from its linear segment, by following the methodology described in Appendix A.2*.

For each composite specimen, the maximum shear stress ($\tau^{max(SBS)}$) calculated using the load associated with the initiation of failure (L_f) was calculated using the equation Eq 3-3 and is listed in Table 3.10. For the control composite, the $\tau^{max(SBS)}$ corresponds to its interlaminar

* Appendix A.5 compares the SBS behaviour of these composites with the SBS behaviour of interleaved composites having all of their CFRP plies separated by TP interleaves.

shear failure strength (ILSS). For all the interleaved composites, $\tau^{max(SBS)}$ corresponds to the shear yield strength of the interleaves. The $\tau^{max(SBS)}$ of the CFRP-SAN and CFRP-ASA+PC composites were determined to be slightly less than that of the control composite, while the $\tau^{max(SBS)}$ of PS and MABS interleaved composites were determined to be much less than that of the control composite.

$$\tau^{max(SBS)} = \frac{3 L_f}{4 w t} \quad \text{Eq 3-3}$$

where, w , t – width, and thickness of each specimen

Table 3.10. Maximum shear stress ($\tau^{max(SBS)}$) of composite specimens in the SBS tests described in Section 3.2.2.1

Composite name	$\tau^{max(SBS)}$ (MPa)
Control	82.67 ± 2.82
CFRP-PS	41.04 ± 2.13
CFRP-SAN	75.22 ± 3.56
CFRP-MABS	51.67 ± 1.15
CFRP-ASA+PC	74.38 ± 1.83

Through 3PB and the SBS tests, it is evident that replacing PS with SAN or ASA+PC can improve the through-thickness shear strength of the interleaved composites and prevent premature shear failure. Both of these materials have their shear yield strength ($\tau^{max(SBS)}$) comparable to the ILSS of the control composite.

From these observations, it can also be understood that the maximum shear strength in an interleaved composite can be achieved when the TP interleaves have the same shear strength as that of the control composite, as long as there is no premature interfacial shear failure. If an interleaf with shear yield strength higher than that of the control composite is used, then

the shear strength of the interleaved composite will still be comparable to that of the control composite, with the shear failure localised at the CFRP plies closest to the mid-thickness of the layup.

3.2.4. Conclusion

When the PS interleaves are replaced with the stronger SAN or ASA+PC interleaves in an interleaved composite, premature through-thickness shear failure can be avoided when the composite is loaded in a 3PB setup. Compared to ASA+PC, SAN has T_g closer to that of PS. Hence, SAN was selected as a replacement for PS. The tests performed to explore the CS and SM behaviour of the SAN-interleaved composites are presented in the following section.

3.3. Investigation of the controllable stiffness and shape memory capabilities of SAN-interleaved CFRP composites

In [Section 3.2](#), it was shown that SAN-interleaved CFRP composites have a much higher through-thickness shear strength than PS-interleaved CFRP composites. Furthermore, SAN also had an acceptable T_g for the SAN-interleaved CFRP composites to exhibit CS and SM properties at 120°C. This section describes the further studies that were performed to compare the 3PB behaviour, and controllable stiffness and shape memory capabilities of SAN-interleaved composites to PS-interleaved composites.

3.3.1. Materials, laminates and sample preparation

As in the previous studies ([Section 3.1](#) and [3.2](#)), unidirectional TS300/914 carbon epoxy prepreg was selected as the CFRP component of the interleaved composite. The interleaf materials selected to be a part of the interleaved composites were PS and SAN.

Composite panels (175 mm x 220 mm) were prepared with layups shown in [Table 3.11](#). These panels were cured at 175°C and 7 bar pressure in an autoclave for 1 hour according to the cure schedule recommended by the manufacturer of the CFRP.

To calculate the thickness of the interleaves in the composite specimens, the thickness of the composite specimen and the thickness of the CFRP laminae (assumed to be 125 μm , as recommended by the manufacturer) were used. Analysis of microsections of composite specimens also revealed the thickness of CFRP laminae to be $133.36 \pm 12.14 \mu\text{m}$, which is comparable to the thickness recommended by the manufacturer. However, in the specimens shown in this chapter (and later in the upcoming chapters of this thesis), the thickness of the interleaves across specimen sets varied from each other and from the nominal thickness of the interleaves. Two reasons were identified for this thickness variability - 1) The nominal thickness of the interleaf films was their approximate thickness, as provided by TCKT. The accuracy of the thickness and its variability are unknown, and 2) During the manufacture process, when the laminates were cured in an autoclave, an uncontrolled quantity of the interleaves were squeezed out, resulting in a decrease of their thickness.

Table 3.11. Names and layups of the composite panels
prepared for the studies shown in Section 3.3

Composite name ¹	Layup	Nominal thickness of interleaf films used in layup (μm)	Thickness of interleaves in cured composite (μm)
Control	$[0^\circ]_{12}$	-	-
CFRP-PS _{174μ}	$[(0^\circ/\text{PS}/\text{PS})_7/0^\circ]$	100	174.14 ± 5.92
CFRP-SAN _{151μ}	$[(0^\circ/\text{SAN}/\text{SAN})_7/0^\circ]$	100	150.57 ± 4.53

¹ The subscript indicates the average thickness of the interleaves in the cured composite.

Specimens having the dimensions shown in Table 3.12, Table 3.13 and Table 3.14 were cut from the cured composite panels using an M2-1313b waterjet cutter (Flow International Corporation, USA) for 3PB, CS and SM tests respectively. The waterjet used in this cutting process had GMA Garnet™ ClassicCut™ 80 almandine garnet abrasives (GMA Garnet Group,

Germany) suspended in water, with a jet diameter of 1 mm, a jet pressure of 50000 psi, and a transverse cutting speed of 150 mm/min.

During this cutting process, the waterjet caused damage to composite specimens (see [Figure 3.8](#)) for a distance of 0.55 ± 0.15 mm and 0.34 ± 0.07 mm from the cuts made using waterjet in PS and SAN interleaved composites respectively. Consequently, it was assumed that the composite will have no load-bearing capability in these regions. Hence, the effective width of all the specimens was calculated to be slightly lower than the geometrical width of the specimens. The influence of waterjet cutting process on the effective dimension of a composite specimen is explained further in detail in [Appendix A.1.2](#).

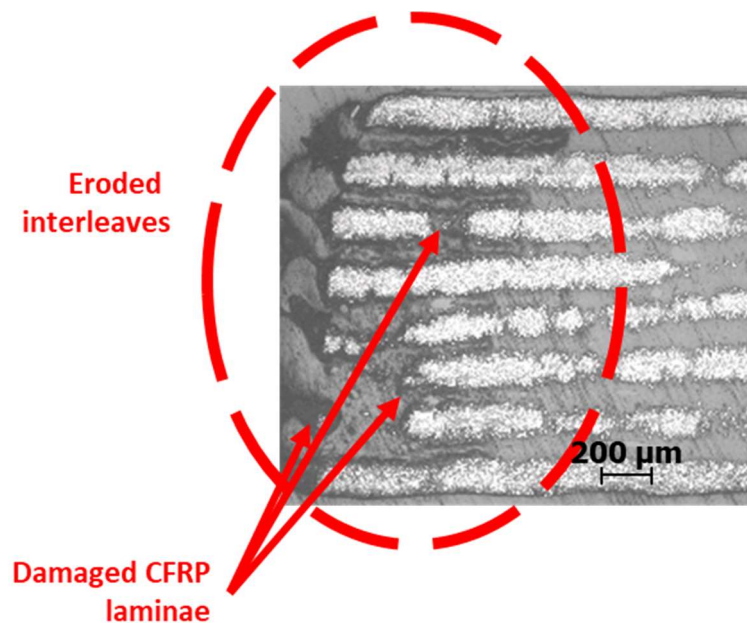


Figure 3.8. Polished microsection of the edges of PS-interleaved CFRP composites cut using waterjet cutter, showing damages to the regions near the cuts made using waterjet

Table 3.12. Dimensions of composite specimens used in the
CS tests described in Section 3.3.2.1

(here, l , w , t – length, width and thickness of the specimens)

Composite name	Dimensions			Support span (mm)
	l (mm)	w (mm)	t (mm)	
Control	79.86 ± 0.04	9.60 ± 0.23	1.45 ± 0.06	50
CFRP-PS _{174\mu}	79.71 ± 0.08	8.88 ± 0.02	2.20 ± 0.04	70
CFRP-SAN _{151\mu}	79.65 ± 0.08	9.19 ± 0.03	2.05 ± 0.03	65

Table 3.13. Dimensions of composite specimens used in the
3PB tests described in Section 3.3.2.2

(here, l , w , t – length, width and thickness of the specimens)

Composite name	Dimensions			Support span (mm)
	l (mm)	w (mm)	t (mm)	
CFRP-PS _{174\mu}	79.74 ± 0.08	8.88 ± 0.01	2.22 ± 0.03	70
CFRP-SAN _{151\mu}	79.64 ± 0.09	9.20 ± 0.03	2.04 ± 0.02	65

Table 3.14. Dimensions of composite specimens used in the
SM studies described in Section 3.3.2.3

(here, l , w , t – length, width and thickness of the specimens)

Composite name	Dimensions		
	l (mm)	w (mm)	t (mm)
CFRP-PS _{174\mu}	79.71 ± 0.08	8.87 ± 0.02	2.20 ± 0.04
CFRP-SAN _{151\mu}	79.62 ± 0.08	9.19 ± 0.03	2.05 ± 0.04

3.3.2. Experimental methodology

3.3.2.1. Controllable stiffness (CS) tests

The CS tests were performed in a 3PB fixture broadly according to ASTM D7264M standard. [Table 3.12](#) also shows the support spans used in this experiment. The support spans ensured that the span-to-thickness ratio of the specimens was close to 32, as recommended in the ASTM D7264M test standard.

It has been well established that the variation of span-to-thickness ratio of the composite specimens can affect their observed flexural properties. Hence, in this thesis (where specified), by varying the test span used for different specimen sets to maintain comparable span-to-thickness ratios, it was ensured that the effect of thickness difference between laminates had minimal impact on their comparative flexural properties, so that they can be compared with one another ([Marszałek, 2022](#)). Analytical and numerical (FE based) predictions can be used to ensure that the varying span for different specimens do not cause any unexpected changes to their flexural properties.

The diameter of the support and loading rollers was 6 mm (whereas the test standard specifies 5 mm). Each specimen was loaded in a universal test machine (Instron 5960 series, USA). The specimens were loaded in a 3PB setup at a constant crosshead speed of 1 mm/min.

At first, the specimens were loaded to a maximum mid-span displacement of 1.5 mm at room temperature (RT1) and unloaded. Then, this test was repeated at 120°C (HT1) and again at room temperature (RT2). An environmental chamber (Instron ElectroPuls 3119-600 Series, USA) mounted on the test machine was used to provide the necessary test temperature conditions for these tests. For the tests performed at room temperature and at 120°C, the universal test machine was equipped with 50 kN and 1 kN load cells respectively.

3.3.2.2. 3PB tests

3PB tests* were performed as described in [Section 3.1.2.1](#), but with a support span shown in [Table 3.13](#). The support spans ensured that the span-to-thickness ratio of the specimens was close to 32, as recommended in the ASTM D7264M test standard.

3.3.2.3. Shape memory (SM) tests

The SM tests were performed in a 3PB fixture broadly according to ASTM D7264M standard. A support span of 65 mm was used. The diameter of the support and loading rollers was 6 mm (whereas the test standard specifies 5 mm). Each specimen was loaded in a universal test machine (Instron 5960 series, USA) equipped with a 50 kN load cell. The specimens were loaded in a 3PB setup at a constant crosshead speed of 1 mm/min. An environmental chamber (Instron ElectroPuls 3119-600 Series, USA) mounted on the test machine was used to provide the test temperature conditions for this test. The temperature of the fixture was monitored using a thermocouple mounted on it.

At first, each initially flat composite specimen was heated to 120°C, inside an environmental chamber pre-heated to 120°C. The specimen was then loaded in the 3PB fixture to a maximum mid-span displacement of 18.72 mm†. The deformed shape of the composite specimen was then fixed by lowering the temperature of the fixture to less than 50°C. After the fixtures in the 3PB setup cooled down to 50°C, the rollers in the 3PB setup were returned to their initial

* SBS tests and their results for these composites can be found in [Appendix A.5](#).

† The combination of 65 mm span and 18.72 mm mid-span displacement was found, through an iterative process, to deform composites specimens to achieve an approximate 90°-bend with a minimal overhang of composites from the roller supports of the 3PB setup. The minimal overhang ensures that the CFRP ply slippage do not cause any kinks along the length of the specimens.

position. Finally, the unconstrained specimen was once again heated to 120°C, inside an environmental chamber pre-heated to 120°C, to recover its shape.

At the different stages of the SM study, the shape profile of composite specimens was measured by covering their cross-sections with a high-contrast pattern ([Figure 3.9 \(a\)](#)) that was then observed using a universal video extensometer (UVX Flexi with IMT-LENS-GP006 lens, iMetrum Ltd, UK). The high-contrast pattern used in this study consists of hand-painted blobs, as suggested by the manufacturer. From the contrast pattern, the associated shape profile was extracted using the Video Gauge™ software tool that uses a proprietary sub-pixel pattern recognition algorithm, as shown in [Figure 3.9 \(b\)](#). While iMetrum claims that the Video Gauge™ tool has a measurement resolution as high as 0.05 µm (or 1/500th of a pixel), the effect of size, shape and change of shape of the contrast pattern is unknown. To ensure that the measured deformation data is accurate, within the scope of this thesis, the resolution of measurement obtained through this tool is fixed as 100 µm, 2000 times larger than the resolution claimed by iMetrum. However, a separate study into the accuracy of the optical measurement tool must be performed to add validity to the accuracy of the data resolution represented in this thesis.

Before and after the SM tests, the flexural moduli of the composite specimens were measured at room temperature by performing the tests described in [Section 3.3.2.1](#).

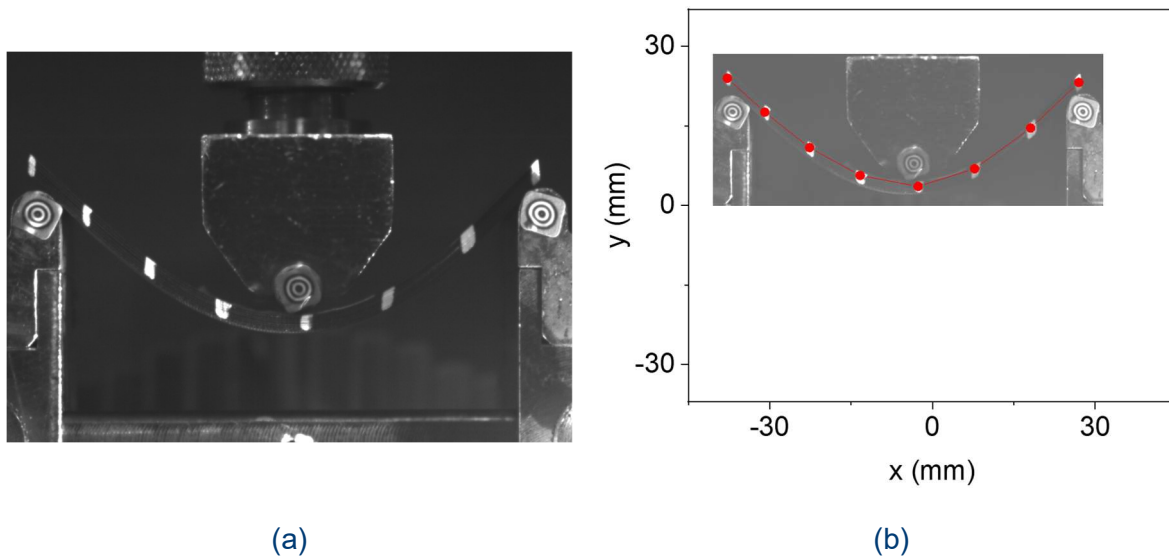


Figure 3.9. (a) A typical high-contrast pattern on a composite specimen, and
(b) the associated shape profile

3.3.2.4. *Optical microscopy of composites*

Using the methodology described in Section 3.1.2.2, the central 20 mm section (i.e., mid-span) and the free end of CFRP-PS_{174μ} and CFRP-SAN_{151μ} specimens after heated to 120°C, after deformation in SM study, and after shape recovery in SM study were inspected using optical microscopy. Additionally, selected specimens subjected to 3PB tests were also inspected using the same method.

3.3.3. Results and discussions

3.3.3.1. *CS test results*

Typical force-displacement curves of the interleaved composites in CS tests, at their RT1, HT1 and RT2 test conditions, are shown in Figure 3.10 (a), (b) and (c) respectively. Here, it can be seen that the force-displacement curves of the interleaved composites at the RT2 test condition are indistinguishable from the curves in Figure 3.10 (a), by the naked eye. From the

slope of the best-fit straight line* of the force-displacement curves $\left(\frac{F}{\delta}\right)$, the apparent flexural modulus (E) of the composites can be obtained using equation Eq 3-4.

$$E = \frac{F}{\delta} \frac{span^3}{48 I} \quad \text{Eq 3-4}$$

where I is the 2nd moment of area of specimen cross-section.

The apparent flexural modulus of the composites in their high stiffness state (E_{RT1}), low stiffness state (E_{HT1}) and again in their high stiffness state (E_{RT2}) are listed in Table 3.15. Here, the predictions of the moduli based on the equations Eq 3-5 and Eq 3-6 are provided in brackets.

$$E_{RT} = \frac{12 \cdot E_c}{h^3} \sum_{i=1}^N \left(\frac{t_i^3}{12} + t_i z_i^2 \right) \quad \text{Eq 3-5}$$

for CFRP layers only

$$E_{HT} = \frac{E_c}{h^3} \sum_{i=1}^N (t_i^3) \quad \text{Eq 3-6}$$

for CFRP layers only

here, E_c – Young's modulus of CFRP = 120 GPa (Maples et al., 2016; Zhang, 2020)

t_i – thickness of each CFRP ply

z_i – distance from the specimen mid-thickness to mid-thickness of each CFRP ply

h – thickness of the composite specimen

In Eq 3-5, the contribution of the interleaves on the apparent flexural modulus of the interleaved composites at high stiffness state is neglected, but it is assumed that the interleaf stiffness is sufficient to ensure that all the plane sections remain plane, in accordance with Euler-Bernoulli beam theory. In Eq 3-6, the residual stiffness of the interleaves is neglected, and it is assumed that the CFRP laminae will be completely free to undergo a relative slippage between one another.

* After ignoring the initial non-linear segment of the force-displacement curves.

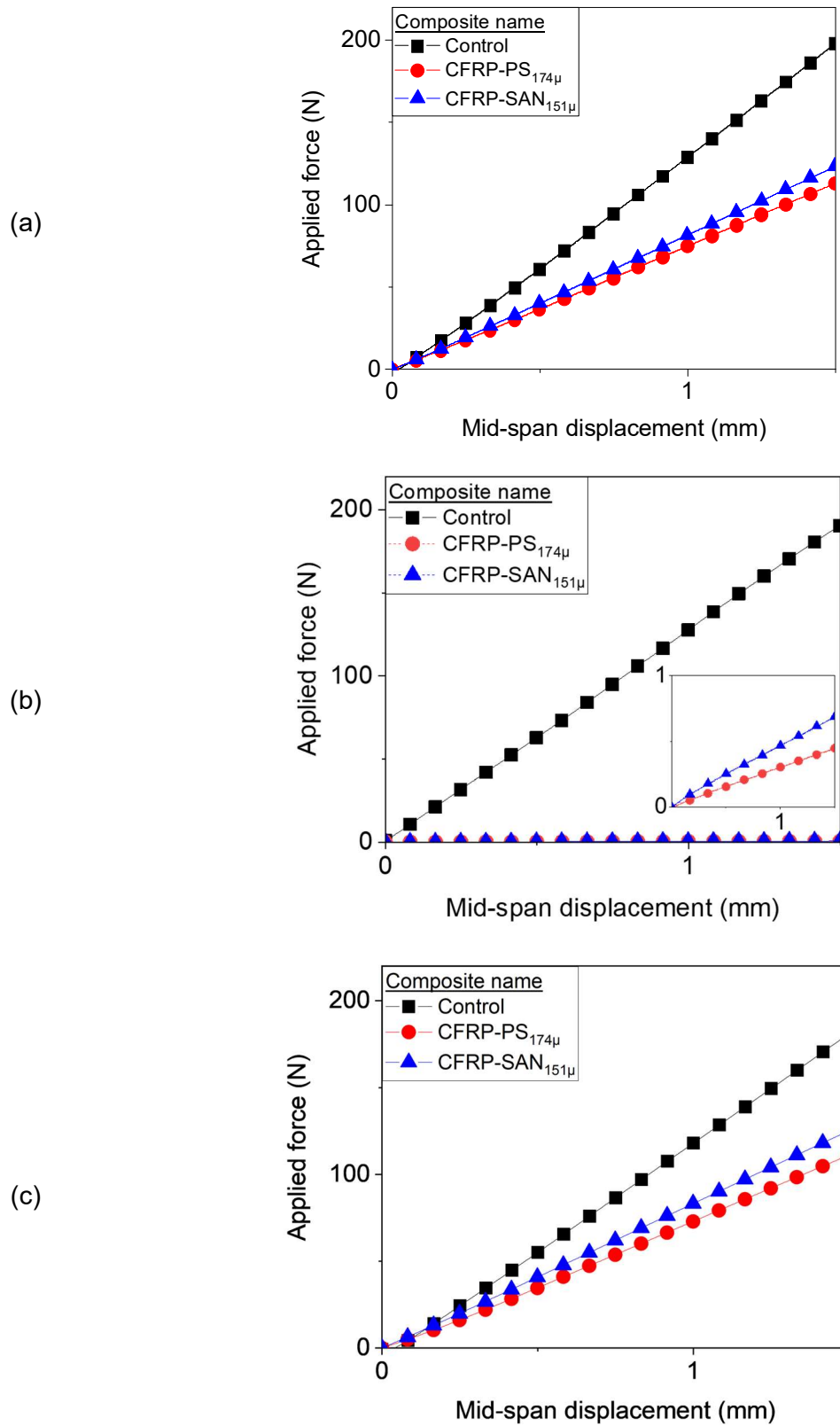


Figure 3.10. Typical force-displacement curves of composite specimens at (a) RT1, (b)

HT1 and (c) RT2 test conditions in the CS tests described in Section 3.3.2.2

(inset shows the same graph but with a smaller range of applied force)

From Table 3.15, it is seen that heating the CFRP-PS_{174μ} and CFRP-SAN_{151μ} composites causes their apparent flexural modulus to drop by more than 99% (E_{RT1} vs E_{HT1}). Upon cooling down, the apparent flexural modulus of the composites is fully restored. In the control composites, a negligible drop in modulus is observed as a result of heating. This observation demonstrates the controllable stiffness capabilities of the PS and SAN-interleaved composites.

Table 3.15. The apparent flexural modulus of composites at RT1, HT1 and RT2 test conditions in the CS tests described in Section 3.3.2.2 (theoretical predictions are specified in brackets)

Composite name	Apparent flexural moduli of composites		
	E_{RT1} [GPa]	E_{HT1} [GPa]	E_{RT2} [GPa]
Control	120.02 ± 4.12	116.27 ± 7.33	119.95 ± 4.68
CFRP-PS _{174μ}	63.63 ± 1.97 (62.08)	0.26 ± 0.01 (0.17)	64.97 ± 1.04 (62.08)
CFRP-SAN _{151μ}	68.29 ± 1.61 (66.47)	0.32 ± 0.04 (0.22)	68.26 ± 2.26 (66.47)

3.3.3.2. 3PB test results

Typical load-displacement curves of the control, CFRP-PS_{174μ} and CFRP-SAN_{151μ} composites in flexural tests are shown in Figure 3.11. Based on the methodology described in Section 3.1.3.1, the load associated with the initiation of failure (L_f) was selected for each load-displacement curve and the corresponding shear (τ^{max}) and bending (σ^{max}) stresses were calculated. In these interleaved composites, the distribution of axial stresses along the thickness of the specimens is not linear. Consequently, the true maximum bending stress experienced by the outmost CFRP ply ($\sigma^{maxCFRP}$) of the interleaved composite can be calculated using Eq 3-7 or Eq 3-8. The τ^{max} , σ^{max} , and $\sigma^{maxCFRP}$ of the CFRP-PS_{174μ} and CFRP-SAN_{151μ} composites are shown in Table 3.16. The polished longitudinal microsection of the composite specimens after failure in 3PB tests is shown in Figure 3.12.

$$\sigma^{\max\text{CFRP}} = \sigma^{\max} \frac{E_c}{E_{RT}} \quad \text{Eq 3-7}$$

By substituting Eq 3-1 and Eq 3-4 in Eq 3-7,

$$\sigma^{\max\text{CFRP}} = \frac{6 L_f E_c t}{\text{span}^2} \left(\frac{F}{\delta} \right)^{-1} \quad \text{Eq 3-8}$$

where, $\left(\frac{F}{\delta} \right)$ is the slope of the linear region of the force-displacement curves obtained from 3PB tests.

Table 3.16. τ^{\max} , σ^{\max} , and $\sigma^{\max\text{CFRP}}$ of the CFRP-PS_{174μ} and CFRP-SAN_{151μ} specimens in the 3PB tests described in Section 3.3.2.2

Composite name	τ^{\max} (MPa)	σ^{\max} (GPa)	$\sigma^{\max\text{CFRP}}$ (GPa)
CFRP-PS _{174μ}	11.25 ± 0.68	0.71 ± 0.04	1.34 ± 0.09
CFRP-SAN _{151μ}	12.46 ± 0.79	0.79 ± 0.04	1.39 ± 0.08

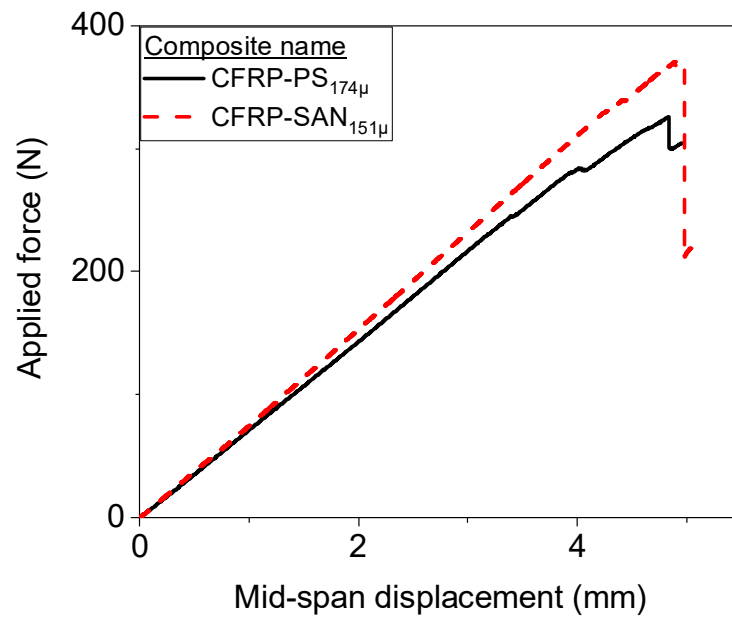


Figure 3.11. Typical load-displacement curves of the composites in the 3PB tests described in Section 3.3.2.2

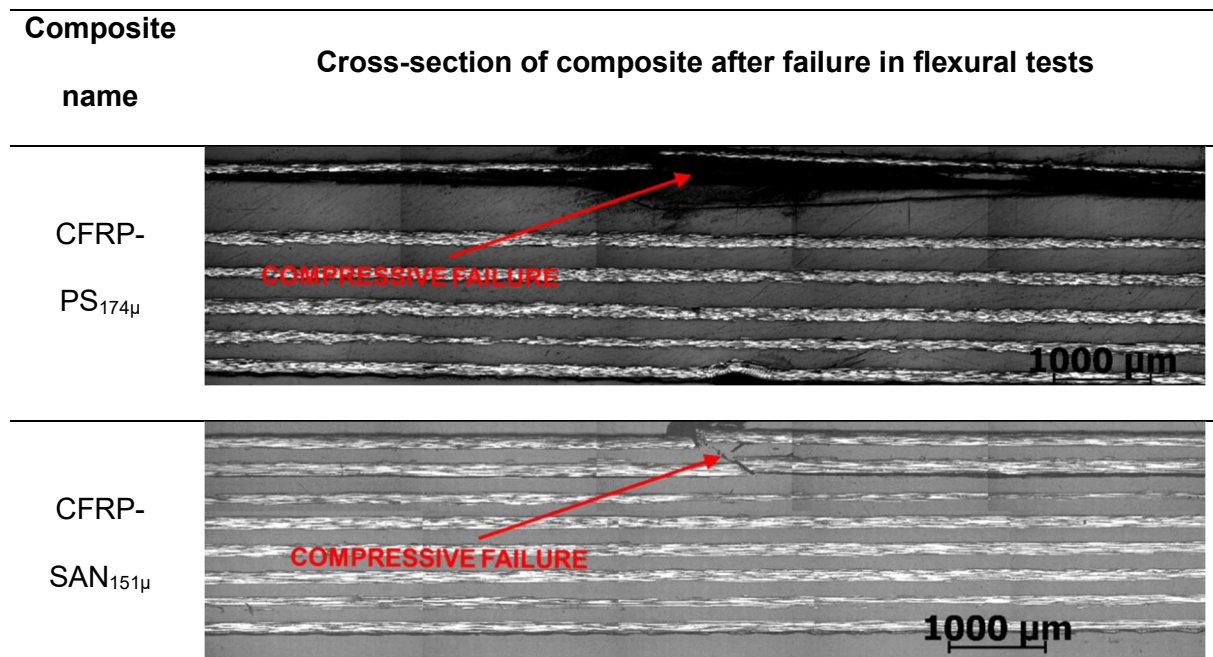


Figure 3.12. Micrographs of polished longitudinal cross-sections of the composite specimens tested until failure in the 3PB tests described in Section 3.3.2.2

From the micrographs of the CFRP-PS_{174μ} and CFRP-SAN_{151μ} composites, it is seen that these composites have failed due to the compressive failure of CFRP. Furthermore, the $\sigma^{\max\text{CFRP}}$ of these composites are also comparable to the compressive strength CFRP (1.35 GPa). These observations indicate that the interleaved composites do not have a premature through-thickness shear failure (as seen in [Section 3.1.3.1](#)) due to the different layups used here.

3.3.3.3. SM test results

Typical shapes of a CFRP-PS_{174μ} composite specimen in various stages of the SM study are shown in [Figure 3.13](#). From the high contrast pattern of the shapes, the respective shape profiles were extracted, as shown in [Figure 3.9](#). Using the shape profiles of the composite specimens in the SM study, the average distance (ζ) between the mid-span and the ends of the specimens in the direction of loading (see [Figure 3.14](#)) was extracted before deformation and after deformation and is listed in [Table 3.17](#). Similarly, the ζ of the specimens after 2 minutes of shape recovery and after 5 minutes of shape recovery is also listed in [Table 3.17](#), where the time of shape recovery is measured from the instance deformed specimens are placed in the preheated oven.

It has previously been shown in [Section 2.3](#) that a deformed interleaved composite, after cooling, will slightly relax upon removal of the deformation load and will slightly recover its original shape in a process known as springback. The change in ζ of the deformed interleaved specimens due to springback can be predicted using equation [Eq 3-9](#) ([Robinson et al., 2017; Zhang, 2020](#)). Using this equation, the change in ζ due to springback of the CFRP-PS_{174μ} and CFRP-SAN_{151μ} composite specimens in SM tests was predicted to be close to 0.09 mm. However, optical tracking of the fixtures revealed that the maximum mid-span displacement gradually reduced by around 0.4 mm as the test setup contracted as it cooled down. As a result of this, the composite specimens are gradually unloaded as the temperature of the setup is reduced (see [Appendix A.6](#)). Hence, the methodology used in this experiment cannot reliably measure the springback of the composite specimens.

$$\text{Springback at mid-span} = \frac{E_{HT}}{E_{RT}} \times \text{maximum mid-span displacement} \quad \text{Eq 3-9}$$

where, E_{RT} and E_{HT} can be considered as E_{RT1} and E_{HT1} respectively, from Table 3.15.

Table 3.17. Distance (ζ) between the mid-span and the ends of composite specimens in the direction of loading at different stages of the SM study

Composite name	Distance (ζ) between the mid-span and the ends of specimens in the direction of loading (mm)			
	Before deformation	After deformation	After shape recovery	
			2 min	5 min
CFRP-PS _{174μ}	0.0	20.0	4.9	1.4
CFRP-SAN _{151μ}	0.0	20.0	9.8	1.8

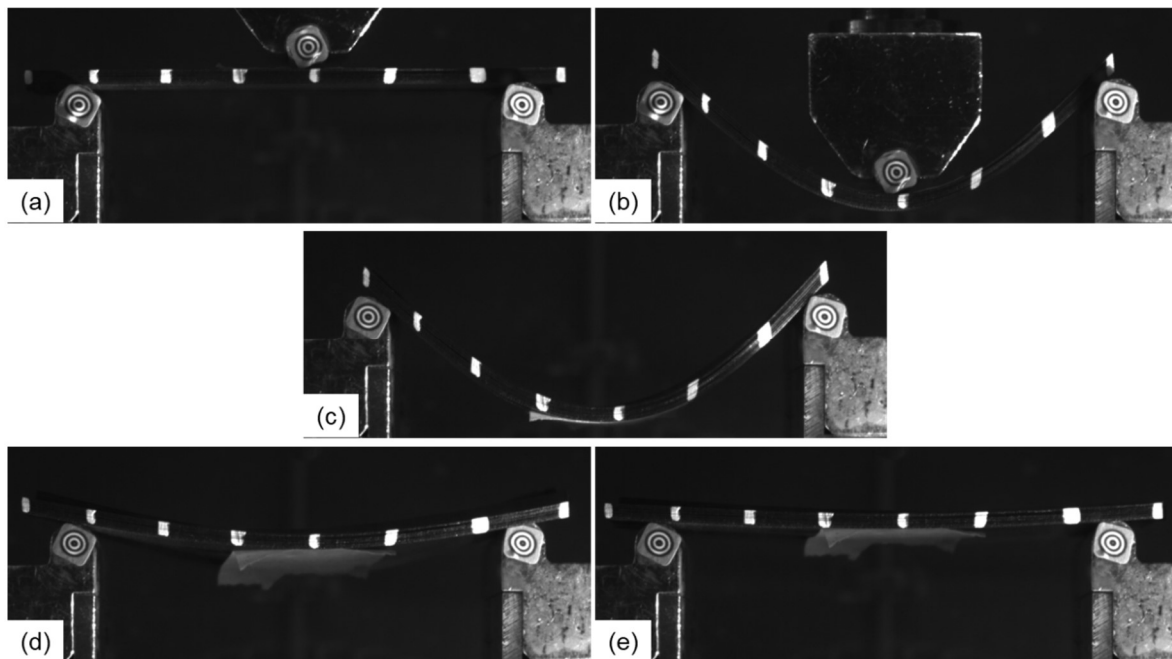


Figure 3.13. Typical shapes of CFRP-PS_{174μ} specimens at (a) initial, (b) deformed, (c) springback, (d) recovery (2 minutes) and (e) recovery (5 minutes) stages of SM tests

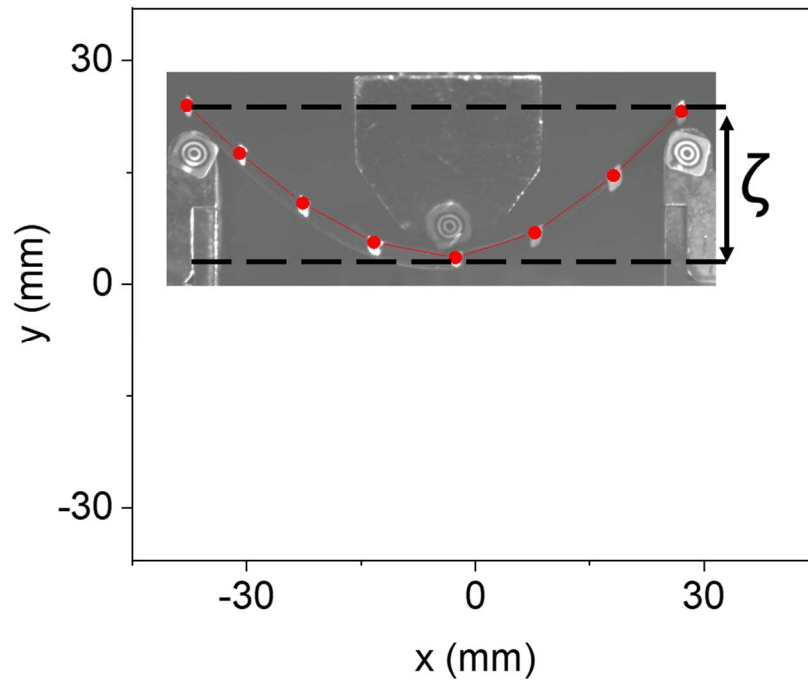


Figure 3.14. Distance (ζ) between the mid-span and the ends of the specimens in the direction of loading, after deformation in SM tests

The SM study shows that when the interleaved composite specimens were heated to 120°C, deformed, cooled to room temperature, and the deformation load was removed, the deformed shape was almost fully retained for the composite specimens with both types of interleaves. On re-heating the composite specimens, their initial shape was almost fully recovered.

The speed of shape recovery is, however, measured to be faster in CFRP-PS_{174μ} composites when compared to CFRP-SAN_{151μ} composites. This is probably due to the higher residual stiffness or higher viscosity of SAN at the recovery temperature, compared to PS at the same temperature.

3.3.3.4. Void formation within the thermoplastic interleaves

The polished longitudinal cross-section of the mid-span and the free end CFRP-PS_{174μ} and CFRP-SAN_{151μ} composite specimens are shown in Figure 3.15, Figure 3.16, Figure 3.17, and

Figure 3.18. These microsections reveals the formation of voids within the interleaf region of the specimens after the shape recovery process in the SM studies.

When the specimens are heated to 120°C and left undeformed, there are no voids formed within the interleaves. This observation indicates that these voids are not a result of outgassing of the interleaves, contradicting the arguments posed by previous research (Robinson *et al.*, 2017; Zhang, 2020). Furthermore, these observations also discount the presence of trapped moisture, or thermal degradation as possible causes of void formation, as highlighted in Section 2.8.

Upon deformation and cooling, a negligible void formation was seen in CFRP-PS_{174μ} specimens, and no void formation was seen in CFRP-SAN_{151μ} specimens. And finally, as highlighted above, significantly higher quantity of voids was observed in the specimens after shape recovery.

These observations indicates that the voids formed during the SM studies are probably due to uneven heating of the composite specimens along their thickness. It is possible that the outer plies of the interleaved composites get heated more quickly than the inner plies causing them to peel away, resulting in the formation of voids. However, this phenomenon has to be studied further. A numerical study (followed by experimental validation) to investigate the variability of parameters such as deformation temperature, deformation rate, shape recovery temperature, shape recovery rate, and material properties of interleaves on the void formation can be useful in accurately identifying the underlying reason behind the formation of voids within the interleaves.

Due to the formation of these voids, the average thickness (t) of the composite specimens increases slightly, leading to small changes to their apparent flexural modulus, as shown in Table 3.18.

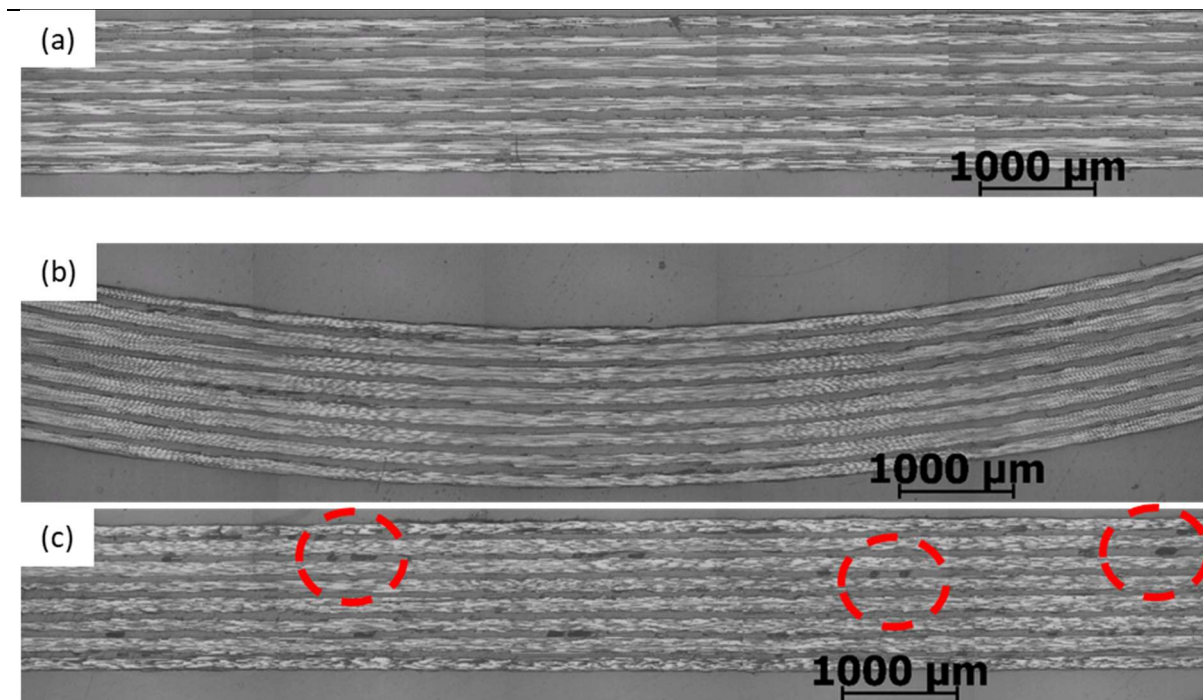


Figure 3.15. Polished longitudinal microsection of the mid-span of CFRP-PS_{110μ} composites (a) after heating to 120°C, (b) after deformation, cooldown, and removal of deformation load, and (c) after 10 minutes of shape recovery at 120°C

(Some of the voids are circled)

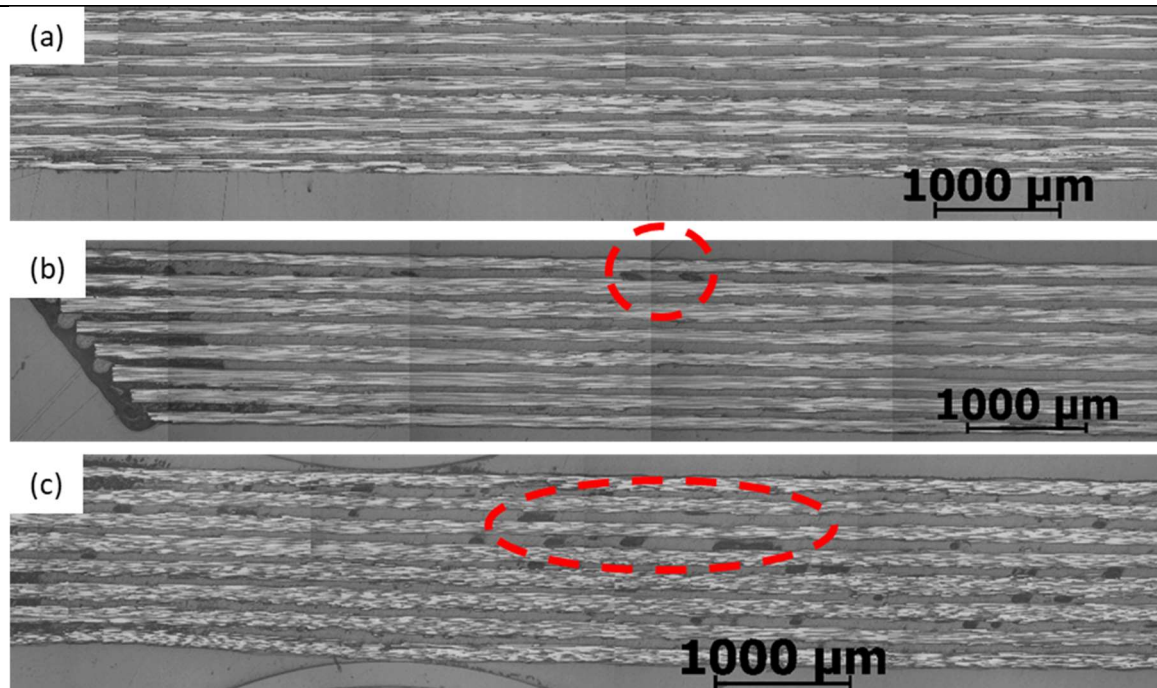


Figure 3.16. Polished longitudinal microsection of the free end of CFRP-PS_{110μ} composites (a) after heating to 120°C, (b) after deformation, cooldown, and removal of deformation load, and (c) after 10 minutes of shape recovery at 120°C
(Some of the voids are circled)

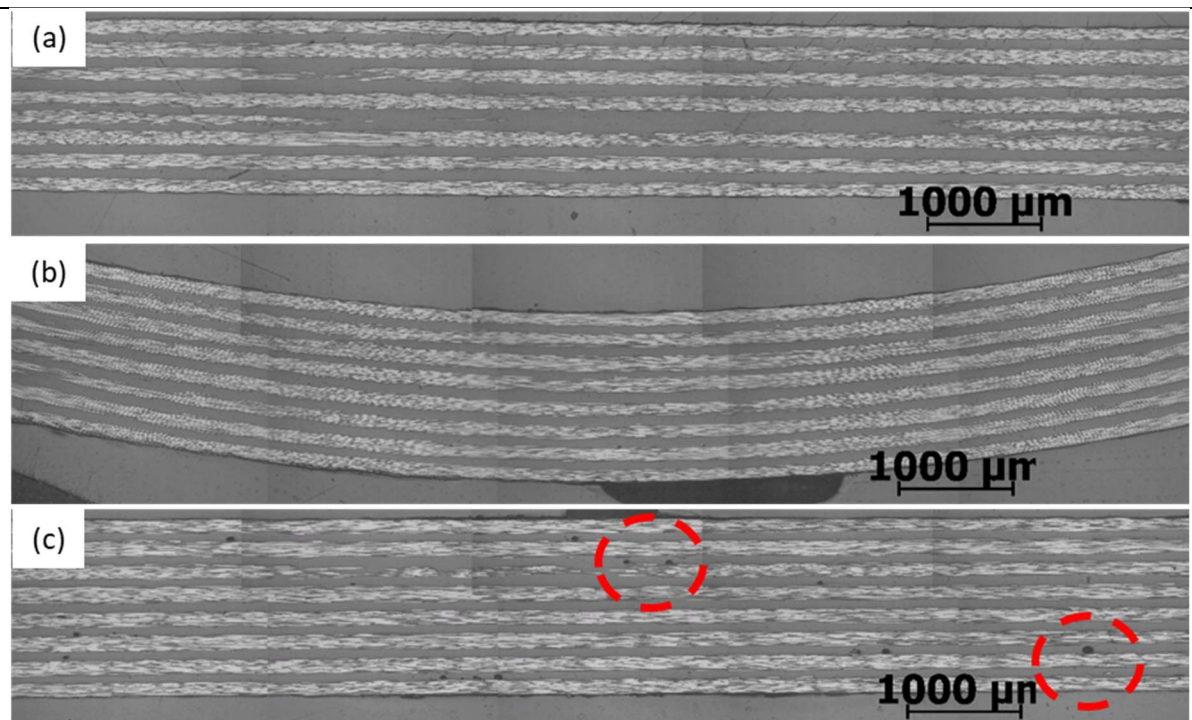


Figure 3.17. Polished longitudinal microsection of the mid-span of CFRP-SAN_{118μ} composites (a) after heating to 120°C, (b) after deformation, cooldown, and removal of deformation load, and (c) after 10 minutes of shape recovery at 120°C
(Some of the voids are circled)

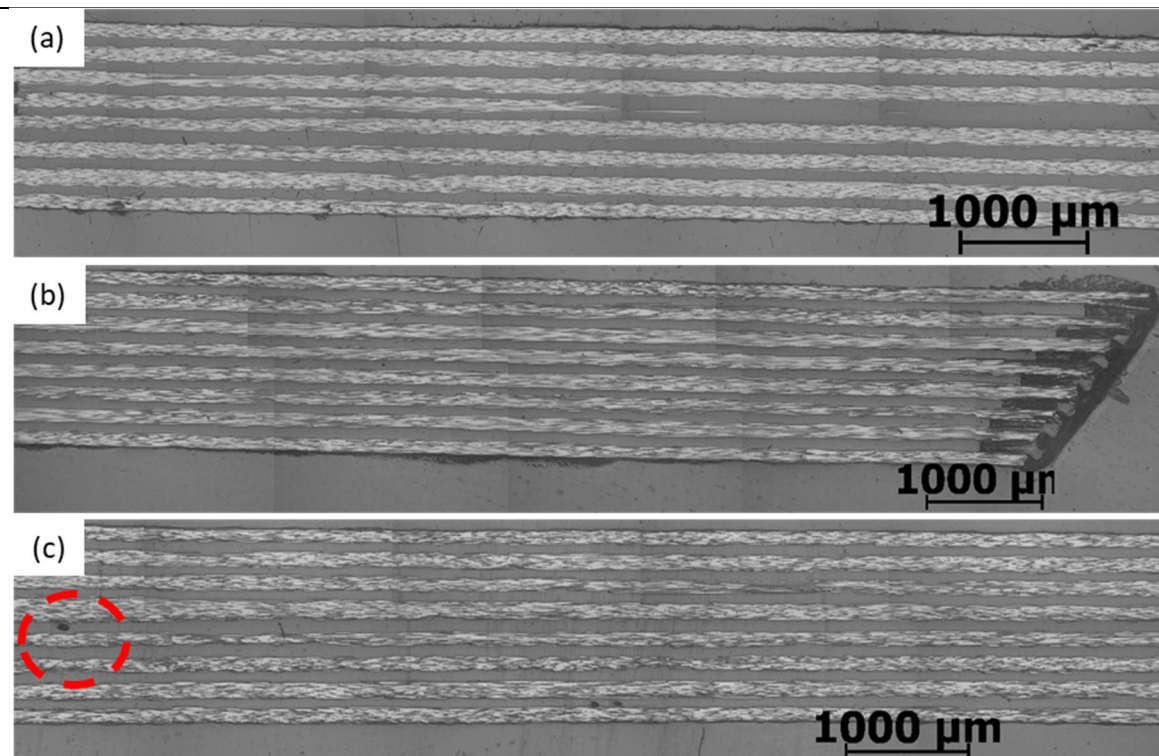


Figure 3.18. Polished longitudinal microsection of the free end of CFRP-SAN_{118μ} composites (a) after heating to 120°C, (b) after deformation, cooldown, and removal of deformation load, and (c) after 10 minutes of shape recovery at 120°C
(Some of the voids are circled)

Table 3.18. Specimen thickness (t) and apparent flexural moduli (E_{RT}) moduli of the composites before and after the SM tests described in Section 3.3.2.3

(theoretically predicted moduli are provided in brackets)

Composite name	$t_{\text{before SM}}^*$ [mm]	$t_{\text{after SM}}$ [mm]	$E_{RT-\text{before SM}}$ [GPa]	$E_{RT-\text{after SM}}$ [GPa]
CFRP-PS _{174μ}	2.20 ± 0.04	2.23 ± 0.04	62.45 ± 2.33 (62.56)	61.75 ± 3.86 (61.92)
CFRP-SAN _{151μ}	2.05 ± 0.04	2.10 ± 0.05	67.24 ± 1.15 (66.69)	61.86 ± 5.42 (65.30)

* Same as ' t ' shown in Table 3.14

3.3.4. Conclusion

The CS studies performed on CFRP-SAN_{151 μ} composite specimens reveal that they can lose over 99% of their initial apparent flexural modulus upon heating, which was then fully recovered when the specimens were cooled to room temperature. During the SM tests, the CFRP-SAN_{151 μ} composite specimens were able to retain their deformed shape upon cooling and were then able to recover their original as-cured shape upon reheating. The CS and SM behaviour of the SAN-interleaved composites were very similar to those exhibited by the - interleaved composites.

3.4. Chapter summary

- The study described in [Section 3.1](#) shows that the premature through-thickness shear failure observed in 3-point flexural tests of PS-interleaved CFRP composites happens inside the PS interleaves.
- The study described in [Section 3.2](#) shows that replacing PS interleaves with stronger SAN interleaves increases the through-thickness shear strength of the interleaved composites to a value comparable to that of pristine CFRP.
- The study described in [Section 3.3](#) demonstrates the CS and SM capabilities of SAN-interleaved CFRP composites, which are very similar to those of PS-interleaved CFRP composites.

Chapter 4. Improvement of the flexural modulus of thermoplastic interleaved carbon-epoxy composites

As described in [Section 2.6](#), CFRP-PS interleaved composites have lower apparent flexural modulus, compared to pristine CFRP ([Maples, 2014](#); [Maples *et al.*, 2016](#); [Zhang *et al.*, 2018](#)). This chapter describes studies to improve the apparent flexural modulus of the interleaved composites.

The first section of this chapter reports on an investigation to improve the apparent flexural modulus of interleaved composites by reducing the thickness of the interleaves. The second section of this chapter describes an investigation to improve the apparent flexural modulus of interleaved composites by introducing reinforcements within the interleaves.

In both these sections, the flexural strength of the interleaved composites, and their CS and SM behaviour were also studied to analyse the effects of thin interleaves and reinforced interleaves on these properties.

4.1. Investigation of improvement of the flexural modulus of interleaved composites by reducing the thickness of the interleaves

To improve the apparent flexural modulus of the interleaved composites, composites with varying thicknesses of interleaves were produced and their flexural moduli were measured. Furthermore, CS and SM behaviours and the flexural strength of these composites were also studied.

4.1.1. Materials, laminates and sample preparation

As in the previous experimental studies described in this thesis, unidirectional TS300/914 carbon epoxy prepreg was selected as the CFRP component of the interleaved composite. The interleaf materials selected to be a part of the interleaved composites were PS and SAN.

Composite panels (175 mm x 220 mm) were prepared with layups specified in Table 4.1. These panels were cured at 175°C and 7 bar pressure in an autoclave for 1 hour according to the cure schedule recommended by the manufacturer of the CFRP. Specimens having the dimensions shown in Table 4.2, Table 4.3 and Table 4.3 were cut from the cured composite panels using a waterjet, as shown in Section 3.3.1 for CS, SM and 3PB tests respectively.

Table 4.1 Names and layups of the composite panels
prepared for the studies shown in Section 4.1

Composite name	Layup sequence	Nominal thickness of PS and SAN films used in the layup (μm)	Thickness of interleaves in cured composite (μm) ¹
CFRP-PS _{33μ}	[(0°/PS) ₇ /0°]	50	33.01 \pm 5.49
CFRP-PS _{110μ}	[(0°/PS) ₇ /0°]	100	110.43 \pm 10.92
² CFRP-PS _{174μ}	[(0°/PS/PS) ₇ /0°]	100	174.14 \pm 5.92
CFRP-SAN _{37μ}	[(0°/SAN/SAN) ₇ /0°]	20	36.71 \pm 5.12
² CFRP-SAN _{151μ}	[(0°/SAN/SAN) ₇ /0°]	100	150.57 \pm 4.53

¹ Calculated from the thickness of the specimens, layup sequence and the nominal cured thickness of the CFRP laminae.

² The data obtained from the characterisation of these composites have previously been shown in Section 3.3.

Table 4.2 Dimensions of composite specimens used in CS tests described in Section 4.1.2.1

(here, l , w , t – length, width and thickness of the specimens)

Composite name	Dimensions			Support span (mm)
	l (mm)	w (mm)	t (mm)	
CFRP-PS _{33μ}	79.43 \pm 0.10	8.68 \pm 0.03	1.22 \pm 0.05	40
CFRP-PS _{110μ}	79.49 \pm 0.16	8.76 \pm 0.04	1.77 \pm 0.08	52
CFRP-PS _{174μ}	79.71 \pm 0.08	8.88 \pm 0.02	2.20 \pm 0.04	70
CFRP-SAN _{37μ}	79.61 \pm 0.08	9.17 \pm 0.04	1.27 \pm 0.03	40
CFRP-SAN _{151μ}	79.65 \pm 0.08	9.19 \pm 0.03	2.05 \pm 0.03	65

Table 4.3 Dimensions of composite specimens used in SM tests described in Section 4.1.2.2

(here, l , w , t – length, width and thickness of the specimens)

Composite name	Dimensions		
	l (mm)	w (mm)	t (mm)
CFRP-PS _{33μ}	79.43 \pm 0.11	8.68 \pm 0.02	1.21 \pm 0.05
CFRP-PS _{110μ}	79.48 \pm 0.21	8.76 \pm 0.06	1.79 \pm 0.10
CFRP-PS _{174μ}	79.71 \pm 0.08	8.87 \pm 0.02	2.20 \pm 0.04
CFRP-SAN _{37μ}	79.61 \pm 0.07	9.17 \pm 0.05	1.26 \pm 0.03
CFRP-SAN _{151μ}	79.62 \pm 0.08	9.19 \pm 0.03	2.05 \pm 0.04

Table 4.4 Dimensions of composite specimens used in
3PB tests described in Section 4.1.2.3
(here, l , w , t – length, width and thickness of the specimens)

Composite name	Dimensions			Support
	l (mm)	w (mm)	t (mm)	span (mm)
CFRP-PS _{33μ}	79.50 ± 0.09	8.66 ± 0.03	1.24 ± 0.03	40
CFRP-PS _{110μ}	79.29 ± 0.13	8.69 ± 0.05	1.66 ± 0.07	52
CFRP-PS _{174μ}	79.74 ± 0.08	8.88 ± 0.01	2.22 ± 0.03	70
CFRP-SAN _{37μ}	79.66 ± 0.08	9.18 ± 0.03	1.27 ± 0.03	40
CFRP-SAN _{151μ}	79.64 ± 0.09	9.20 ± 0.03	2.04 ± 0.02	65

4.1.2. Experimental methodology

4.1.2.1. CS tests

Following the methodology described in Section 3.3.2.1, CS tests were performed on the specimens, but with the support span shown in Table 4.2 to ensure that the span-to-thickness ratio of the specimens was close to 32, as recommended in the ASTM D7264M test standard.

4.1.2.2. SM tests

Following the methodology described in Section 3.3.2.3, SM tests were performed. Before and after the SM tests, the flexural moduli of the composite specimens were measured at room temperature using the methodology described in Section 4.1.2.1.

4.1.2.3. 3PB tests

Following the methodology described in Section 3.1.2.1, 3PB tests were performed, but with the support span shown in Table 4.4 to ensure that the span-to-thickness ratio of the specimens was close to 32, as recommended in the ASTM D7264M test standard.

4.1.2.4. *Optical microscopy of composites*

The central 20 mm section (i.e., mid-span) of selected specimens in the pristine as-cured state, after 3PB tests, and after SM tests were inspected by optical microscopy, following the methodology described in [Section 3.1.2.2](#).

4.1.3. Results and discussion

4.1.3.1. *CS test results*

Typical force-displacement curves of the interleaved composites in CS tests, in the RT1 and HT1 test conditions, are shown in [Figure 4.1 \(a\)](#) and [\(b\)](#) respectively. The force-displacement curves of the interleaved composites at the RT2 test condition are not shown here as they are not distinguishable from the curves in [Figure 4.1 \(a\)](#) by the naked eye, as highlighted in [Section 3.3.3.1](#). From the average slope of each force-displacement curve (after ignoring the initial non-linear segment), the corresponding apparent flexural modulus was calculated, as shown in [Section 3.3.3.1](#).

The apparent flexural modulus of the composites in their high stiffness state (E_{RT1}), low stiffness state (E_{HT1}) and again at high stiffness state (E_{RT2}) are listed in [Table 4.5](#), where the theoretical predictions (using [Eq 3-5](#) and [Eq 3-6](#)) are also shown. To further visualise the effects of varying interleaf thicknesses, E_{RT1} , E_{HT1} , and E_{RT2} of all the specimens are plotted against their interleaf thicknesses in [Figure 4.2](#), where the theoretically predicted E_{RT} and E_{HT} are also shown.

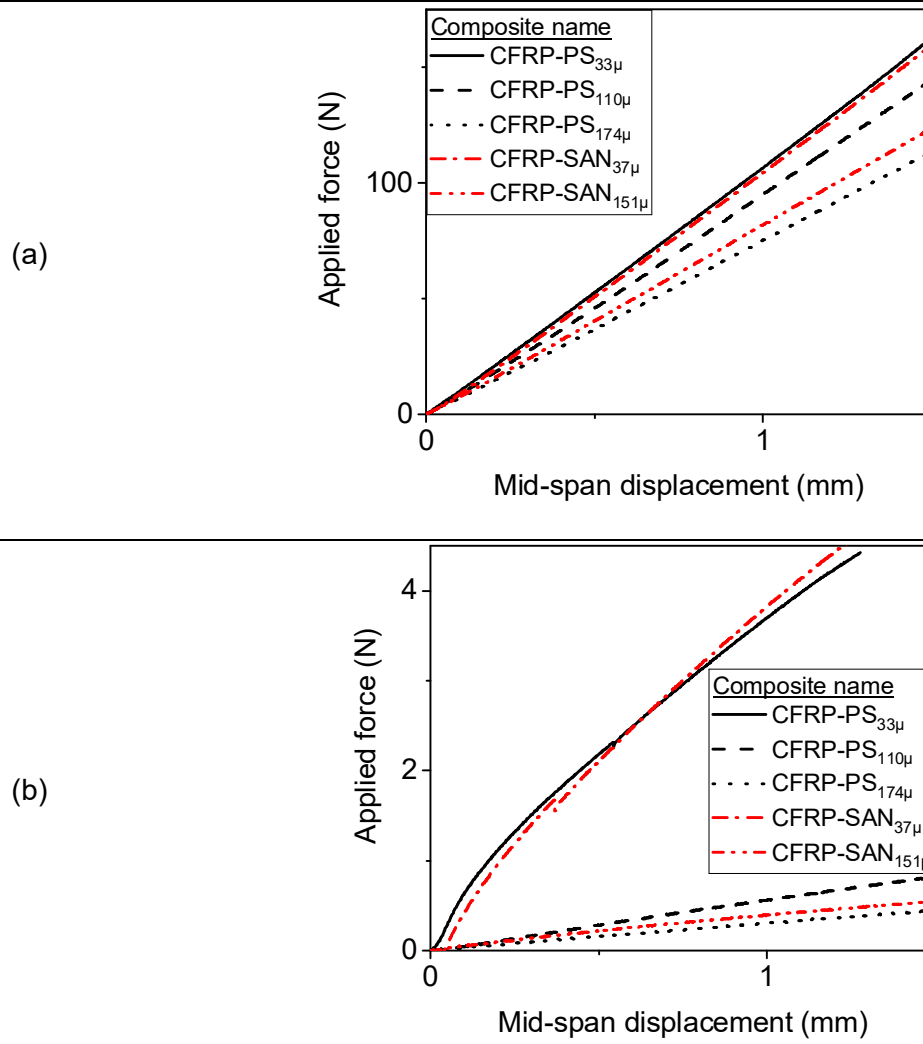


Figure 4.1 Typical force-displacement curves of composite specimens at (a) RT1 and (b) HT1 test conditions in the CS tests described in Section 4.1.2.1

Table 4.5. The apparent flexural modulus of composites at RT1, HT1 and RT2 test

conditions in the CS tests described in Section 4.1.2.1

(theoretical predictions are specified in brackets)

Composite name	Apparent flexural moduli of composites		
	E_{RT1} (GPa)	E_{HT1} (GPa)	E_{RT2} (GPa)
¹ Control	120.02 ± 4.12	116.27 ± 7.33	119.95 ± 4.68
CFRP-PS _{33μ}	108.61 ± 2.93	4.62 ± 4.59	108.17 ± 3.94
	(102.17)	(1.00)	(102.17)
CFRP-PS _{110μ}	74.97 ± 3.02	0.37 ± 0.04	75.53 ± 2.81
	(75.52)	(0.34)	(75.52)
CFRP-PS _{174μ}	63.63 ± 1.97	0.26 ± 0.01	64.97 ± 1.04
	(62.08)	(0.17)	(62.08)
CFRP-SAN _{37μ}	101.56 ± 2.49	2.45 ± 0.56	101.52 ± 3.27
	(100.49)	(0.94)	(100.49)
CFRP-SAN _{151μ}	68.29 ± 1.61	0.32 ± 0.04	68.26 ± 2.26
	(66.47)	(0.22)	(66.47)

¹ From Section 3.3.

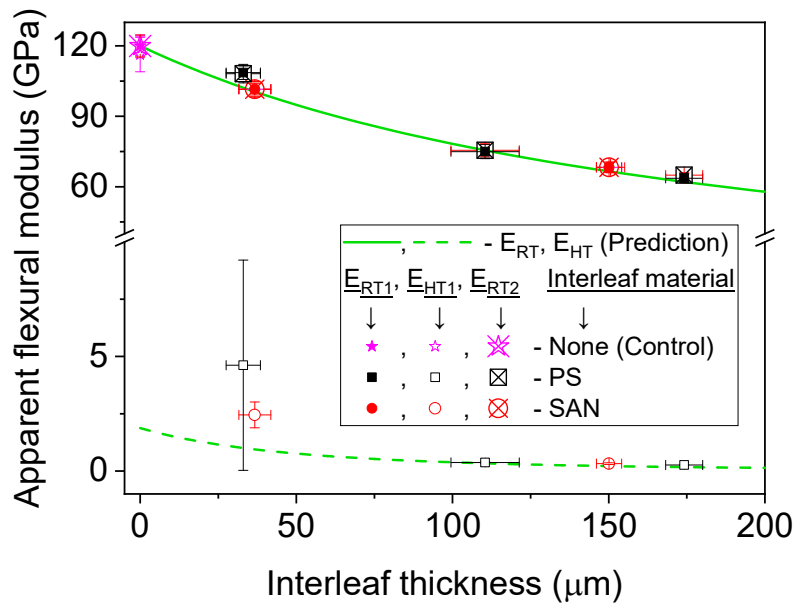


Figure 4.2 E_{RT1} , E_{HT1} , and E_{RT2} (see Table 4.5) of composites plotted against their interleaf thickness

(Inset shows E_{HT1} of CFRP-PS_{33μ} and CFRP-SAN_{37μ} when the outlier is removed)

As postulated and predicted, the apparent flexural modulus of all the interleaved composites (E_{RT1}) increases with a decrease in the thickness of the interleaves. E_{RT1} of CFRP-PS_{33μ} and CFRP-SAN_{37μ} appear to be 90% and 85% of that of the control composite, compared to around 55% that was achieved in CFRP-PS_{174μ} and CFRP-SAN_{151μ}. The trend (shown in Figure 4.2) indicates that the E_{RT1} of an interleaved composite can be further increased if the thickness of the interleaves is further decreased.

The results from the CS tests indicate that the apparent flexural modulus of all interleaved composites drops by more than 95% (E_{RT1} vs E_{HT1}) upon heating. Upon cooling down, the apparent flexural modulus of the composites is fully restored. Furthermore, a good agreement between the theoretical prediction and the experimental observation of E_{RT1} , E_{RT2} and E_{HT1} (at interleaf thickness greater than 100 μm) can be seen. The experimentally obtained E_{HT1} of CFRP-PS_{33μ} and CFRP-SAN_{37μ}, however, show a significant deviation from the theoretical predictions. This deviation could be due to bridging between adjacent CFRP plies caused probably by intermittent perforation of the thin interleaves, as shown in Figure 4.3.

The presence of randomly distributed bridging could potentially cause adjacent CFRP plies to not undergo relative slip as effectively as described in [Section 2.3](#). In such scenario, the apparent flexural modulus of the laminates at low stiffness state will be significantly higher than that predicted using [Eq 3-6](#). As a result, the drop in apparent flexural modulus upon heating of the specimens would also be less effective than predicted. Furthermore, such bridging could also result in development in large stresses within the CFRP plies during deformation in SM studies, potentially causing them to fail.

Interestingly, one of the CFRP-PS_{33μ} specimens showed E_{HT1} of 12.81 GPa, while the four other samples showed 2.57 ± 0.22 GPa. The existence of this outlier further indicates that the bridging of adjacent CFRP plies due to probable intermittent perforation of the thin interleaves is non-uniform. The effect of this non-uniform bridging is discussed further in the next section.

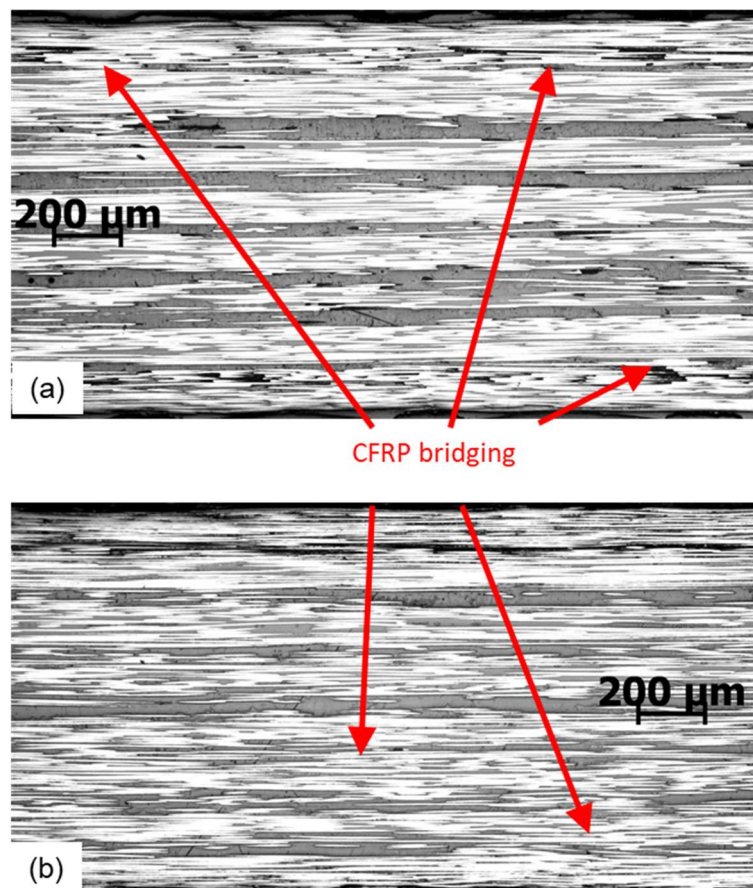
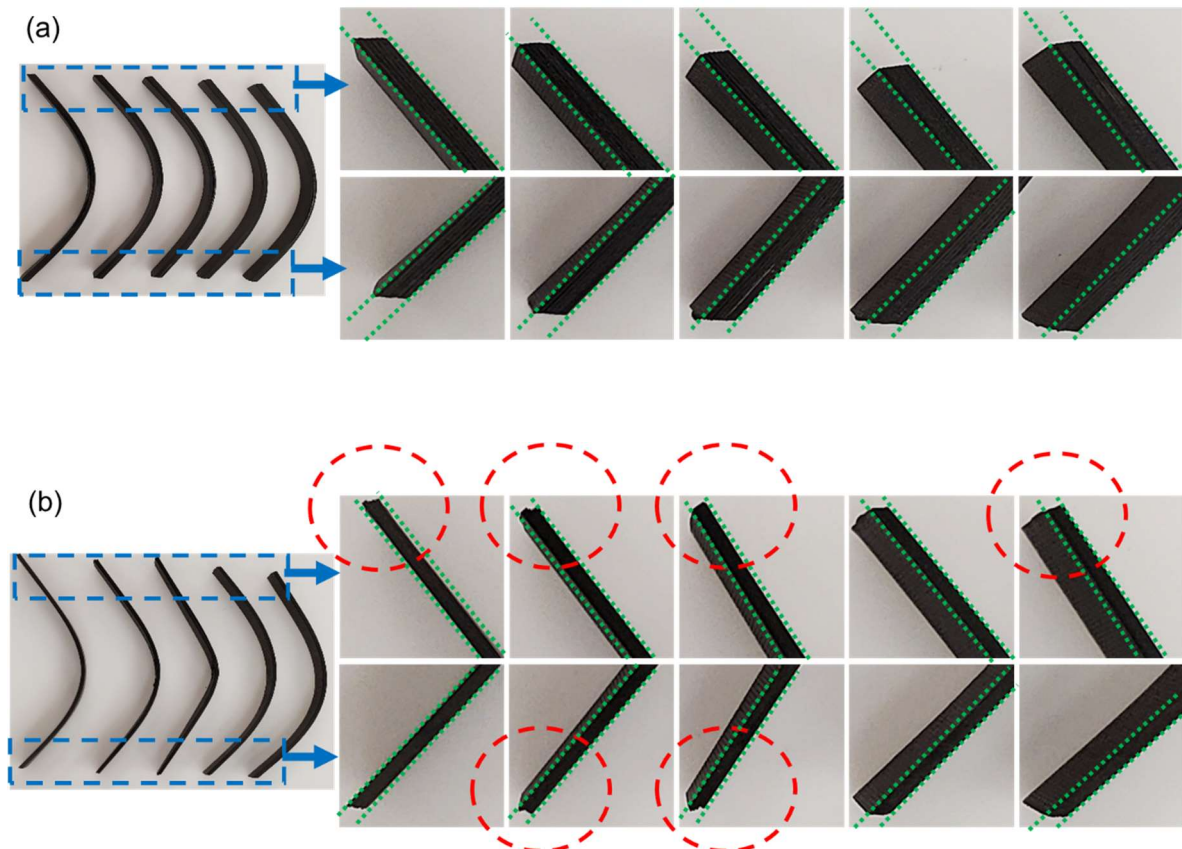


Figure 4.3 Polished longitudinal microsection of pristine CFRP-PS_{33μ} and CFRP-SAN_{37μ}, showing bridging of CFRP

4.1.3.2. SM test results

In the SM study when the composite specimens were heated to 120°C, deformed, cooled to room temperature, and the deformation load was removed, the deformed shape was retained for all the CFRP-PS_{110μ}, CFRP-PS_{174μ}, and CFRP-SAN_{151μ} specimens, and most of the CFRP-PS_{33μ} and CFRP-SAN_{37μ} specimens. Some of the CFRP-PS_{33μ} and CFRP-SAN_{37μ} specimens underwent compression failure or through-thickness shear failure.

The free ends of the deformed CFRP-PS_{174μ}, CFRP-PS_{33μ} and CFRP-SAN_{37μ} are shown in Figure 4.4. The free ends of the deformed CFRP-PS_{174μ} specimens (see Figure 4.4 (a)) show ply slippage that is expected in an interleaved composite (Maples, 2014). The free ends of the deformed CFRP-PS_{33μ} and CFRP-SAN_{37μ} specimens (see Figure 4.4 (b) and (c)) show poor CFRP ply slippage probably due to the bridging of CFRP plies. In the deformed CFRP-PS_{33μ} specimens with poor CFRP ply slippage at only one end, the deformed shape was maintained.



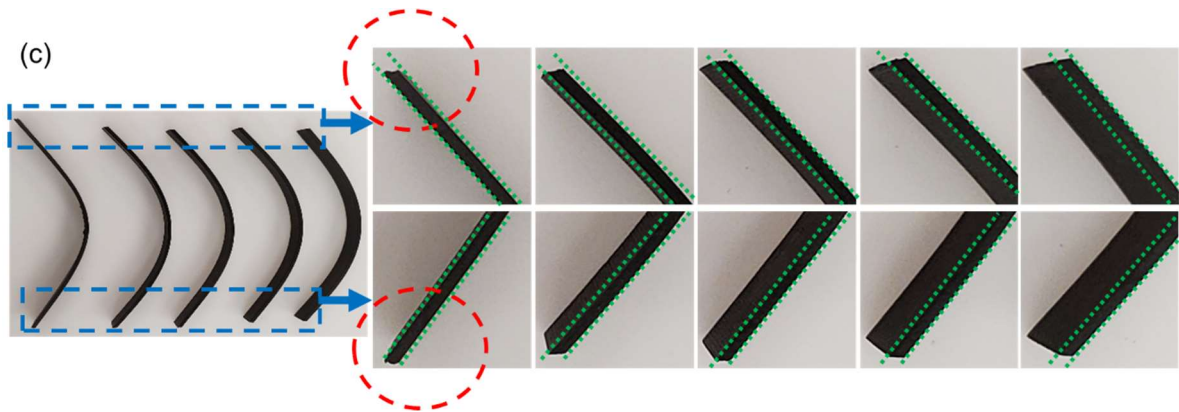


Figure 4.4 Free ends of (a) CFRP-PS_{174μ}, (b) CFRP-PS_{33μ}, and (c) CFRP-SAN_{37μ} specimens after deformation in SM study, where the specimen edges are highlighted using green dotted lines, and poor CFRP ply slippages are circled.

(Due to the orientation of the specimens in the photograph, the side and the top faces of the specimens can be seen in Figure 4.4. Hence, for easier visualisation of the edges of sides of the specimens, they are highlighted by dotted green lines.)

The deformed CFRP-PS_{33μ} and CFRP-SAN_{37μ} specimens with poor CFRP ply slippage at both ends failed due to compressive failure of CFRP and/or through-thickness shear failure leading to delamination. These observations indicate that the SM behaviour of interleaved composites with very thin interleaves (such as CFRP-PS_{33μ} and CFRP-SAN_{37μ}) are also affected by CFRP bridging, similar to the hypotheses specified in Section 3.1.3.1.

When all the successfully deformed composite specimens were reheated to 120°C, their initial as-cured shape was almost fully recovered. Using the shape profiles of the composite specimens in the SM study, the average distance (ζ) between the mid-span and the ends of the specimens in the direction of loading (see Figure 3.14) was extracted before deformation and after deformation and is listed in Table 4.6. Similarly, the ζ of the specimens after 2 minutes of shape recovery and after 5 minutes of shape recovery is also listed in Table 4.6, where the time of shape recovery is measured from the instance deformed specimens are placed in the preheated oven. From this data, it is evident that the shape recovery in thick specimens (i.e., CFRP-PS_{174μ} and CFRP-SAN_{151μ}) is slightly slower than that in thinner

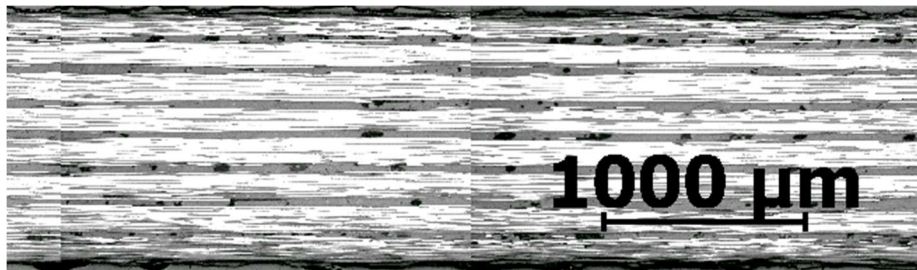
interleaves. Further work can be done in the future to explore the influence of interleaf material and thickness on the speed of shape recovery of interleaved composites.

As seen previously in [Section 3.3.3.3](#), voids are formed in the interleaves of the specimens that achieved successful shape recovery in the SM study (see [Figure 4.5](#)). As a result, the average thickness (t) of the specimens increases slightly, leading to a small change in their apparent flexural modulus, as shown in [Table 4.7](#).

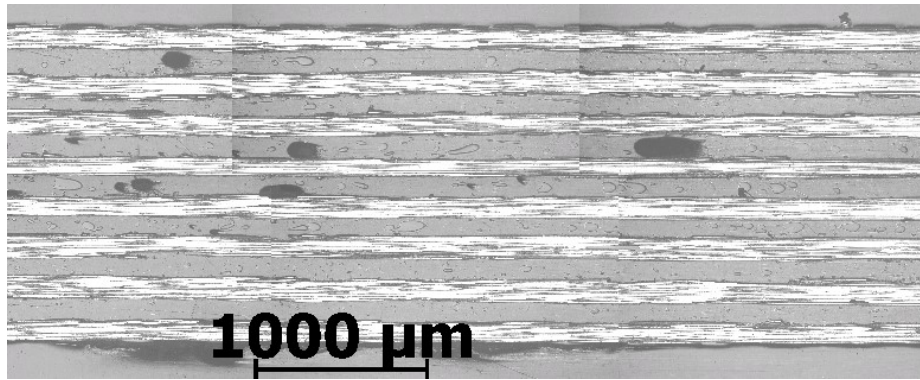
Table 4.6. Distance (ζ) between the mid-span and the ends of composite specimens in the direction of loading at different stages of the SM tests described in [Section 4.1.2.2](#)

Composite name	Distance (ζ) between the mid-span and the ends of specimens in the direction of loading (mm)			
	Before deformation	After deformation	After shape recovery	
			2 min	5 min
CFRP-PS _{33μ}	0.0	19.5	1.5	1.2
CFRP-PS _{110μ}	0.0	19.9	1.2	0.6
CFRP-PS _{174μ}	0.0	20.0	4.9	1.4
CFRP-SAN _{37μ}	0.0	19.3	1.0	0.6
CFRP-SAN _{151μ}	0.0	20.0	9.8	1.8

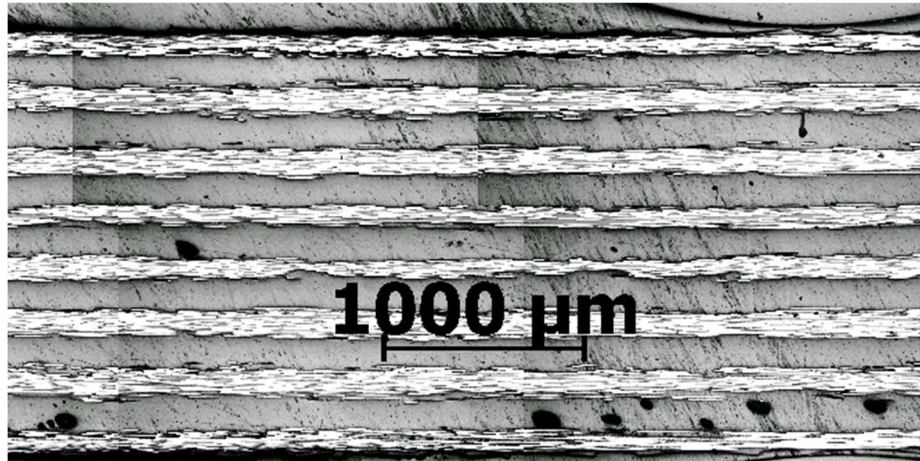
(a)



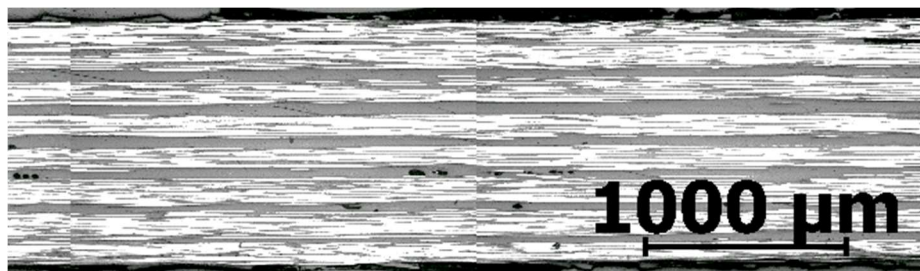
(b)



(c)



(d)



(e)

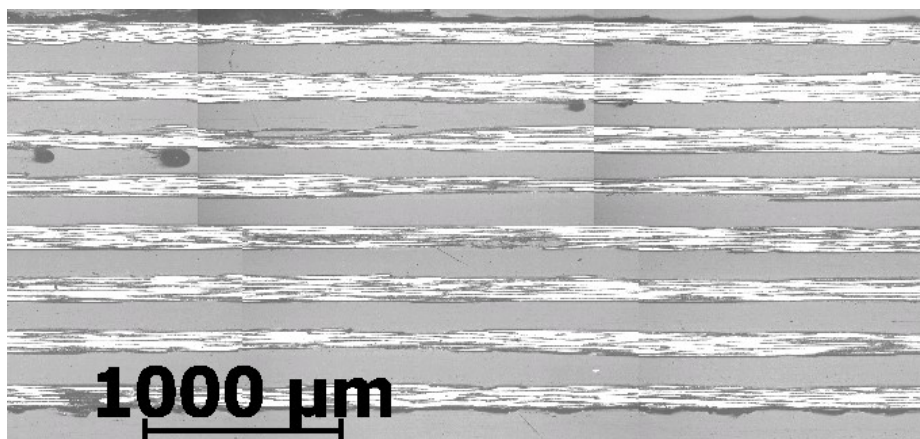


Figure 4.5 Polished longitudinal microsection of (a) CFRP-PS_{33μ}, (b) CFRP-PS_{110μ}, (c) CFRP-PS_{174μ}, (d) CFRP-SAN_{37μ} and (e) CFRP-SAN_{151μ} composites after SM tests

Table 4.7. Specimen thickness (t) and apparent flexural moduli (E_{RT}) moduli of the composites before and after the SM tests described in Section 4.1.2.2

(theoretically predicted moduli are provided in brackets)

Composite name	$t_{\text{before SM}}^*$ [mm]	$t_{\text{after SM}}$ [mm]	$E_{RT-\text{before SM}}$ [GPa]	$E_{RT-\text{after SM}}$ [GPa]
CFRP-PS _{33μ}	1.21 ± 0.05	1.25 ± 0.03 ^a	109.71 ± 2.66 (103.45)	105.56 ± 3.89 ^a (102.80)
CFRP-PS _{110μ}	1.79 ± 0.10	1.84 ± 0.08	75.53 ± 3.47 (75.05)	71.83 ± 1.80 (73.01)
^c CFRP-PS _{174μ}	2.20 ± 0.04	2.23 ± 0.04	62.45 ± 2.33 (62.56)	61.75 ± 3.86 (61.92)
CFRP-SAN _{37μ}	1.26 ± 0.03	1.29 ± 0.02 ^b	101.74 ± 1.31 (100.04)	101.85 ± 3.18 ^b (98.73)
^c CFRP-SAN _{151μ}	2.05 ± 0.04	2.10 ± 0.05	67.24 ± 1.15 (66.69)	61.86 ± 5.42 (65.30)

^a This data was obtained from 3 specimens

^b This data was obtained from 4 specimens

^c This data has already been presented in Table 3.18

* Same as 't' shown in Table 4.3

4.1.3.3. 3PB test results

Typical load-displacement curves of the control, CFRP-PS_{174μ} and CFRP-SAN_{151μ} composites in flexural tests are shown in Figure 4.6. Based on the methodologies described in Section 3.1.3.1 and Section 3.3.3.2, the load associated with the initiation of failure (L_f) was determined for each load-displacement curve and the corresponding τ^{max} , σ^{max} and $\sigma^{maxCFRP}$ were calculated and are shown in

Table 4.8. From the average slope of each force-displacement curve (after ignoring the initial non-linear segment and prior to the initiation of failure), the corresponding apparent flexural moduli (E_{RT-3PB}) were calculated as shown in [Section 3.3.3.1](#) and are shown in [Table 4.8](#). Furthermore, the polished longitudinal microsection of the composite specimens after failure in 3PB tests is shown in [Figure 4.7](#).

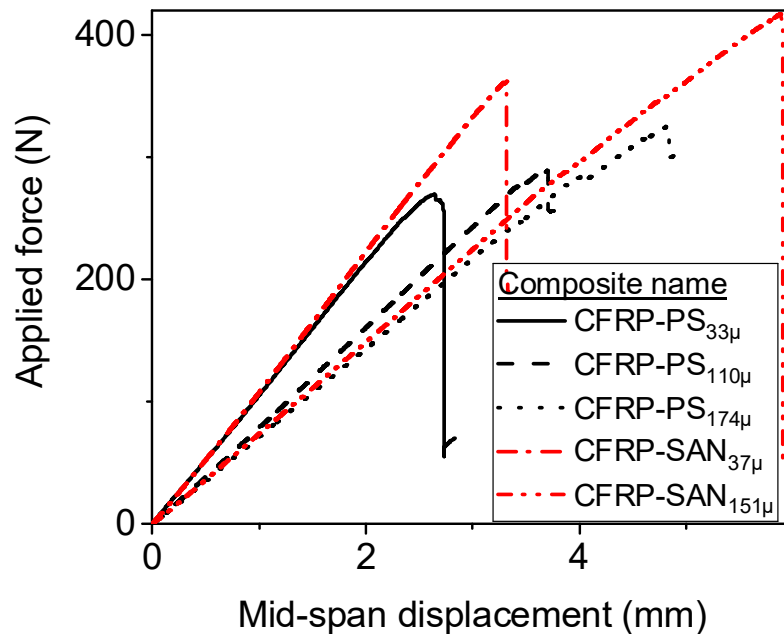


Figure 4.6 Typical load-displacement curves of the composites in the 3PB tests described in [Section 4.1.2.3](#)

Table 4.8. τ^{max} , σ^{max} , and $\sigma^{maxCFRP}$, and E_{RT-3PB} of interleaved composite specimens in the 3PB tests described in Section 4.1.2.3

(Theoretical predictions are specified in brackets. These values have already been presented in Table 4.5)

Composite name	τ^{max} (MPa)	σ^{max} (GPa)	$\sigma^{maxCFRP}$ (GPa)	E_{RT-3PB} (GPa)
CFRP-PS _{33μ}	17.96 \pm 2.44	1.16 \pm 0.17	1.34 \pm 0.17	104.44 \pm 2.96 (102.17)
CFRP-PS _{110μ}	12.88 \pm 0.99	0.81 \pm 0.05	1.28 \pm 0.12	77.61 \pm 3.36 (75.52)
CFRP-PS _{174μ}	11.25 \pm 0.68	0.71 \pm 0.04	1.34 \pm 0.09	63.61 \pm 1.26 (62.08)
CFRP-SAN _{37μ}	23.36 \pm 0.41	1.47 \pm 0.06	1.75 \pm 0.02	101.11 \pm 3.60 (100.49)
CFRP-SAN _{151μ}	12.46 \pm 0.74	0.79 \pm 0.04	1.39 \pm 0.08	66.85 \pm 0.31 (66.47)

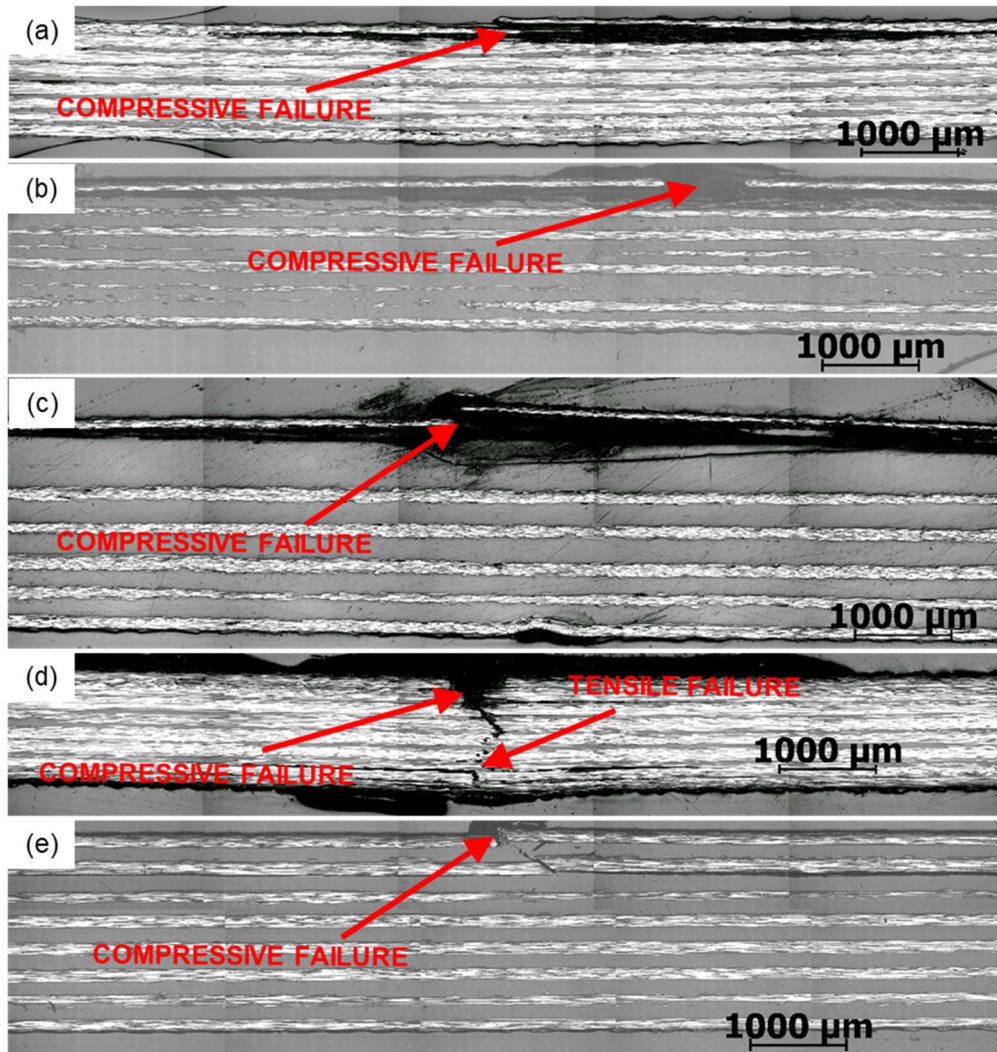


Figure 4.7 Polished longitudinal microsection of (a) CFRP-PS_{33μ}, (b) CFRP-PS_{110μ}, (c) CFRP-PS_{174μ}, (d) CFRP-SAN_{37μ} and (e) CFRP-SAN_{151μ} specimens after failure in 3PB tests

The micrographs of the interleaved composite specimens show that their failure in 3PB tests happens in the CFRP laminae and is not due to shear failure within the interleaves. Furthermore, the $\sigma^{\max\text{CFRP}}$ of CFRP-PS_{33μ}, CFRP-PS_{110μ}, CFRP-PS_{174μ}, and CFRP-SAN_{151μ} composites are also comparable to the compressive strength of CFRP (1.35 GPa (Ciba-Geigy Plastics, 1989)). However, the $\sigma^{\max\text{CFRP}}$ of CFRP-SAN_{37μ} composite (1.75 ± 0.02 GPa) is found to be significantly higher, and comparable to the tensile strength of CFRP (1.65 GPa (Ciba-Geigy Plastics, 1989)). The reason behind the unusually high $\sigma^{\max\text{CFRP}}$ of CFRP-SAN_{37μ} is not clear and should be explored in the future.

4.1.4. Conclusion

When the thickness of PS or SAN interleaves is reduced, the resultant interleaved composites have a higher flexural modulus. The reduction in the thickness of the interleaves does not have any detrimental effect on the flexural failure strength of the interleaved composites. However, when the thickness of the PS or SAN interleaves is reduced too much (such as in CFRP-PS_{33μ}, and CFRP-SAN_{37μ} composites), adjacent CFRP plies may connect in some places, leading to inconsistent CS and SM properties. The reproducibility of composites with very thin interleaves can be improved by improving the production process (or using different materials) to avoid bridging of CFRP layers.

4.2. Investigation of improvement of the flexural modulus of interleaved composites by reinforcing the interleaves

To improve the apparent flexural modulus of the interleaved composites, composites with reinforced interleaves were produced and their apparent flexural moduli were studied. Furthermore, CS and SM behaviour and the flexural strength properties of these composites were also studied.

4.2.1. Materials and laminates

As in the previous experimental studies described in this thesis, unidirectional TS300/914 carbon epoxy prepreg was selected as the CFRP component of the interleaved composite. The interleaf materials selected to be a part of the interleaved composites were PS and SAN. Plain weave carbon fibre (WCF) fabric (weft and warp fibres: Toray T300 1K, Weave: 1/1 Plain) of thickness 100 μm and areal weight of 90 gsm ([Easy Composites Ltd, no date](#)), procured from Easy Composites Ltd (UK) was used to reinforce the PS and SAN interleaves.

Composite panels (175 mm x 220 mm) were produced by following a 2-step approach. In the first step, WCF was sandwiched between two interleaf films (PS or SAN) and heated to 120°C and 1 bar pressure (provided by vacuum bag) using Global Vacuum Presses G-SUB 1310 (Höchsmann GmbH, Germany) heated vacuum table. After 1 hour at this temperature and

pressure, the sandwiched layers were cooled down to room temperature and the applied pressure was then removed. This process results in the production of semi-consolidated PS-WCF and SAN-WCF reinforced thermoplastic (RTP) laminae.

In the second step, the panels with layups specified in Table 4.9 were prepared and cured at 175°C and 7 bar pressure in an autoclave for 1 hour according to the cure schedule recommended by the manufacturer of the CFRP. During this second step, the curing of epoxy in CFRP laminae and the full consolidation of the PS-WCF and SAN-WCF laminae happen simultaneously.

Table 4.9 Names and layups of the composite panels
prepared for the studies shown in Section 4.2

Composite name	Layup sequence ¹	Nominal thickness of PS/SAN films used in layup (μm)	Thickness of reinforced interleaves in cured composite (μm) ²
CFRP-PS-WCF	[(0°/PS/WCF/PS) ₇ /0°]	100	175.29 ± 7.41
CFRP-SAN-WCF	[(0°/SAN/WCF/SAN) ₇ /0°]	100	235.24 ± 7.59

¹ Here, PS/WCF/PS and SAN/WCF/SAN are the semi-consolidated laminae

² Calculated from the thickness of the specimens, layup sequence and the thickness of the CFRP laminae.

4.2.2. Experimental methodology

4.2.2.1. Prediction of moduli of RTPs

From the dimensions and weights of the composite specimens prepared in this study and the areal weight of CFRP (198 g/m²) and the woven reinforcement (90 g/m²), the total fibre volume

fraction (V_f) of WCF in RTPs was calculated. The theoretical modulus of reinforced thermoplastic films (E_{RTP} in Eq 4-1) was predicted using the mosaic model that considers woven fabric as a series of discontinuous unidirectional fabric (Byström, Jekabsons and Varna, 2000). The V_f in the RTP films and their modulus (E_{RTP}), predicted using the mosaic model are provided in Table 4.10.

$$E_{RTP} = (0.5 * V_f * E_f) + (0.5 * (1 - V_f) * E_m) + (0.5) \left(\frac{V_f}{E_f} + \frac{(1 - V_f)}{E_m} \right)^{-1} \quad \text{Eq 4-1}$$

where,

E_f (Modulus of fibre in WCF) = 230 GPa,

E_m (Modulus of matrix) = 3.2 GPa for PS and 3.7 GPa for SAN, as per manufacturer's datasheet

Table 4.10. E_{RTP} prediction based on mosaic model

RTP	Vf	E_{RTP} (GPa)
PS-WCF	0.30 ± 0.02	46.1
SAN-WCF	0.19 ± 0.01	32.7

Similarly, to predict E_{RTP} using the method of inclusions, the proprietary software WiseTex and TexComp (procured from KU Leuven, Belgium) were used to model the RTP layer. The parameters used in this model are shown in Table 4.11.

Table 4.11. Parameters used to model the RTP layer in Wisetex and Texcomp software

Material	Parameter	Value
WCF	Fibre diameter	$7 \mu\text{m}^a$
	Fibre density	1760 kg/m^3^a
	Fibre Young's modulus	230 GPa^a

	Number of fibres in yarn	1000
	Yarn width	0.83 mm ^b
	Yarn thickness	0.05 mm ^c
	Yarn count (warp and weft)	7/cm ^c
	Crimp	50%
PS	Young's modulus	3.2 GPa ^d
SAN	Young's modulus	3.7 GPa ^e

^a Obtained from (Toray Composite Materials America Inc., 2018)

^b Obtained by visual analysis of the fabric

^c Obtained from (Easy Composites Ltd, no date)

^d Obtained from (UL Prospector, 2012)

^e Obtained from (UL Prospector, 2000b)

The areal density of the modelled fabric, the V_f and the E_{RTP} obtained through the WiseTex and TexComp software are provided in Table 4.12. Here, it can be seen that the predicted areal weight of WCF (92.5 g/m²) is close to the areal weight suggested by the manufacturer (90 g/m²).

Table 4.12. E_{RTP} prediction based on the method of inclusions

RTP	Areal weight of WCF (g/m ²)	V_f	E_{RTP} (GPa)
PS-WCF	92.5	0.31	42.1
SAN-WCF	92.5	0.23	32.3

A comparison of the predicted E_{RTP} values in Table 4.10 and Table 4.12, reveals a considerable similarity between the predictions by the two models used here. In these models, the mosaic model does not consider the waviness of the fibres, and so, the predictions obtained from this method could be expected to be an overprediction of E_{RTP} . Therefore, the

predictions based on the method of inclusions are used in this study for further predictions of the moduli of the interleaved composite.

4.2.2.2. CS tests

Specimens having the dimensions shown in Table 4.13 were cut from the cured composite panels using a waterjet, as shown in Section 3.3.2.1. Following the methodology described in Section 3.3.2.1, CS tests were performed using the support spans shown in Table 4.13. The support spans ensured that the span-to-thickness ratio of the specimens was close to 30, while the span stays less than 70. This was done to ensure that the specimens do not slip off the 3PB setup while being loaded. Furthermore, as the apparent moduli of the CFRP-PS-WCF and CFRP-SAN-WCF specimens are not compared against each other, so the matching of the span-to-thickness ratio was not considered.

4.2.2.3. SM tests

Specimens having the dimensions shown in Table 4.14 were cut from the cured composite panels using a waterjet, as shown in Section 3.3.2.1. Following the methodology described in Section 3.3.2.3, SM tests were performed. Before and after the SM tests, the apparent flexural moduli of the composite specimens were measured at room temperature using the methodology described in Section 4.2.2.2.

4.2.2.4. 3PB tests

Specimens having the dimensions shown in Table 4.15 were cut from the cured composite panels using a waterjet, as shown in Section 3.3.2.1. Following the methodology described in Section 3.1.2.1, 3PB tests were performed with the support spans shown in Table 4.15. The support spans were fixed to be 70 mm to ensure that the specimens do not slip off the 3PB setup while being loaded. Furthermore, as the strengths (or stresses) of the CFRP-PS-WCF and CFRP-SAN-WCF specimens are not compared against each other, so the matching of the span-to-thickness ratio was not considered.

Table 4.13 Dimensions of composite specimens used in the
CS tests described in Section 4.2.2.2

(here, l , w , t – length, width and thickness of the specimens)

Composite name	Dimensions			Support span (mm)
	l (mm)	w (mm)	t (mm)	
CFRP-PS-WCF	79.69 ± 1.12	8.95 ± 0.02	2.25 ± 0.03	66
CFRP-SAN-WCF	79.98 ± 0.14	9.21 ± 0.03	2.62 ± 0.06	70

Table 4.14 Dimensions of composite specimens used in the
SM tests described in Section 4.2.2.3

(here, l , w , t – length, width and thickness of the specimens)

Composite name	Dimensions		
	l (mm)	w (mm)	t (mm)
CFRP-PS-WCF	79.65 ± 0.04	8.64 ± 0.03	2.25 ± 0.03
CFRP-SAN-WCF	80.00 ± 0.09	9.22 ± 0.03	2.66 ± 0.05

Table 4.15 Dimensions of composite specimens used in the
3PB tests described in Section 4.2.2.4

(here, l , w , t – length, width and thickness of the specimens)

Composite name	Dimensions			Support span (mm)
	l (mm)	w (mm)	t (mm)	
CFRP-PS-WCF	79.64 ± 0.07	8.67 ± 0.02	2.20 ± 0.06	70
CFRP-SAN-WCF	79.98 ± 0.12	9.20 ± 0.05	2.66 ± 0.04	70

4.2.2.5. Optical microscopy of composites

The central 20 mm section (i.e., mid-span) of selected specimens in the pristine as-cured state, after 3PB tests, and after SM tests were inspected by optical microscopy, following the methodology described in Section 3.1.2.2.

4.2.3. Results and discussion

4.2.3.1. CS test results

Typical force-displacement curves of the interleaved composites in CS tests, at their RT1 and the HT1 test conditions, are shown in Figure 4.8 (a) and (b) respectively. The force-displacement curves of the interleaved composites at the RT2 test condition are not shown here as they are not distinguishable from the curves in Figure 4.8 (a), by the naked eye. From the average slope of each force-displacement curve (after ignoring the initial non-linear segment), the corresponding apparent flexural modulus was calculated, as shown in Section 3.3.3.1. The apparent flexural modulus of the composites in their high stiffness state (E_{RT1}), low stiffness state (E_{HT1}) and again at high stiffness state (E_{RT2}) are listed in Table 4.16.

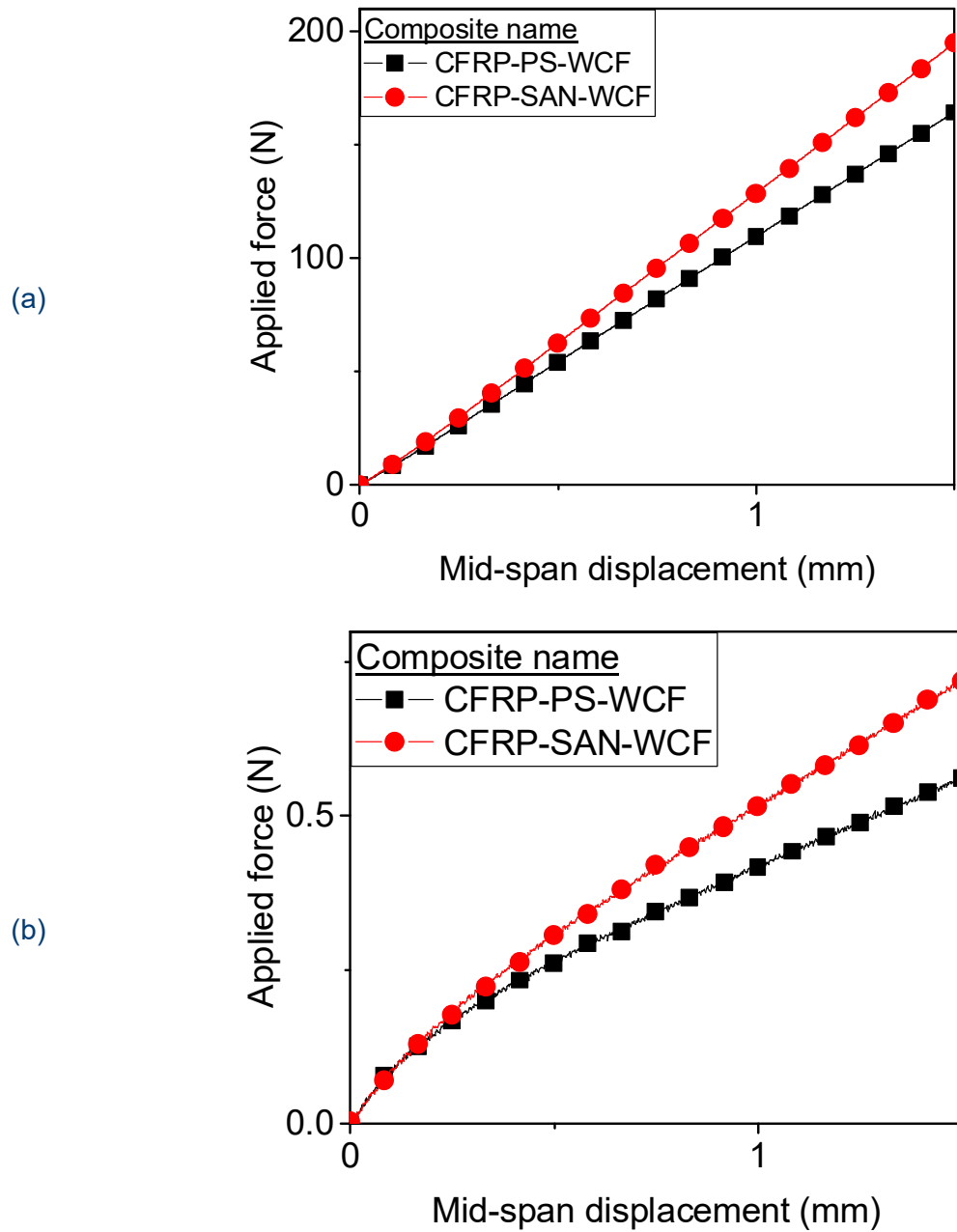


Figure 4.8 Typical force-displacement curves of composite specimens at (a) RT1 and (b) HT1 test conditions in the CS tests described in Section 4.2.2.2

Table 4.16. The apparent flexural modulus of composites at RT1, HT1 and RT2 test conditions in the CS tests described in Section 4.2.2.2

Composite name	Apparent flexural moduli of composites		
	E_{RT1} (GPa)	E_{HT1} (GPa)	E_{RT2} (GPa)
CFRP-PS-WCF	79.48 ± 1.49	0.45 ± 0.17	80.77 ± 1.55
CFRP-SAN-WCF	69.43 ± 1.30	0.21 ± 0.02	70.63 ± 0.75

As seen in previous investigations, heating CFRP-PS-WCF and CFRP-SAN-WCF specimens cause their apparent flexural modulus to drop by more than 99% (E_{RT1} vs E_{HT1}). Upon cooling down, the apparent flexural modulus of the composites is fully restored.

4.2.3.2. Quantifying the increase in apparent flexural modulus of interleaved composites due to introducing WCF reinforcement in the interleaves

Unlike previously discussed interleaved composites, the interleaved composites used in this study have their room temperature apparent flexural modulus ($E_{RT-Reinf}$) influenced by the modulus of the reinforced interleaf layers (E_{RTP}). The apparent flexural modulus of the composites interleaved with RTPs in their high stiffness state ($E_{RT-Reinf}$) can be predicted using Eq 4-2. The apparent flexural modulus of the composites interleaved with RTPs in their low stiffness state can still be predicted using Eq 3-6.

$$E_{RT-Reinf} = \frac{12}{h^3} \left(\sum_{i=1}^N E_c \left(\frac{t_i^3}{12} + t_i z_i^2 \right) + \sum_{j=1}^M E_{RTP} \left(\frac{t_j^3}{12} + t_j z_j^2 \right) \right) \quad \text{Eq 4-2}$$

where,

E_c – Young's modulus of CFRP = 120 GPa (Maples et al., 2016; Zhang, 2020)

t_i – thickness of each CFRP ply

t_j – thickness of each RTP ply

z_i – distance from the specimen mid-thickness to mid-thickness of each CFRP ply

z_j – distance from the specimen mid-thickness to mid-thickness of each RTP ply

h – thickness of the composite specimen

N – Number of CFRP laminae

M – Number of RTP laminae

As the thickness of the interleaves of CFRP-PS-WCF and CFRP-SAN-WCF are different from that seen in previous investigations, their apparent flexural moduli cannot be compared directly to the previous works. So, the numerically predicted and experimentally observed moduli of the composites with reinforced interleaves have to be compared against the numerically predicted moduli of the composites with unreinforced interleaves but with the same interleaf thickness. The apparent flexural moduli of the composites with unreinforced interleaves in their high stiffness state can be obtained by Eq 4-3. The analytical predictions (based on Eq 4-2 and Eq 4-3) and experimental observation (E_{RT1}) of the apparent flexural modulus of CFRP-PS-WCF and CFRP-SAN-WCF in their high stiffness state are listed in Table 4.17.

$$E_{RT-Unrein} = \frac{12}{h^3} \left(\sum_{i=1}^N E_c * \left(\frac{t_i^3}{12} + t_i z_i^2 \right) + \sum_{j=1}^M E_m * \left(\frac{t_j^3}{12} + t_j z_j^2 \right) \right) \quad \text{Eq 4-3}$$

where,

E_m – Modulus of the matrix. Assumed to be the same as tensile modulus from Table 3.7.

Table 4.17. Experimentally measured and theoretically predicted apparent flexural modulus of composites with reinforced interleaves in high stiffness state

Composite name	Theoretical prediction		Experimental observation	
	$E_{RT-Unrein}$	$E_{RT-Reinf}$	E_{RT1}	% difference
	(GPa)	(GPa)	(GPa)	compared to $E_{RT-Unrein}$
CFRP-PS-WCF	63.44	82.28	79.48 ± 1.49	25.3
CFRP-SAN-WCF	55.08	71.07	69.43 ± 1.30	26.0

It can be seen from Table 4.17 that the apparent flexural modulus of CFRP-PS-WCF and CFRP-SAN-WCF in the high stiffness state (E_{RT1}) is in reasonable agreement with the theoretical predictions ($E_{RT-Reinf}$). Furthermore, compared to composites with unreinforced

interleaves, the composites with reinforced interleaves (i.e., $E_{RT-Unrein}$ vs E_{RT1}) have a more than 25% increase in apparent flexural modulus. This observation shows that the introduction of reinforcements within the interleaves causes the overall flexural modulus of the composite to increase as predicted. To improve the apparent flexural modulus of the composite closer to that of pristine CFRP (120 GPa), it is necessary to improve the RTP laminae by increasing the V_f along the longitudinal direction.

4.2.3.3. SM test results

As seen in previous sections, when the composite specimens were heated to 120°C, deformed, cooled to room temperature, and the deformation load was removed, the deformed shape was almost fully retained for all the composite specimens. On re-heating the composite specimens, they recovered towards their initial shape.

When the deformed composite specimens were reheated to 120°C, their initial as-cured shape was almost fully recovered. Using the shape profiles of the composite specimens in the SM study, the average distance (ζ) between the mid-span and the ends of the specimens in the direction of loading (see Figure 3.14) was extracted before deformation and after deformation and is listed in Table 4.18. Similarly, the ζ of the specimens after 2 minutes of shape recovery and after 5 minutes of shape recovery is also listed in Table 4.18, where the time of shape recovery is measured from the instance deformed specimens are placed in the preheated oven. As seen in Section 3.3.3.3, the composites with reinforced SAN interleaves (CFRP-SAN-WCF) have slower shape recovery than the composites with reinforced PS interleaves (CFRP-PS-WCF). The slow shape recovery of CFRP-SAN-WCF could probably be due to higher T_g of SAN, or the thicker reinforced SAN interleaves.

Table 4.18. Distance (ζ) between the mid-span and the ends of composite specimens in the direction of loading at different stages of the SM tests described in Section 4.2.2.3

Composite name	Distance (ζ) between the mid-span and the ends of specimens in the direction of loading (mm)			
	Before deformation	After deformation	After shape recovery	
			2 min	5 min
CFRP-PS-WCF	0.0	20.0	4.5	0.9
CFRP-SAN-WCF	0.0	19.5	9.2	1.6

The polished longitudinal microsection of the composite specimens after the SM study reveals the formation of voids within the interleaf region (see Figure 4.9), as seen in Section 3.3.3.3. As a result, the average thickness (t) of the CFRP-PS-WCF specimens increases slightly, leading to a small change in their apparent flexural modulus, as shown in Table 4.19.

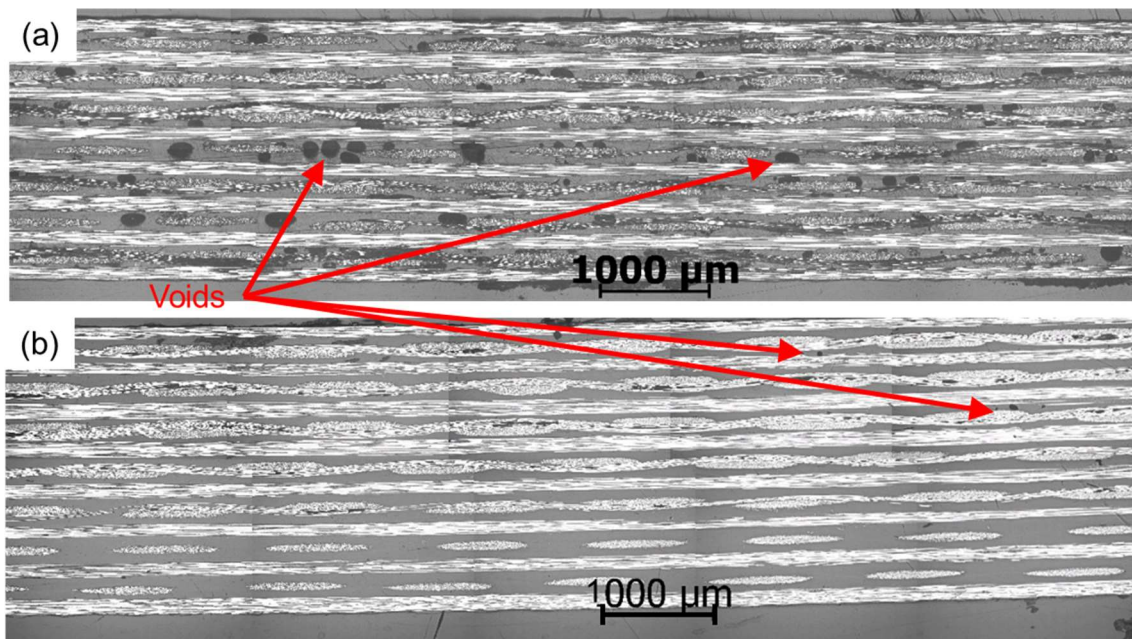


Figure 4.9 Polished longitudinal microsection of (a) CFRP-PS-WCF, and
(b) CFRP-SAN-WCF after SM study

Table 4.19. Specimen thickness (t) and apparent flexural moduli (E_{RT}) moduli of the composites before and after the SM tests described in Section 4.2.2.3

(theoretically predicted moduli, calculated using Eq 3-6, are provided in brackets)

Composite	$t_{\text{before SM}}^*$	$t_{\text{after SM}}$	$E_{RT-\text{before SM}}$	$E_{RT-\text{after SM}}$
name	[mm]	[mm]	[GPa]	[GPa]
CFRP-PS-WCF	2.25 ± 0.03	2.32 ± 0.03	79.48 ± 1.49 (83.93)	80.73 ± 1.24 (82.85)
CFRP-SAN-WCF	2.66 ± 0.05	2.66 ± 0.05	68.88 ± 1.28 (78.60)	69.12 ± 1.33 (78.58)

* Same as ' t ' shown in Table 4.14

4.2.3.4. 3PB test results

Typical load-displacement curves of the CFRP-PS-WCF and CFRP-SAN-WCF in flexural tests are shown in Figure 4.10. Based on the methodologies described in Section 3.1.3.1 and Section 3.3.3.2, the load associated with the initiation of failure (L_f) was selected for each load-displacement curve and the corresponding τ^{\max} , σ^{\max} and $\sigma^{\max\text{CFRP}}$ were calculated. In these composites, the RTP laminae have a significantly higher modulus than pristine PS or SAN. Hence, significant bending stresses are developed in the RTP laminae. The maximum bending stress developed in the RTP layers can be calculated using Eq 4-4, which is obtained by suitably modifying Eq 3-7.

$$\sigma^{\max\text{RTP}} = \frac{6 L_f E_{RTP}}{\text{span}^2} (t - 2t_{\text{CFRP}}) \left(\frac{F}{\delta} \right)^{-1} \quad \text{Eq 4-4}$$

where,

E_{RTP} is obtained from Table 4.12

t is the thickness of each specimen

$t_{\text{CFRP}} = 120 \mu\text{m}$ is the thickness of the CFRP plies used in the layup

The τ^{max} , σ^{max} , $\sigma^{maxCFRP}$ and σ^{maxRTP} of CFRP-PS-WCF and CFRP-SAN-WCF are provided in Table 4.20. Furthermore, the polished longitudinal microsection of the composite specimens after failure in 3PB tests is shown in Figure 4.11.

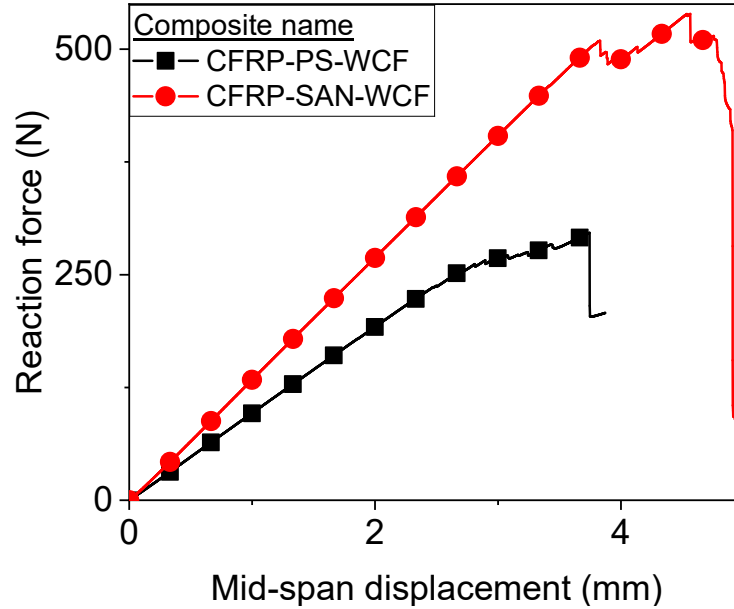


Figure 4.10 Typical load-displacement curves of the composites in the 3PB tests described in Section 4.2.2.4

Table 4.20. τ^{max} , σ^{max} , $\sigma^{maxCFRP}$, and σ^{maxRTP} of interleaved composite specimens in the 3PB tests described in Section 4.2.2.4

Composite name	τ^{max} (MPa)	σ^{max} (GPa)	$\sigma^{maxCFRP}$ (GPa)	σ^{maxRTP} (GPa)
CFRP-PS-WCF	8.78 ± 0.79	0.56 ± 0.04	0.85 ± 0.07	0.32 ± 0.02
CFRP-SAN-WCF	16.06 ± 0.51	0.85 ± 0.02	1.46 ± 0.04	0.40 ± 0.01

The microsections show that the CFRP-SAN-WCF specimens loaded in 3PB fail due to the compressive failure of CFRP, as seen previously in Section 3.3.3.3. This idea is further reinforced by the fact that the $\sigma^{maxCFRP}$ of CFRP-SAN-WCF is comparable to the compressive strength of CFRP (1.35 GPa).

The CFRP-PS-WCF specimens loaded in 3PB tests, however, fail prematurely at lower stresses. The microsections of CFRP-PS-WCF specimens indicate the presence of a compressive failure inside the PS-WCF RTP laminae. Furthermore, the failure of the CFRP laminae adjacent to the failed RTP layer at different locations along the span indicates that the damages in these CFRP laminae are probably not due to compressive failure. However, further studies are required to understand the exact failure mechanism in CFRP-PS-WCF specimens.

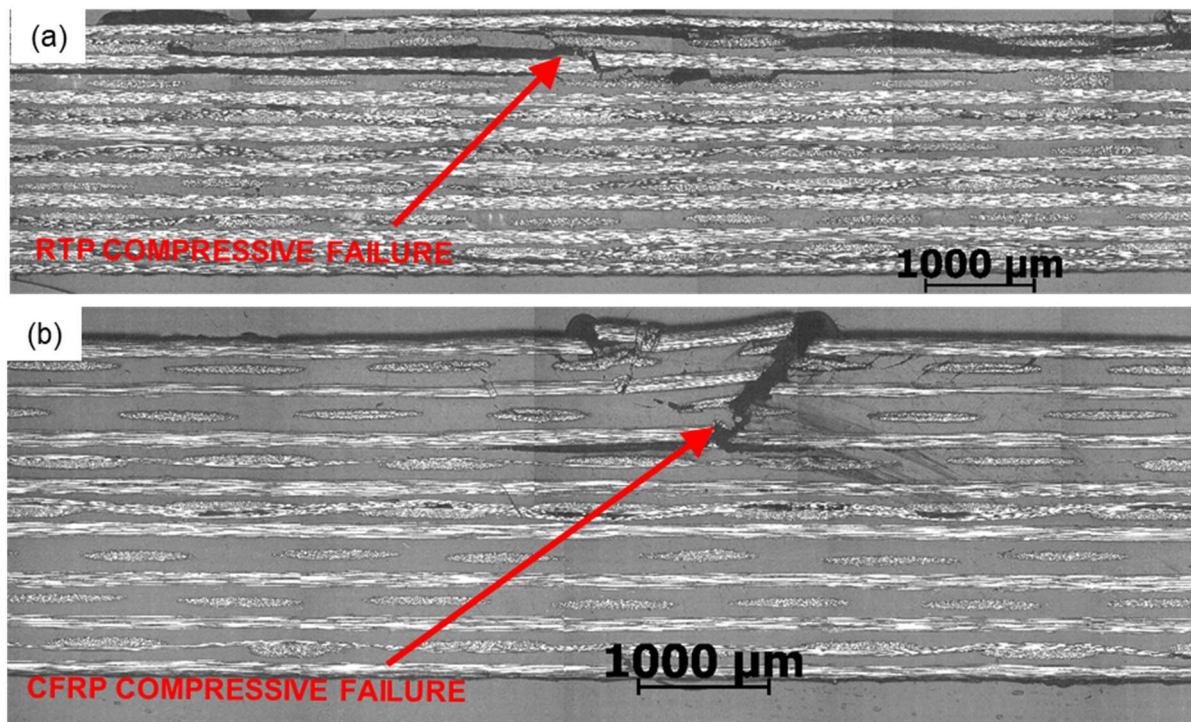


Figure 4.11 Polished longitudinal microsection of (a) CFRP-PS-WCF and (b) CFRP-SAN-WCF specimens after failure in 3PB tests

4.2.4. Conclusion

By introducing reinforcements within the interleaves of an interleaved composite, the apparent flexural modulus of the composite can be improved. The CFRP-PS-WCF and CFRP-SAN-WCF specimens had fibre volume fractions of 0.30 and 0.19 (respectively) in their RTP interleaves and, achieved 25% and 26% (respectively) higher apparent flexural modulus than a composite with pristine interleaves. It can also be expected by achieving higher V_f in the

RTP laminae, and by orienting a higher fraction of fibres in the longitudinal direction, interleaved composites with even higher apparent flexural modulus can be produced.

Furthermore, when loaded in flexure, premature failure was seen in CFRP-PS-WCF specimens, and not in CFRP-SAN-WCF specimens. Further studies have to be done in detail to understand the reason behind this premature failure.

4.3. Chapter summary

- By reducing the thickness of the PS and SAN interleaves to as low as 33 μm and 37 μm respectively, the apparent flexural modulus (and consequently, stiffness) of the corresponding composites can be increased to as high as 90% and 85% of that of pristine CFRP respectively.
- Using such very thin PS and SAN interleaves can result in bridging between adjacent CFRP plies in some cases, leading to the composites having inconsistent CS and SM properties.
- By introducing reinforcements within the PS and SAN interleaves, the apparent flexural modulus of the resultant composites has been increased by 25%, compared to other composites with unreinforced interleaves. Higher apparent flexural modulus can be achieved by improving the manufacturing process to achieve a higher fibre volume fraction within the interleaves, and by increasing the V_f in the reinforced interleaves along the longitudinal direction of the specimens.
- Composites with reinforced PS interleaves showed premature compressive failure, while the composites with reinforced SAN interleaves did not. This phenomenon has to be explored in detail in the future.

This page is intentionally left blank.

Chapter 5. Achieving intrinsic heating capability in thermoplastic interleaved carbon-epoxy composites

To activate controllable stiffness (CS) and shape memory (SM) properties in thermoplastic interleaved CFRP composites, it is necessary to increase their temperature. In the previous works described in [Section 2.3](#) and the experimental studies shown in [Chapter 3](#) and [Chapter 4](#), the temperature increase was achieved using an oven. In this chapter, introducing an intrinsic heating capability to the interleaved composites is explored. Such a heating capability will allow these composites to exhibit their CS and SM capabilities outside an environmental chamber, and eventually, outside a laboratory environment.

A preliminary approach to achieve intrinsic heating in the interleaved composites by resistive heating of the CFRP plies was discussed in [Section 2.8](#), where its disadvantages were also reviewed. This chapter describes the study where an alternative intrinsic heating strategy is explored. To achieve intrinsic heating of interleaved composites, resistive heater layers were embedded within the interleaves. In this study, the CS and SM properties of the intrinsically heated composites containing different embedded heaters were investigated for a range of direct currents (i_{DC}).

5.1. Materials, laminates, and specimens

As in the previous experimental studies described in this thesis, unidirectional TS300/914 carbon epoxy prepreg was selected as the CFRP component of the interleaved composite, and the interleaf material was SAN (100 μm thick film). The selected heaters were woven carbon fibre (WCF) fabric (see [Section 4.2.1](#)) and SS304 grade stainless steel (SS) wire mesh/fabric with an aperture of 82 μm , wire diameter of 28 μm and areal weight of around 90 gsm, procured from The Mesh Company Ltd (UK).

Composite panels were produced in a 3-step modular process. In the first step of the manufacturing process, composite laminates (450 mm x 175 mm) with a layup of $[(0^\circ/\text{SAN})_4]$ (see [Figure 5.1 \(a\)](#)) were prepared and cured at 175°C and 7 bar pressure in an autoclave for 1 hour according to the cure schedule recommended by the manufacturer of the CFRP. During this step, the thickness of the SAN film on the outermost ply of the modules/laminates decreased slightly due to the leaking of SAN through the porous debonding layer (i.e., peel ply) that was used to cover the laminates when they were vacuum bagged inside the autoclave. From these large laminates, smaller modules having dimensions of 160 mm x 90 mm were cut using a waterjet (see [Section 3.3.2.1](#)). The 0° fibre direction in the CFRP laminae in these modules was parallel to the edge that has a length of 90 mm.

In the second step of the manufacturing process, dry WCF and SS fabrics (700 mm x 160 mm) were sandwiched between two SAN films (120 mm x 160 mm). This sandwich occupied the central 120 mm x 160 mm section of SS and WCF, with 290 mm x 160 mm of dry SS and WCF left on either side of the sandwich, as shown in (see [Figure 5.1 \(b\)](#)). This sandwich was then heated to 175°C and 1 bar pressure (provided by vacuum bagging) using Global Vacuum Presses G-SUB 1310 (Höchsmann GmbH, Germany) heated vacuum table. After 1 hour at this temperature and pressure, the sandwiched laminates were cooled down to room temperature and the applied pressure was then removed. This process resulted in the production of fully consolidated SAN-SS and SAN-WCF laminae.

In the third step of the manufacturing process, the SAN-SS and SAN-WCF laminae were sandwiched between two modules (having a layup of $[(0^\circ/\text{SAN})_4]$ and dimensions of 160 mm x 90 mm) with the SAN side of these modules facing the SAN-SS and SAN-WCF laminae (see [Figure 5.1 \(c\)](#)). These sandwiched laminates were then heated to 175°C and 1 bar pressure using an HLP40 hot press (Höfer Presstechnik GmbH, Austria). After 1 hour at this temperature and pressure, the sandwiched laminates were cooled down to room temperature and the applied pressure was then removed. [Figure 5.2](#) shows the composite panels at the start of this step in the production process.

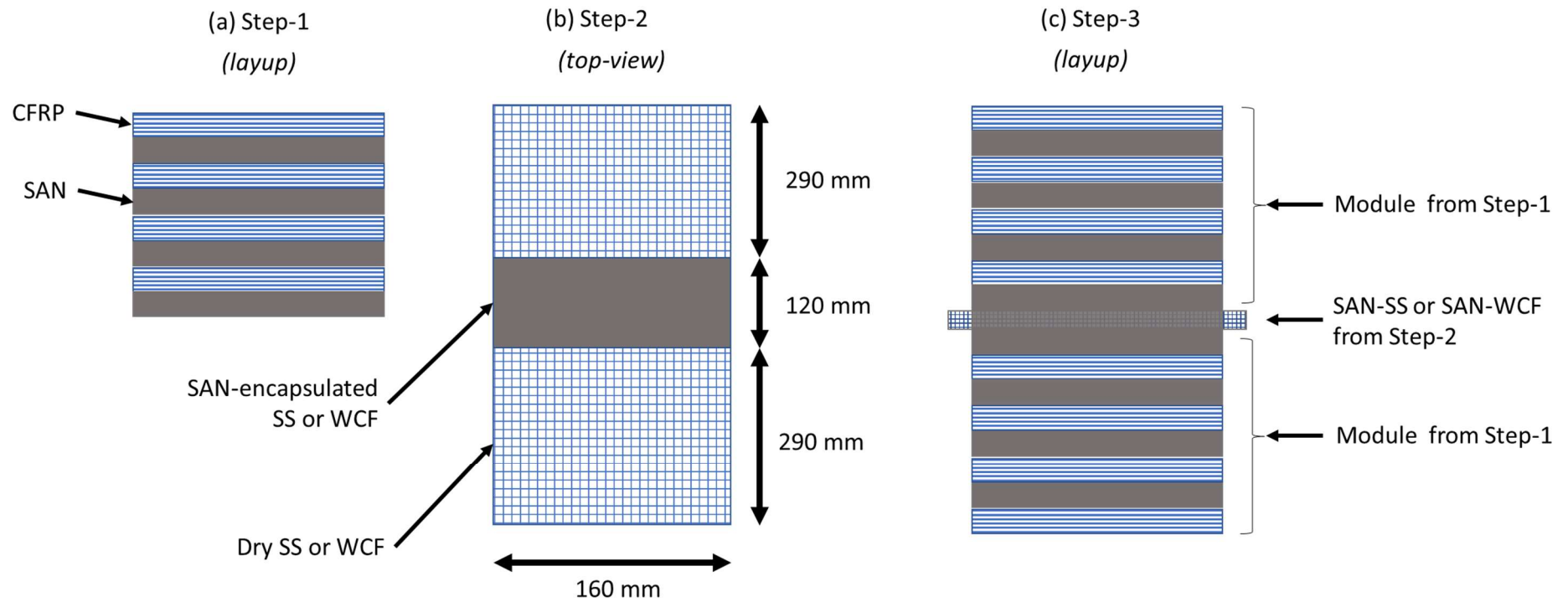


Figure 5.1 (a) Layup of the laminate during the first step of the manufacturing process, (b) top-view of the heater layer during the second step, and (c) the layup of the laminate during the third step described in Section 5.1

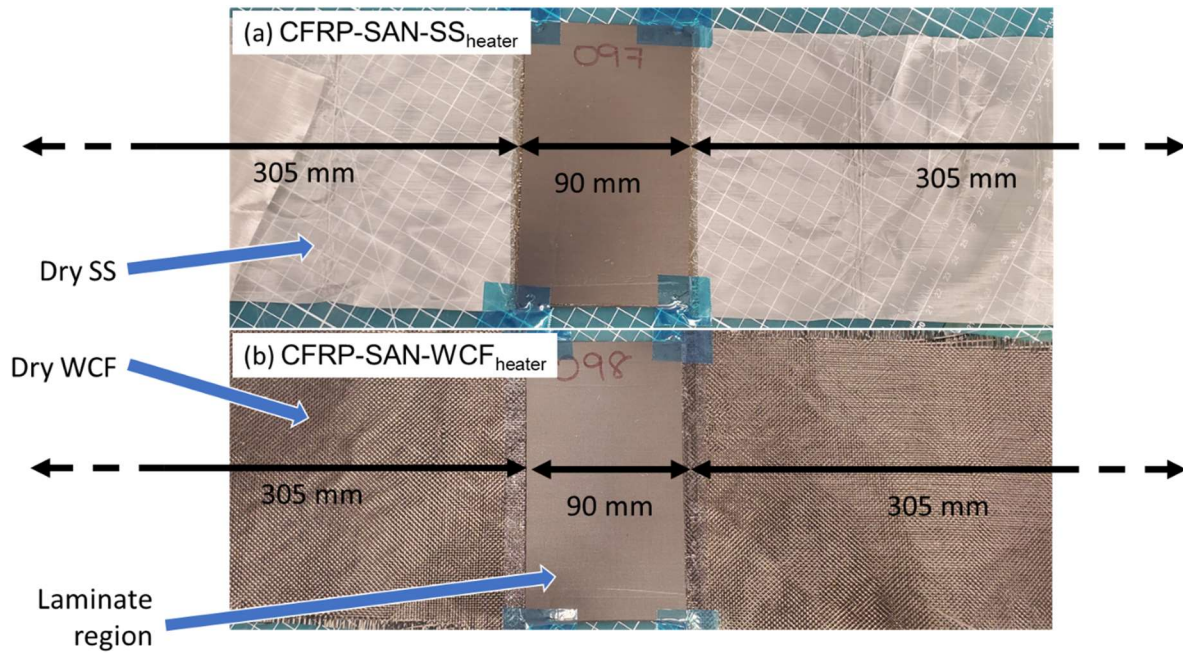


Figure 5.2 (a) CFRP-SAN-SS_{heater} and (b) CFRP-SAN-WCF_{heater} composites at the start of the step-3 of the production process

This 3-step manufacturing process resulted in the production of composite panels specified in Table 5.1. Using a waterjet (see Section 3.3.2.1), specimens were cut from the cured panels. The dimensions of the specimens are shown in Table 5.2. The 0° fibre direction in the CFRP laminae in these specimens was parallel to the long edge.

These specimens (see Figure 5.3) had dry SS and WCF protruding out of them to allow connection to a DC power supply. To facilitate a good electrical connection to a DC power supply, the dry SS and WCF of the specimens were connected to a 12 mm wide Hi-Bond HB 740 conductive copper tape using silver loaded adhesive (both procured from RS Components Ltd. (UK)), at a distance of around 300 mm from the ends of the CFRP section of the specimens, as shown in Figure 5.4. The total end-to-end length of the heaters was around 690 mm in all the specimens. An additional set of conductive copper tapes was connected to the dry SS and WCF using a silver conductive paint at a distance of around 20 mm from the ends of the CFRP section of the specimens to help ensure that current flow through the

heaters is uniform across the width of the specimens. The specimens were produced with long leads to allow the leads to be connected to the electrical circuit setup described in Section 5.2.1, while their free ends are still freely able to move when they are deformed during the SM tests.

Table 5.1. Names and layups of the composite panels
prepared for the studies shown in Chapter 5

Composite name	Layup sequence ^{1 2}
CFRP-SAN-SS _{heater}	$[(0^\circ/\text{SAN})_4/\text{SAN}/\text{SS}/\text{SAN}/(\text{SAN}/0^\circ)_4]$
CFRP-SAN-WCF _{heater}	$[(0^\circ/\text{SAN})_4/\text{SAN}/\text{WCF}/\text{SAN}/(\text{SAN}/0^\circ)_4]$

¹ $(0^\circ/\text{SAN})_4$ laminae are obtained from step-1 of the manufacturing process

² SAN/SS/SAN and SAN/WCF/SAN laminae are obtained from step-2 of the manufacturing process

Table 5.2. Dimensions of composite specimens prepared for the studies shown in Chapter 5
(here, w , t –width and thickness of the specimen)

Composite name	Dimensions		
	l (mm)	w (mm)	t (mm)
CFRP-SAN-SS _{heater}	~90	9.09 ± 0.02	1.77 ± 0.01
CFRP-SAN-WCF _{heater}		9.10 ± 0.01	1.84 ± 0.02

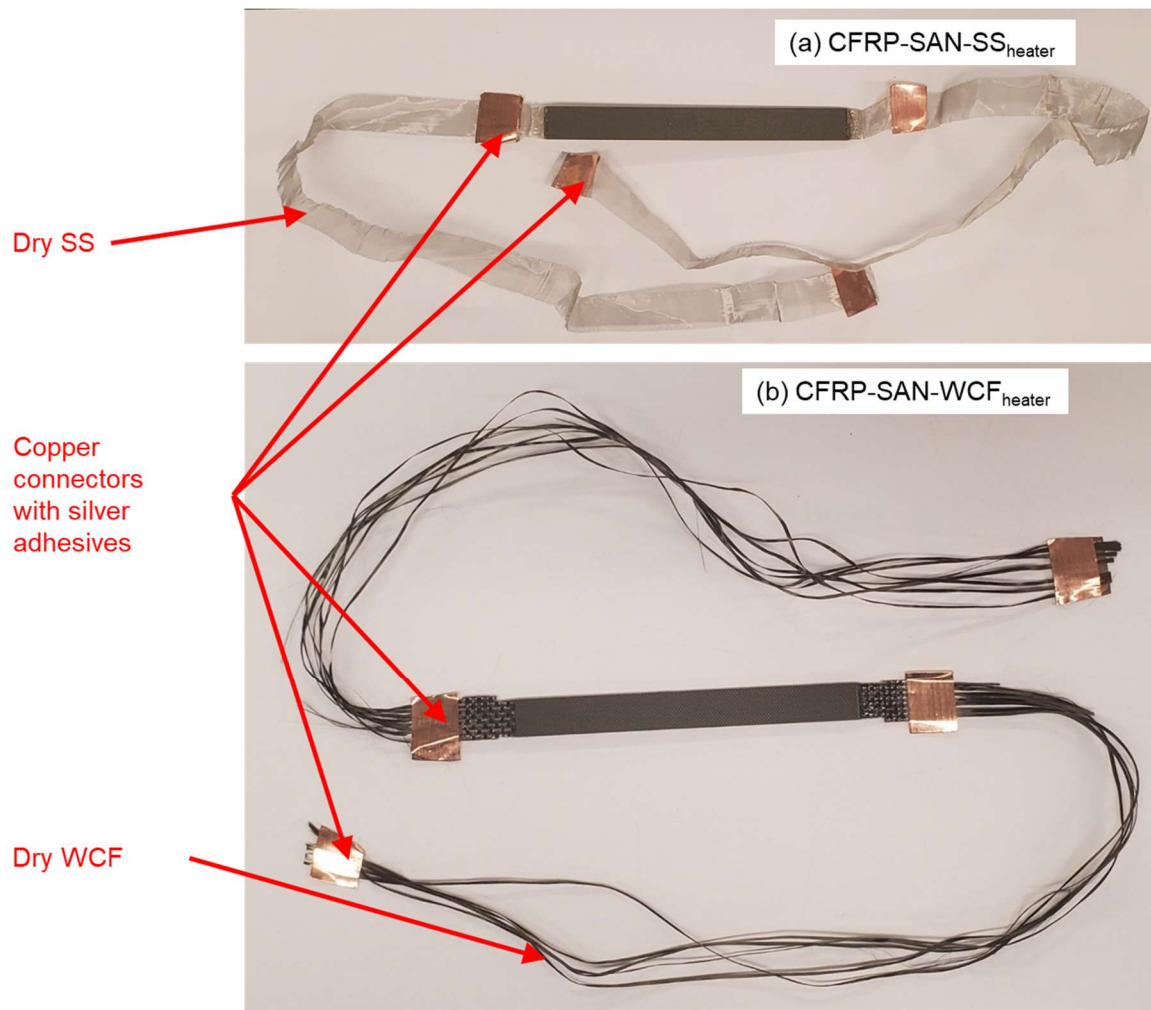


Figure 5.3 (a) CFRP-SAN-SS_{heater} and (b) CFRP-SAN-WCF_{heater} specimens
showing the dry heaters and copper connectors

(Note: Due to the absence of any binding material and sufficient friction, the weft tows in the dry WCF fall off when after the CFRP-SAN-WCF_{heater} specimens are cut)

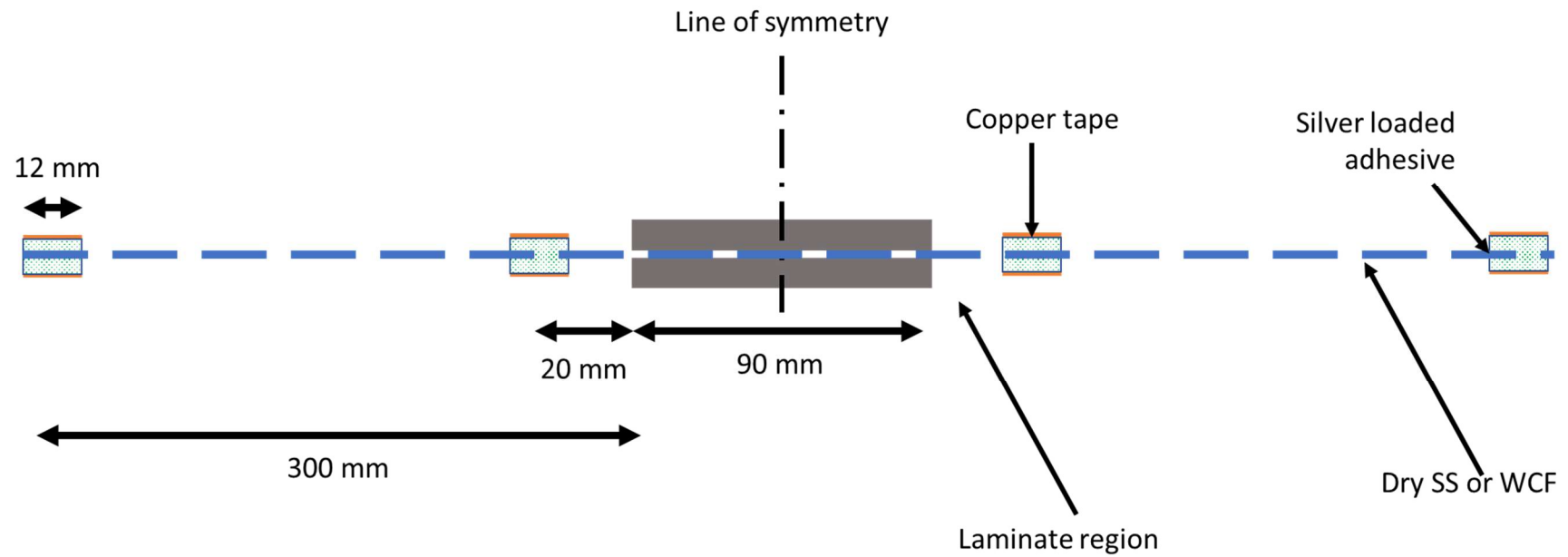


Figure 5.4 Positions where conductive copper tape and silver loaded adhesive were used to facilitate a good electrical connection in each CFRP-SAN-SS_{heater} and CFRP-SAN-WCF_{heater} specimen

5.2. Experimental methodology

5.2.1. Modified test setup used in 3PB loading of intrinsically heated interleaved composite specimens

To study the flexural behaviour of the intrinsically heated CFRP-SAN-SS_{heater} and CFRP-SAN-WCF_{heater}, a modified 3PB loading test setup (see [Figure 5.5](#)) was used. This setup consists of a standard 3PB loading fixture mounted on a universal test machine (Instron 5960 series, USA) equipped with a 1 kN load cell. The diameter of the support and loading rollers was 6 mm.

Additionally, wooden supports with conductive clamps made of copper strips were mounted next to the 3PB loading fixture. The conductive copper regions at the ends of SS and WCF heaters in the specimens were placed inside these conductive clamps which were then connected to a DC power supply (EA-PS 8080-60 DT, EA Elektro-Automatik, Germany) through power leads. This setup ensures that the effect of the weight of the power leads on the composite specimens is eliminated.

A PTFE layer was placed at the interface between the specimens and the 3PB fixture to insulate the fixture from the applied DC flowing through the specimens. Furthermore, the low electrical conductivity of the wooden fixtures insulated the rest of the test setup from the applied DC.

To measure the surface temperature of some of the composite specimens, a resistive temperature detector (RTD) (RS PRO PT100, RS Components Ltd. (UK)) was clamped on the composite specimens at their quarter-span using a PTFE-coated stainless steel crocodile clip. The leads from the RTD were then connected to a data acquisition unit (Agilent 34972A, Keysight Technologies, USA) to measure and store information on the surface temperature of the specimens.

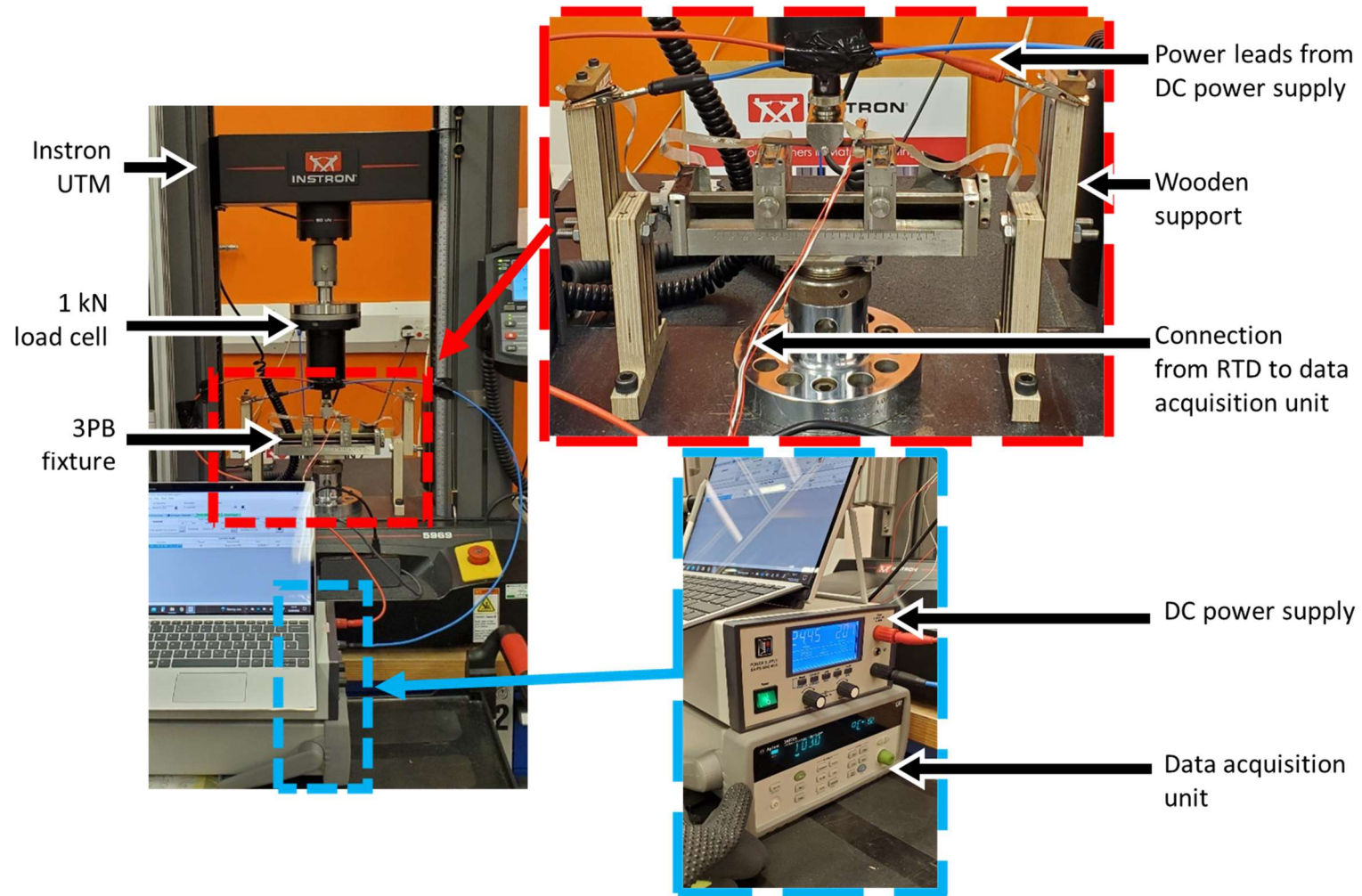


Figure 5.5 Modified 3PB setup used in the characterisation of intrinsically heated interleaved composite specimens

5.2.2. Investigation of intrinsic heating capabilities of the interleaved composites with embedded heaters

A fixed displacement 3PB test was performed using the modified setup described in Section 5.2.1. A support span of 60 mm was used in this experiment. The specimens were loaded in a 3PB setup at a constant crosshead speed of 1 mm/min.

At first, the specimens were loaded to a maximum mid-span displacement of 1.5 mm at room temperature. Then, DC (i_{DC}) was applied to the specimens (see Table 5.3) while maintaining the mid-span displacement constant for 200 s. During this period, the force applied to the specimens and their surface temperature were continuously measured.

Table 5.3. Current applied to composite specimens in the fixed displacement 3PB tests described in Section 5.2.2

Composite name	i_{DC} (A)	Voltage at room temperature (V)
CFRP-SAN-SS _{heater}	2.0 ^a	30.72 ± 2.16
	2.5 ^b	38.15 ± 1.15
CFRP-SAN-WCF _{heater}	1.1 ^a	45.42 ± 2.49
	1.4 ^b	55.24 ± 2.11

(Experimental trials were conducted to select i_{DC} which, when applied, causes specimens to

^a lose 99% of their reaction force in a 3PB test within 200 s, or

^b achieve a steady state surface temperature of around $120 \pm 10^\circ\text{C}$ within 200 s.)

5.2.3. CS tests

CS tests were performed on the composite specimens broadly following the methodology described in Section 3.3.2.1, but with a support span of 60 mm and using the modified setup described in Section 5.2.1.

At first, the specimens were loaded to a maximum mid-span displacement of 1.5 mm at room temperature (RT1) and unloaded. Then, i_{DC} (specified in Table 5.3) was applied through the

specimens for 200 s and the load-displacement test was repeated, while keeping the i_{DC} constant, to maintain a constant high temperature (HT1) in the specimens. Finally, the test was once again repeated after the specimens cooled to room temperature (RT2).

5.2.4. SM tests

After the CS tests, SM tests were performed on the same composite specimens broadly following the methodology described in [Section 3.3.2.3](#) using the modified setup described in [Section 5.2.1](#).

At first, each initially flat composite specimen was heated using applied i_{DC} (specified in [Table 5.3](#)) for 200 s and then loaded in a 3PB setup to a maximum mid-span displacement of 18.72 mm. The deformed shape of the composite specimen was then fixed by switching off the i_{DC} allowing the specimen to cool down to room temperature. At this temperature, the specimen was unloaded. Finally, the unconstrained specimen was once again heated using i_{DC} (specified in [Table 5.3](#)) to recover its shape.

During the SM tests, the shape profile of the composite specimens was measured as specified in [Section 3.3.2.3](#). Before and after the SM tests, the flexural moduli of the composite specimens were measured at room temperature using the methodology described in [Section 5.2.3](#).

5.2.5. Optical microscopy

The 20 mm sections at the centre and at one end of selected specimens (i.e., mid-span and free end) in the pristine as-cured state, after CS tests, and after SM tests were inspected by optical microscopy, following the methodology described in [Section 3.1.2.2](#).

5.3. Results and discussion

5.3.1. Analysing the quality of the 3-step modular manufacturing process

The polished longitudinal microsections of the pristine composite specimens in their as-cured state are shown in [Figure 5.6](#) and [Figure 5.7](#). These microsections indicate the production method resulted in the composites having fully consolidated SAN-SS and SAN-WCF laminae

with no voids present in them. In the CFRP-SAN-WCF_{heater} specimens, polishing causes small flakes of SAN interleaves to get chipped away from WCF, leading to the formation of dark regions shown in Figure 5.7 (b).

Significant undulations can be seen in the SS heaters in the CFRP-SAN-SS_{heater} specimens (see Figure 5.6 (a)). However, as the SS heater lies on the mid-plane, this undulation will have no significant effect on the flexural modulus of the CFRP-SAN-SS_{heater} specimens. Furthermore, a small number of voids were found in one of the pristine SAN interleaves in CFRP-SAN-WCF_{heater} (Figure 5.7 (b)), indicating the need for further improvement of the manufacturing process.

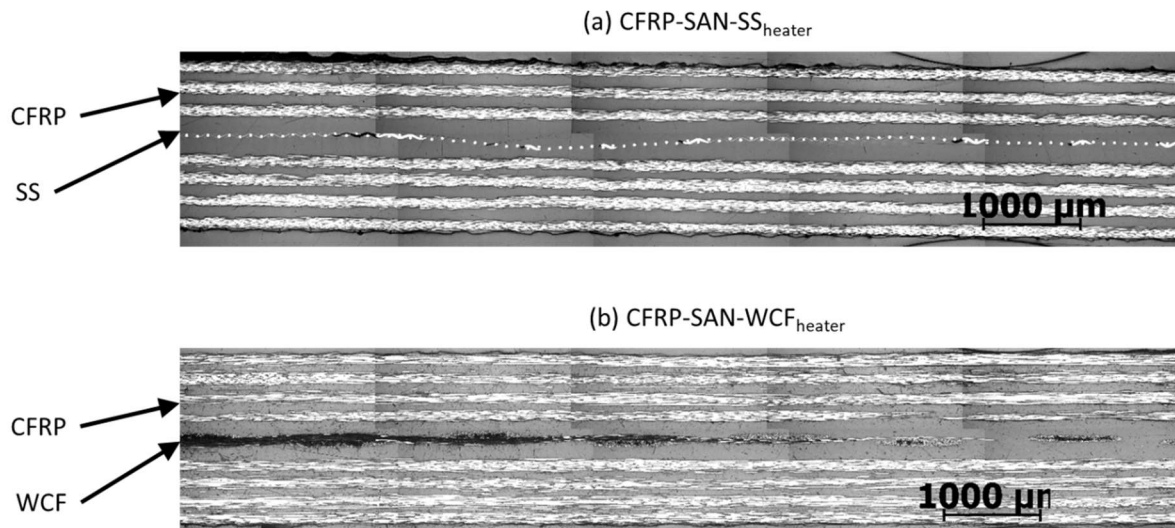


Figure 5.6 Polished longitudinal microsection of the mid-span (a) CFRP-SAN-SS_{heater} and (b) CFRP-SAN-WCF_{heater} in their as-cured state

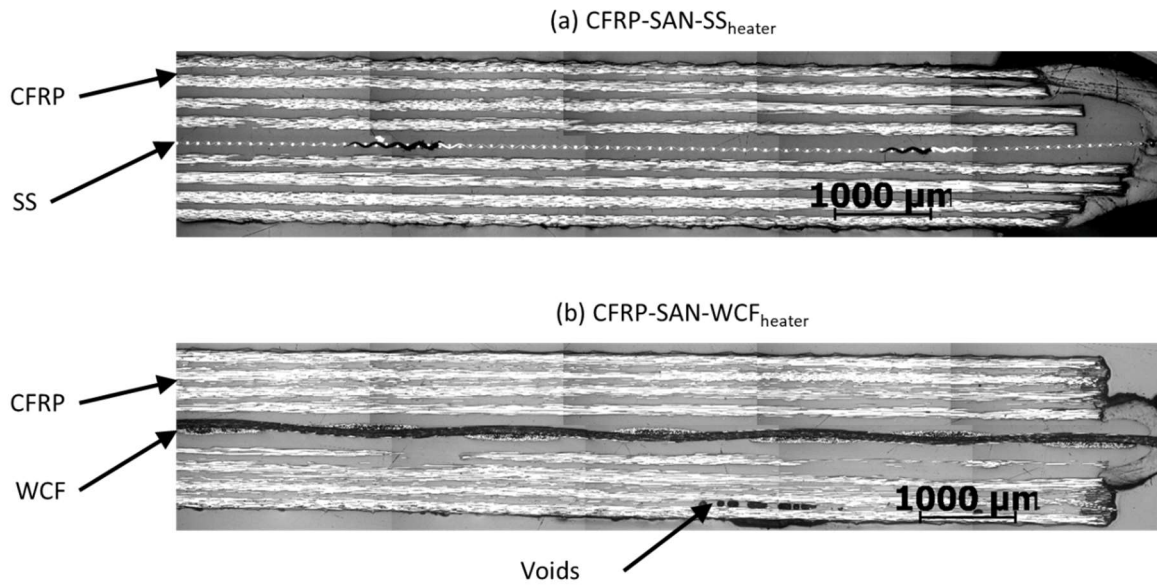


Figure 5.7 Polished longitudinal microsection of the free end (a) CFRP-SAN-SS_{heater} and (b) CFRP-SAN-WCF_{heater} in their as-cured state

5.3.2. Flexural tests on intrinsically heated composite specimens

Typical normalised applied force ($100 \times \text{force} / \text{max. force}$) and the surface temperature of the specimens of the intrinsically heated interleaved composites obtained during the fixed displacement 3PB tests (see Section 5.2.2) are shown in Figure 5.8, where the horizontal axis represents time. In this figure, normalisation of the applied force is done to provide a simplified way to compare the effect of different i_{DC} on the composites with different heaters.

Table 5.4 shows the time taken for the specimens (after applying i_{DC}) to lose more than 99% of their applied force, and the almost-stable surface temperature of the specimens measured 200 s after applying i_{DC} . From Figure 5.8 and Table 5.4, it can be seen that the applied force on the composite specimens reduces by more than 99% within 200 s^{†††} when i_{DC} of 2 A and 1.1 A were applied through CFRP-SAN-SS_{heater} and CFRP-SAN-WCF_{heater} specimens respectively. However, at these i_{DC} , the surface temperature of the specimens stabilises at

^{†††} The 200 s duration was selected arbitrarily to avoid performing the experiment for extended durations of time.

around 92°C and 94°C respectively, which is much less than the deformation (and HT1) temperature of 120°C, used in the studies described in previous chapters.

When i_{DC} of 2.4 A and 1.4 A were applied through CFRP-SAN-SS_{heater} and CFRP-SAN-WCF_{heater} respectively, a loss of 99% of their applied force was achieved much more quickly. At these applied currents, the surface temperature of the specimens stabilises at around 131°C and 127°C respectively which is slightly higher than the deformation (and HT1) temperature of 120°C, used in previous sections.

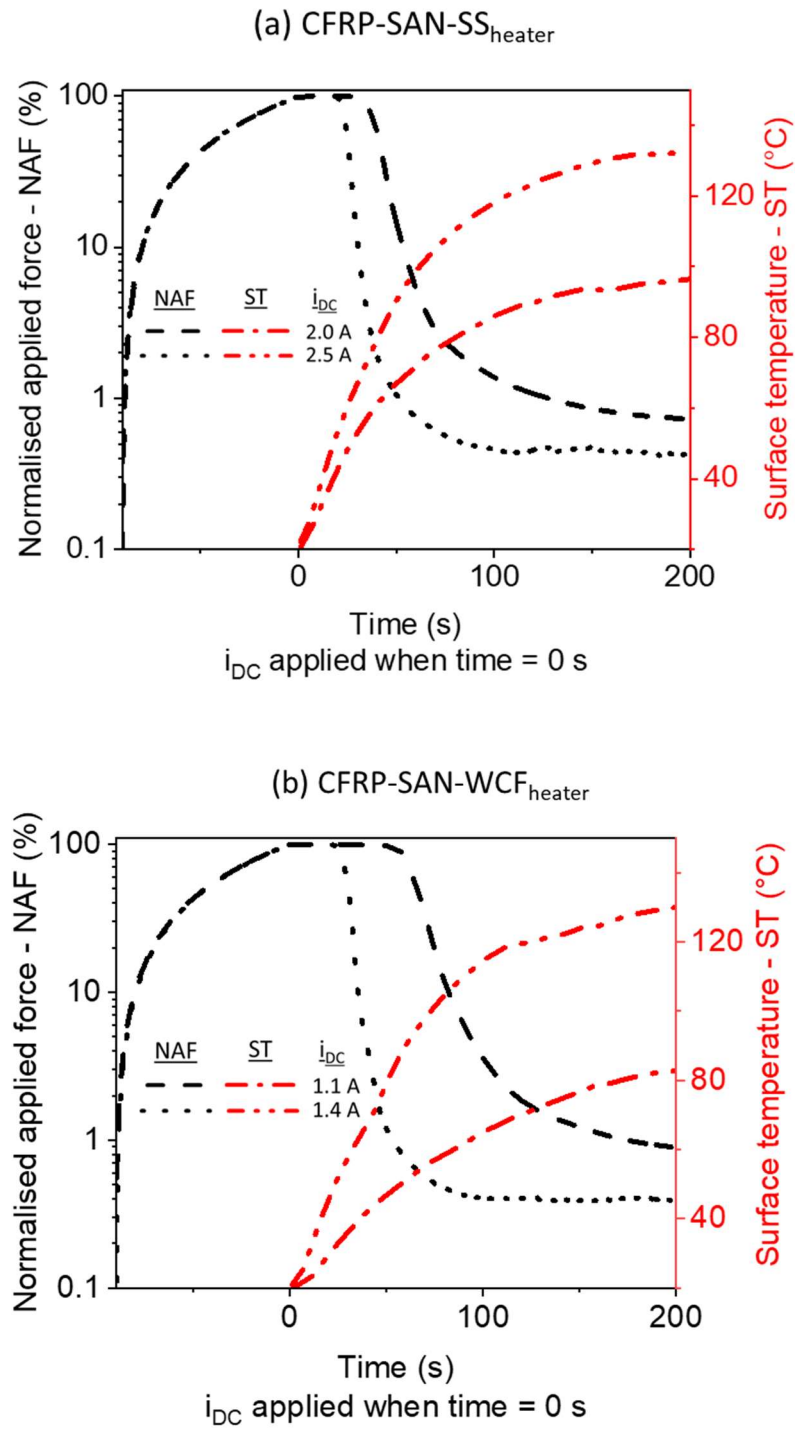


Figure 5.8 Typical normalised applied force and surface temperature of the
 (a) CFRP-SAN-SS_{heater} and (b) CFRP-SAN-WCF_{heater} specimens
 in the fixed displacement 3PB tests described in Section 5.2.2

Table 5.4. Time taken for specimens to lose 99% of their applied force, and the surface temperature of specimens in the fixed displacement 3PB tests described in Section 5.2.2

Composite name	Time taken (after applying i_{DC}) to achieve a 99% reduction in applied force (s)		Surface temperature of specimens measured 200 s after applying i_{DC} (°C)
	i_{DC} (A)		
CFRP-SAN-SS _{heater}	2.0	128 ± 24	92 ± 4 ^a
	2.5	49 ± 4	131 ± 1 ^a
CFRP-SAN-WCF _{heater}	1.1	140 ± 39	94 ± 5 ^a
	1.4	55 ± 7	127 ± 8 ^a

^a This data was obtained from 4 specimens.

5.3.3. CS test results

Typical force-displacement curves of the interleaved composites in CS tests, at their RT1 and HT1 test conditions, are shown in Figure 5.9 (a) and (b). The force-displacement curves of the interleaved composites at the RT2 test condition are not shown here as they are not distinguishable from the curves in Figure 5.9 (a), by the naked eye. After testing the specimens in the HT1 condition, a slight increase in their thickness was observed (see Table 5.5).

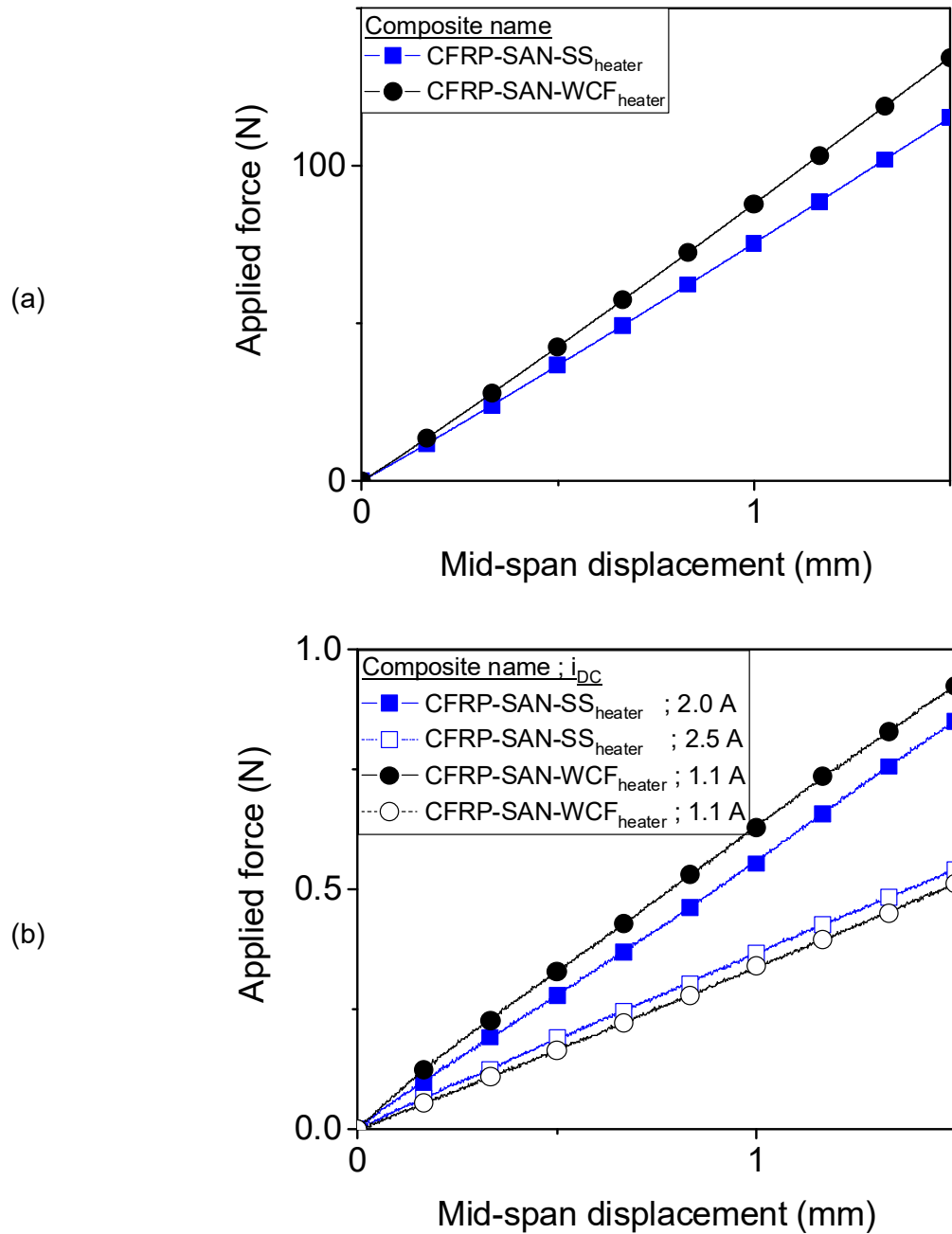


Figure 5.9 Typical force-displacement curves of intrinsically heated composite specimens at (a) RT1 and (b) HT1* test conditions in CS tests.

(* i_{DC} used to achieve HT1 test conditions are provided in the legend)

Table 5.5. Thickness of the composite specimens before and after the CS studies described in Section 5.2.3

Composite name	i_{DC} (A)	$t_{\text{before CS}}^*$ [mm]	$t_{\text{after CS}}^{**}$ [mm]
----------------	--------------	-------------------------------	---------------------------------

CFRP-SAN-SS _{heater}	2.0	1.78 ± 0.02	1.80 ± 0.02
	2.5	1.77 ± 0.01	1.83 ± 0.04
CFRP-SAN-WCF _{heater}	1.1	1.84 ± 0.01	1.85 ± 0.01
	1.4	1.83 ± 0.03	1.87 ± 0.03

* Taken from 't' shown in [Table 5.2](#)

** This thickness was taken as the average thickness of the central 20 mm section (i.e., mid-span) of the specimens

From the average slope of each force-displacement curve (after ignoring the initial non-linear segment), the corresponding apparent flexural modulus was calculated, as shown in [Section 3.3.3.1](#). The thickness of the specimens was selected as t_{beforeCS} to calculate E_{RT1} and E_{HT1} , and as t_{afterCS} to calculate E_{RT2} .

The apparent flexural modulus of the composites in their high stiffness state (E_{RT1}), low stiffness state (E_{HT1}) and again at high stiffness state (E_{RT2}) are listed in [Table 5.6](#). As the theoretical predictions of flexural moduli of interleaved composites have already been explored in detail in previous chapters, they are not discussed here.

Table 5.6. The apparent flexural modulus of composites at RT1, HT1 and RT2 test conditions in the CS studies described in [Section 5.2.3](#)

Composite name	i_{DC} (A)	Apparent flexural moduli of composites		
		E_{RT1} (GPa)	E_{HT1} (GPa)	E_{RT2} (GPa)
CFRP-SAN-SS _{heater}	2.0	84.81 ± 1.56	0.54 ± 0.05	86.46 ± 3.32
	2.5	84.95 ± 3.61	0.35 ± 0.03	85.15 ± 2.06
CFRP-SAN-WCF _{heater}	1.1	86.26 ± 1.76	0.53 ± 0.06	88.90 ± 1.87
	1.4	85.44 ± 2.26	0.31 ± 0.03	84.78 ± 1.69

The results from the CS tests indicate that the apparent flexural modulus of all interleaved composites dropped by more than 99% (E_{RT1} vs E_{HT1}) when the composites are heated using the intrinsic heating method. Upon cooling down, the apparent flexural modulus of the composites was fully restored. This observation demonstrates the controllable stiffness capabilities of the intrinsically heated interleaved composites. The polished longitudinal microsection of the composite specimens after the CS study reveals the formation of voids within the interleaf region, as shown in Figure 5.10 and Figure 5.11.

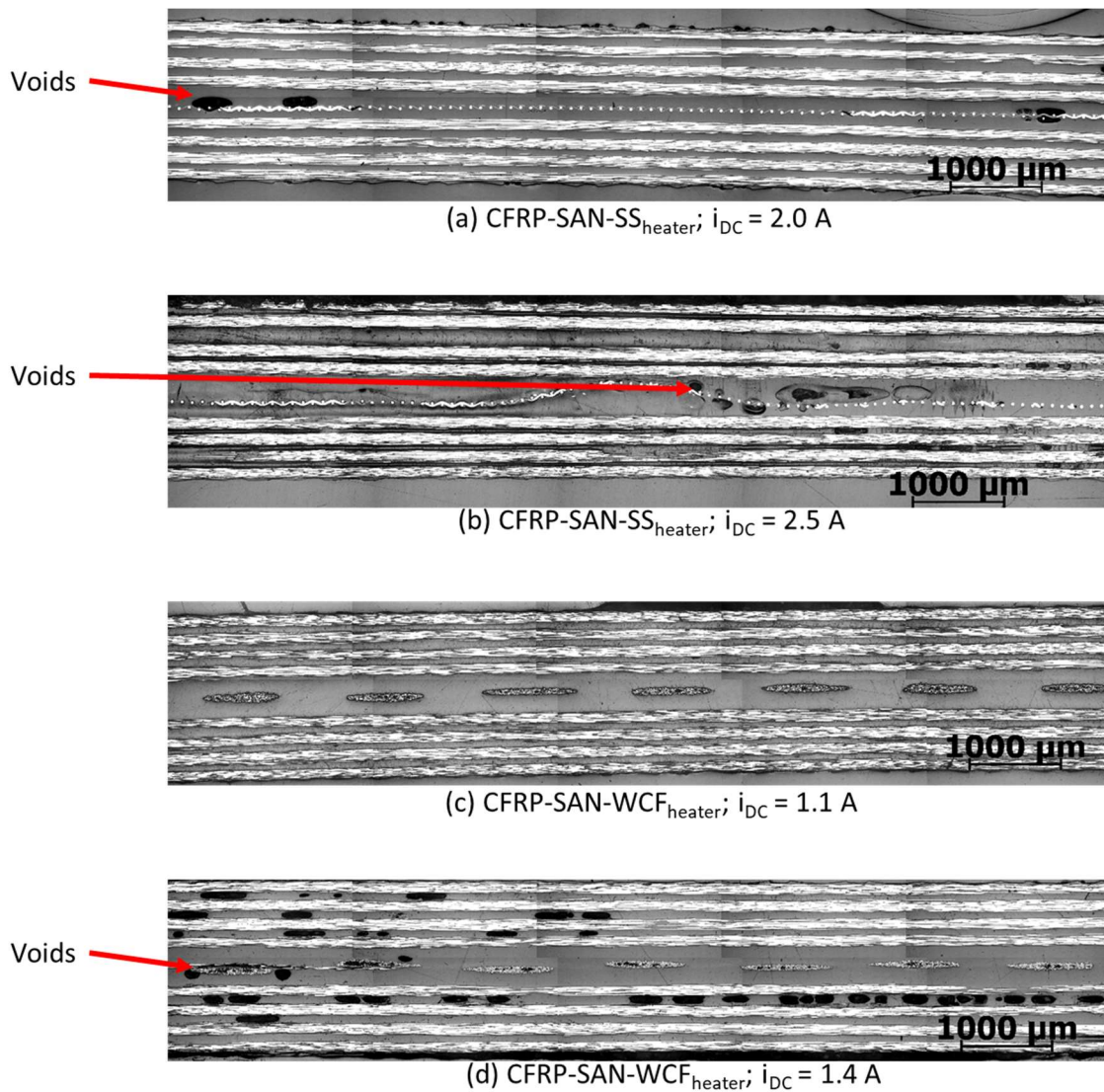


Figure 5.10 Polished longitudinal microsection of the mid-span of CFRP-SAN-SS_{heater} and CFRP-SAN-WCF_{heater} specimens showing void formation within the interleaves after CS tests where i_{DC} of (a) 2.0 A, (b) 2.5 A, (c) 1.1 A, and (d) 1.4 A were used

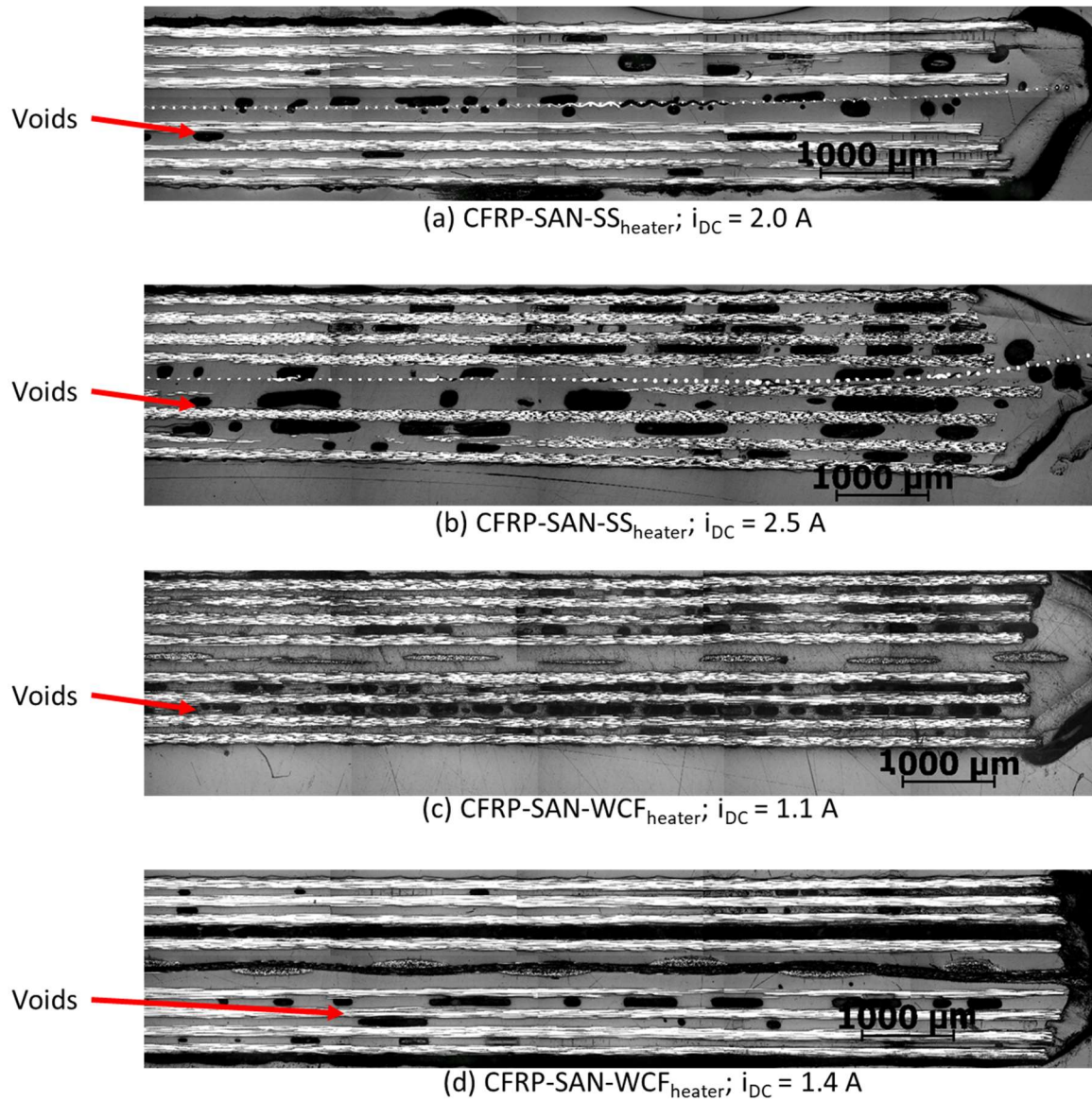


Figure 5.11 Polished longitudinal microsection of the free end of CFRP-SAN-SS_{heater} and CFRP-SAN-WCF_{heater} specimens showing void formation within the interleaves after CS tests where i_{DC} of (a) 2.0 A, (b) 2.5 A, (c) 1.1 A, and (d) 1.4 A were used

The major difference between the CS study performed on composites in this study, and the composites in previous studies in the heating technique. Hence, the development of excessive voids can be attributed solely to the intrinsic heating technique used here (see [Section 3.3.3.4](#) for information on void development in composites heated using an oven).

One of the reasons behind the formation of a large number of voids, compared to oven-heated laminates, could be thermal degradation. It is possible that the internal temperature of the

composite specimens is much higher than that measured by the RTD sensor. Hence, it is possible that the local internal temperature of the specimens goes beyond the degradation temperature of SAN. Furthermore, the number of voids greatly increases near the free end of the specimens, compared to their mid-spans. This observation indicates that the temperature distribution across the span of the specimens might be non-uniform, with excessive temperatures reached at the free ends.

5.3.4. SM test results

In the SM study, when the composite specimens were heated using i_{DC} , deformed, cooled to room temperature, and the deformation load was removed, the deformed shape was almost fully retained for all the composite specimens. On re-heating the composite specimens, their initial shape was almost fully recovered.

Using the shape profiles of the composite specimens in the SM study, the average distance (ζ) between the mid-span and the ends of the specimens in the direction of loading (see [Figure 3.14](#)) was extracted before deformation and after deformation is listed in [Table 5.7](#). Similarly, the ζ of the specimens after 1 minute, 2 minutes and 5 minutes of shape recovery is also listed in [Table 5.7](#), where the time of shape recovery is measured from the instance i_{DC} is applied to the specimens.

Table 5.7. Distance (ζ) between the mid-span and the ends of composite specimens in the direction of loading at different stages of the SM tests described in Section 5.2.4

Composite name	i_{DC} (A)	Distance (ζ) between the mid-span and the ends of specimens in the direction of loading (mm)				
		Before deformation	After deformation	After shape recovery		
				1 min	2 min	5 min
CFRP-SAN- SS _{heater}	2.0	0.0	25.3	20.2	3.9	0.8
			± 0.1	± 1.0	± 0.3	± 0.7
	2.5	0.0	25.0	4.8	0.4	0.1
			± 0.3	± 0.3	± 0.2	± 0.1
CFRP-SAN- WCF _{heater}	1.1	0.0	25.6	18.8	4.2	0.4
			± 0.1	± 1.1	± 1.6	± 0.2
	1.4	0.0	25.9	5.9	0.7	0.3
			± 0.2	± 1.7	± 0.3	± 0.1

Here, it can be seen that for a given heater type the shape recovery of the composite is faster when higher i_{DC} is applied. The faster shape recovery can be attributed to the faster heating rate and the higher temperature as seen in Section 5.3.1.

In all the cases, the shape recovery of the composites is faster than the comparable SAN-interleaved composites seen previously (such as CFRP-SAN_{151 μ} in Section 4.1.3.2 and CFRP-SAN-WCF in Section 4.2.3.3). Such a faster shape recovery further reinforces the idea that the temperature achieved during shape recovery in the intrinsically heated composite specimens must be higher than 120°C, which is inconsistent with their measured surface temperature (see Section 5.3.1). This faster shape recovery could have also been due to a higher rate of heating in intrinsically heated composite specimens. Further investigation in this regard can look into the dependency of the heating method on the speed of shape recovery of interleaved composite specimens.

The polished longitudinal microsection of the composite specimens after the SM study reveals the formation of voids within the interleaf region (see Figure 5.12 and Figure 5.13), as seen in Section 5.3.3. As a result, the average thickness (t) of the specimens increases considerably, leading to a considerable change in their apparent flexural modulus, as shown in Table 5.8.

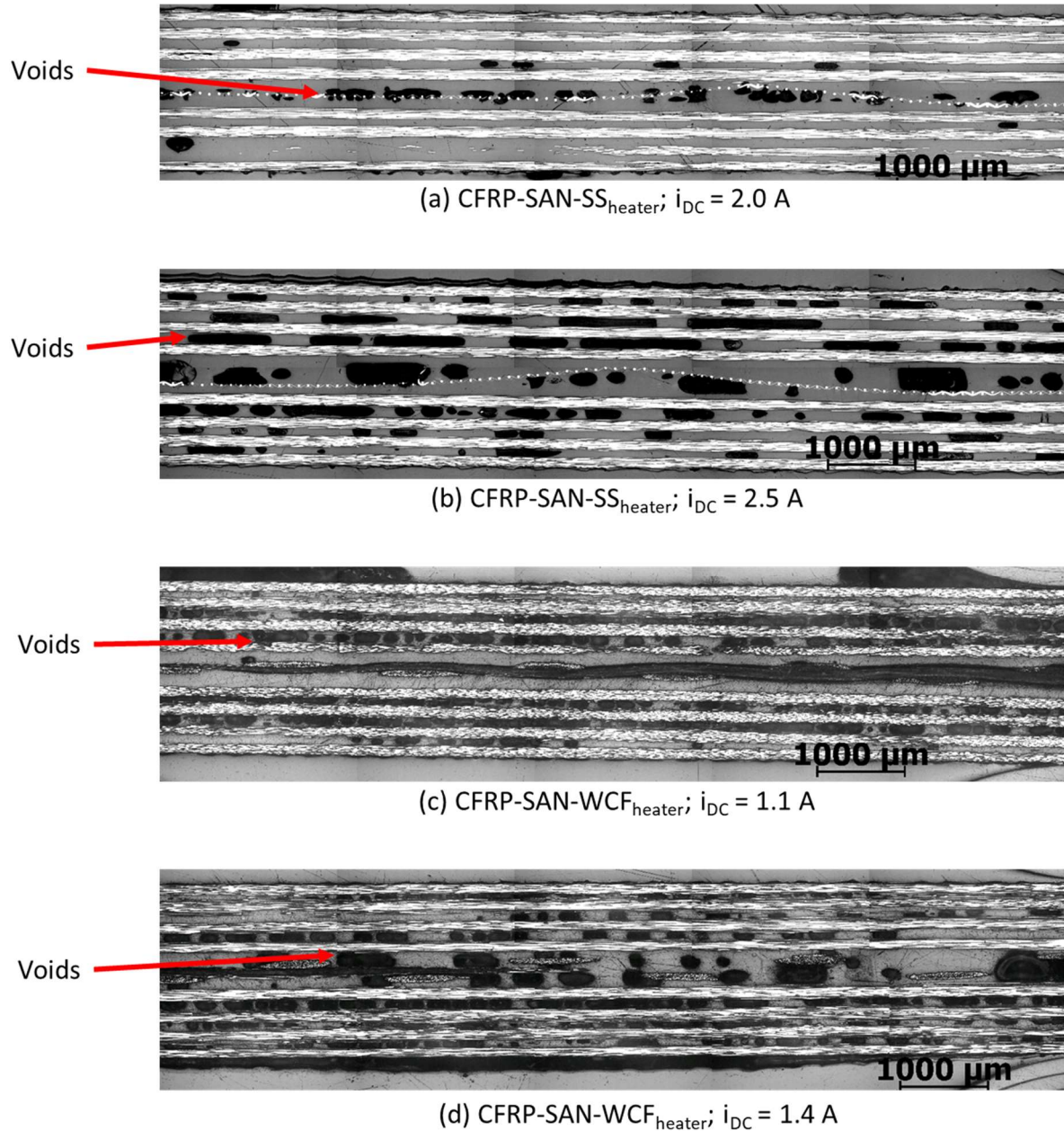
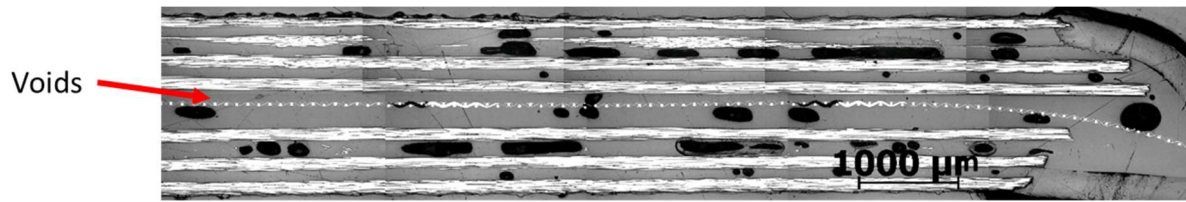
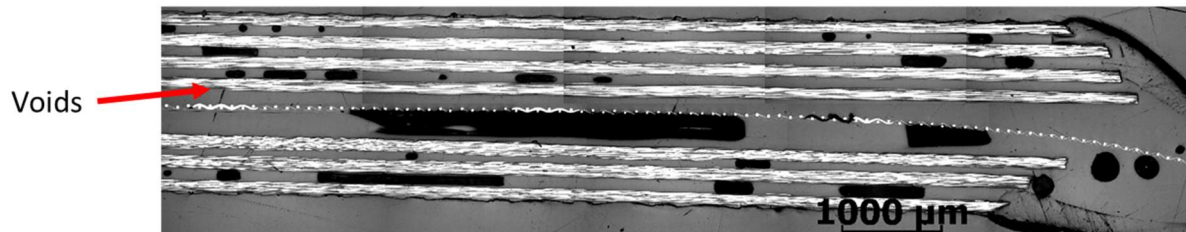


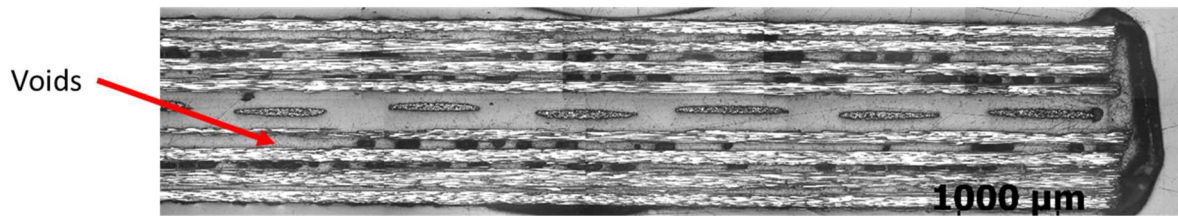
Figure 5.12 Polished longitudinal microsection of the mid-span of CFRP-SAN-SS_{heater} and CFRP-SAN-WCF_{heater} specimens showing void formation within the interleaves after SM tests where i_{DC} of (a) 2.0 A, (b) 2.5 A, (c) 1.1 A, and (d) 1.4 A were used



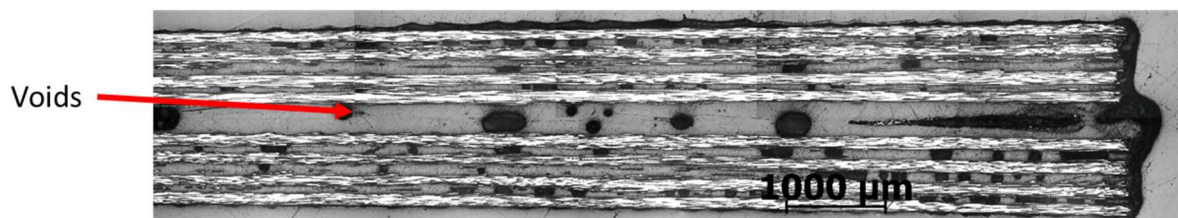
(a) CFRP-SAN-SS_{heater}; $i_{DC} = 2.0$ A



(b) CFRP-SAN-SS_{heater}; $i_{DC} = 2.5$ A



(c) CFRP-SAN-WCF_{heater}; $i_{DC} = 1.1$ A



(d) CFRP-SAN-WCF_{heater}; $i_{DC} = 1.4$ A

Figure 5.13 Polished longitudinal microsection of the free end of CFRP-SAN-SS_{heater} and CFRP-SAN-WCF_{heater} specimens showing void formation within the interleaves after SM tests where i_{DC} of (a) 2.0 A, (b) 2.5 A, (c) 1.1 A, and (d) 1.4 A were used

Table 5.8. Specimen thickness (t) and apparent flexural moduli (E_{RT}) moduli of the composites before and after the SM tests described in Section 5.2.4

Composite	i_{DC}	$t_{\text{before SM}}^*$	$t_{\text{after SM}}$	$E_{RT\text{-before SM}}^{**}$	$E_{RT\text{-after SM}}$
name	(A)	[mm]	[mm]	[GPa]	[GPa]
CFRP-SAN-	2.0	1.78 ± 0.02	2.04 ± 0.02	84.81 ± 1.56	68.37 ± 2.97
SS _{heater}	2.5	1.77 ± 0.01	2.03 ± 0.02	84.95 ± 3.61	68.25 ± 4.39
CFRP-SAN-	1.1	1.84 ± 0.01	2.10 ± 0.05	86.26 ± 1.76	68.20 ± 4.00
WCF _{heater}	1.4	1.83 ± 0.03	2.03 ± 0.07	85.44 ± 2.26	73.15 ± 6.42

* Taken from ' t ' shown in Table 5.2

** This is E_{RT1} from Table 5.6

As the same specimens were used for CS tests, followed by SM tests, a higher number of voids were seen within the interleaves after the specimens underwent shape recovery in SM tests, as these samples were exposed to i_{DC} for a longer duration. As a result, the specimens subjected to SM tests could have been more thermally degraded than the specimens subjected to CS tests.

Due to the development of a significant number of voids, the specimens get considerably thicker at their mid-spans, and their apparent flexural modulus drops considerably. This phenomenon could further cause these composites to undergo premature through-thickness shear failure when loaded in flexure. However, the change to the strength of the interleaved composites due to the formation of voids within the interleaves is not explored in this research.

It is expected that by achieving a more accurate temperature measurement and uniform temperature distribution, the development of voids can be reduced. More accurate control over composite temperature can be achieved by monitoring the temperature-induced change in the resistance of the heaters and adjusting the i_{DC} accordingly. More uniformity in temperature distribution can be achieved by including multiple heaters within the layup and applying a lower current through them. Furthermore, conductive fillers can also be introduced within the layup

to enable a more uniform distribution of the heat generated from the heaters. Another approach to reducing void formation could be through the use of interleaf materials that are less susceptible to the formation of voids for the heating strategy used.

5.4. Conclusion and chapter summary

By applying i_{DC} through the heaters embedded within the composite specimens, resistive intrinsic heating of the specimens was achieved. The CS and SM tests revealed that the intrinsically heated composites exhibited successful out-of-oven CS and SM capabilities.

Furthermore, the CS tests showed that upon intrinsic heating, these composites achieved over 99% loss in apparent flexural modulus, which was then fully recovered upon further cooling. The SM studies of these composites showed that the specimens were able to recover their initial shape from their deformed shape upon intrinsically heating them using i_{DC} .

However, a large number of voids were formed within the specimens as a result of the intrinsic heating strategy used here. The development of these voids indicates that the internal temperature of the composite specimens could have been significantly higher than the temperature measured by RTD. To reduce the formation of voids, further studies can explore improving the heating and temperature measurement techniques, and the development of an effective temperature regulation technique.

Chapter 6. Developing deployable meshes with intrinsic heating capabilities

The shape memory studies described in Chapters 3, 4, and 5 have shown that thermoplastic interleaved composites can be deformed at a suitably elevated temperature from the as-cured shape to another shape. This new shape will be retained if the laminate is cooled while being held in this shape. When the unconstrained deformed laminate is subsequently heated, the laminate will return to its as-cured shape.

The shape memory behaviour reported so far implies that a deployable structure made using interleaved composites should be manufactured in the deployed shape and then re-shaped to a compact form prior to deployment. However, as discussed in [Section 2.4](#), manufacturing the structure in the deployed form and re-shaping it to the compact form may pose significant challenges depending on the complexity of the deployed structure.

Previous research on the design of a deployable mesh structure (described in [Section 2.5](#)) has shown that it is possible to design an interleaved laminate configuration which will have a compact form after autoclave curing and which will deploy to an expanded planar mesh on heating. This chapter extends the previous work by developing laminate configurations which can deploy into curved mesh surfaces, and also incorporate the intrinsic heating capability investigated in Chapter 5.

The first section of the chapter explores the conceptualisation of composite meshes that are capable of planar or curved deployment. In the second section of the chapter, the numerical studies performed on the layup design of deployable composite meshes are shown. The third section of the chapter explores the manufacturing, deployment, and characterisation of the deployable composite meshes.

6.1. Concept development of deployable composite meshes

6.1.1. Planar deployable mesh layup and working principle

A mesh can be considered as a structure that is made of several repeating segments, as shown in [Figure 6.1 \(a\)](#). The shape of the repeating segment of a planar mesh (i.e., a mesh that lies in the x-z plane) can be produced by modifying the technique discussed in [Section 2.4](#). While composite laminates consisting of unsymmetric (cross-plyed) pairs of CFRP plies interleaved with thermoplastics are capable of a single curvature as shown in [Figure 2.22 \(b\)](#), combining multiple such cross-plyed pairs (see [Figure 6.1 \(b\)](#)) can result in the production of the repeating segment of a mesh structure.

This phenomenon has been exploited previously by ([Zhang *et al.*, 2018](#)) to create deployable composite meshes (shown in [Figure 2.25](#)). In that original work, the curvature of the mesh cell was produced by the cross-ply layup shown in [Figure 6.1 \(b\)](#). After autoclave curing, the repeating segment (which contains several $0^\circ/90^\circ$ sub-laminates within its thickness) has a curvature which is small (compared to that of a laminate consisting of only a single $0^\circ/90^\circ$ pair) and this curvature decreases as the number of $0^\circ/90^\circ$ sub-laminates within the thickness of this laminate is increased.

On subsequently heating the unconstrained laminate to a temperature above the T_g of PS^{§§§}, the individual $0^\circ/90^\circ$ sub-laminates are free to adopt the curvature of a single $0^\circ/90^\circ$ pair and so, the mesh deploys.

§§§ As the research presented in this chapter focuses on the development of deployable meshes as a concept and not as a product, the type of thermoplastic interleaf will have negligible impact on the study as long as they possess suitable material properties (highlighted in [Section 3.2.1](#)). Furthermore, unlike SAN films, PS films were available in sufficient quantities necessary for the experimental activities presented in the thesis. Hence, PS was selected as the thermoplastic interleaf of the composites described in this chapter.

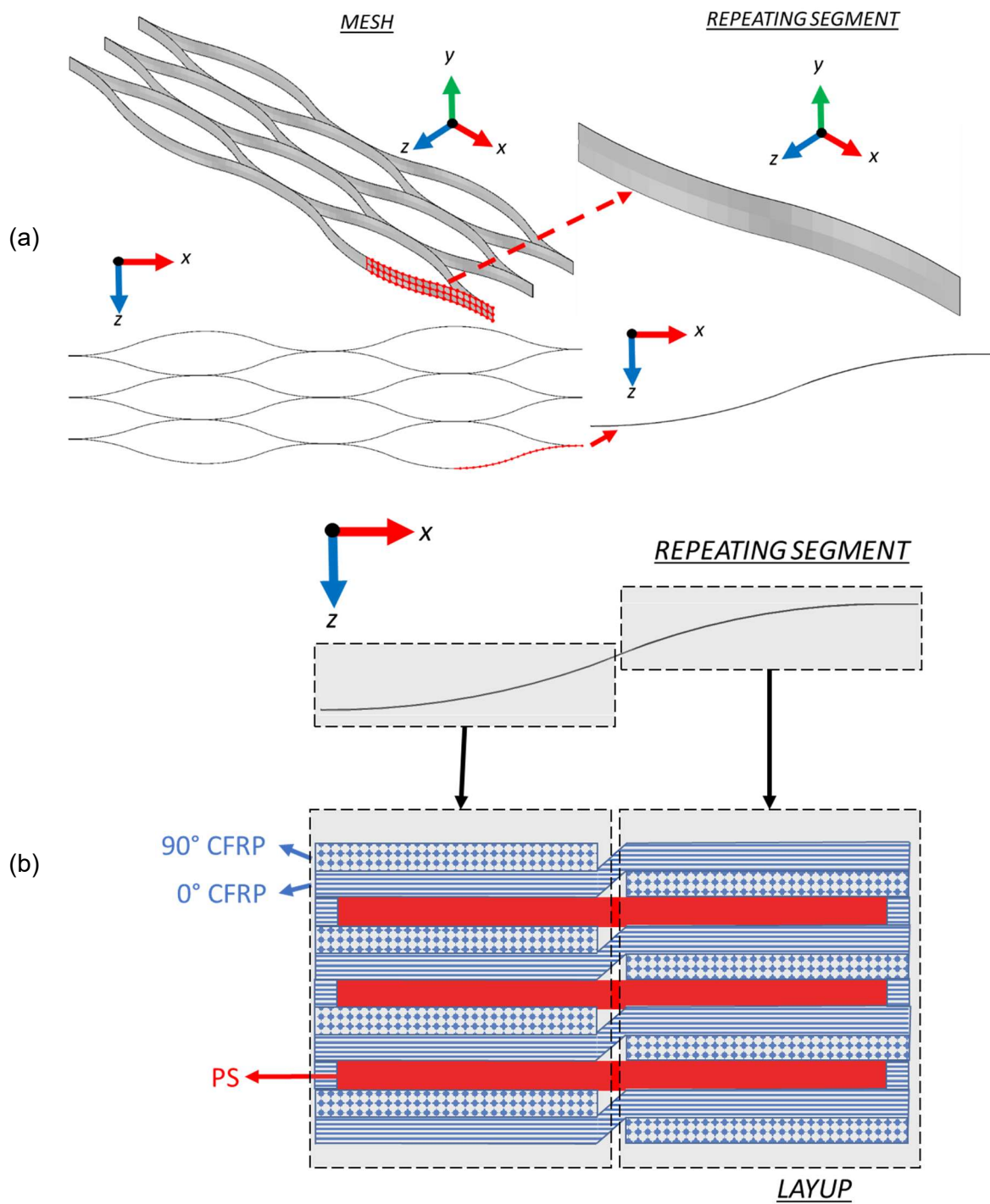


Figure 6.1. (a) Schematic of a mesh made of several repeating segments, and (b) layup of the repeating segment

6.1.2. Layup proposal for a non-planar deployable mesh

The cross-ply sub-laminates used in the previous research have a curvature in the x-direction (see [Figure 6.1 \(a\)](#)). However, if the 90° plies are replaced with the $\pm\theta^\circ$ plies (i.e., $0^\circ/\pm\theta^\circ$ sub-laminates where $0^\circ < \theta < 90^\circ$), the laminate will have a curvature along with a twist in the x-direction.

To exploit this curvature and twist to create laminates capable of deployment into curved mesh surfaces, the layup proposed in [Figure 6.2 \(a\)](#) can be used to produce one-half of a mesh cell. The actual path of the 0° CFRP plies in the layup is also highlighted in [Figure 6.2 \(a\)](#) indicating that the 0° CFRP plies in the sub-laminates are continuous across the length of the layup. In the deploying zones (Z_D), the $0^\circ/\pm\theta^\circ$ sub-laminates are separated in the thickness direction by PS plies. In the straight junction zones (Z_{SJ}), the $0^\circ/\pm\theta^\circ$ sub-laminates are separated in the thickness direction by 0° CFRP plies.

By suitably mirroring this layup a simple cell in a mesh can be produced, as shown in [Figure 6.2 \(b\)](#). As shown in [Figure 6.2 \(b\)](#), a polytetrafluoroethylene (PTFE) layer is introduced between the top and bottom halves of a mesh cell (but not at the end junction zones) to prevent the halves from bonding to each other when the composite panel is cured.

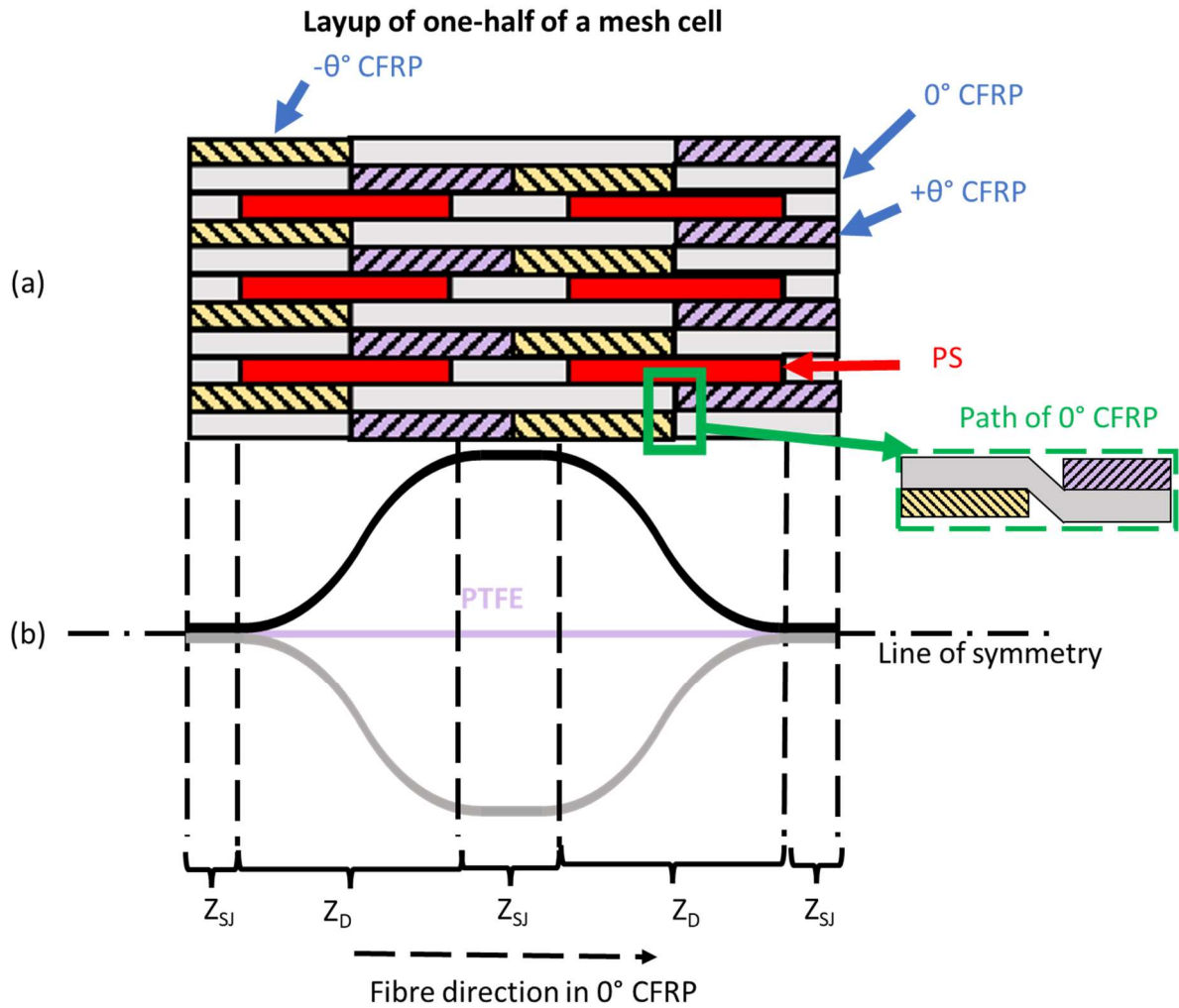


Figure 6.2. (a) Proposed layup of the repeating segment of a mesh and (b) a schematic showing how the layup should be mirrored to achieve a full mesh cell
(Here, Z_{SJ} indicates zones of straight junction and Z_D indicates zones of deployment)

6.1.3. Parameters proposed to quantify the deployment of the meshes

As the composite meshes deploy from an 'almost flat' shape to a deployed mesh shape (see Figure 6.3), it is necessary to develop metrics to quantify the shape change of the mesh. To quantify the deployed shapes of the composite meshes, expansion ratio (*Expansion ratio (%)* = $100 * \delta / span$) and deployment angle (ϕ°) are proposed, where δ , span and ϕ can be obtained from the deployable meshes, as shown in Figure 6.3. These deployment parameters have been used in quantifying the shape change of the meshes in FE models and experimental studies described in this chapter.

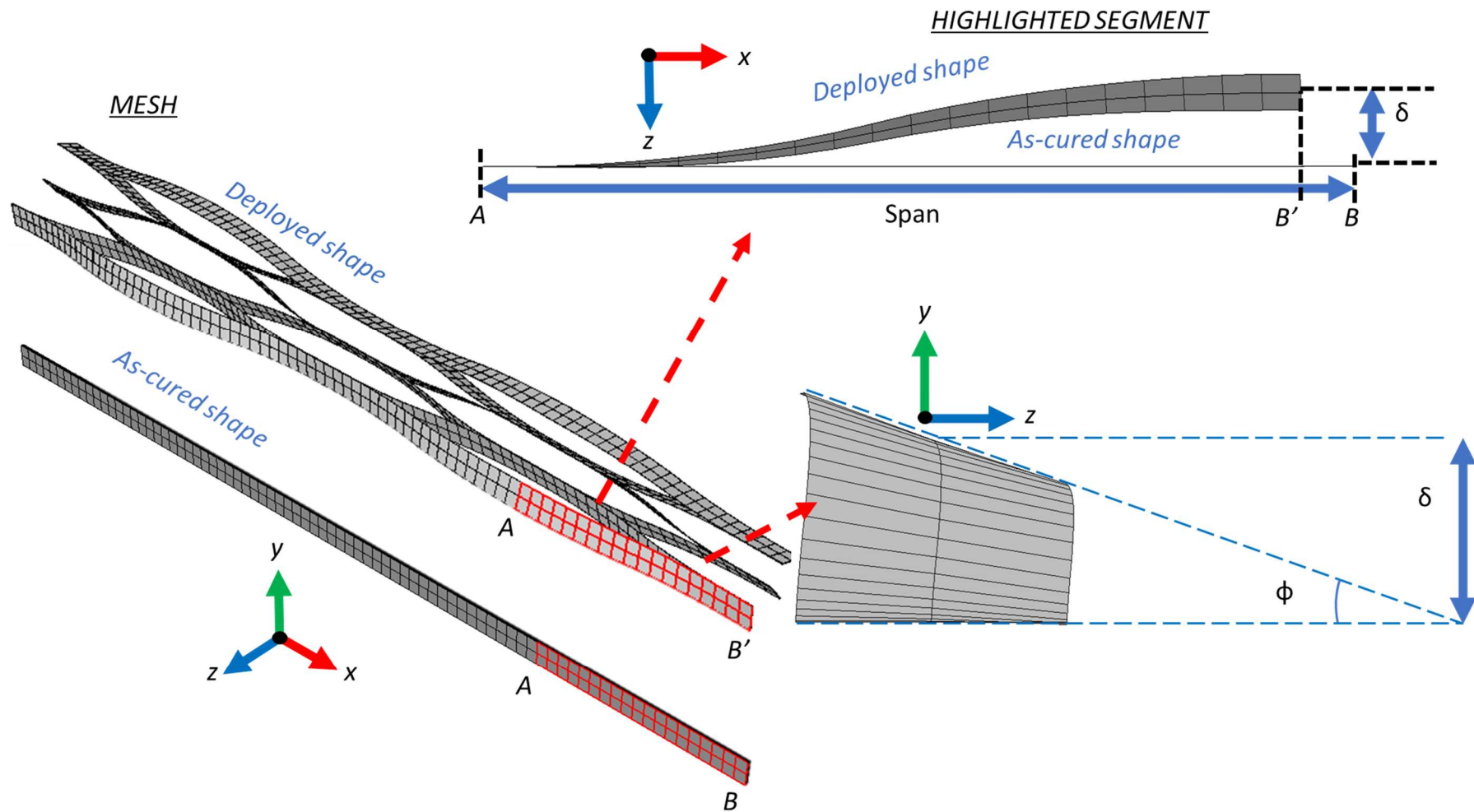


Figure 6.3. Schematic showing a deployed curved mesh with a segment of it highlighted.

Here, A, B and B' are used to indicate the limits of the highlighted segment along the x-axis.

6.2. Numerical study of deployable composite meshes

The morphing behaviour of flat composite specimens in previous chapters were predicted using simple analytical tools. However, for an accurate prediction of the complex thermomechanical behaviour of the composite proposed in Section 6.1.2, an ABAQUS finite element (FE) model was used.

6.2.1. Mesh convergence study of CFRP sub-laminates

As the first step to modelling a segment of the deployable mesh, the $0^\circ/90^\circ$ CFRP sub-laminates (layup shown in Figure 6.4) were modelled, and a convergence study was performed to identify the mesh size to be used for subsequent studies.

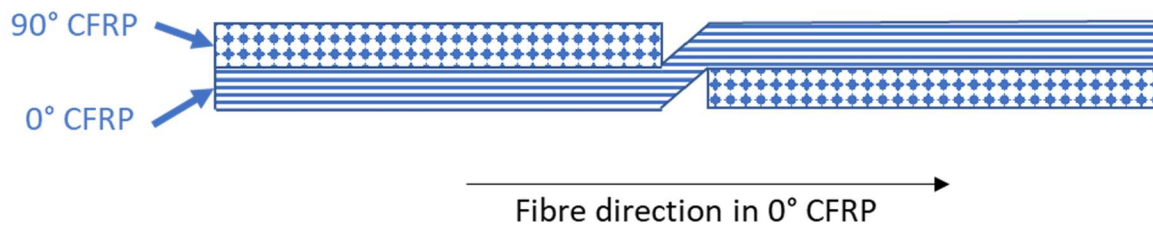


Figure 6.4. Layup of the model used in the mesh convergence study of CFRP sub-laminates used in the proposed layup

6.2.1.1. Materials

As in the previous experimental studies described in this thesis, unidirectional TS300/914 carbon epoxy prepreg was selected as the CFRP component of the layup. The properties of the CFRP used in FE modelling are shown in Table 6.1.

Table 6.1. Thermal and mechanical properties of CFRP in FE modelling

Material	Property	Value
Hexcel TS300/914	E11	120 GPa ^a
(also known as Fibredux	E22, E33	8.5 GPa ^b
914C-TS-5-34%)	v12	0.32 ^c

G12	5.27 GPa ^c
α_{11}	$-4.5 \times 10^{-7}/^{\circ}\text{C}^{\text{d}}$
α_{22}	$2.8 \times 10^{-5}/^{\circ}\text{C}^{\text{d}}$

^a obtained from (Zhang, 2020) and the experimental results shown in Table 3.15,

^b obtained from (Waili, 2019), and

^c obtained from (Bezazi, Boukharouba and Scarpa, 2009)

^d obtained from (Ciba-Geigy Plastics, 1989)

6.2.1.2. Details of modelling

The CFRP sub-laminates in the FE model were designed to be 2-dimensional shells having the dimensions as shown in Figure 6.5 and having a width of 10 mm in the Z-direction. The CFRP plies were assigned a thickness of 125 μm (Ciba-Geigy Plastics, 1989) and a material property as specified in Table 6.1. To represent the mechanical and thermal behaviour, the CFRP plies were meshed with 2-dimensional 4-node thermally coupled general-purpose shell with finite strains (S4T).

To ensure that the sub-laminate shown here will form one-quarter of a mesh cell as discussed previously, the following boundary conditions were used (see Figure 6.5),

- (i) BC1 – Zero displacement along X-axis and zero rotation around Y and Z-axes
- (ii) BC2 – Zero displacement along Y-axis
- (iii) BC3 – Plane section remains plane
- (iv) BC4 – Zero rotation around Y and Z-axes

The parallel CFRP plies were constrained using a 'Tie' constraint to represent a primary bond. The entire model was assigned a pre-defined temperature of 175°C (i.e., curing temperature of CFRP (Ciba-Geigy Plastics, 1989)) in its initial flat shape and was then modelled to cool to

88°C (i.e., T_g of PS, as shown in [Section 3.2.1](#))*. In all the FE studies in this thesis, no failures were modelled. Furthermore, as no viscosity or other time-dependent parameters are modelled here, this FE model is quasi-static.

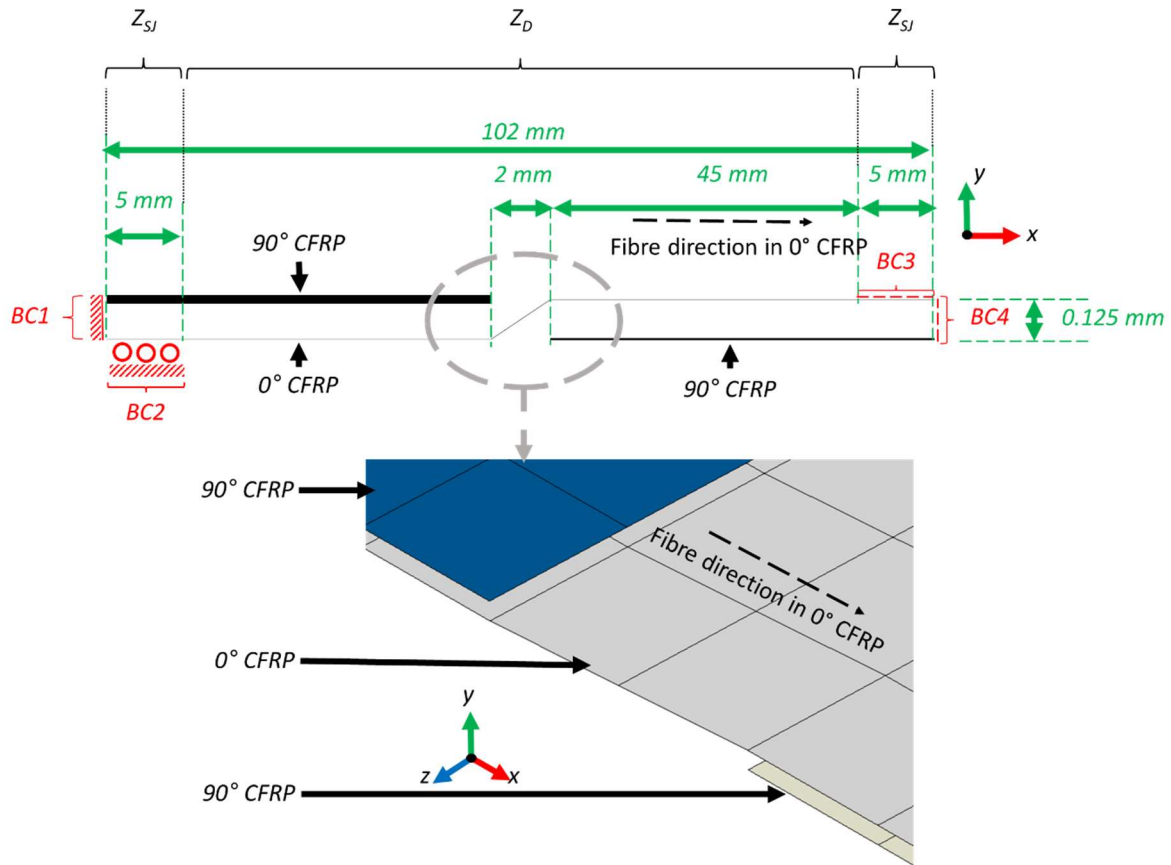


Figure 6.5. A schematic of the layup in the FE model to study the mesh convergence of CFRP sub-laminates.

* As the FE models consider fixed modulus and thermal expansion coefficient, the mesh convergence of the models should be independent of the final temperature of the model. However, as explained subsequently in [Section 6.2.3](#), to predict the deployment parameters of the composite proposed in [Section 6.1.2](#), a two-step model is considered (one to model cooling of composite from 175°C to 88°C, and another from 88°C to 25°C). For direct comparison when needed, the mesh convergence studies consider only the first step of the two-step model (i.e., cooling from 175°C to 88°C).

(Here, the dimensions and boundary condition regions (BC1, BC2, BC3 and BC4) are highlighted. As BC3 and BC4 cannot be represented in a 2D illustration of the model in the XY plane, only their regions are highlighted. The descriptions of BC1, BC2, BC3 and BC4 are provided in [Section 6.2.1.2](#). Z_{SJ} indicates zones of straight junction and Z_D indicates zones of deployment)

6.2.1.3. Analysing the mesh convergence of CFRP plies

To study the mesh convergence of the CFRP plies used in the proposed layup, they were meshed with a global mesh size of 5 mm, 2.5 mm, 1 mm, 0.5 mm, and 0.25 mm. The expansion ratio (defined in [Section 6.1.3](#), and shown again in [Figure 6.6](#)) for the models, after cooling to 88°C, with different global mesh sizes were calculated from the coordinates of the nodes at four corners of the top surface of the model. The expansion ratio, the time taken by the CPU to process the models, and the percentage difference in the expansion ratio of each model with respect to the previous coarser mesh are shown in [Table 6.2](#).

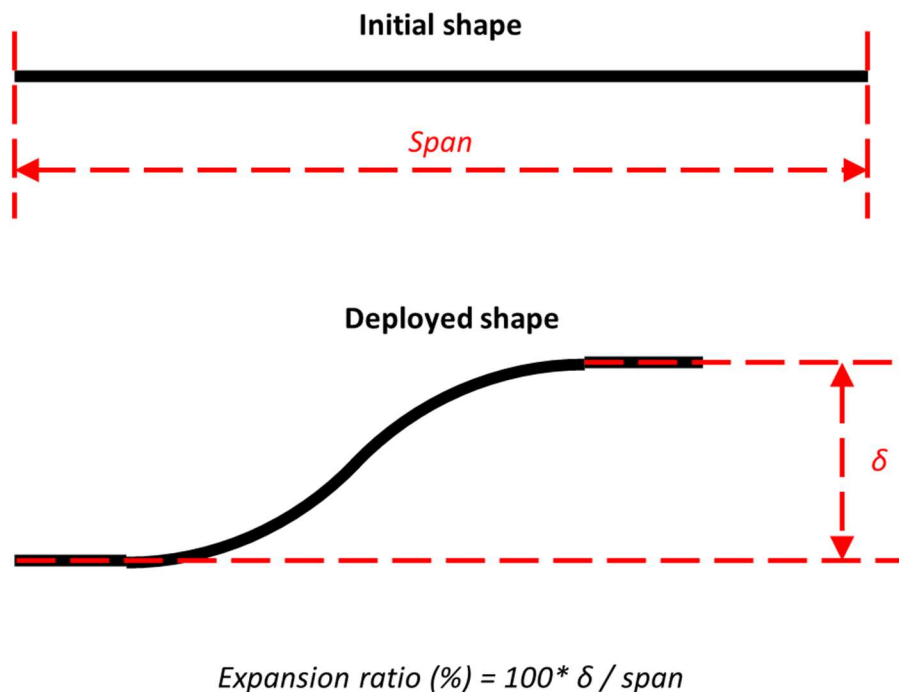


Figure 6.6. Shape of the FE model used to study the mesh convergence of CFRP sub-laminates in its initial flat and final deployed shapes

Table 6.2. Results of convergence studies performed on the
CFRP sub-laminates in Section 6.2.1

Global mesh size in CFRP layers (mm)	Expansion ratio (%)	CPU time (s)	% difference in expansion ratio, compared to the coarser mesh
5	15.24	18	-
2.5	13.91	110	-9.6
1	14.23	177	+2.3
0.5	14.26	740	+0.2
0.25	14.26	4833	0

From Table 6.2, it can be seen that a decrease in the global mesh size leads to an increase in computation time while the expansion ratio converges around 14.26. The difference between the expansion ratio of model with a global mesh size of 1 mm and the that with 0.5 mm is less than 1%. Hence, the mesh is considered converged at a global mesh size of 1 mm, and so, a global mesh size of 1 mm is used to mesh the CFRP plies in all subsequent FE models shown in this chapter.

The deployed shape predicted by FE showed good agreement with analytical predictions (see Appendix A.7).

6.2.2. Mesh convergence study of PS interleaves in the proposed layup

As the next step to model the repeating segment of the deployable mesh, the layup shown in Figure 6.7 was modelled, and a convergence study was performed on the PS interleaves to identify the mesh size of PS to be used for subsequent numerical studies.

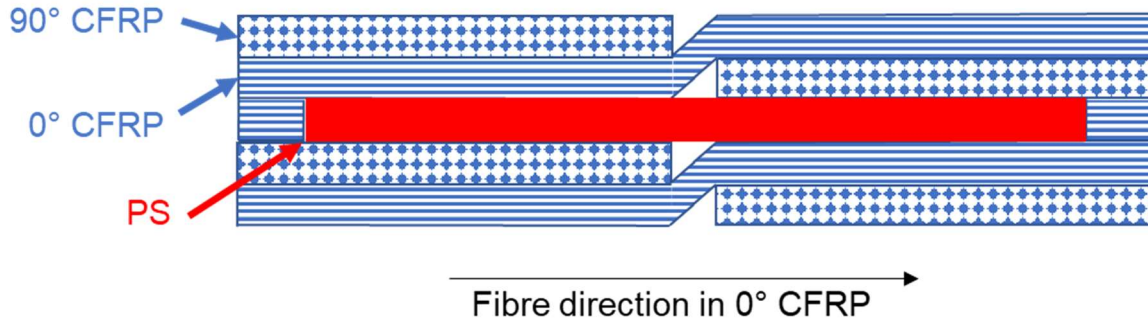


Figure 6.7. Layup of the model used in the convergence study of PS interleaves used in the proposed layup

6.2.2.1. Materials

The properties of the PS used in the FE models are shown in Table 6.1.

Table 6.3. Thermal and mechanical properties of PS in FE modelling

Material	Property	Value
PS (Styrolution 124N)	E	3.2 GPa ^d at $T < T_{g-PS}$
		0.1 Mpa ^e at $T > T_{g-PS}$
		where $T_{g-PS} = 88^{\circ}\text{C}$
	ν	0.35 ^b

^b obtained from (Waili, 2019),

^d obtained from (UL Prospector, 2012),

^e assumed value to represent PS in a low-modulus state, inspired from (Waili, 2019) and (Zhang, 2020). The impact of this assumption is discussed in detail in this Section 6.2.2.3.

6.2.2.2. Details of modelling

To study the mesh convergence of PS interleaves, the model shown in Figure 6.8 was created, having a width of 10 mm in the Z-direction. The properties of the CFRP laminae and the boundary conditions (BC1, BC2, BC3 and BC4) were the same as that shown in Section 6.2.1. The PS interleaves were assigned a material property as shown in Table 6.3. To represent

the mechanical and thermal behaviour, the PS plies were meshed with 8-node thermally coupled brick elements with linear thermal and displacement definitions (C3D8T). Unlike CFRP elements, PS elements were modelled with 3D elements to represent their large strains.

As shown in Section 6.2.1, 'Tie' constraints were used between the parallel CFRP plies.

Similarly, 'Tie' constraints were used between the PS interleaves and the adjacent CFRP plies.

As shown in Section 6.2.1, the entire model was assigned a pre-defined temperature of 175°C in its initial flat shape and was then modelled to cool to 88°C.

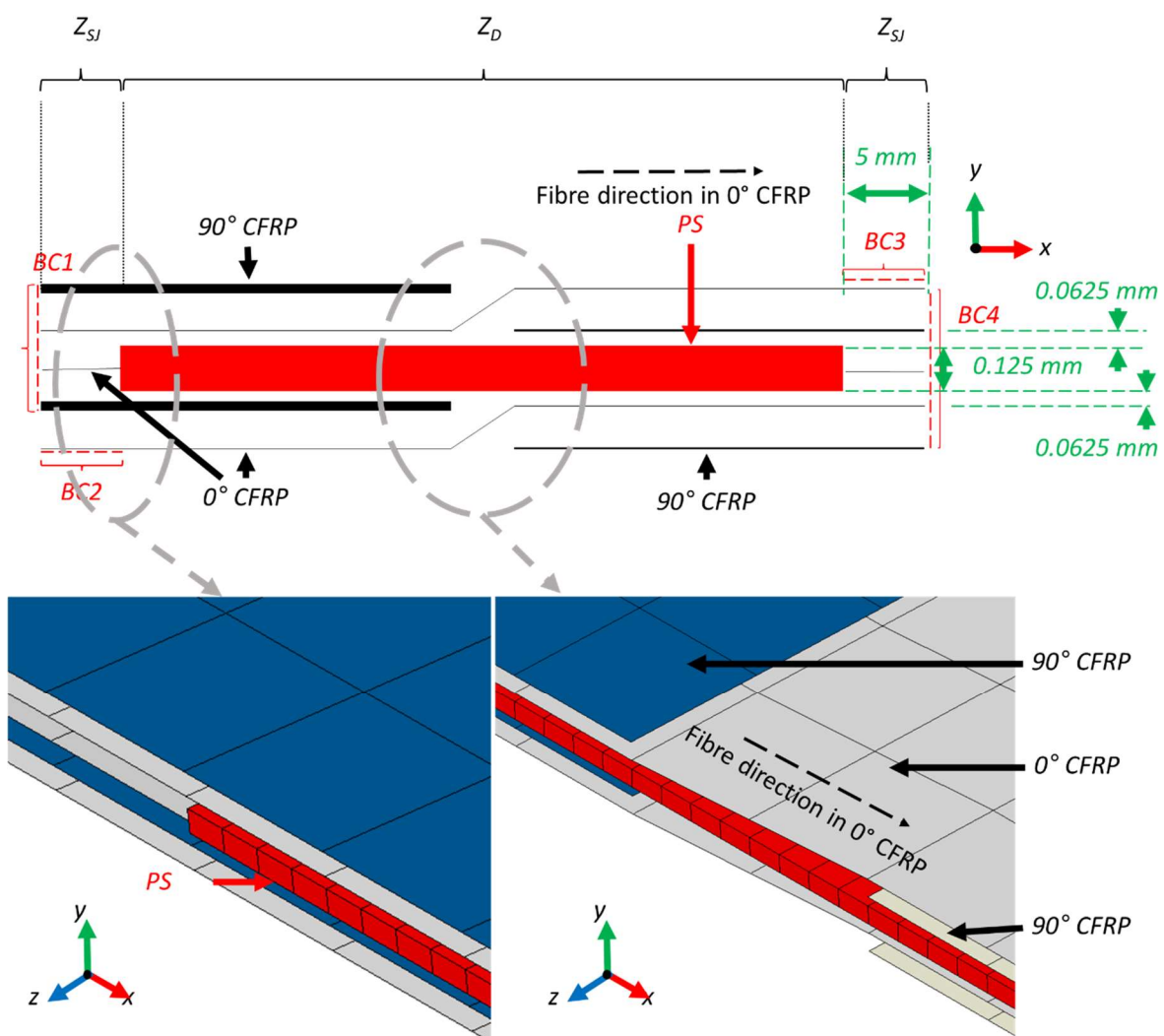


Figure 6.8. A schematic of the layup in the FE model to study the mesh convergence of PS interleaves.

(Here, some dimensions and boundary condition regions (BC1, BC2, BC3 and BC4) are highlighted. Further details of the dimensions are shown in [Figure 6.5](#). As BC3 and BC4 cannot be represented in a 2D illustration of the model in the XY plane, only their regions are highlighted. The descriptions of BC1, BC2, BC3 and BC4 are provided in [Section 6.2.1.2](#). Z_{SJ} indicates zones of straight junction and Z_D indicates zones of deployment.)

6.2.2.3. Analysing the mesh convergence of PS interleaves

To study the mesh convergence of PS interleaves, they were meshed with a global mesh size of 2.5 mm, 1 mm, 0.5 mm, and 0.25 mm. The CFRP plies were meshed with a global mesh size of 1 mm, in accordance with the convergence study described in [Section 6.2.1](#). The expansion ratio (defined in [Section 6.1.3](#)) for the models, after they cool down to 88°C, with different global mesh sizes in PS interleaves was calculated from the coordinates of the nodes at four corners of the top surface of the model. The expansion ratio, the time taken by the CPU to process the models, and the percentage difference in the expansion ratio of each model with respect to the coarser mesh are shown in [Table 6.4](#).

From [Table 6.4](#), it can be seen that the mesh size of PS has a negligible effect on the expansion ratio of the model. Hence, for the sake of uniformity with the CFRP sub-laminates, a global mesh size of 1 mm is used to mesh the PS interleaves in all subsequent FE models shown in this chapter.

The computational time for the model with 2.5 mm mesh in PS layers was significantly higher than the other models probably because the meshes were larger than that in the adjacent CFRP plies. This mismatch results in the CFRP plies having floating nodes, possibly causing the model require larger number of iterations for the solution to converge. However, for mesh sizes less than 1 mm, as the aspect ratio of the mesh cells in PS layer approached 1, a slight decrease in computation time was observed despite an increase in the number of mesh elements. The reason behind this decrease in computation time has to be explored in detail.

Table 6.4. Results of convergence studies performed on the
PS interleaves in Section 6.2.2

Global mesh size in PS layers (mm)	Expansion ratio (%)	CPU time (s)	% difference in expansion ratio, compared to the coarser mesh
2.5	10.08	152609	-
1	10.07	4809	0.1
0.5	10.04	4267	0.3
0.25	10.02	4223	0.2

Furthermore, the expansion ratio shown in Table 6.4 is found to be significantly lower than that shown in Table 6.2. The reason for this discrepancy is the influence of the modulus of PS interleaves on the overall stiffness of the modelled structure. If the numerical model shown above (see Figure 6.8) is repeated with the PS interleaves having a global mesh size of 1 mm, and elastic moduli ranging from 10^0 to 10^6 Pa, the expansion ratios of the model are predicted to range from 14.05% to 3.37% respectively, as shown in Figure 6.8.

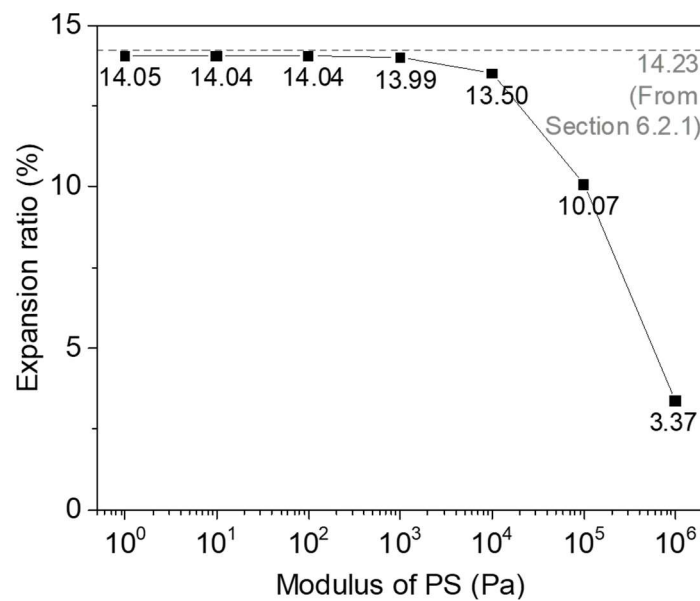


Figure 6.9. The predicted expansion ratio of the FE model (shown in Figure 6.8) for a
range of elastic moduli of PS

Here, it can be seen that as the modulus of PS approaches from 10^6 Pa to 10^0 Pa, the expansion ratio of the model shown in Figure 6.8 approaches that of the model shown in Figure 6.5. This observation demonstrates the influence of the modulus of the PS interleaves on the prediction of deformation capabilities of the layup proposed in Section 6.2.2. Furthermore, this observation indicates the need for a more accurate measurement of the elastic modulus of PS at elevated temperatures to be used for future FE models.

6.2.3. Modelling a segment of a deployable mesh with different layups

To study the effect of different layups on the deployment capabilities of the proposed laminate (see Figure 6.2 (a)), the layup shown in Figure 6.7 was used to model a segment of the deployable mesh. The material properties of CFRP and PS used in this layup have previously been shown in Sections 6.2.1 and 6.2.2.

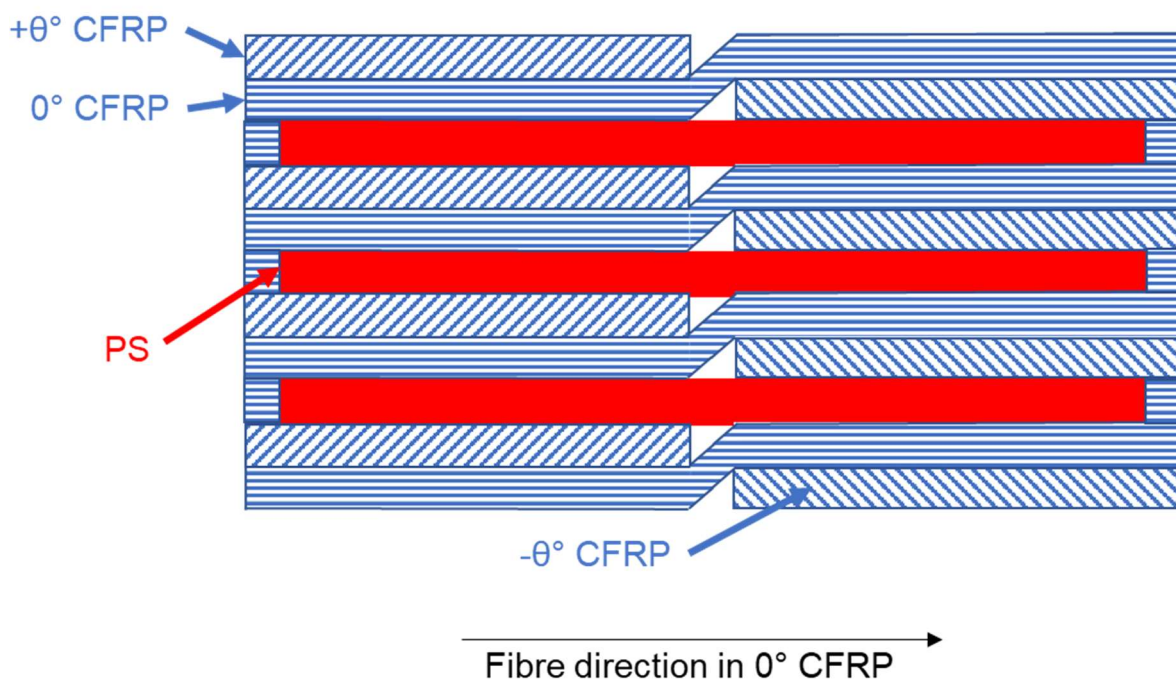


Figure 6.10. Layup of the model used to study the effect of different layups on the deployment capabilities of a mesh

6.2.3.1. Details of modelling

To study the effect of the proposed layup on the deployment capability of the mesh, the model shown in [Figure 6.11](#) was designed, having a width of 10 mm in the Z-direction. Models with layups having θ of 90°, 80°, 75°, 60° and 45° were used in this study.

Details on the dimensions of the layup, boundary conditions (BC1, BC2, BC3 and BC4), material properties, mesh properties and constraints of the layup can be found in [Sections 6.2.1](#) and [6.2.2](#). The entire model was meshed with a global mesh size of 1 mm, in accordance with the convergence studies shown previously.

The model was assigned a pre-defined temperature of 175°C in its initial flat shape and was then modelled to cool to 25°C in two steps. In the first step, the entire model was modelled to cool from 175°C to 88°C, during which the PS interleaves had a modulus of 0.1 MPa (see [Table 6.3](#)). In the second step, the shape of the entire model at 88°C was extracted, with the strains in PS laminates ignored. The deformed model was then modelled to cool from 88°C to 25°C, during which the PS interleaves had a modulus of 3.2 GPa (see [Table 6.3](#)). This two-step approach ensures that the strains developed in PS interleaves of the FE model at $T > T_{g-PS}$ do not induce an applied force when the modulus of PS is restored at $T < T_{g-PS}$. By modelling the temperature-based viscoelastic properties of PS interleaves, this two-step modelling process could be avoided.

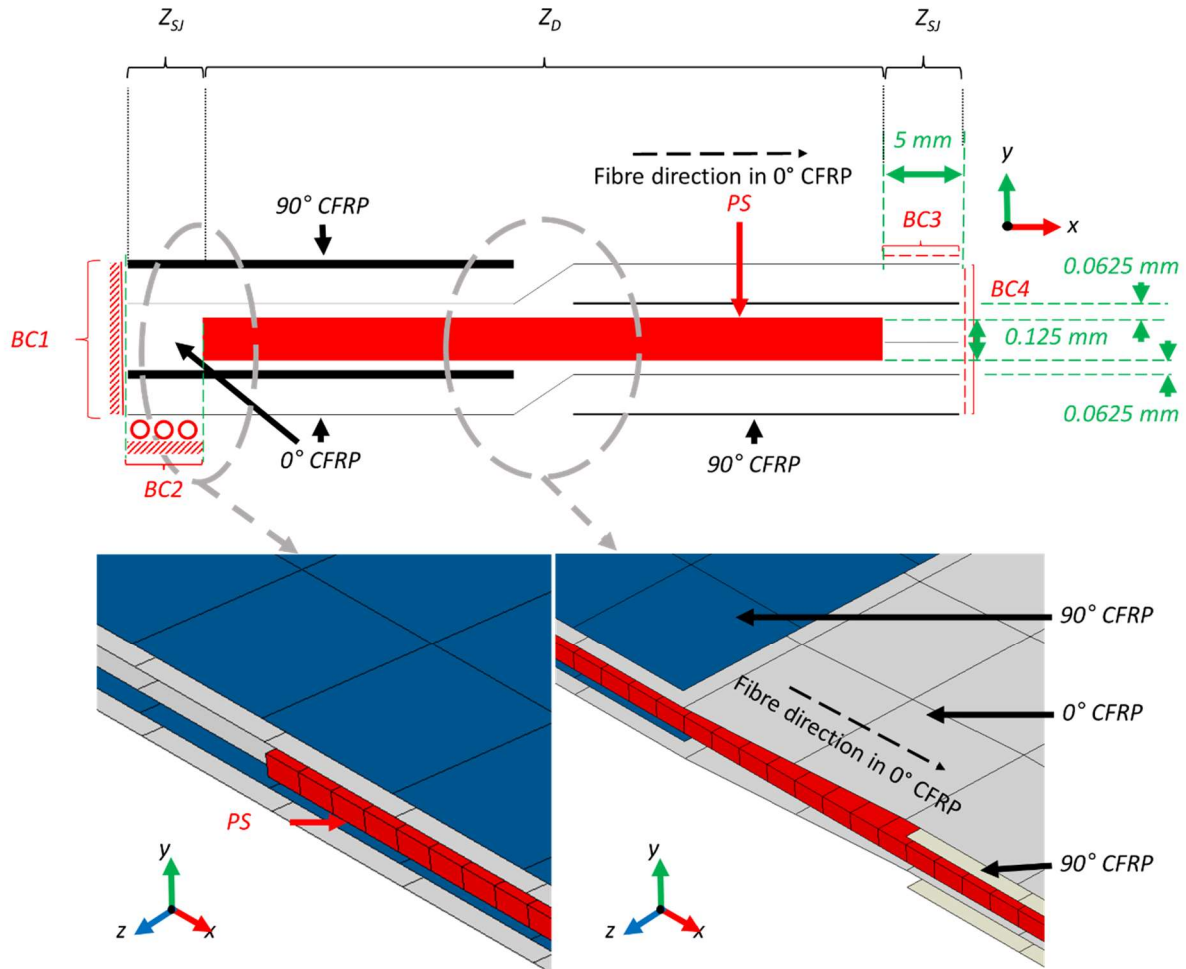


Figure 6.11. A schematic of the layup in the FE model used to study the effect of different layups on the deployment capabilities of a mesh

(Here, boundary condition regions (BC1, BC2, BC3 and BC4) are highlighted. Further details of the dimensions are shown in Figure 6.5. As BC3 and BC4 cannot be represented in a 2D illustration of the model in the XY plane, only their regions are highlighted. The descriptions of BC1, BC2, BC3 and BC4 are provided in Section 6.2.1.2. Z_{SJ} indicates zones of straight junction and Z_D indicates zones of deployment.)

6.2.3.2. Comparison of deployment parameters of meshes with different layups

The FE model of a segment of a deployable mesh with $\theta=45^\circ$ in its layup is (after it cools down to 25°C) shown in Figure 6.12. From the shape of the models, after they cool down to 25°C ,

the expansion ratio and deployment angle (defined in [Section 6.1.3](#), and shown again in [Figure 6.12](#)) for the models with different layups were calculated from the coordinates of the nodes at four corners of the top surface of the model, and are shown in [Table 6.5](#).

When $\theta=90^\circ$ in the layup, the CFRP sub-laminates have a cross-ply layup. Hence, a deployable mesh with $\theta=90^\circ$ in its layup will be capable of only expansion along the x-y plane (i.e., deployment angle equal to zero), as shown in [Table 6.5](#). Similarly, a deployable mesh with $45^\circ \leq \theta < 90^\circ$ in its layup will be capable of curved deployment with both expansion (represented by expansion ratio) and out-of-plane curvature (represented by deployment angle).

Furthermore, it is also seen that around 95% of deployment (i.e., 95% of maximum expansion ratio or deployment angle for each layup) is achieved when the FE model cools down from 175°C to 88°C when the PS interleaves have an elastic modulus of 0.1 MPa. The remaining 5% of deployment is achieved when the FE model cools down from 88°C to 25°C when the PS interleaves have an elastic modulus of 3.2 GPa.

In the proposed layup, when $0^\circ \leq \theta < 45^\circ$, the resultant laminates will have a lower expansion ratio and deployment angle than that of a mesh with $\theta=45^\circ$. Hence, they are not explored here.

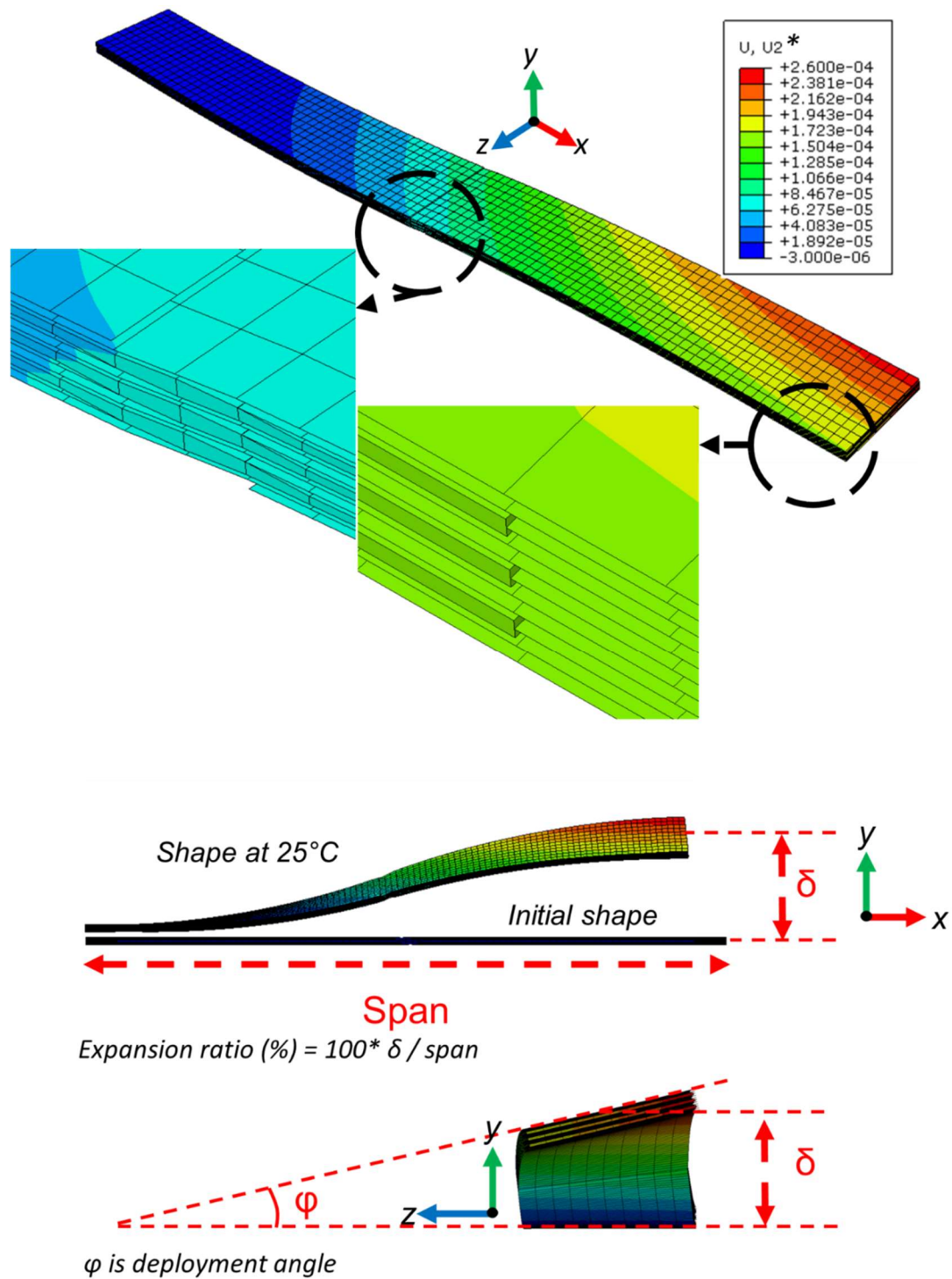


Figure 6.12. FE model of a repeating segment of a deployable mesh with $\theta=45^\circ$ in its layup, after cooling to 25°C

* U2 is the displacement along Y-axis in metres.

Table 6.5. Predicted expansion ratio and deployment angle obtained from the FE models
with different θ in the proposed layup at 25°C

(The data in brackets indicate the predicted expansion ratio and deployment angle at 88°C)

θ° in layup	Expansion ratio, %	Deployment angle, °
90°	9.00	0
	(8.73)	(0)
85°	8.93	1.51
	(8.66)	(1.42)
75°	8.40	4.47
	(8.14)	(4.24)
60°	6.83	8.57
	(6.58)	(8.20)
45°	4.75	11.39
	(4.54)	(10.94)

6.2.4. Conclusion

The numerical models of the layup proposed in [Section 0](#) confirm the previous findings that the proposed deployable composite mesh with $\theta=90^\circ$ in its layup will be able to expand along its thickness direction when heated and subsequently cooled (i.e., planar deployment). Similarly, a deployable composite mesh with θ in the range of $45^\circ \leq \theta < 90^\circ$ in its layup will be able to curve out-of-plane, in addition to expanding along its thickness direction when heated and subsequently cooled (i.e., curved deployment).

6.3. Manufacture and characterisation of deployable composite meshes

To validate the numerical model shown in [Section 6.2.3](#), an experimental study was conducted. Composite meshes capable of deployment inside a convection oven, and through intrinsic heating were manufactured, deployed, and characterised.

6.3.1. Materials, laminates, and specimens

As in the previous experimental studies described in this thesis, unidirectional TS300/914 carbon epoxy prepreg was selected as the CFRP component of the interleaved composite. The interleaf material was PS (70 μm thick film). Aerovac MR-FILM polytetrafluoroethylene (PTFE) release film was used to prevent bonding of the surfaces which are required to separate during composite mesh deployment. Stainless steel (SS) wire mesh/fabric (see [Section 5.1](#)) was selected as the heater to be embedded within the layup of intrinsically heated deployable composite mesh. Depending on whether the composite mesh was capable of deployment using an external heating source, or through intrinsic heating, different manufacturing processes were used.

6.3.1.1. *Manufacturing composite meshes capable of deployment only using an external heating source*

To manufacture composite meshes capable of deployment only using an external heat source, composite panels (planar dimension of 440 mm x 160 mm) were prepared with layups shown in [Figure 6.13](#). Each PS and PTFE region shown in the layup was formed of two films to achieve thicknesses of 140 μm and 100 μm * respectively to closely match the thickness of the adjoining CFRP ply. Two composite panels Mesh_{0/90} and Mesh_{0/45} were prepared with the layup shown in [Figure 6.13](#), with $\theta=90^\circ$ and $\theta=45^\circ$ respectively. To help visualise the

* 50 μm thick PTFE film was used here

deployment capabilities of a mesh produced using the layup shown in [Figure 6.13](#), a schematic of a deployed mesh (with $\theta=90^\circ$ in the layup) is shown in [Figure 6.14](#).

These panels were cured at 175°C and 7 bar pressure in an autoclave for 1 hour according to the cure schedule recommended by the manufacturer of the CFRP. From these panels, specimens having dimensions of 440 mm x 10 mm (i.e., 10 mm wide strips) were cut using a waterjet (see [Section 3.3.2.1](#)).

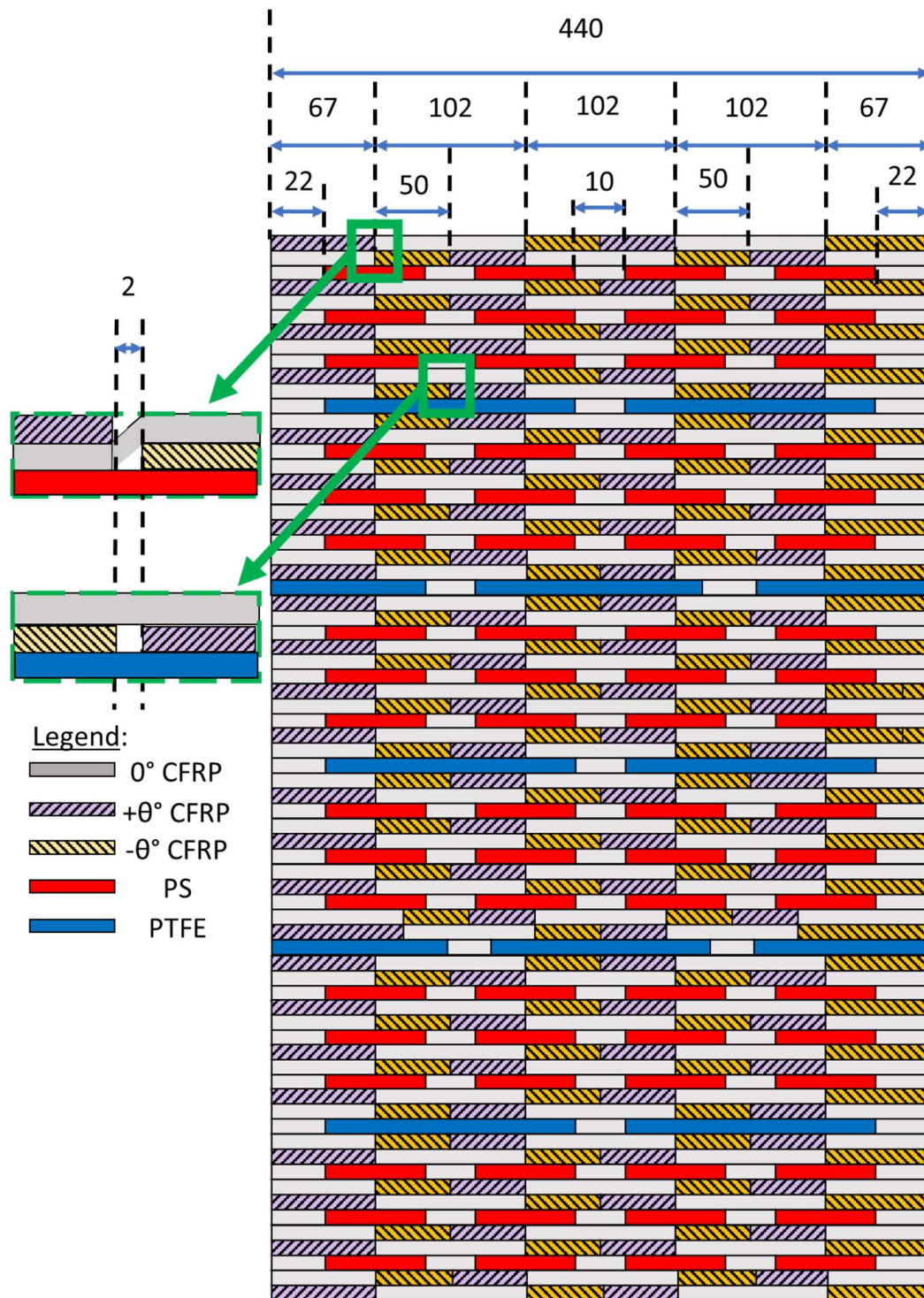


Figure 6.13. Layup of the composite panels prepared using the method described in Section 6.3.1.1
(all dimensions are in mm)

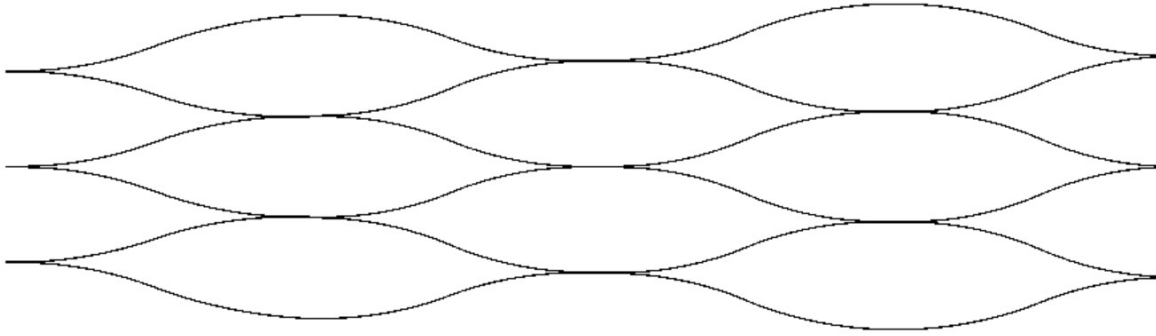


Figure 6.14. Schematic of a deployed mesh with layup shown in Figure 6.13, with $\theta=90^\circ$

6.3.1.2. *Manufacturing composite meshes capable of deployment using an external heating source and also through intrinsic heating*

To manufacture composite meshes capable of deployment through intrinsic heating, composite panels were produced in a 3-step modular process broadly following the production technique specified in [Section 5.1](#).

In the first step of the manufacturing process, several panels of composite sublaminates (440 mm x 160 mm) with layups shown in [Figure 6.15](#) were prepared and cured at 175°C and 7 bar pressure in an autoclave for 1 hour according to the cure schedule recommended by the manufacturer of the CFRP. In these sublaminates, θ was fixed as 90°. Each PS and PTFE* region shown in the layup was formed of two and three films respectively. During this step, the thickness of the PS film on the outermost ply of the modules/laminates decreased due to the leaking of PS through the porous debonding layer that was used to cover the laminates when they were in the autoclave.

In the second step of the manufacturing process, six SS fabrics (700 mm x 160 mm) were sandwiched between two PS films (460 mm x 160 mm) each. The PS-SS-PS sandwich occupied the central 410 mm x 160 mm section of SS, with the rest of the dry SS left on either side of the sandwich[†]. This sandwich was then heated to 175°C at 1 bar pressure (provided

* 20 μm thick PTFE film was used here

[†] See [Section 5.1](#) for further details on the production process

by vacuum bagging) using a Global Vacuum Presses G-SUB 1310 (Höchsmann GmbH, Germany) heated vacuum table. After 1 hour at this temperature and pressure, the PS-SS-PS sublaminates were cooled down to room temperature and the applied pressure was then removed.

In the third step of the manufacturing process, the PS-SS-PS sublaminates were sandwiched between the composite sublaminates prepared during the first step of the manufacturing process, as shown in [Figure 6.16](#). These sandwiched laminates were then heated to 175°C at 1 bar pressure using an HLP40 hot press (Höfer Presstechnik GmbH, Austria). After 1 hour at this temperature and pressure, the laminate was cooled down to room temperature and then the applied pressure was removed. [Figure 6.17](#) shows the composite panels at the start of the third step in the production process. This laminate had $\theta=90^\circ$ in its layup and is referred to as Mesh_{0/90-SS} in this thesis.

Using a waterjet (see [Section 3.3.2.1](#)), 10 mm wide Mesh_{0/90-SS} specimens were cut from the cured laminate. These specimens (see [Figure 6.18](#)) had dry SS protruding out of them to allow connection to a DC power supply. To facilitate a good electrical connection to a DC power supply, all the dry SS fabrics were connected together at each end of the specimens using conductive copper tape and silver conductive paint (see [Section 5.1](#)), at a distance of around 120 mm from the ends of the CFRP section of the specimens. The total end-to-end length of the heaters was around 680 mm in all the Mesh_{0/90-SS} specimens.

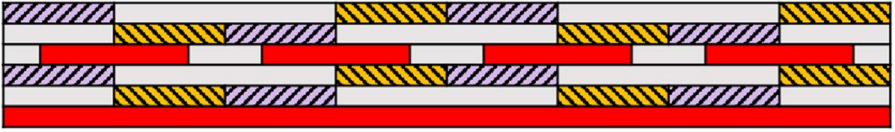
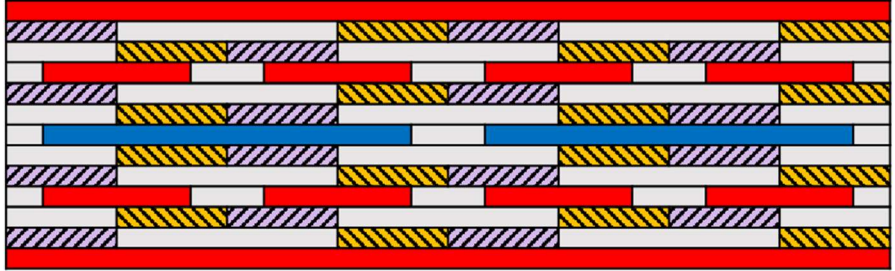
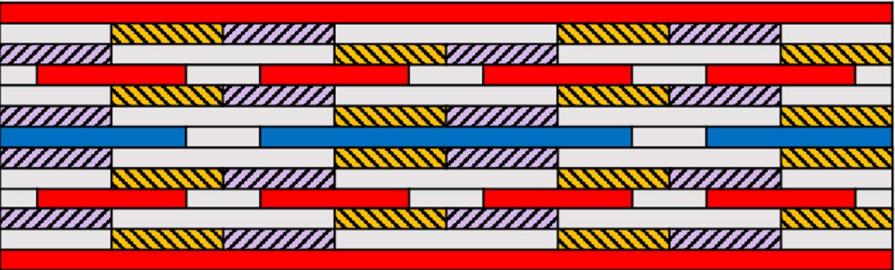

Sublamine name	No. of panels	Layup*
A	1	
B	3	
C	2	
D	1	

Figure 6.15. Names and layups of the composite sublaminates prepared during the first step of the manufacturing process described in Section 6.3.1.2

*Dimensions and legend for the layup can be found in Figure 6.13

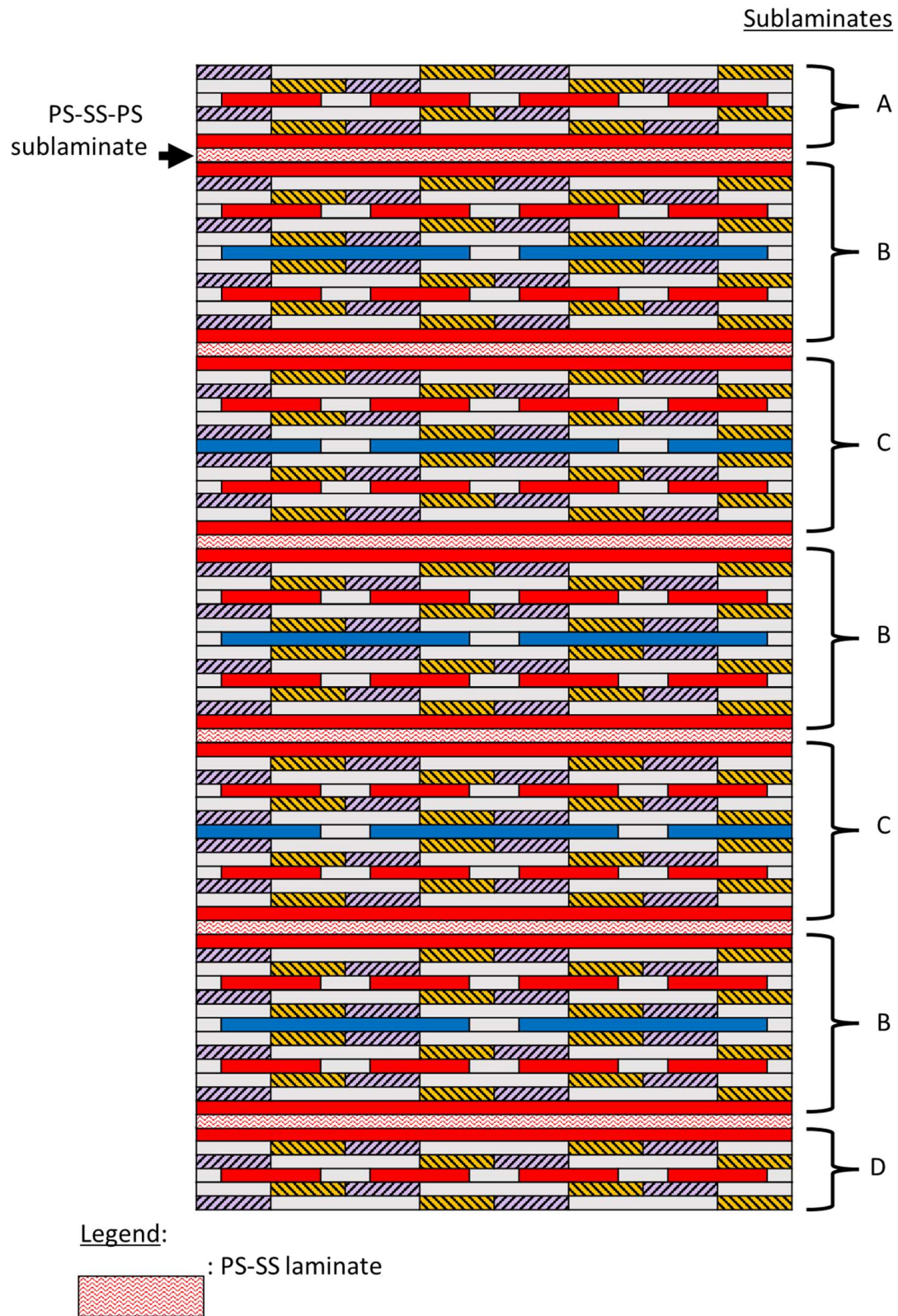


Figure 6.16. Layup of the Mesh_{0/90-SS} laminate prepared during the third step of the manufacturing process described in Section 6.3.1.2

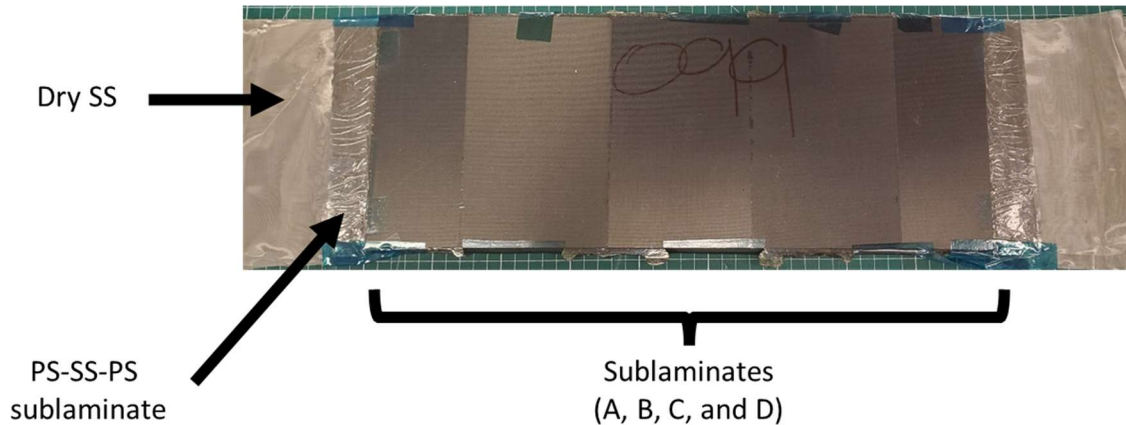


Figure 6.17. Mesh_{0/90-SS} panel at the start of the third step of the manufacturing process described in Section 6.3.1.2



Figure 6.18. Mesh_{0/90-SS} specimens showing the dry SS heaters and copper connectors

6.3.2. Experiment methodology

6.3.2.1. Deployment of composite meshes using a convection oven

To deploy the Mesh_{0/90}, Mesh_{0/45}, and Mesh_{0/90-SS} specimens using an external thermal energy source, they were heated to 135°C inside a convection oven and held at that temperature for 60 minutes before being cooled to room temperature. During this process, the composites were laid flat in the oven, with the expansion happening along the horizontal direction. By positioning the specimens in such a way, the effect of the self-weight of the composite mesh

on its deployment can be reduced. The dimensions of the deployed composite meshes were then measured to determine the mesh expansion ratio and the deployment angle (defined in previous sections).

6.3.2.2. *Deployment of composite meshes through intrinsic heating*

To deploy the Mesh_{0/90-SS} specimens through intrinsic heating, they were heated using applied DC (i_{DC}) inside a fume hood. To avoid thermal shocks within the specimens, the i_{DC} was increased gradually in steps of 0.5 A. During this process, the composites were laid on a flat surface, as specified in [Section 6.3.2.1](#). One thermocouple was mounted on the surface of each specimen at mid-length to measure its surface temperature.

The i_{DC} used to heat the specimens, the duration of applying i_{DC} (t_{DC}), and the surface temperature of the specimens at the end of t_{DC} are shown in

[Table 6.6](#). In preliminary investigations, an arbitrary i_{DC} (higher than that specified in [Table 6.6](#)) was selected as to investigate the intrinsically heated deployment capabilities. However, the high i_{DC} caused the composite to thermally degrade and release fumes visible to the naked eye. Hence, for subsequent investigations, the magnitude of i_{DC} , and duration of applying i_{DC} (t_{DC}) were manually controlled to ensure that the deployment of the composite meshes occurred with minimal thermal degradation visible to the naked eye. The dimensions of the resulting deployed shapes were measured to determine the mesh expansion ratio and the deployment angle.

6.3.2.3. *Optical microscopy of composites*

The 20 mm sections at the free end and at a point of inflection (see [Figure 6.19](#)) of a mesh cell from selected Mesh_{0/90}, Mesh_{0/45}, and Mesh_{0/90-SS} specimens in the pristine as-cured state, and deployed conditions were inspected by optical microscopy, following the methodology described in [Section 3.1.2.2](#).



Figure 6.19. Positions in a composite mesh cell where optical microscopy was performed
(The left and right ends of the images appear cropped due to the physical constraints of the scanner used in imaging)

Table 6.6. Experimental parameters used and measured while deploying Mesh_{0/90-SS} specimens through intrinsic heating

Specimen number	I_{DC} (A)	Voltage (V)	Duration of applying DC - t_{DC} (min)	Surface temperature at the end t_{DC} - T_{surf} (°C)
1	7.0	13.00	5	91
	7.5	14.91	15	100
	8.0	15.83	15	110
	8.5	16.78	15	110
2	7.0	13.36	10	*
	7.5	15.43	10	*
3	6.5	13.51	15	98
	7.0	14.49	15	105
4**	6.5	12.72	15	88
	7.0	14.09	7	85
	7.5	15.08	10	106

*Temperature not measured for this specimen

** A video of the deployment of this specimen is available online at youtu.be/lolw5liTugI

6.3.3. Results and discussions

The deployed Mesh_{0/90} and Mesh_{0/45} specimens are shown in Figure 6.20, where the difference between planar and curved deployment is evident. A deployed Mesh_{0/90-SS} specimen is shown in Figure 6.21. The expansion ratio and the deployment angle of the specimens after deployment are shown in Table 6.7.

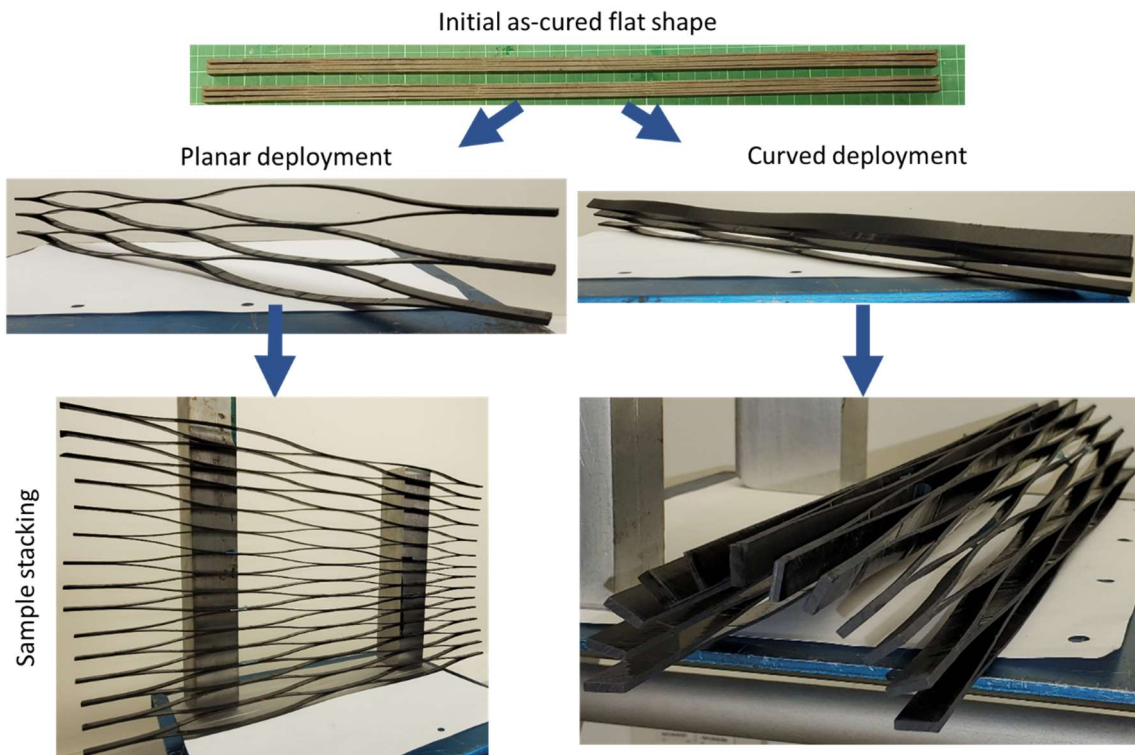


Figure 6.20. Mesh_{0/90} and Mesh_{0/45} specimens in their as-cured and deployed states

* To emphasise the planar and curved deployment, multiple specimens were stacked to form a composite mesh wall (made of five specimens of Mesh_{0/90}) and a composite mesh tunnel (made of four specimens of Mesh_{0/45})

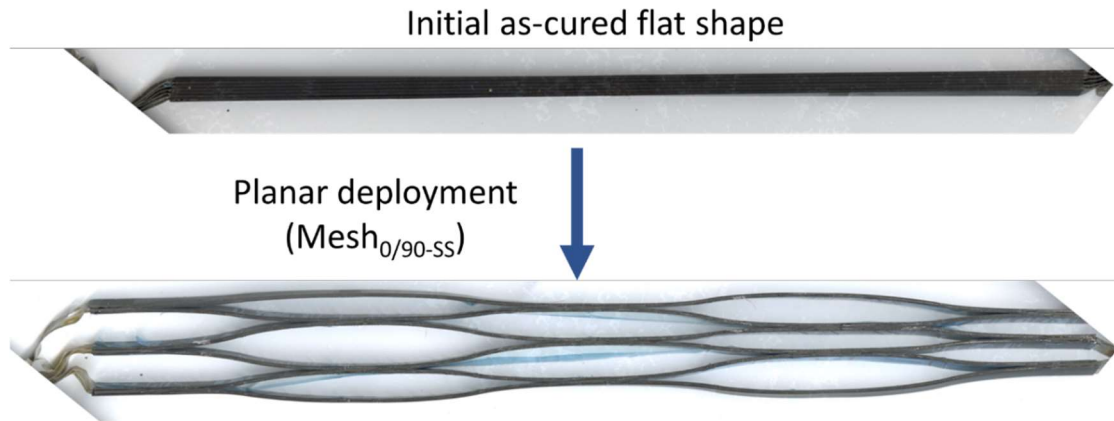


Figure 6.21. Mesh_{0/90-SS} specimen in its as-cured and deployed states

(The left and right ends of the images appear cropped due to the physical constraints of the scanner used in imaging)

Table 6.7. Expansion ratio and deployment angle of composite meshes after deployment

Composite name	Expansion ratio (%)	Deployment angle (°)
Mesh _{0/90}	8.03 ± 0.92	0
Mesh _{0/45}	3.19 ± 0.27	8.77 ± 0.84
Mesh _{0/90-SS} (Deployment using an oven)	7.05 ± 1.39	0
Mesh _{0/90-SS} (Deployment through intrinsic heating)	5.43 ± 1.61	0

The numerically predicted and experimentally observed expansion ratio and deployment angle of Mesh_{0/90} and Mesh_{0/45}, as plotted in Figure 6.22. As discussed previously, the numerical model does not consider the temperature-dependent viscoelastic properties of PS, and this may account for the predicted expansion ratio and deployment angle from the FE models being higher than the experimentally observed ones.

The Mesh_{0/90-SS} specimens deployed using an oven (see Figure 6.23 (a)) had an expansion ratio comparable to that of Mesh_{0/90}, as shown in Figure 6.22. However, the Mesh_{0/90-SS} specimens deployed through intrinsic heating (see Figure 6.23 (b)) showed a lower expansion ratio than Mesh_{0/90}. Furthermore, the dimensions of the meshes of the intrinsically heated Mesh_{0/90-SS} specimens after deployment were far more uneven than that in oven-heated Mesh_{0/90} specimens. It is possible that the temperature distribution within the composite mesh during intrinsic heating could have been uneven, leading to a non-uniform mesh deployment.

Compared to their pristine as-cured state (see Figure 6.24), the deployed Mesh_{0/90}, Mesh_{0/45}, and Mesh_{0/90-SS} specimens (see Figure 6.25 and Figure 6.26) showed the development of voids within the PS interleaves.

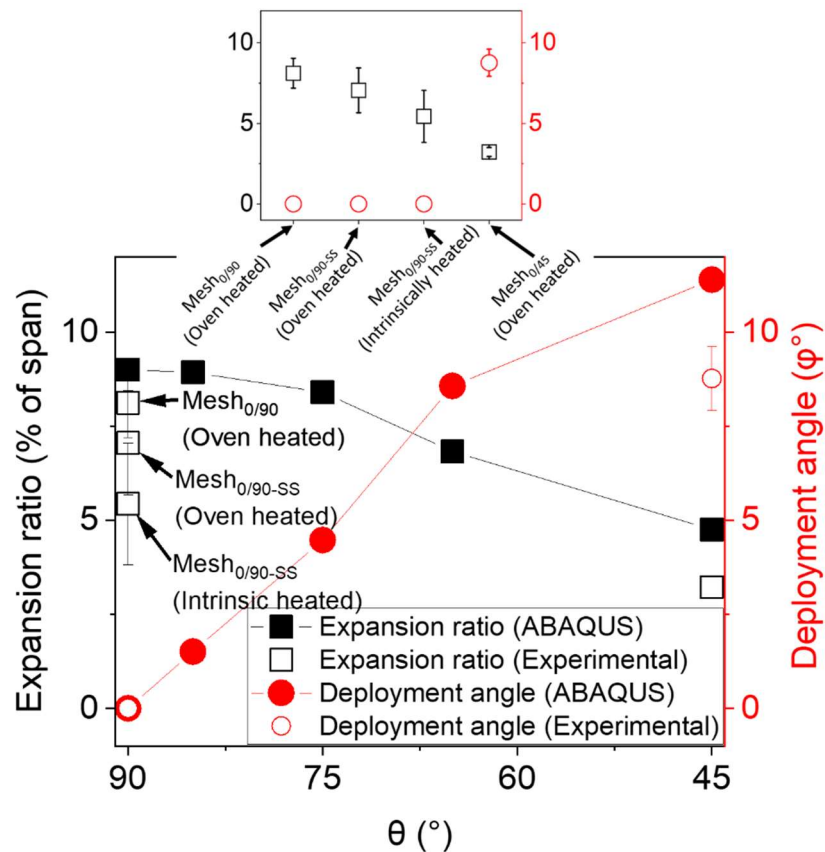


Figure 6.22. Comparison of numerically predicted (from Section 6.2.3.2) and experimentally observed expansion ratio and deployment angle

(The overlapping datapoints are labelled. Inset shows the experimentally observed expansion ratio and deployment angle for Mesh_{0/90}, Mesh_{0/45} and Mesh_{0/90-ss} specimens. The legend and the vertical axes of the inset are the same as that of the larger graph.)

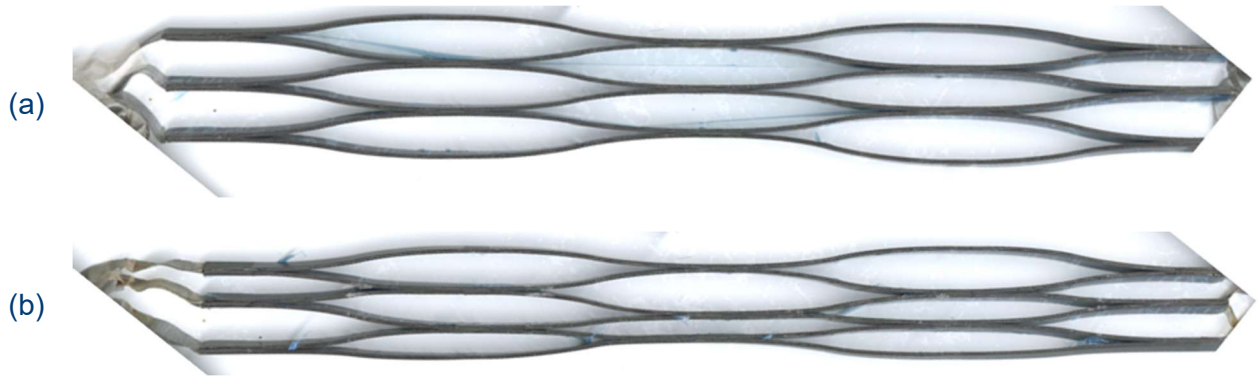
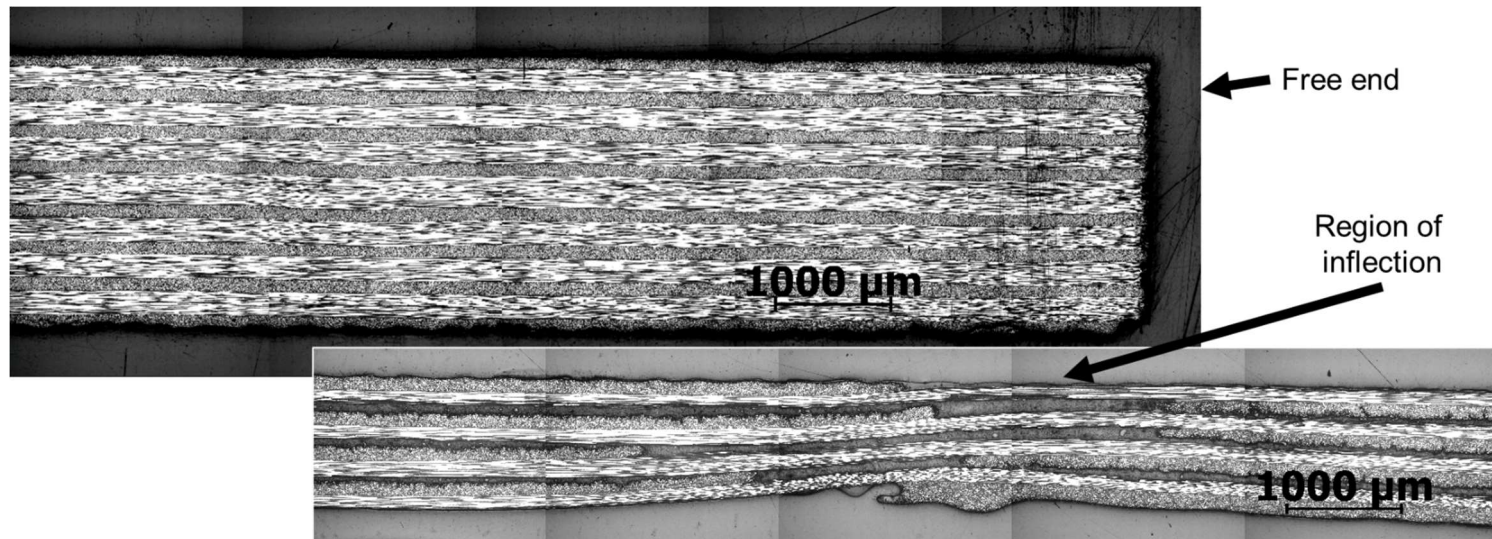


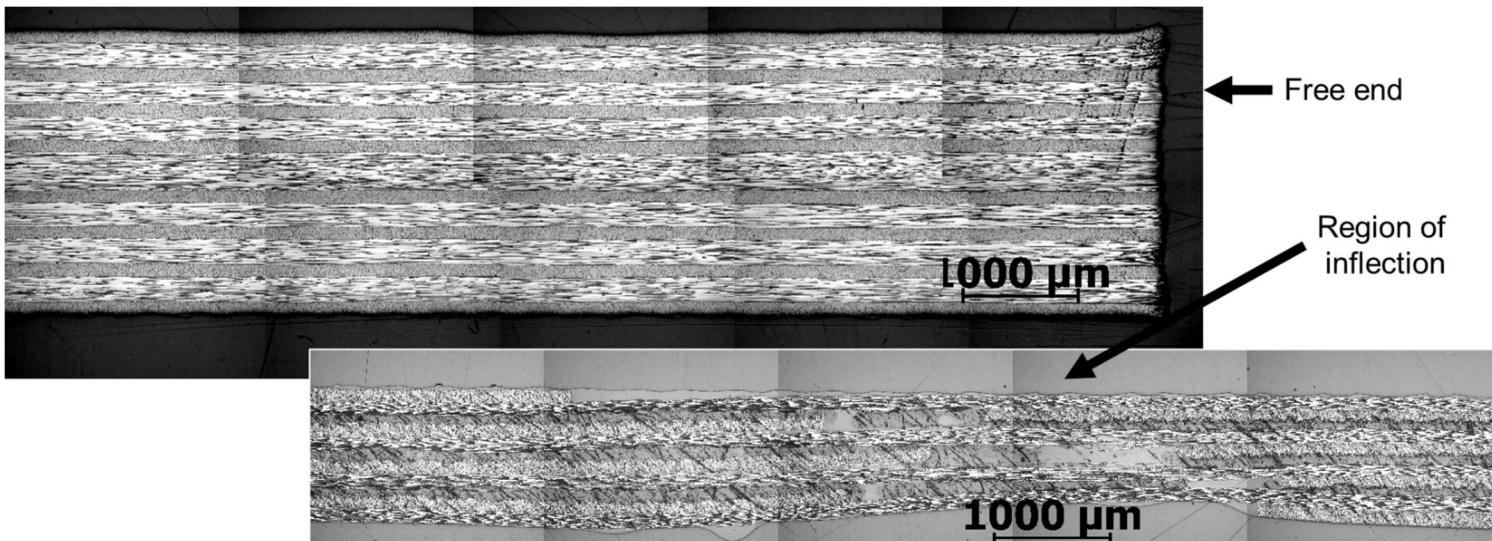
Figure 6.23. Mesh_{0/90-ss} specimens deployed (a) using an oven and (b) through intrinsic heating

(The left and right ends of the images appear cropped due to the physical constraints of the scanner used in imaging)

(a)



(b)



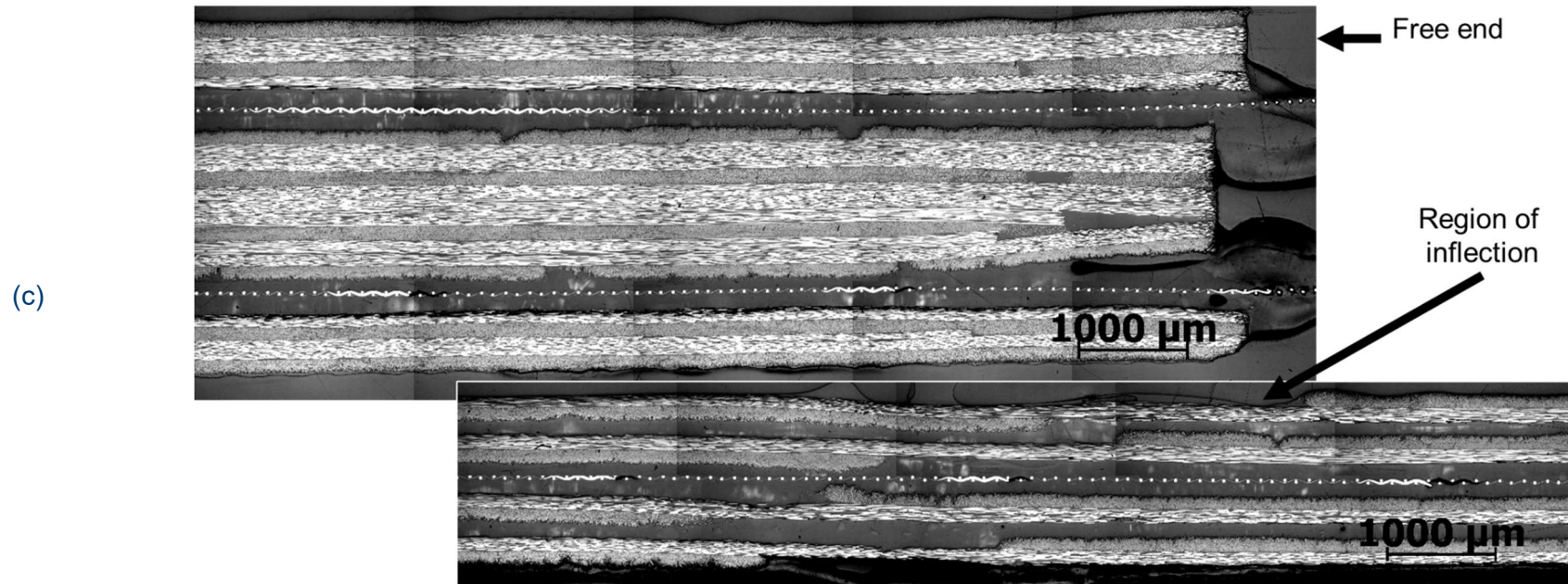
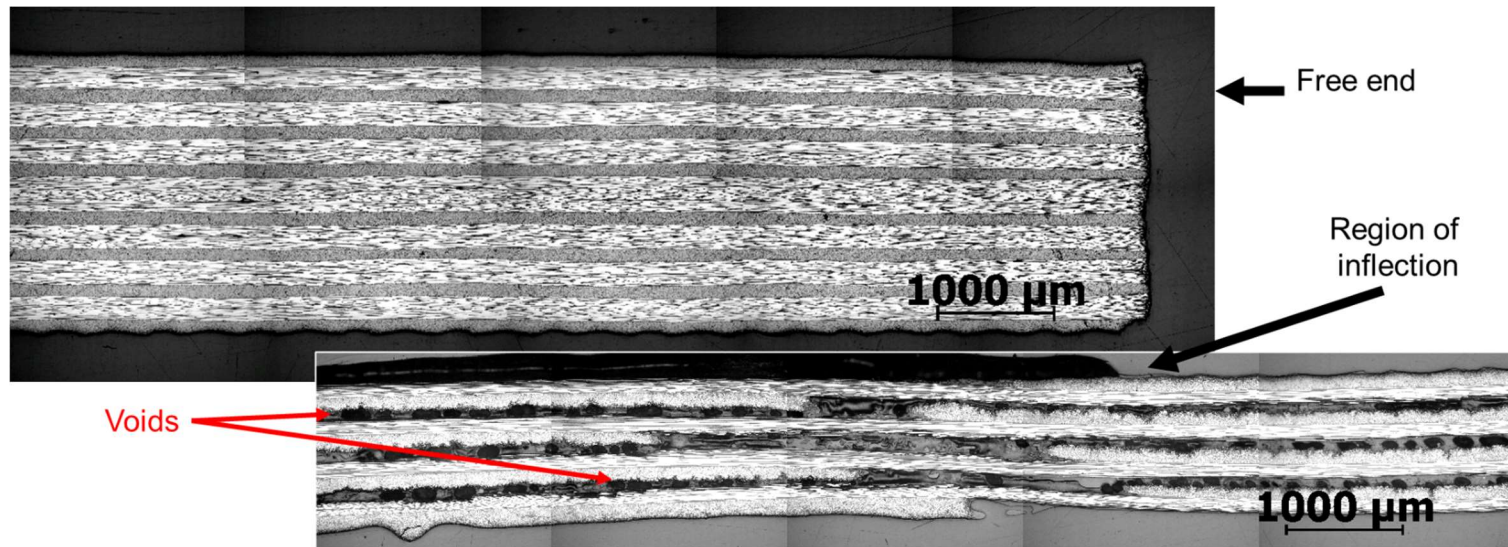
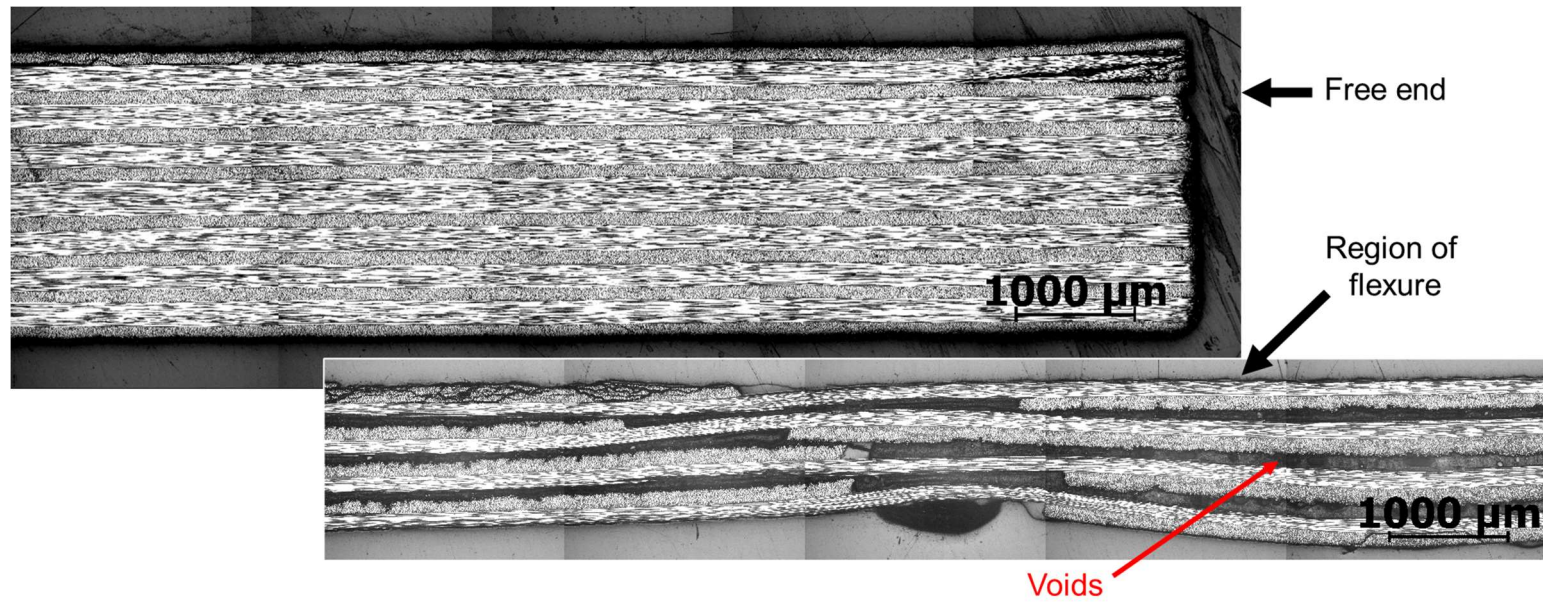


Figure 6.24. Longitudinal microsection of (a) Mesh_{0/90}, (b) Mesh_{0/45} and (c) Mesh_{0/90-SS} specimens in their pristine as-cured state

(a)



(b)



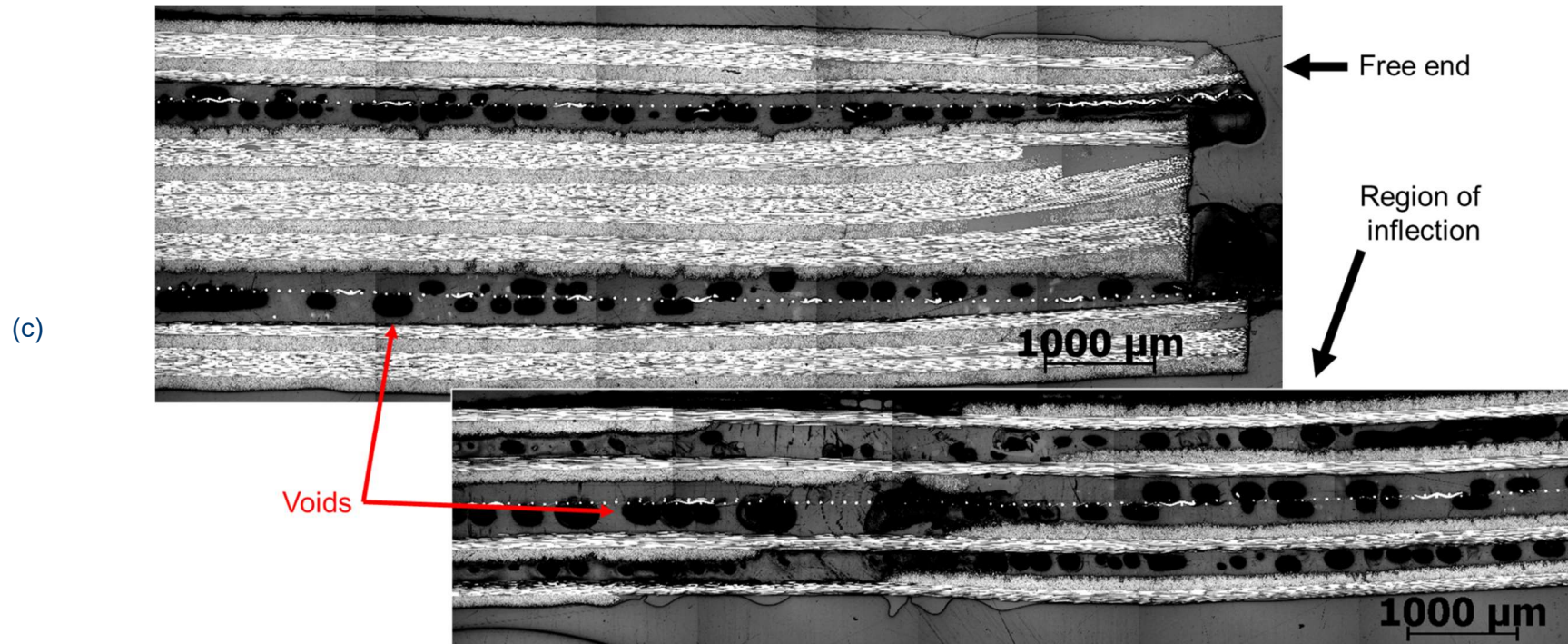


Figure 6.25. Longitudinal microsection of (a) Mesh_{0/90}, (b) Mesh_{0/45} and (c) Mesh_{0/90-SS} specimens after deployment inside an oven

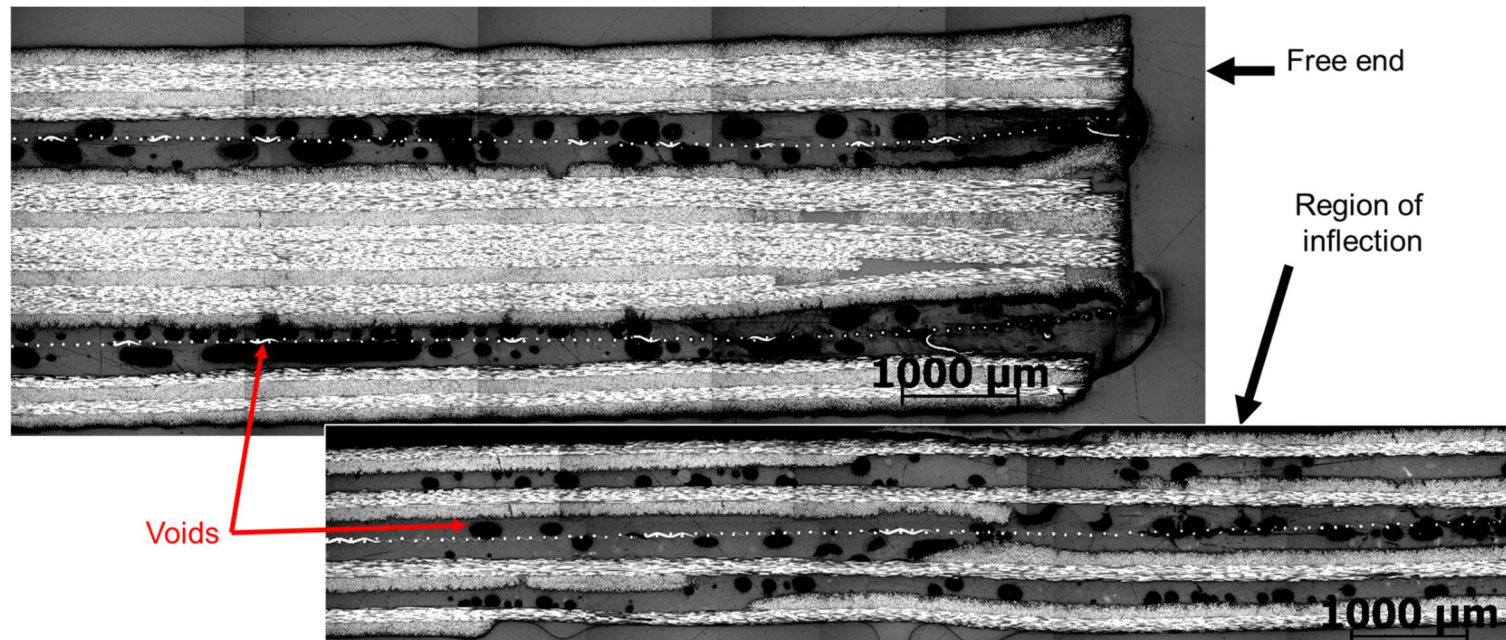


Figure 6.26. Longitudinal microsection of Mesh0/90-SS specimen after intrinsically heated deployment

Fewer voids were developed within the PS interleaves of deployed Mesh_{0/45} specimens, compared to other specimens (see Figure 6.25 (b)). The PS interleaves of deployed Mesh_{0/90} specimens (see Figure 6.25 (a)) showed a comparatively higher quantity of voids. Furthermore, the highest quantity of voids was developed within the PS interleaves of deployed Mesh_{0/90-SS} specimens (see Figure 6.25 (b) and Figure 6.26), irrespective of the deployment method.

While deploying, the deformation of CFRP plies cause the PS plies to undergo shear deformations. The shear deformation of PS and the prevalence of voids are both higher in Mesh_{0/90} and Mesh_{0/90-SS} specimens, compared to Mesh_{0/45} specimens. While a correlation between the magnitude of shear deformation and the prevalence of voids can be seen here, the underlying reason behind this observation has to be investigated further. Furthermore, as discussed in Section 5.3, an uneven temperature distribution within the Mesh_{0/90-SS} specimens due to intrinsic heating by i_{DC} could have also contributed to void formation.

6.3.4. Conclusion

Deployable composite meshes were successfully manufactured based on the layup proposed in Section 6.1. The composite meshes were then deployed using a convection oven or through intrinsic heating. Subsequently, the deployed meshes were characterised and compared against the numerical predictions shown in Section 6.2. This comparison revealed a strong qualitative agreement between the simplified numerical predictions and experimental observations.

As expected, the deployable composite mesh with $\theta=90^\circ$ in its layup underwent planar deployment and the deployable composite mesh with $\theta=45^\circ$ in its layup underwent curved deployment. A significant number of voids were, however, formed within the PS interleaves in the deployed composite meshes. Through the study described in this chapter, the morphing capabilities of intrinsically heated interleaved composites have been demonstrated.

6.4. Chapter summary

- It was postulated that using the layup proposed in [Section 6.1](#), a deployable composite structure can be produced. This structure was expected to have a flat shape when cured and deploy into a mesh when heated and subsequently cooled down.
- The numerical (FE) studies described in [Section 6.2](#) was useful to predict the shape of the deployed mesh depending on the variations in the proposed layup.
- The composite meshes capable of planar and curved deployment were manufactured and deployed, as described in [Section 6.3](#). A qualitative agreement was found between the numerically predicted and experimentally observed shapes of deployed composite meshes.

This page is intentionally left blank.

Chapter 7. Discussion, conclusions and suggestions for future work

7.1. Discussion

Through a detailed literature study, the state of the art of morphing composites was explored, and the morphing of interleaved composites was selected as topic of study in this thesis. Upon investigating previous research on interleaved composites, several potential improvements and propositions to achieve them were identified (see [Section 2.9](#)). It was determined that prevention of premature through-thickness shear failure of interleaved composites, improvement of their flexural modulus, and developing their out-of-oven morphing capabilities and further exploration of their capability to deploy from as-cured state were the valuable next steps in the development of interleaved composites for application within morphing aerostructures.

To prevent the premature failure in interleaved composites, the cause of failure was first identified. In previous research, when PS interleaved CFRP laminates were loaded in flexure, they underwent premature through thickness failure. However, the underlying reason behind such failure was not established. In this work, a similar experimental activity was performed to induce a similar failure, and the failure surfaces were analysed using XPS. This activity revealed the presence of PS on both the fracture surfaces, thereby indicating that the premature failure of the PS interleaved CFRP laminates was caused by the shear failure of the PS interleaf.

Consequently, to prevent such premature failure, alternative stronger interleaves were explored. Among the explored alternative interleaves, it was identified that replacing PS interleaves with SAN interleaves will enable the prevention of premature failure in the interleaved composites. Furthermore, the failure strength of SAN interleaved CFRP laminates were found to be comparable to that of pristine CFRP. The SAN interleaved CFRP laminates

also showed controllable stiffness (CS) and shape memory (SM) properties comparable to PS interleaved CFRP laminates.

To improve the apparent flexural modulus of the interleaved composites, two approaches were taken. In the first approach, the thickness of the interleaf layers was decreased, and in the second approach, reinforcements were introduced within the interleaves. Both of these approaches ensured that the overall fibre volume fraction (V_f) of the laminates increased.

When the thickness of the interleaves was decreased, the laminates showed an increase in apparent flexural modulus, as predicted using analytical tools. However, the laminates with the lowest interleaf thicknesses (around 35 μm) showed inconsistent CS and SM properties. Furthermore, the microsections of the laminates with low interleaf thicknesses revealed the presence of bridging of adjacent CFRP layers. It is hypothesised that the discontinuous CFRP bridging across different plies and laminates could prevent an effective slip between the CFRP plies, thereby affecting the CS and SM properties. To validate this hypothesis, a series of extensive numerical studies (FE based) can be performed by analysing the flexural properties of the interleaved composites with controlled bridging of the CFRP plies.

The addition of reinforcements within the previously unreinforced interleaves was also successful in increasing the apparent flexural modulus of the laminates. However, the achieved modulus was significantly lower than that of pristine CFRP laminates mainly due to the reinforced interleaves (RTP) having lower V_f than the CFRP laminae. By increasing the V_f in the RTPs, especially in the longitudinal direction, higher modulus can be achieved in the interleaved laminates. However, an increase in V_f within the RTP could decrease their shear deformation capabilities at elevated temperature, thereby decreasing the effectiveness of decoupling of adjacent CFRP. Consequently, it could affect morphing capabilities of the interleaved composites. Any study into the improvement of V_f in RTP for higher apparent flexural modulus of the interleaved composite should, therefore, also examine the shear deformation capabilities of the RTPs. Furthermore, the addition of reinforcements could also

allow generation of flexural stresses within the RTPs, making them potentially susceptible to flexural failure.

The morphing capabilities in the laminates in the experimental activities specified above relied on an oven for the necessary thermal energy. To bring these morphing capabilities out of laboratory and into real-world applications, resistive heater layers were embedded within the layup of the laminates. The laminates were then heated using direct current applied to the heaters, thereby achieving intrinsic heating. Through this method, out-of-oven morphing capabilities were successfully achieved.

In both oven-heated and intrinsically heated laminates, voids were seemed to develop within the interleaves after morphing. The oven-heated laminates showed no void formation from just heating the laminates, thereby indicating the absence of outgassing and thermal degradation. However, after extensive deformation in SM studies, voids were seen to develop within the interleaves. To further understand the reason behind the formation of the voids, a thermomechanical FE model capable of simulating the viscoelastic properties of the interleaves can be explored.

The intrinsically heated laminates, however, showed significantly more voids than the oven-heated laminates. One possible reason for this higher void generation could be thermal degradation. With the heat generation localised at their mid-thickness of the laminates and their polymeric layers effectively acting as thermal barriers, it is possible that the temperature within the laminates was significantly higher than that measured on the surface. Furthermore, the temperature measurement also relied on a bulky and exposed sensor, which could have provided inaccurate temperature readings. Future numerical and experimental studies can focus on modifying the location and distribution of the heaters within the layup to make the temperature distribution within the composite more uniform. A numerical or analytical model that could accurately predict the temperature distribution within the laminates (through intrinsic heating) would be valuable in these studies. Furthermore, as the resistance of heaters such as metallic meshes varies with temperature, one way to have better control over the

temperature of the laminate within the expected range could be through measurement of the resistance of such heaters in real-time and making necessary changes to the DC power supply in-situ.

The laminates in the above-mentioned studies were able to change their shape when they were deformed at an elevated temperature, and were able to retain the shape when cooled down to room temperature in the deformed shape. These laminates were then able to return to their original shapes upon reheating. Hence, the final shape of these laminates is governed by shape in which the laminates are cured. One way to achieve a complex deployed shape is therefore to cure the laminate in the deployed shape, re-shape it to a compact form at elevated temperature and subsequently deploy it back to the as-cured complex shape when required by raising its temperature again. However from a manufacturing perspective this is undesirable. Deployment of interleaved composites (changing from one shape to another) directly from as-cured state has received very little attention so far. Hence, in this work, simplified numerical studies were conducted to design a composite laminate that is flat when cured, but is capable of deployment into a planar or curved mesh when heated. Subsequently, the designed laminates were manufactured and successfully deployed. The deployment concept developed in this work allows the composite to change its shape only once without external actuation.

Once developed further, this deployment concept can potentially be used to produce (one-time) deployable space structures such as antenna, solar panels or solar sails. In their current stage of development, deployment temperature of these meshes could be considered too low for many aerospace structural applications. By producing interleaved composites that have only high-performance engineering thermoset and/or thermoplastic polymers as matrices, the deployment temperature of the composites can be increased so that they can be considered for deployable aerospace structures. In addition to the challenge with deployment temperature, the reason behind the formation of voids within the interleaves must be explored in detail and relevant mitigation strategies must be employed. Furthermore, as a next step,

the studies into deployable structures can move ahead from abstract designs such as flat coupons and meshes, and can focus on development of prototypes for real-world applications.

The morphing behaviour of the flat coupons described in early sections of this thesis, and of the deployable meshes in later sections of the thesis, is reliant of the stresses developed and stored within the CFRP plies. Within the scope of the work, it was expected that the stresses within the CFRP plies will be fully retained until the laminates are heated to allow change of shape. However, over a longer duration of time, the viscoelastic creep of the thermoplastic interleaves could cause the laminates to partially (or fully) undergo deployment even in the absence of high temperatures (Chevali, Dean and Janowski, 2009; Doan and Mertiny, 2020). Furthermore, when the composite laminates are stored in their pre-deployment state for extended durations of time, the CFRP plies can undergo stress relaxation that is governed by factors such as the viscoelastic properties, storage temperature and moisture content (Arao *et al.*, 2010; Brinkmeyer *et al.*, 2016; Ornaghi *et al.*, 2020). Such stress relaxation can reduce the effectiveness of deployment, with the final deployed shape varying from the designed shape. Hence, the design of deployable structures should also take such time and atmosphere dependant parameters into account.

7.2. Conclusions

From the studies conducted in this research work, the following conclusions are drawn:

- (i) Premature through-thickness shear failure observed in 3-point bending (3PB) tests of PS-interleaved CFRP composites occurs within PS interleaf due to its shear failure.
- (ii) Replacing PS interleaves with SAN interleaves improves the through-thickness shear strength of a thermoplastic (TP) interleaved CFRP composite. When loaded in flexure, the SAN interleaved laminates have failure strength comparable to that of pristine CFRP..
- (iii) Reducing the thickness of the interleaves causes the flexural modulus of the TP interleaved CFRP composites to increase. By reducing the thickness of interleaves from

around 174 μm to around 33 μm , the flexural modulus of the TP interleaved CFRP composites increased from around 64 GPa to around 109 GPa (a 70% increase).

- (iv) Reinforcing the TP interleaves causes the flexural modulus of the interleaved CFRP composites to increase. Interleaved laminates with reinforced interleaves showed more than 25% higher flexural modulus compared to those with unreinforced interleaves.
- (v) Intrinsic heating capability can be achieved in interleaved composites by the embedding stainless steel or woven carbon fabric heater layers within some of their interleaves and heating them using applied direct current.
- (vi) A composite structure that is flat in its as-cured shape and can deploy into a planar or curved mesh upon heating was produced to demonstrate the scope of morphing capabilities of the TP interleaved composites.

7.3. Suggestions for future work

Based on the observations from various studies performed in this research work, and their critical analysis, several avenues for future studies can be identified. One of the important challenges to address is the development of voids within the interleaves of the deployable interleaved composites. While some speculations have been made regarding the reasons behind the development of voids, no definitive reasons have been identified yet. Identifying the reasons behind the formation of voids and finding opportunities to mitigate them is vital in reducing the deterioration of the interleaved composites undergoing deployment.

While reduction of thickness interleaves has been useful in increasing the apparent flexural modulus of the laminates, further improvements to ensure repeatable morphing capabilities in laminates with thin interleaves can be explored. Furthermore, some of the specimens with very low interleaf thicknesses showed an unexpected increase in their flexural strength. The reason behind such a high flexural strength remains unknown and could be investigated further to identify and exploit the phenomenon to achieve high failure strength in composites.

The addition of reinforcements within the interleaves have also been useful in increasing the apparent flexural modulus of the laminates. Future work can explore achieving an even higher flexural modulus by increasing the V_f of the interleaves in the longitudinal direction. It can be expected that the increase of V_f within the interleaves could decrease their morphing capabilities. Hence, the morphing capabilities of these laminates should also be explored in parallel to increasing the V_f in the interleaves.

The laminates with successful out-of-oven morphing capabilities developed in this work showed probable signs of thermal degradation. Hence, studies into modifying the location and distribution of the heaters within the laminates can be useful in achieving a more uniform temperature distribution within them. Furthermore, a resistance-based temperature sensing and in-situ DC power control can also be used to avoid thermal degradation within the laminates.

The simplified numerical model developed to predict the shape of the deployable meshes in this work relies on several assumptions such as the deployment phenomenon being quasi-static, and the interleaves having partially temperature-independent elastic properties and no viscous properties. A more detailed numerical model that is capable of modelling the temperature-dependent viscoelastic properties of the interleaves could be developed to model the morphing capabilities of interleaved composites with higher accuracy. By improving the numerical model, the deployment duration and the final shape of the deployed structure can be predicted with even better certainty.

This page is intentionally left blank.

References

- Ageorges, C., Ye, L. and Hou, M. (2000a) 'Experimental investigation of the resistance welding for thermoplastic-matrix composites. Part I: heating element and heat transfer', *Composites Science and Technology*, 60(7), pp. 1027–1039. Available at: [https://doi.org/10.1016/S0266-3538\(00\)00005-1](https://doi.org/10.1016/S0266-3538(00)00005-1).
- Ageorges, C., Ye, L. and Hou, M. (2000b) 'Experimental investigation of the resistance welding of thermoplastic-matrix composites. Part II: optimum processing window and mechanical performance', *Composites Science and Technology*, 60(8), pp. 1191–1202. Available at: [https://doi.org/10.1016/S0266-3538\(00\)00025-7](https://doi.org/10.1016/S0266-3538(00)00025-7).
- Airoldi, A. *et al.* (2017) 'Design and manufacturing of skins based on composite corrugated laminates for morphing aerodynamic surfaces', *Smart Materials and Structures*, 26(4). Available at: <https://doi.org/10.1088/1361-665X/aa6069>.
- Ajaj, R.M. *et al.* (2014) 'An integrated conceptual design study using span morphing technology', *Journal of Intelligent Material Systems and Structures*, 25(8), pp. 989–1008. Available at: <https://doi.org/10.1177/1045389X13502869>.
- Ajaj, R.M. *et al.* (2016) 'Span morphing using the GNATSpar wing', *Aerospace Science and Technology*, 53, pp. 38–46. Available at: <https://doi.org/10.1016/j.ast.2016.03.009>.
- Ajaj, R.M. *et al.* (2021) 'Recent developments in the aeroelasticity of morphing aircraft', *Progress in Aerospace Sciences*, 120, p. 100682. Available at: <https://doi.org/10.1016/J.PAEROSCI.2020.100682>.
- Ajaj, R.M., Beaverstock, C.S. and Friswell, M.I. (2016a) 'Morphing aircraft: The need for a new design philosophy', *Aerospace Science and Technology*, 49, pp. 154–166. Available at: <https://doi.org/10.1016/j.ast.2015.11.039>.
- Ajaj, R.M., Beaverstock, C.S. and Friswell, M.I. (2016b) 'Morphing aircraft: The need for a new design philosophy', *Aerospace Science and Technology*, 49, pp. 154–166. Available at:

<https://doi.org/10.1016/J.AST.2015.11.039>.

Ajaj, R.M., Beaverstock, C.S. and Friswell, M.I. (2016c) 'Morphing aircraft: The need for a new design philosophy', *Aerospace Science and Technology*, 49, pp. 154–166. Available at: <https://doi.org/10.1016/j.ast.2015.11.039>.

Ajaj, R.M., Bouchak, M. and Friswell, M.I. (2014) 'Span morphing using the GNAT spar for a mini-UAV: designing and testing', in *4th RAeS Aircraft Structural Design Conference*.

De Almeida, O., Bessard, E. and Bernhart, G. (2012) 'Influence of processing parameters and semi-finished product on consolidation of carbon/peek laminates', in *ECCM15 - 15TH European Conference On Composite Materials, Venice, Italy, 24-28 June*.

American Chemical Society, A. (2021) *High-energy shape memory polymer could someday help robots flex their muscles*. Available at: <https://www.acs.org/content/acs/en/pressroom/newsreleases/2021/september/high-energy-shape-memory-polymer-could-someday-help-robots-flex-their-muscles.html> (Accessed: 10 June 2022).

Andersen, G., Cowan, D. and Piatak, D. (2007) 'Aeroelastic Modeling, Analysis and Testing of a Morphing Wing Structure', in *48th AIAA/ASME/ASCE/AHS/ASC Structures, Structural Dynamics, and Materials Conference*. Honolulu, Hawaii. Available at: <https://doi.org/10.2514/6.2007-1734>.

Angel, G.D. and Haritos, G. (2013) 'An Immediate Formula for the Radius of Curvature of A Bimetallic Strip', *International Journal of Engineering Research & Technology (IJERT)*, 2(12), pp. 1312–1319. Available at: www.ijert.org (Accessed: 13 June 2022).

Arao, Y. *et al.* (2010) 'Residual Stress Relaxation in CFRP Cross-ply Laminate', *Journal of Solid Mechanics and Materials Engineering*, 4(11), pp. 1595–1604. Available at: <https://doi.org/10.1299/jmmp.4.1595>.

Arrieta, A.F. *et al.* (2012) 'Dynamic response modelling and aerodynamic study for a

piezoelectric cantilevered Bi-stable composite', in *23rd International Conference on Adaptive Structures and Technologies, ICAST 2012*.

Arzberger, S.C. *et al.* (2005) 'Elastic memory composites (EMC) for deployable industrial and commercial applications', in *Smart Structures and Materials 2005: Industrial and Commercial Applications of Smart Structures Technologies*, pp. 35–47. Available at: <https://doi.org/10.1117/12.600583>.

Asanuma, H., Haga, O. and Imori, M. (2006) 'Development of High Performance CFRP/Metal Active Laminates', *JSME International Journal Series A*, 49(1), pp. 32–37. Available at: <https://doi.org/10.1299/jsmea.49.32>.

Atique, M.S.A., Probha, N.N. and Nafi, A.S. (2014) 'Polymer composites : a blessing to modern aerospace engineering', *International Conference on Mechanical, Industrial and Energy Engineering 2014* [Preprint].

Baier, H. and Datashvili, L. (2011) 'Active and morphing aerospace structures-a synthesis between advanced materials, structures and mechanisms', *International Journal of Aeronautical and Space Sciences*, 12(3), pp. 225–240. Available at: <https://doi.org/10.5139/IJASS.2011.12.3.225>.

Bañón, F. *et al.* (2020) 'On the surface quality of cfrtp/steel hybrid structures machined by AWJM', *Metals*, 10(7), pp. 1–21. Available at: <https://doi.org/10.3390/MET10070983>.

Bañón, F. *et al.* (2021) 'Evaluation of geometrical defects in AWJM process of a hybrid CFRTP/Steel structure', *International Journal of Mechanical Sciences*, 210. Available at: <https://doi.org/10.1016/j.ijmecsci.2021.106748>.

Barbarino, S. *et al.* (2011) 'A Review of Morphing Aircraft', *Journal of Intelligent Material Systems and Structures*, 22(9), pp. 823–877. Available at: <https://doi.org/10.1177/1045389X11414084>.

Barrett, R. and Gross, R.S. (1996) 'Super-active shape-memory alloy composites', *Smart*

- Materials and Structures*, 5, pp. 255–260. Available at: <https://doi.org/10.1088/0964-1726/5/3/003>.
- Barvosa-Carter, W. and McKnight, G. (2011) 'Variable stiffness structure', *US Patent* 7,892,630 [Preprint]. Available at: <https://patents.google.com/patent/US7892630B1/en> (Accessed: 2 April 2019).
- Beamson, G. and Briggs, D. (1993) 'High Resolution XPS of Organic Polymers: The Scienta ESCA300 Database (Beamson, G.; Briggs, D.)', *Journal of Chemical Education*, 70(1), p. A25. Available at: <https://doi.org/10.1021/ed070pA25.5>.
- Bergamini, A. *et al.* (2006) 'A sandwich beam with electrostatically tunable bending stiffness', *Smart Materials and Structures*, 15, pp. 678–686. Available at: <https://doi.org/10.1088/0964-1726/15/3/002>.
- Bergamini, A., Christen, R. and Motavalli, M. (2005) 'Electrostatic tuning of the bending stiffness of simple slender multilayer composite structures', in K.-W. Wang (ed.) *Smart Structures and Materials 2005: Damping and Isolation*, pp. 152–163. Available at: <https://doi.org/10.1117/12.598748>.
- Bergamini, A., Christen, R. and Motavalli, M. (2007) 'Electrostatically tunable bending stiffness in a GFRP-CFRP composite beam', *Smart Materials and Structures*, 16, pp. 575–582. Available at: <https://doi.org/10.1088/0964-1726/16/3/004>.
- Bernet, N. *et al.* (1999) 'An Impregnation Model for the Consolidation of Thermoplastic Composites Made from Commingled Yarns', *Journal of Composite Materials*, 33(8), pp. 751–772. Available at: <https://doi.org/10.1177/002199839903300806>.
- Bezazi, A., Boukharouba, W. and Scarpa, F. (2009) 'Mechanical properties of auxetic carbon/epoxy composites: Static and cyclic fatigue behaviour', *Physica Status Solidi (B) Basic Research*, 246(9), pp. 2102–2110. Available at: <https://doi.org/10.1002/pssb.200982042>.

- Bigg, D.M. *et al.* (1988) 'Thermoplastic matrix sheet composites', *Polymer Composites*, 9(3), pp. 222–228. Available at: <https://doi.org/10.1002/PC.750090309>.
- Bishay, P.L. *et al.* (2019) 'Development of a New Span-Morphing Wing Core Design', *Designs 2019*, Vol. 3, Page 12, 3(1), p. 12. Available at: <https://doi.org/10.3390/DESIGNS3010012>.
- Blackman, B. and Kinloch, A. (2001) 'Fracture tests on structural adhesive joints', in *European Structural Integrity Society*, pp. 225–267. Available at: [https://doi.org/10.1016/S1566-1369\(01\)80036-4](https://doi.org/10.1016/S1566-1369(01)80036-4).
- Bowen, C.R. *et al.* (2007) 'Morphing and shape control using unsymmetrical composites', *Journal of Intelligent Material Systems and Structures*, 18(1), pp. 89–98. Available at: <https://doi.org/10.1177/1045389X07064459>.
- Brampton, C.J. *et al.* (2014) 'Actuation of Bistable Laminates by Conductive Polymer Nanocomposites for use in Thermal-Mechanical Aerosurface De-icing Systems', in *55th AIAA/ASME/ASCE/AHS/SC Structures, Structural Dynamics, and Materials Conference*. Available at: <https://doi.org/10.2514/6.2014-0105>.
- Brassard, D., Dubé, M. and Tavares, J.R. (2019) 'Resistance welding of thermoplastic composites with a nanocomposite heating element', *Composites Part B: Engineering*, 165, pp. 779–784. Available at: <https://doi.org/10.1016/j.compositesb.2019.02.038>.
- Brinkmeyer, A. *et al.* (2016) 'Effects of Long-Term Stowage on the Deployment of Bistable Tape Springs'. Available at: <https://doi.org/10.1115/1.4031618>.
- Buschhorn, S.T. *et al.* (2013) 'Electrothermal Icing protection of Aerosurfaces Using Conductive Polymer Nanocomposites', in *Collection of Technical Papers - AIAA/ASME/ASCE/AHS/ASC Structures, Structural Dynamics and Materials Conference*. Available at: <https://doi.org/10.2514/6.2013-1729>.
- Byström, J., Jekabsons, N. and Varna, J. (2000) 'Evaluation of different models for prediction

of elastic properties of woven composites', *Composites Part B: Engineering*, 31(1), pp. 7–20. Available at: [https://doi.org/10.1016/S1359-8368\(99\)00061-X](https://doi.org/10.1016/S1359-8368(99)00061-X).

Chang, I.Y. and Lees, J.K. (1988) 'Recent Development in Thermoplastic Composites: A Review of Matrix Systems and Processing Methods', *Journal of Thermoplastic Composite Materials*, 1(3), pp. 277–296. Available at: <https://doi.org/10.1177/089270578800100305>.

Chen, Y. *et al.* (2012) 'Variable stiffness property study on shape memory polymer composite tube', *Smart Materials and Structures*, 21(9), p. 094021. Available at: <https://doi.org/10.1088/0964-1726/21/9/094021>.

Chevali, V.S., Dean, D.R. and Janowski, G.M. (2009) 'Flexural creep behavior of discontinuous thermoplastic composites: Non-linear viscoelastic modeling and time–temperature–stress superposition', *Composites Part A: Applied Science and Manufacturing*, 40(6–7), pp. 870–877. Available at: <https://doi.org/10.1016/J.COMPOSITESA.2009.04.012>.

Chillara, V.S.C. and Dapino, M.J. (2017) 'Mechanically-prestressed bistable composite laminates with weakly coupled equilibrium shapes', *Composites Part B: Engineering*, 111, pp. 251–260. Available at: <https://doi.org/10.1016/j.compositesb.2016.12.011>.

Chillara, V.S.C. and Dapino, M.J. (2019) 'Bistable laminates with non-cylindrical curved shapes', *Composite Structures*, 230, p. 111502. Available at: <https://doi.org/10.1016/j.compstruct.2019.111502>.

Cho, M. and Kim, S. (2005) 'Structural morphing using two-way shape memory effect of SMA', *International Journal of Solids and Structures*, 42(5–6), pp. 1759–1776. Available at: <https://doi.org/10.1016/j.ijsolstr.2004.07.010>.

Choi, S. and Lee, J.J. (1998) 'The shape control of a composite beam with embedded shape memory alloy wire actuators', *Smart Materials and Structures*, 7(6), pp. 759–770. Available at: <https://doi.org/10.1088/0964-1726/7/6/004>.

Chu, L. *et al.* (2022) 'Design, modeling, and control of morphing aircraft: A review', *Chinese*

Journal of Aeronautics, 35(5), pp. 220–246. Available at:

<https://doi.org/10.1016/J.CJA.2021.09.013>.

Ciba-Geigy Plastics (1989) *Fiberdux 914 High temperature resistant unidirectional prepregs (Information Sheet No. FTA 49f)*. Cambridge.

Cumming, S.B. *et al.* (2016) 'Aerodynamic flight-test results for the adaptive compliant trailing edge', in *AIAA Atmospheric Flight Mechanics Conference*. American Institute of Aeronautics and Astronautics Inc. Available at: <https://doi.org/10.2514/6.2016-3855>.

Dano, M.L. and Hyer, M.W. (2003) 'SMA-induced snap-through of unsymmetric fiber-reinforced composite laminates', *International Journal of Solids and Structures*, 40(22), pp. 5949–5972. Available at: [https://doi.org/10.1016/S0020-7683\(03\)00374-3](https://doi.org/10.1016/S0020-7683(03)00374-3).

Daynes, S. *et al.* (2010) 'Bistable prestressed symmetric laminates', *Journal of Composite Materials*, 44(9), pp. 1119–1137. Available at: <https://doi.org/10.1177/0021998309351603>.

Daynes, S. and Weaver, P.M. (2013) 'Review of shape-morphing automobile structures: Concepts and outlook', *Proceedings of the Institution of Mechanical Engineers, Part D: Journal of Automobile Engineering*, pp. 1603–1622. Available at: <https://doi.org/10.1177/0954407013496557>.

Dayyani, I. *et al.* (2015) 'The mechanics of composite corrugated structures: A review with applications in morphing aircraft', *Composite Structures*. Elsevier, pp. 358–380. Available at: <https://doi.org/10.1016/j.compstruct.2015.07.099>.

Deplante, H. (1969) 'The Dassault Mirage G', *The Aeronautical Journal*, 73(708), pp. 1027–1028. Available at: <https://doi.org/10.1017/S0001924000051162>.

Diaconu, C.G., Weaver, P.M. and Mattioni, F. (2008) 'Concepts for morphing airfoil sections using bi-stable laminated composite structures', *Thin-Walled Structures*, 46(6), pp. 689–701. Available at: <https://doi.org/10.1016/j.tws.2007.11.002>.

Doan, H.G.M. and Mertiny, P. (2020) 'Creep Testing of Thermoplastic Fiber-Reinforced

- Polymer Composite Tubular Coupons', *Materials*, 13(20), pp. 1–17. Available at: <https://doi.org/10.3390/MA13204637>.
- Donadon, M.V. and Iannucci, L. (2014) 'A Numerical Study on Smart Material Selection for Flapped and Twisted Morphing Wing Configurations', *Journal of Aerospace Technology and Management*, 6(3), pp. 281–290. Available at: <https://doi.org/10.5028/jatm.v6i3.341>.
- Dubé, M. *et al.* (2011) 'Metal mesh heating element size effect in resistance welding of thermoplastic composites', *Journal of Composite Materials*, 46(8), pp. 911–919. Available at: <https://doi.org/10.1177/0021998311412986>.
- Easy Composites Ltd (no date) *90g Plain Weave 1k Carbon Fibre Cloth (CF-PL-90-100)*. Available at: <https://www.easycomposites.co.uk/90g-plain-weave-1k-carbon-fibre-cloth> (Accessed: 11 March 2022).
- Eckstein, E., Halbig, M.C. and Weaver, P. (2016) 'Thermally-Driven Morphing with High Temperature Composites', in *57th AIAA/ASCE/AHS/ASC Structures, Structural Dynamics, and Materials Conference*. Reston, Virginia: American Institute of Aeronautics and Astronautics. Available at: <https://doi.org/10.2514/6.2016-1241>.
- Eckstein, E., Pirrera, A. and Weaver, P.M. (2014) 'Multi-mode morphing using initially curved composite plates', *Composite Structures*, 109(1), pp. 240–245. Available at: <https://doi.org/10.1016/j.compstruct.2013.11.005>.
- Ermakova, A. and Dayyani, I. (2017) 'Shape optimisation of composite corrugated morphing skins', *Composites Part B: Engineering*, 115, pp. 87–101. Available at: <https://doi.org/10.1016/j.compositesb.2016.10.029>.
- Filippo Mattioni, Paul M Weaver, Kevin Potter, M.I.F. (2005) 'Multi-stable composites application concept for morphing aircraft', in *Sixteenth International Conference on Adaptive Structure and Technologies*. Paris, pp. 45–52.
- Francis, W. *et al.* (2003) 'Development and Testing of a Hinge/Actuator Using Elastic

- Memory Composites', in *44th AIAA/ASME/ASCE/AHS/ASC Structures, Structural Dynamics, and Materials Conference*. Reston, Virginia: American Institute of Aeronautics and Astronautics. Available at: <https://doi.org/10.2514/6.2003-1496>.
- Friswell, M.I. (2014) 'Morphing Aircraft : An Improbable Dream?', in *Proceedings of the ASME 2014 Conference on Smart Materials, Adaptive Structures and Intelligent Systems*. Available at: <https://doi.org/10.1115/SMASIS20147754>.
- Gall, K. *et al.* (2000) 'Carbon Fiber Reinforced Shape Memory Polymer Composites', *Journal of Intelligent Material Systems and Structures*, 11(11), pp. 877–886. Available at: <https://doi.org/10.1106/EJGR-EWNM-6CLX-3X2M>.
- Gandhi, F. and Kang, S.-G. (2007) 'Beams with controllable flexural stiffness', *Smart Materials and Structures*, 16(4), pp. 1179–1184. Available at: <https://doi.org/10.1088/0964-1726/16/4/028>.
- Gibson, A.G. and Manson, J.-A. (1992) 'Impregnation technology for thermoplastic matrix composites', *Composites Manufacturing*, 3(4), pp. 223–233. Available at: [https://doi.org/10.1016/0956-7143\(92\)90110-G](https://doi.org/10.1016/0956-7143(92)90110-G).
- Gordon, B. and Clark, W. (2007) 'Morphing Structures by way of Stiffness Variations', in *48th AIAA/ASME/ASCE/AHS/ASC Structures, Structural Dynamics, and Materials Conference*. Reston, Virginia: American Institute of Aeronautics and Astronautics. Available at: <https://doi.org/10.2514/6.2007-1717>.
- Grouve, W.J.B. and Akkerman, R. (2010) 'Consolidation process model for film stacking glass/PPS laminates', *Plastics, Rubber and Composites*, 39(3–5), pp. 208–215. Available at: <https://doi.org/10.1179/174328910X12647080902457>.
- Gude, M., Hufenbach, W. and Kirvel, C. (2011) 'Piezoelectrically driven morphing structures based on bistable unsymmetric laminates', *Composite Structures*, 93(2), pp. 377–382. Available at: <https://doi.org/10.1016/j.compstruct.2010.09.004>.

Han, M.-W. *et al.* (2016) 'Shape memory alloy/glass fiber woven composite for soft morphing winglets of unmanned aerial vehicles', *Composite Structures*, 140, pp. 202–212. Available at: <https://doi.org/10.1016/j.compstruct.2015.12.051>.

Harrison, J.S. *et al.* (1998) 'Innovative materials for aircraft morphing', in *5th Annual International Symposium on Smart Structures and Materials*, p. 240. Available at: <https://doi.org/10.1117/12.310639>.

Herath, H.M.C.M. *et al.* (2018) 'Structural performance and photothermal recovery of carbon fibre reinforced shape memory polymer', *Composites Science and Technology*, 167, pp. 206–214. Available at: <https://doi.org/10.1016/J.COMPSCITECH.2018.07.042>.

Huang, T. *et al.* (2020) 'Experimental and Numerical Simulation Studies of Failure Behaviour of Carbon Fibre Reinforced Aluminium Laminates under Transverse Local Quasi-static Loading', *Journal of Physics: Conference Series*, 1624(2), p. 022042. Available at: <https://doi.org/10.1088/1742-6596/1624/2/022042>.

Humphreys, F.E. (1910) 'The Wright Flyer and its Possible Uses in War', *Professional Memoirs, Corps of Engineers, United States Army, and Engineer Department at Large*, 2(5), pp. 99–107.

Hyer, M.W. (1981) 'Calculations of the Room-Temperature Shapes of Unsymmetric Laminates', *Composite Materials*, 15(4), pp. 296–310. Available at: <https://doi.org/10.1177/002199838101500401>.

James, T. *et al.* (2009) 'Morphing Skins: Development of New Hybrid Materials', in *Proceedings of the 4th SEAS DTC Technical Conference*. Edinburgh, UK. Available at: https://www.researchgate.net/publication/237709485_Morphing_Skins_Development_of_New_Hybrid_Materials (Accessed: 9 June 2022).

Jeon, S.J., Hauser, A.W. and Hayward, R.C. (2017) 'Shape-Morphing Materials from Stimuli-Responsive Hydrogel Hybrids', *Accounts of Chemical Research*, 50(2), pp. 161–169.

Available at: <https://doi.org/10.1021/acs.accounts.6b00570>.

Jeon, S.K. and Murphey, T.W. (2011) 'Design and analysis of a meter-class CubeSat boom with a motor-less deployment by bi-stable tape springs', *Collection of Technical Papers - AIAA/ASME/ASCE/AHS/ASC Structures, Structural Dynamics and Materials Conference* [Preprint]. Available at: <https://doi.org/10.2514/6.2011-1731>.

Jones, R.M. (1999) *Mechanics of Composites Materials*. Taylor & Francis. Available at: <https://www.routledge.com/Mechanics-Of-Composite-Materials/Jones/p/book/9781560327127> (Accessed: 9 June 2022).

Kadiyala, A.K. *et al.* (2022) 'Evaluation of the flexural properties and failure evolution of a hybrid composite manufactured by automated dry fibre placement followed by liquid resin infusion', *Composites Part A: Applied Science and Manufacturing*, 154, p. 106764. Available at: <https://doi.org/10.1016/J.COMPOSITESA.2021.106764>.

Kanzleiter, T. (2018) *FE investigation of interleaved composites for controllable stiffness and morphing capabilities (Masters thesis)*. Imperial College London.

Kesarwani, S. (2017) 'Polymer Composites in Aviation Sector A Brief Review Article', *IJERT*, 6(6), pp. 518–525. Available at: www.ijert.org (Accessed: 24 October 2019).

Khani Aminjan, K. *et al.* (2023) 'Numerical and experimental investigation to design a novel morphing airfoil for performance optimization', *Propulsion and Power Research*, 12(1), pp. 83–103. Available at: <https://doi.org/10.1016/J.JPPR.2023.02.004>.

Khurshid, M.F. *et al.* (2019) 'Recent developments in the processing of waste carbon fibre for thermoplastic composites – A review', *Journal of Composite Materials*. SAGE Publications Ltd, p. 002199831988604. Available at: <https://doi.org/10.1177/0021998319886043>.

Kim, M.S. *et al.* (2011) 'Manufacturing of inchworm robot using shape memory alloy (SMA) embedded composite structure', *International Journal of Precision Engineering and*

Manufacturing, 12(3), pp. 565–568. Available at: <https://doi.org/10.1007/s12541-011-0071-2>.

Kishi, H. *et al.* (2017) 'Carbon fiber reinforced thermoplastic composites from acrylic polymer matrices: Interfacial adhesion and physical properties', *Express Polymer Letters*, 11(4), pp. 334–342. Available at: <https://doi.org/10.3144/expresspolymlett.2017.32>.

Kota, S., Flick, P. and Collier, F. (2016) 'Flight testing of the FlexFloil™ adaptive compliant trailing edge', in *54th AIAA Aerospace Sciences Meeting*. Reston, Virginia: American Institute of Aeronautics and Astronautics. Available at: <https://doi.org/10.2514/6.2016-0036>.

Kuder, I.K. *et al.* (2013) 'Variable stiffness material and structural concepts for morphing applications', *Progress in Aerospace Sciences*, 63, pp. 33–55. Available at: <https://doi.org/10.1016/j.paerosci.2013.07.001>.

Kuder, I.K. *et al.* (2016) 'Aeroelastic response of a selectively compliant morphing aerofoil featuring integrated variable stiffness bi-stable laminates', *Journal of Intelligent Material Systems and Structures*, 27(14), pp. 1949–1966. Available at: <https://doi.org/10.1177/1045389X15620038>.

Kudva, J.N. (2004) 'Overview of the DARPA smart wing project', *Journal of Intelligent Material Systems and Structures*, pp. 261–267. Available at: <https://doi.org/10.1177/1045389X04042796>.

Lan, X., Liu, Y., *et al.* (2009) 'Fiber reinforced shape-memory polymer composite and its application in a deployable hinge', *Smart Materials and Structures*, 18(2). Available at: <https://doi.org/10.1088/0964-1726/18/2/024002>.

Lan, X., Wang, X., *et al.* (2009) 'Shape recovery performances of a deployable hinge fabricated by fiber-reinforced shape-memory polymer', in Z. Ounaies and J. Li (eds) *Behavior and Mechanics of Multifunctional Materials and Composites*. International Society for Optics and Photonics. Available at: <https://doi.org/10.1117/12.815715>.

Le, V.L., Le, V.T. and Goo, N.S. (2019) 'Deployment performance of shape memory polymer

- composite hinges at low temperature', *Journal of Intelligent Material Systems and Structures*, 30(17), pp. 2625–2638. Available at: <https://doi.org/10.1177/1045389X19873403>.
- Lee, J.G. *et al.* (2015) 'Effect of initial tool-plate curvature on snap-through load of unsymmetric laminated cross-ply bistable composites', *Composite Structures*, 122, pp. 82–91. Available at: <https://doi.org/10.1016/J.COMPSTRUCT.2014.11.037>.
- Lee, S.H. and Waas, A.M. (1999) 'Compressive response and failure of fiber reinforced unidirectional composites', *International Journal of Fracture* 1999 100:3, 100(3), pp. 275–306. Available at: <https://doi.org/10.1023/A:1018779307931>.
- Leng, J. *et al.* (2011) 'Shape-memory polymers and their composites: Stimulus methods and applications', *Progress in Materials Science*, 56(7), pp. 1077–1135. Available at: <https://doi.org/10.1016/j.pmatsci.2011.03.001>.
- Li, H., Dai, F. and Du, S. (2012) 'Numerical and experimental study on morphing bi-stable composite laminates actuated by a heating method', *Composites Science and Technology*, 72(14), pp. 1767–1773. Available at: <https://doi.org/10.1016/j.compscitech.2012.07.015>.
- Li, J. and Cai, C.L. (2011) 'The carbon fiber surface treatment and addition of PA6 on tensile properties of ABS composites', *Current Applied Physics*, 11(1), pp. 50–54. Available at: <https://doi.org/10.1016/j.cap.2010.06.017>.
- Li, J. and Sun, F.F. (2009a) 'The effect of maleic anhydride graft on the interfacial adhesion of carbon fiber reinforced thermoplastic polystyrene composite', *Journal of Composite Materials*, 43(23), pp. 2717–2725. Available at: <https://doi.org/10.1177/0021998309345338>.
- Li, J. and Sun, F.F. (2009b) 'The effect of nitric acid oxidization treatment on the interface of carbon fiber-reinforced thermoplastic polystyrene composite', *Polymer - Plastics Technology and Engineering*, 48(7), pp. 711–715. Available at: <https://doi.org/10.1080/03602550902824580>.

- Li, J. and Zhou, Z. (2010) 'The TPB properties of plasma-treated carbon fiber-reinforced polystyrene composites', *Polymer - Plastics Technology and Engineering*, 49(1), pp. 20–23. Available at: <https://doi.org/10.1080/03602550903283000>.
- Li, Z.H. and Chen, T. (2012) 'Mechanical behavior of polystyrene-grafted carbon nanotubes on carbon fiber/polystyrene composites', *Mechanics of Composite Materials*, 48(2), pp. 235–240. Available at: <https://doi.org/10.1007/s11029-012-9269-3>.
- Liang, X. *et al.* (2000) 'Resistivity of carbon fibers/ABS resin composites', *Materials Letters*, 43(3), pp. 144–147. Available at: [https://doi.org/10.1016/S0167-577X\(99\)00247-5](https://doi.org/10.1016/S0167-577X(99)00247-5).
- Di Lillo, L. *et al.* (2011) 'Quasi-static electric properties of insulating polymers at a high voltage for electro-bonded laminates', *Smart Materials and Structures*, 20. Available at: <https://doi.org/10.1088/0964-1726/20/5/057002>.
- Liu, B. *et al.* (2018) 'On thermomechanical behaviors of the functional graded shape memory alloy composite for jet engine chevron':, *Journal of Intelligent Material Systems and Structures*, 29(14), pp. 2986–3005. Available at: <https://doi.org/10.1177/1045389X18781257>.
- Liu, Y. *et al.* (2014) 'Shape memory polymers and their composites in aerospace applications: A review', *Smart Materials and Structures*, 23(2), p. 023001. Available at: <https://doi.org/10.1088/0964-1726/23/2/023001>.
- Lu, M., Ye, L. and Mai, Y.W. (2004) 'Thermal de-consolidation of thermoplastic matrix composites—II. "Migration" of voids and "re-consolidation"', *Composites Science and Technology*, 64(2), pp. 191–202. Available at: [https://doi.org/10.1016/S0266-3538\(03\)00233-1](https://doi.org/10.1016/S0266-3538(03)00233-1).
- Lustiger, A. and Jang, B.Z. (1992) 'Advanced thermoplastic composites', *Polymer Composites*, pp. 413–413. Available at: <https://doi.org/10.1002/pc.750130602>.
- Mabe, J. (2008) 'Variable area jet nozzle for noise reduction using shape memory alloy

actuators', *The Journal of the Acoustical Society of America*, 123(5), pp. 3871–3871.

Available at: <https://doi.org/10.1121/1.2935758>.

Mallon, P.J., O'Brádaigh, C.M. and Pipes, R.B. (1989) 'Polymeric diaphragm forming of complex-curvature thermoplastic composite parts', *Composites*, 20(1), pp. 48–56. Available at: [https://doi.org/10.1016/0010-4361\(89\)90682-4](https://doi.org/10.1016/0010-4361(89)90682-4).

Maples, H. (2014) *Composites with Controllable Stiffness*. Imperial College London.

Available at: [https://spiral.imperial.ac.uk/bitstream/10044/1/24670/1/H Maples PhD thesis_7-4-14.pdf](https://spiral.imperial.ac.uk/bitstream/10044/1/24670/1/H%20Maples%20PhD%20thesis_7-4-14.pdf) (Accessed: 11 October 2018).

Maples, H.A. *et al.* (2014) 'High performance carbon fibre reinforced epoxy composites with controllable stiffness', *Composites Science and Technology*, 105, pp. 134–143. Available at: <https://doi.org/10.1016/j.compscitech.2014.09.008>.

Maples, H.A. *et al.* (2016) 'Improving the ply/interleaf interface in carbon fibre reinforced composites with variable stiffness', *Composites Science and Technology*, 128, pp. 185–192. Available at: <https://doi.org/10.1016/j.compscitech.2016.03.028>.

Marszałek, J. (2022) 'Span length effect on flexural properties of composite laminate reinforced with a plain weave carbon fiber fabric in a polymer matrix', *Science and Engineering of Composite Materials*, 29(1), pp. 322–334. Available at: <https://doi.org/10.1515/SECM-2022-0155/MACHINEREADABLECITATION/RIS>.

Matthews, F.L. and Rawlings, R.D. (1999) *Composite Materials: Engineering and Science*. CRC Press. Available at:

https://www.google.co.uk/books/edition/Composite_Materials/0p4I5VRJmrsC?hl=en&gbpv=0 (Accessed: 9 June 2022).

Mattioni, F. *et al.* (2008a) 'Analysis of thermally induced multistable composites', *International Journal of Solids and Structures*, 45(2), pp. 657–675. Available at: <https://doi.org/10.1016/j.ijsolstr.2007.08.031>.

- Mattioni, F. *et al.* (2008b) 'The application of thermally induced multistable composites to morphing aircraft structures', in L.P. Davis, B.K. Henderson, and M.B. McMickell (eds) *Industrial and Commercial Applications of Smart Structures Technologies 2008*. International Society for Optics and Photonics, p. 693012. Available at: <https://doi.org/10.1117/12.776226>.
- McKnight, G. *et al.* (2010) 'Segmented Reinforcement Variable Stiffness Materials for Reconfigurable Surfaces', *Journal of Intelligent Material Systems and Structures*, 21(17), pp. 1783–1793. Available at: <https://doi.org/10.1177/1045389X10386399>.
- McKnight, G. *et al.* (2007) 'Bill Armstrong memorial session: elastic modulus and strain recovery testing of variable stiffness composites for structural reconfiguration applications', in M.J. Dapino (ed.) *Behavior and Mechanics of Multifunctional and Composite Materials 2007*, p. 652617. Available at: <https://doi.org/10.1117/12.717287>.
- McKnight, G. and Henry, C. (2005) 'Variable stiffness materials for reconfigurable surface applications', in W.D. Armstrong (ed.) *Smart Structures and Materials 2005: Active Materials: Behavior and Mechanics*, p. 119. Available at: <https://doi.org/10.1117/12.601495>.
- McKnight, G.P. and Henry, C.P. (2010) 'Deformable Variable-Stiffness Cellular Structures. U.S. Patent 7,678,440 B1'.
- Meng, H. and Li, G. (2013) 'A review of stimuli-responsive shape memory polymer composites', *Polymer*, 54(9), pp. 2199–2221. Available at: <https://doi.org/10.1016/j.polymer.2013.02.023>.
- Morrison, G. (2019) *Tupolev Tu-144: Inside Russia's supersonic airliner*, CNET. Available at: <https://www.cnet.com/pictures/tupolev-tu-144-russias-supersonic-airliner/> (Accessed: 27 May 2020).
- Mrazova, M. (2013) 'Advanced composite materials of the future in aerospace industry', *INCAS Bulletin*, 5(3), pp. 139–150. Available at: <https://doi.org/10.13111/2066-8201.2013.5.3.14>.

- Muhammed, S.P., Ajaj, R.M. and Khan, K.A. (2020) 'A compliant polymorphing wing for small UAVs', *Chinese Journal of Aeronautics*, 33(10), pp. 2575–2588. Available at: <https://doi.org/10.1016/j.cja.2020.03.027>.
- Murali, G.G. *et al.* (2021) 'Development of intrinsically heated, interleaved composites with controllable flexural stiffness and shape memory capability', in *MECHCOMP7 conference*.
- Murugan, S. *et al.* (2012) 'Optimal design of variable fiber spacing composites for morphing aircraft skins', *Composite Structures*, 94(5), pp. 1626–1633. Available at: <https://doi.org/10.1016/j.compstruct.2011.12.023>.
- Murugan, S. and Friswell, M.I. (2013) 'Morphing wing flexible skins with curvilinear fiber composites', *Composite Structures*, 99, pp. 69–75. Available at: <https://doi.org/10.1016/j.compstruct.2012.11.026>.
- Nedelcu, R. and Redon, P. (2012) 'Composites materials for aviation industry', in *International conference of scientific paper AFASES 2012*.
- O'Shaughnessey, P.G., Dubé, M. and Villegas, I.F. (2016) 'Modeling and experimental investigation of induction welding of thermoplastic composites and comparison with other welding processes', *Journal of Composite Materials*, 50(21), pp. 2895–2910. Available at: <https://doi.org/10.1177/0021998315614991>.
- Ornaghi, H.L. *et al.* (2020) 'Stress relaxation, creep, and recovery of carbon fiber non-crimp fabric composites', *Composites Part C: Open Access*, 3, p. 100051. Available at: <https://doi.org/10.1016/J.JCOMC.2020.100051>.
- Pahuja, R. and Mamidala, R. (2017) 'Machinability of Ti/CFRP stacks in trimming and drilling using abrasive waterjet', *International SAMPE Technical Conference*, (March 2019), pp. 2064–2076.
- Pahuja, R., Ramulu, M. and Hashish, M. (2016) 'Abrasive Waterjet Profile Cutting of Thick Titanium/Graphite Fiber Metal Laminate', in. American Society of Mechanical Engineers

Digital Collection. Available at: <https://doi.org/10.1115/imece2016-67136>.

Panesar, A.S. and Weaver, P.M. (2012) 'Optimisation of blended bistable laminates for a morphing flap', *Composite Structures*, 94(10), pp. 3092–3105. Available at: <https://doi.org/10.1016/J.COMPSTRUCT.2012.05.007>.

Peters, J.E., Papavassiliou, D. V. and Grady, B.P. (2008) 'Unique thermal conductivity behavior of single-walled carbon nanotube-polystyrene composites', *Macromolecules*, 41(20), pp. 7274–7277. Available at: <https://doi.org/10.1021/ma8011569>.

Portela, P. *et al.* (2008) 'Analysis of morphing, multi stable structures actuated by piezoelectric patches', *Computers and Structures*, 86(3–5), pp. 347–356. Available at: <https://doi.org/10.1016/j.compstruc.2007.01.032>.

Psarras, G.C., Parthenios, J. and Galiotis, C. (2001) 'Adaptive composites incorporating shape memory alloy wires part I probing the internal stress and temperature distributions with a laser Raman sensor', *Journal of Materials Science*, 36(3), pp. 535–546. Available at: <https://doi.org/10.1023/A:1004869613018>.

Puig, L., Barton, A. and Rando, N. (2010) 'A review on large deployable structures for astrophysics missions', *Acta Astronautica*. Pergamon, pp. 12–26. Available at: <https://doi.org/10.1016/j.actaastro.2010.02.021>.

Quadrini, F. *et al.* (2021) 'Shape memory polymer composite unit with embedded heater', *Smart Materials and Structures*, 30(7), p. 075009. Available at: <https://doi.org/10.1088/1361-665X/ac00cb>.

Rajesh, M., Rajkumar, K. and Annamalai, V.E. (2021) 'Abrasive water jet machining on Ti metal-interleaved basalt-flax fiber laminate', *Materials and Manufacturing Processes*, 36(3), pp. 329–340. Available at: <https://doi.org/10.1080/10426914.2020.1832692>.

Read, B. (2021) *Shape shifters*. Available at: <https://www.aerosociety.com/news/shape-shifters/> (Accessed: 16 February 2022).

- Rezaei, F. *et al.* (2008) 'Development of short-carbon-fiber-reinforced polypropylene composite for car bonnet', *Polymer - Plastics Technology and Engineering*, 47(4), pp. 351–357. Available at: <https://doi.org/10.1080/03602550801897323>.
- Rivero, A.E. *et al.* (2022) 'Design, Manufacture and Wind Tunnel Test of a Modular FishBAC Wing with Novel 3D Printed Skins', *Applied Sciences* 2022, Vol. 12, Page 652, 12(2), p. 652. Available at: <https://doi.org/10.3390/APP12020652>.
- Robinson, P. *et al.* (2013) 'Carbon fibre reinforced epoxy composites with variable stiffness for use in morphing aerostructures', in *The 19th International Conference on Composite Materials*, pp. 270–277.
- Robinson, P. *et al.* (2017) 'Deployable, shape memory carbon fibre composites without shape memory constituents', *Composites Science and Technology*, 145, pp. 96–104. Available at: <https://doi.org/10.1016/j.compscitech.2017.02.024>.
- Rodriguez, A. (2013) 'Morphing Aircraft Technology Survey', in *45th AIAA Aerospace Sciences Meeting and Exhibit*. Reston, Virginia: American Institute of Aeronautics and Astronautics. Available at: <https://doi.org/10.2514/6.2007-1258>.
- Rodriguez, A.R. (2007) 'Morphing aircraft technology survey', *Collection of Technical Papers - 45th AIAA Aerospace Sciences Meeting*, 21, pp. 15064–15079. Available at: <https://doi.org/10.2514/6.2007-1258>.
- Rodriguez, J.N. *et al.* (2016) 'Shape-morphing composites with designed micro-architectures', *Scientific Reports*, 6. Available at: <https://doi.org/10.1038/srep27933>.
- Roulette, J. and Overbye, D. (2022) 'What We Know About Unfolding the James Webb Space Telescope', *The New York Times*. Available at: <https://www.nytimes.com/2022/01/08/science/webb-telescope-nasa-time-livestream.html> (Accessed: 28 January 2022).
- Russello, M. *et al.* (2020) 'Welding of thermoplastics by means of carbon-nanotube web',

- Composites Communications*, 17, pp. 56–60. Available at:
<https://doi.org/10.1016/j.coco.2019.11.001>.
- Schultz, M.R. (2008) 'A concept for airfoil-like active bistable twisting Structures', *Journal of Intelligent Material Systems and Structures*, 19(2), pp. 157–169. Available at:
<https://doi.org/10.1177/1045389X06073988>.
- Schuster, A. *et al.* (2018) 'Smart Manufacturing of Thermoplastic CFRP Skins', *Procedia Manufacturing*, 17, pp. 935–943. Available at: <https://doi.org/10.1016/j.promfg.2018.10.147>.
- Shaw, A.D., Dayyani, I. and Friswell, M.I. (2015) 'Optimisation of composite corrugated skins for buckling in morphing aircraft', *Composite Structures*, 119, pp. 227–237. Available at:
<https://doi.org/10.1016/j.compstruct.2014.09.001>.
- Shi, H., Villegas, I.F. and Bersee, H.E.N. (2016) 'Analysis of void formation in thermoplastic composites during resistance welding', <https://doi.org/10.1177/0892705716662514>, 30(12), pp. 1654–1674. Available at: <https://doi.org/10.1177/0892705716662514>.
- Sofla, A.Y.N. *et al.* (2010) 'Shape morphing of aircraft wing: Status and challenges', *Materials and Design*, 31(3), pp. 1284–1292. Available at:
<https://doi.org/10.1016/j.matdes.2009.09.011>.
- Soutis, C. (2015) 'Introduction: engineering requirements for aerospace composite materials', in *Polymer Composites in the Aerospace Industry*. Elsevier, pp. 1–18. Available at: <https://doi.org/10.1016/B978-0-85709-523-7.00001-3>.
- Stavrov, D. and Bersee, H.E.N. (2005) 'Resistance welding of thermoplastic composites-an overview', *Composites Part A: Applied Science and Manufacturing*, 36(1), pp. 39–54. Available at: [https://doi.org/10.1016/S1359-835X\(04\)00182-4](https://doi.org/10.1016/S1359-835X(04)00182-4).
- Sugahara, T. *et al.* (2014) 'Interfacial properties of carbon fiber reinforced thermoplastic and thermosetting composites', in *ASME International Mechanical Engineering Congress and Exposition, Proceedings (IMECE)*. Available at: <https://doi.org/10.1115/IMECE2014-37757>.

- Sun, J., Liu, Y. and Leng, J. (2014) 'Mechanical properties of shape memory polymer composites enhanced by elastic fibers and their application in variable stiffness morphing skins', <http://dx.doi.org/10.1177/1045389X14546658>, 26(15), pp. 2020–2027. Available at: <https://doi.org/10.1177/1045389X14546658>.
- Suzhu, Y. and Hing, P. (2008) 'Thermal and dielectric properties of fiber reinforced polystyrene composites', *Polymer Composites*, 29(11), pp. 1199–1202. Available at: <https://doi.org/10.1002/pc.20527>.
- Tabata, O. *et al.* (2001) 'Micro fabricated tunable bending stiffness devices', *Sensors and Actuators, A: Physical*, 89(1–2), pp. 119–123. Available at: [https://doi.org/10.1016/S0924-4247\(00\)00538-0](https://doi.org/10.1016/S0924-4247(00)00538-0).
- Tawfik, S.A., Stefan Dancila, D. and Armanios, E. (2011) 'Unsymmetric composite laminates morphing via piezoelectric actuators', *Composites Part A: Applied Science and Manufacturing*, 42(7), pp. 748–756. Available at: <https://doi.org/10.1016/j.compositesa.2011.03.001>.
- Thill, C. *et al.* (2008) 'Morphing skins', *Aeronautical Journal*, 112(1129), pp. 117–139. Available at: <https://doi.org/10.1017/S0001924000002062>.
- Thill, C., Downsborough, J.D., *et al.* (2010) 'Aerodynamic study of corrugated skins for morphing wing applications', *Aeronautical Journal*, 114(1154), pp. 237–244. Available at: <https://doi.org/10.1017/S0001924000003687>.
- Thill, C., Etches, J.A., *et al.* (2010) 'Composite corrugated structures for morphing wing skin applications', *Smart Materials and Structures*, 19(12). Available at: <https://doi.org/10.1088/0964-1726/19/12/124009>.
- Thill, Christophe *et al.* (2010) 'Investigation of trapezoidal corrugated aramid/epoxy laminates under large tensile displacements transverse to the corrugation direction', *Composites Part A: Applied Science and Manufacturing*, 41(1), pp. 168–176. Available at:

<https://doi.org/10.1016/j.compositesa.2009.10.004>.

Timoshenko, S. (1925) 'Analysis of Bi-Metal Thermostats', *Journal of the Optical Society of America*, 11(3), p. 233. Available at: <https://doi.org/10.1364/josa.11.000233>.

Tobushi, H. *et al.* (2009) 'Thermomechanical properties of shape-memory alloy and polymer and their composites', *Mechanics of Advanced Materials and Structures*, 16(3), pp. 236–247. Available at: <https://doi.org/10.1080/15376490902746954>.

Tobushi, H. *et al.* (2010) 'Fabrication and two-way deformation of shape memory composite with SMA and SMP', in *Materials Science Forum*, pp. 2189–2194. Available at: <https://doi.org/10.4028/www.scientific.net/MSF.638-642.2189>.

Tolley, M.T. *et al.* (2014) 'Self-folding origami: Shape memory composites activated by uniform heating', *Smart Materials and Structures*, 23(9). Available at: <https://doi.org/10.1088/0964-1726/23/9/094006>.

Toray Composite Materials America Inc. (2018) *T300 Technical data sheet*. Available at: <https://www.toraycma.com/products/carbon-fiber/> (Accessed: 11 March 2022).

Totla, H.S. *et al.* (2023) 'Resistance welding analysis of thermoplastic composite structures in aeronautical applications', *International Journal on Interactive Design and Manufacturing*, pp. 1–13. Available at: <https://doi.org/10.1007/S12008-022-01151-1/TABLES/1>.

Tridech, C. *et al.* (2013) 'High performance composites with active stiffness control', *ACS Applied Materials and Interfaces*, 5(18), pp. 9111–9119. Available at: <https://doi.org/10.1021/am402495n>.

UL Prospector (2000a) *LG MABS TR557*. Available at: <https://materials.ulprospector.com/en/profile/default?e=37755> (Accessed: 22 July 2022).

UL Prospector (2000b) *Luran® 368R*. Available at: <https://materials.ulprospector.com/en/profile/default?e=14144> (Accessed: 22 July 2022).

- UL Prospector (2012) *Styrolution PS 124N/L*. Available at:
<https://materials.ulprospector.com/en/profile/default?e=160634> (Accessed: 22 July 2022).
- UL Prospector (2013) *Luran® S KR2863C*. Available at:
<https://materials.ulprospector.com/en/profile/default?e=214393> (Accessed: 22 July 2022).
- Villegas, I.F. and Bersee, H.E. (2015) 'Characterisation of a metal mesh heating element for closed-loop resistance welding of thermoplastic composites', *Journal of Thermoplastic Composite Materials*, 28(1), pp. 46–65. Available at:
<https://doi.org/10.1177/0892705712475012>.
- Waili, M.B. (2019) *FE investigation of interleaved composites for controllable stiffness and morphing capabilities (Masters thesis)*. Imperial College London.
- Wang, B. and Fancey, K.S. (2015) 'A bistable morphing composite using viscoelastically generated prestress', *Materials Letters*, 158, pp. 108–110. Available at:
<https://doi.org/10.1016/j.matlet.2015.05.129>.
- Wang, C.C. *et al.* (2012) 'Repeated instant self-healing shape memory composites', *Journal of Materials Engineering and Performance*, 21, pp. 2663–2669. Available at:
<https://doi.org/10.1007/s11665-012-0374-1>.
- Wang, J., Lee, D. and Liu, Y. (2017) 'Joule-Heating Activated Flexible Composite Structures Using Shape Memory Epoxy', in *ASME 2017 International Mechanical Engineering Congress and Exposition*. ASME. Available at: <https://doi.org/10.1115/imece2017-72141>.
- Wang, W., Rodrigue, H. and Ahn, S.-H. (2015) 'Smart soft composite actuator with shape retention capability using embedded fusible alloy structures', *Composites Part B: Engineering*, 78, pp. 507–514. Available at:
<https://doi.org/10.1016/j.compositesb.2015.04.007>.
- Wang, X., Mayer, C. and Neitzel, M. (1997) 'Some issues on impregnation in manufacturing of thermoplastic composites by using a double belt press', *Polymer Composites*, 18(6), pp.

701–710. Available at: <https://doi.org/10.1002/PC.10323>.

Weaver, P. and Daynes, S. (no date) *Morphing Composites*. Available at: <https://www.bristol.ac.uk/media-library/sites/composites/migrated/documents/weaver-conference2010.pdf> (Accessed: 17 July 2019).

Weisshaar, T.A. (2006) 'Morphing Aircraft Technology – New Shapes for Aircraft Design'. Available at: <http://www.rto.nato.int/abstracts.asp>. (Accessed: 2 April 2019).

Weisshaar, T.A. (2013) 'Morphing aircraft systems: Historical perspectives and future challenges', *Journal of Aircraft*, 50(2), pp. 337–353. Available at: <https://doi.org/10.2514/1.C031456/ASSET/IMAGES/LARGE/FIGURE33.JPEG>.

Wolfrath, J., Michaud, V. and Manson, J.A.E. (2005) 'Deconsolidation in glass mat thermoplastic composites: Analysis of the mechanisms', *Composites Part A: Applied Science and Manufacturing*, 36(12), pp. 1608–1616. Available at: <https://doi.org/10.1016/J.COMPOSITESA.2005.04.001>.

Wong, K.H. *et al.* (2012) 'Effect of coupling agents on reinforcing potential of recycled carbon fibre for polypropylene composite', *Composites Science and Technology*, 72(7), pp. 835–844. Available at: <https://doi.org/10.1016/j.compscitech.2012.02.013>.

Woods, B.K., Bilgen, O. and Friswell, M.I. (2014) 'Wind tunnel testing of the fish bone active camber morphing concept', *Journal of Intelligent Material Systems and Structures*, 25(7), pp. 772–785. Available at: <https://doi.org/10.1177/1045389X14521700>.

Xiao, X.R. (1993) 'A model for the deconsolidation phenomenon in induction heating of thermoplastic resin composites', in *Ninth international conference on composite materials (ICCM9)*. Spain, pp. 243–250.

Yang, S.-M., Han, J.-H. and Lee, I. (2018) 'Characteristics of smart composite wing with SMA actuators and optical fiber sensors', *International Journal of Applied Electromagnetics and Mechanics*, 23(3–4), pp. 177–186. Available at: <https://doi.org/10.3233/jae-2006-736>.

- Yao, S.S. *et al.* (2018) 'Recent advances in carbon-fiber-reinforced thermoplastic composites: A review', *Composites Part B: Engineering*. Elsevier Ltd, pp. 241–250. Available at: <https://doi.org/10.1016/j.compositesb.2017.12.007>.
- Yi, X.-S. (2018) 'An Introduction to Composite Materials', in *Composite Materials Engineering, Volume 1*. Singapore: Springer Singapore, pp. 1–61. Available at: https://doi.org/10.1007/978-981-10-5696-3_1.
- Yokozeki, T. *et al.* (2006) 'Mechanical properties of corrugated composites for candidate materials of flexible wing structures', *Composites Part A: Applied Science and Manufacturing*, 37(10), pp. 1578–1586. Available at: <https://doi.org/10.1016/j.compositesa.2005.10.015>.
- Yu, K. *et al.* (2009) 'Novel deployable morphing wing based on SMP composite', in J. Leng, A.K. Asundi, and W. Ecke (eds) *Second International Conference on Smart Materials and Nanotechnology in Engineering*. Available at: <https://doi.org/10.1117/12.845408>.
- Yuan, L.Y., Shyu, S.S. and Lai, J.Y. (1991) 'Plasma surface treatments on carbon fibers. II. Mechanical property and interfacial shear strength', *Journal of Applied Polymer Science*, 42(9), pp. 2525–2534. Available at: <https://doi.org/10.1002/app.1991.070420918>.
- Zal, V. *et al.* (2016) 'Experimental evaluation of blanking and piercing of PVC based composite and hybrid laminates', *Advances in Manufacturing*, 4(3), pp. 248–256. Available at: <https://doi.org/10.1007/S40436-016-0147-4>.
- Zhang, B. *et al.* (2018) 'Made to order: composites with controllable stiffness', in *ECCM18 Keynote lecture, Athens, Greece*.
- Zhang, B. (2020) *Interleaved composites for controllable stiffness, shape memory and easy repair capabilities (PhD thesis)*. Imperial College London. Available at: <https://spiral.imperial.ac.uk/handle/10044/1/82298>.
- Zhang, C.-S. and Ni, Q.-Q. (2007) 'Bending behavior of shape memory polymer based

laminates', *Composite Structures*, 78(2), pp. 153–161. Available at:
<https://doi.org/10.1016/j.compstruct.2005.08.029>.

Zhang, Z. *et al.* (2017) 'A novel thermo-mechanical anti-icing/de-icing system using bi-stable laminate composite structures with superhydrophobic surface', *Composite Structures*, 180, pp. 933–943. Available at: <https://doi.org/10.1016/j.compstruct.2017.08.068>.

Zhang, Z. *et al.* (2019) 'Bistable morphing composite structures: A review', *Thin-Walled Structures*. Elsevier, pp. 74–97. Available at: <https://doi.org/10.1016/j.tws.2019.04.040>.

Zhao, Q. *et al.* (2023) 'On accurate characterization of interfacial morphology and damage evolution of thermoplastic composite welded joints: A microscale study via in-situ micro-CT', *Composites Science and Technology*, 236, p. 110004. Available at:
<https://doi.org/10.1016/J.COMPSCITECH.2023.110004>.

Zhao, Q., Qi, H.J. and Xie, T. (2015) 'Recent progress in shape memory polymer: New behavior, enabling materials, and mechanistic understanding', *Progress in Polymer Science*, 49–50, pp. 79–120. Available at: <https://doi.org/10.1016/j.progpolymsci.2015.04.001>.

Zopp, C. *et al.* (2019) 'Quasi-static and fatigue bending behavior of a continuous fiber-reinforced thermoplastic/metal laminate', *Composites Part B: Engineering*, 174, p. 107043. Available at: <https://doi.org/10.1016/j.compositesb.2019.107043>.

Appendices

A.1. Measuring dimensions of composite specimens

A.1.1. Samples cut with a circular dry saw

Positions, where the physical dimensions of composite specimens were measured using a digital vernier calliper with a resolution of 0.01 mm, are shown in [Figure A.1](#). Here, the cuboid represents a composite specimen.

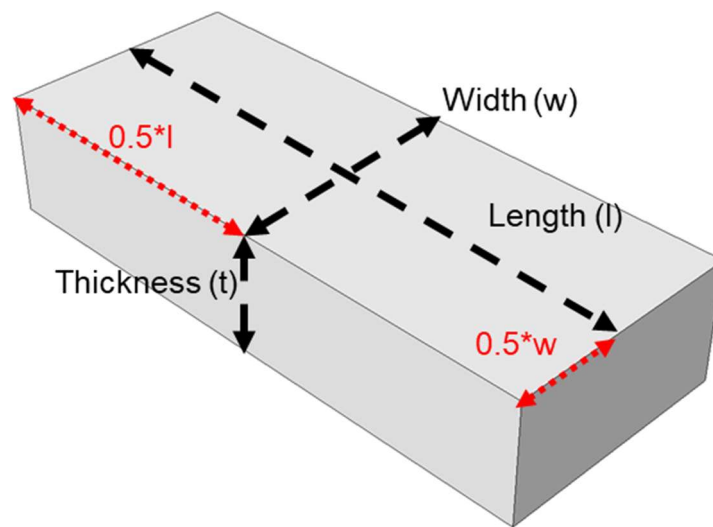


Figure A.1. Positions where measurements of dimensions of composite specimens were made for composites cut using a circular dry saw

A.1.2. Samples cut with a waterjet cutter

When interleaved composite specimens, are cut using a waterjet as specified in [Section 3.3.2.1](#), the thermoplastic interleaves close to the cuts get eroded as shown in [Figure A.2 \(a\)](#). Similar erosions and/or delamination have also been seen when samples of composites made of metal laminae, interleaved with reinforced thermoplastic laminae were cut using a waterjet (Pahuja, Ramulu and Hashish, 2016; Pahuja and Mamidala, 2017; Bañon *et al.*, 2020, 2021; Rajesh, Rajkumar and Annamalai, 2021). By improving the waterjet-based cutting process, such erosions can be avoided.

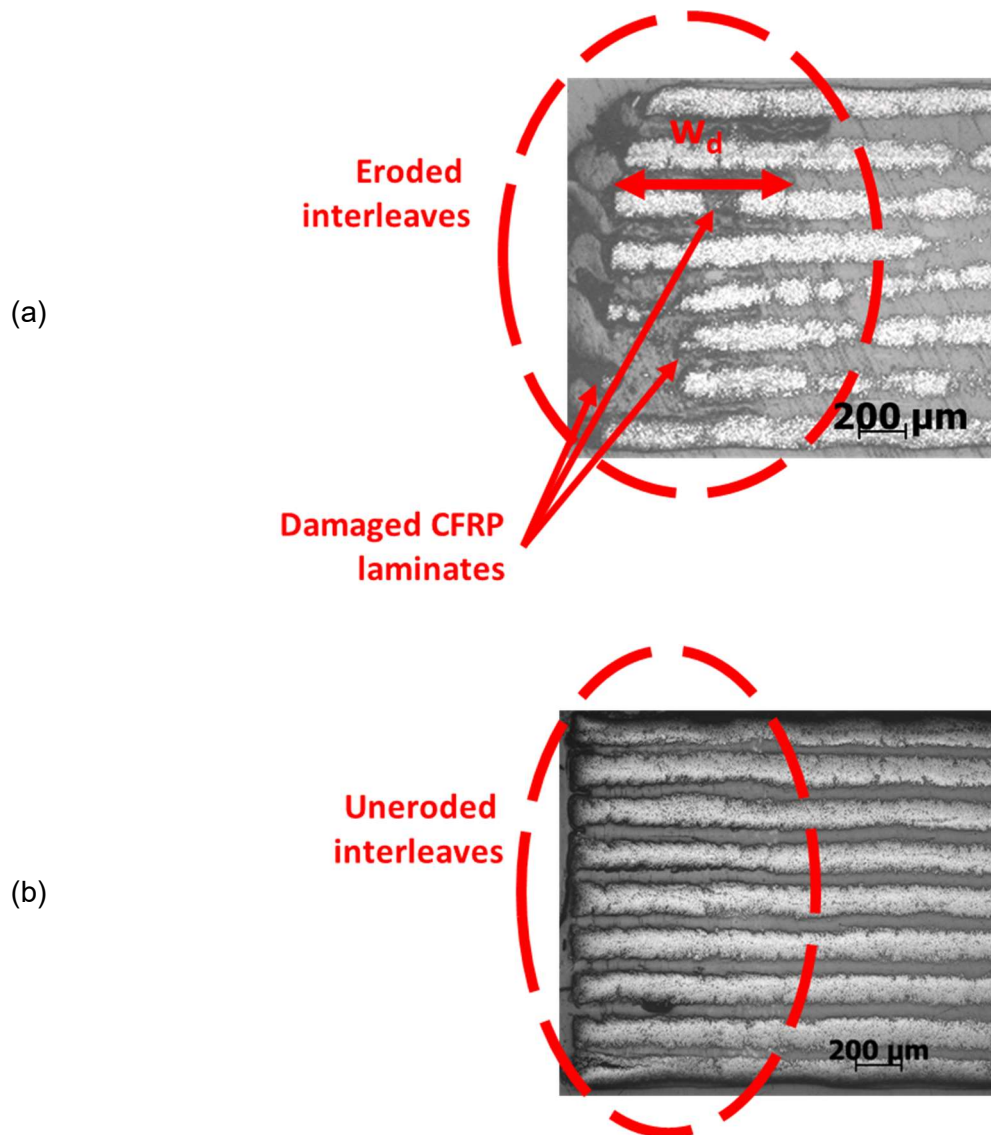


Figure A.2. Polished transverse microsection of the edges of PS-interleaved CFRP composites cut using (a) waterjet cutter and (b) circular dry saw.

(Here, w_d is the length of the eroded region of the interleaves.)

Such erosions and/or damages were not seen when these composites are cut using a circular dry saw as shown in Figure A.2 (b). However, when the composites are cut using the circular dry saw, the increase in temperature caused by the friction between the blade and the composite causes the thermoplastic material to melt and settle on the blade, leading to its deterioration. Hence, for composite laminates with significant thermoplastic content, a waterjet was used to cut the specimens.

From the polished microsections of the composite specimens cut with a waterjet cutter, the length of the erosion (w_d in [Figure A.2 \(a\)](#)) can be measured. Statistical analysis of over 1000 such eroded interleaves* reveals that the w_d for PS and SAN interleaves were 0.55 ± 0.15 mm and 0.34 ± 0.07 mm respectively.

If the erosion had happened only within the PS or SAN interleaves, and the CFRP laminae were left undisturbed, then the effect of erosion on the flexural behaviour of the PS or SAN-interleaved CFRP composites will be negligible. However, it is possible that when the PS or SAN interleaves get eroded, the adjacent CFRP plies also get damaged. Therefore, it can be assumed that the specimens cut using a waterjet will have no load-bearing capabilities in these eroded regions.

As a consequence, the effective width (w) of these composites to be used for all flexural strength and flexural modulus calculations are measured as shown in [Figure A.3](#) and [Eq A-1](#). The physical dimensions such as length (l), thickness (t) and total width (w_t) of composites were measured using a digital vernier calliper with a resolution of 0.01 mm. Furthermore, in the calculation of the effective width (w in [Figure A.3](#) and [Eq A-1](#)) of the composite specimens, w_d is taken as the statistical average shown above.

$$w = w_t - 2 w_d \quad \text{Eq A-1}$$

The agreement between the theoretically predicted and experimentally measured flexural modulus and various stresses (such as τ^{max} and σ^{max}) of the composites in this report validate the above assumption that the composite specimens will effectively have no load-bearing capabilities in these eroded regions.

* The data was extracted from multiple composite specimens and from multiple production cycles. The specimens included composites with pristine and reinforced PS and SAN interleaves.

Furthermore, as the length of the composite specimens, no not play any significant role in the flexural strength and flexural modulus calculations, the effect of erosion of interleaves on the length of the composites is not considered in this work.

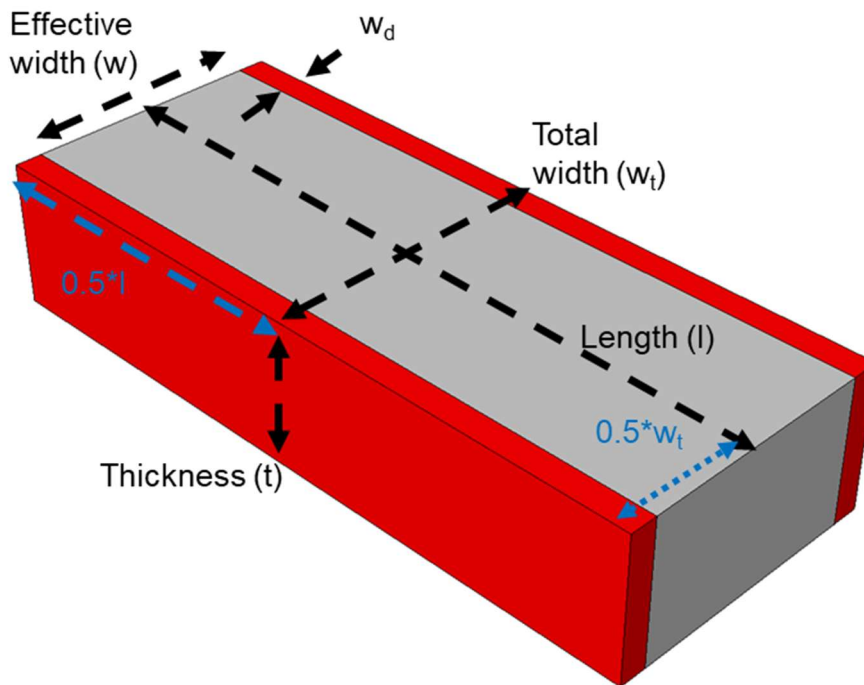


Figure A.3. Dimensions of the composite specimens cut using a waterjet

A.2. Methodology to extract load associated with the initiation of failure (L_f) from the force-displacement plots obtained from the 3PB and SBS tests of composite specimens

The protocol to select the initiation of non-linearity in a load-displacement curve obtained from a double cantilever test has previously been discussed (Blackman and Kinloch, 2001). In this protocol, the non-linearity initiation load is selected as the load at which the slope of the load-displacement curve decreases by 5%. Drawing inspiration from this protocol, the following methodology to select the load associated with the initiation of non-linearity of the load-displacement curves (from SBS tests) has been developed.

A representative force (F)-displacement (d) curve obtained from an SBS test of a composite specimen is shown in Figure A.4. To identify the linear section of this curve, derivative $\frac{\Delta F}{\Delta d}$ is first calculated from the raw data and is shown in Figure A.5 as a function of the mid-span displacement (d). The peak of the $\frac{\Delta F}{\Delta d}$ curve in Figure A.5 can be associated with the linear segment in the force-displacement curve in Figure A.4. The range of mid-span displacement (from d_1 to d_2 in Figure A.5) at which the $\frac{\Delta F}{\Delta d}$ curve varies less than 1% of its peak value is arbitrarily considered as the plateau region of the $\frac{\Delta F}{\Delta d}$ curve. This plateau region and the associated d_1 and d_2 values indicate the range of mid-span displacement at which the force-displacement curve in Figure A.4 is linear.

A linear fit can now be obtained from the initial force-displacement curve for a mid-span displacement range of d_1 to d_2 (see Figure A.6). Using the slope and X-intercept of the linear fit, a new line (the 'C_{5%} line') can be plotted with the X-intercept of that of the linear fit and a slope of 95% of that of the linear fit. The 'C_{5%} line' is shown in Figure A.6. The applied force associated with the intercept between the 'C_{5%} line' and the initial force-displacement curve is extracted as the load associated with the initiation of failure (L_f). For load-displacement curves that have a higher load before this intercept, the maximum load before the intercept is selected as the load associated with the initiation of failure (L_f) (see Figure A.7)

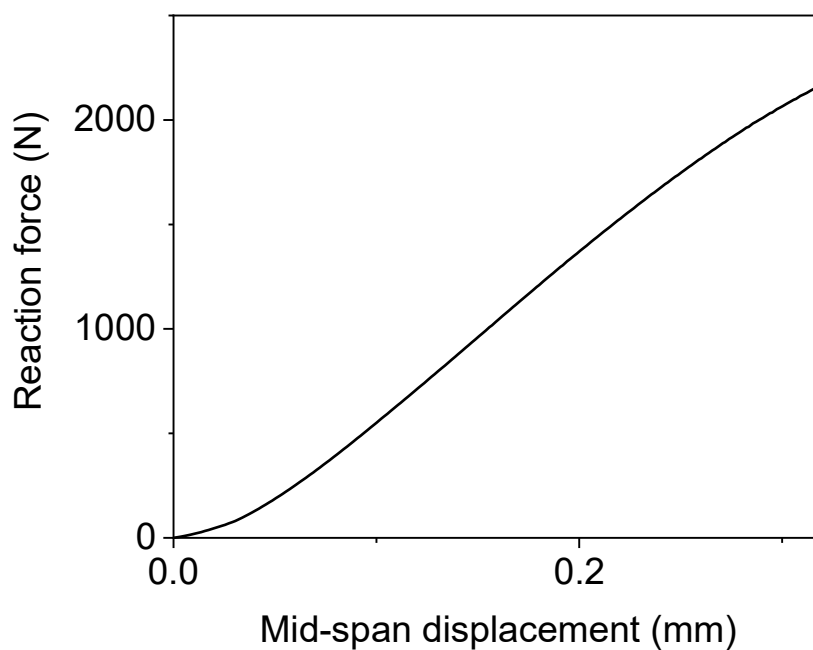


Figure A.4. Representation of a force-displacement plot obtained from 3PB and SBS tests

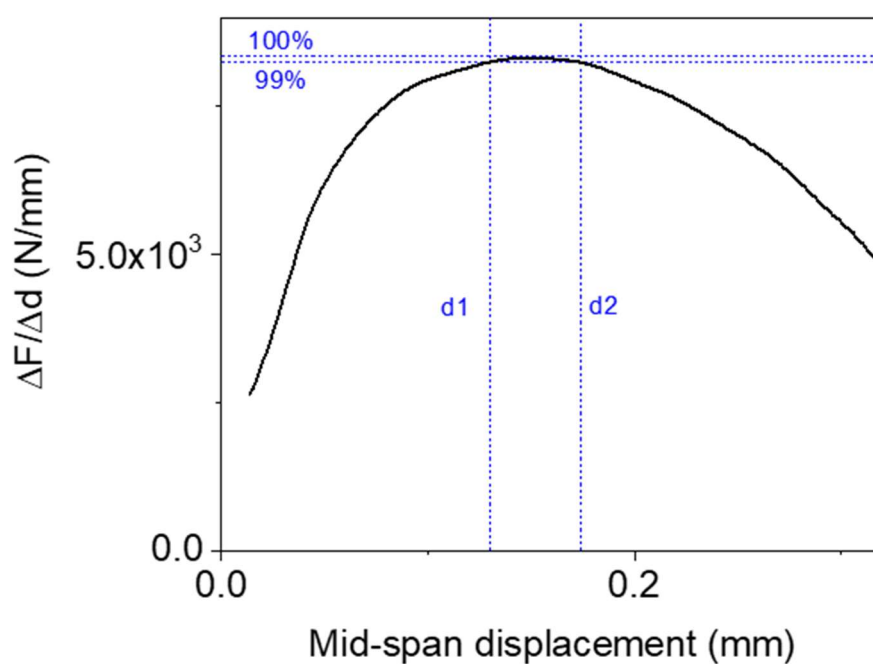


Figure A.5. $\frac{\Delta F}{\Delta d}$ curve and identification of the plateau region of the curve

shown in Figure A.4.

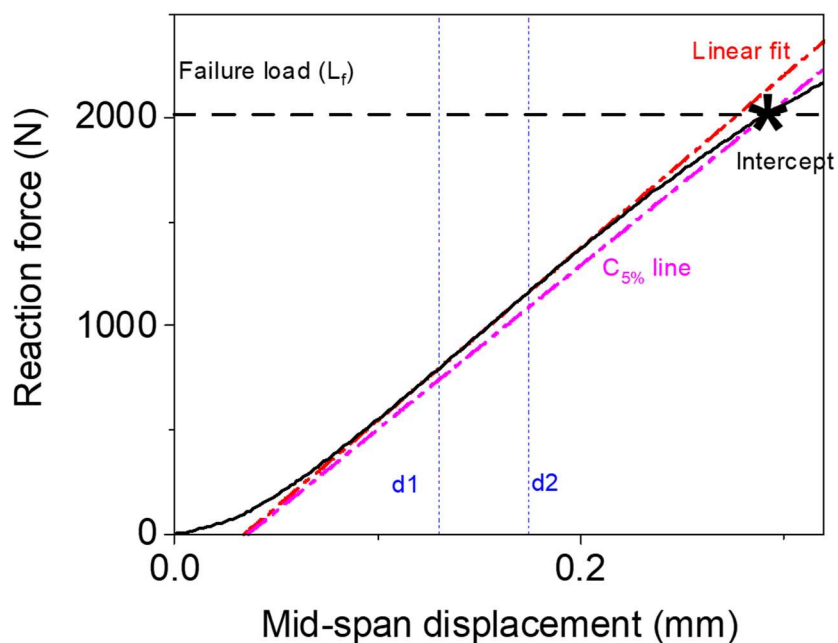


Figure A.6. Mathematical operations performed on a representative force-displacement plot to obtain the load associated with the initiation of failure (L_f)

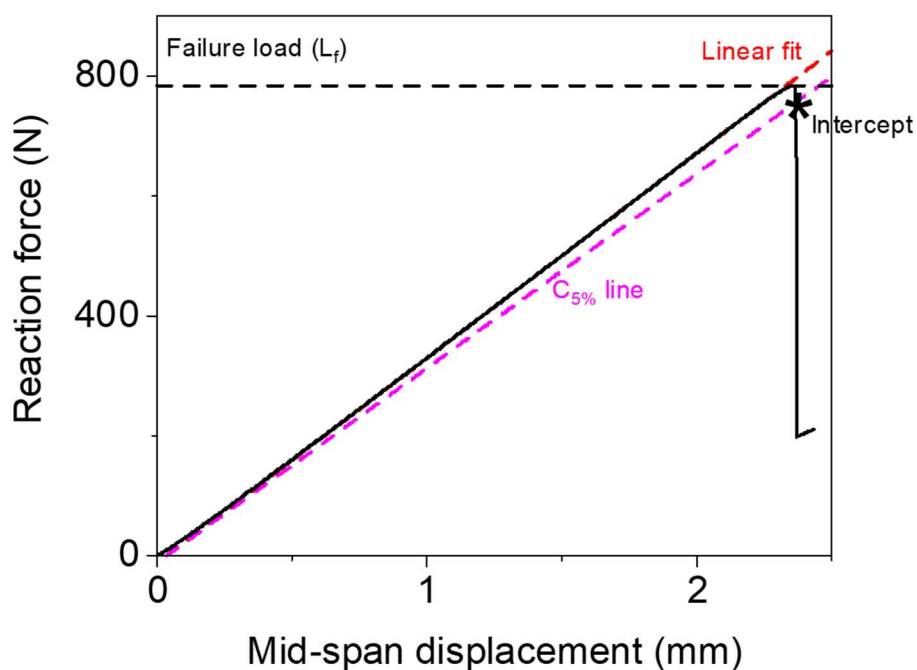


Figure A.7. Load associated with the initiation of failure (L_f) where a load-displacement curve has a higher load before its intercept with the C_{5%} line

A.3. Repairability of CFRP-PS composites

It is seen in [Section 3.1](#) that CFRP-PS composites loaded in 3PB fail due to the shear failure of PS interleaves. As PS residues were found on both the fracture surfaces, it must be possible to repair these fractures by fusing the PS layers back together.

To repair the composite, the two fracture surfaces were stacked back together, taking care to ensure a precise alignment, placed on a heated vacuum table (Global vacuum heat-press, Nabuurs Developing S.L., Spain), and covered with PTFE release films and breather cloth. This assembly was then heated from room temperature to a repair temperature of 175°C at 1 bar pressure (provided by vacuum bagging). After 5 minutes at this temperature and pressure, the assembly cooled down to room temperature and the vacuum bagging was removed.

The repaired specimens were re-tested in 3PB tests until failure, as shown in [Section 3.1.2.1](#) to determine the efficacy of the repair process. This damage-repair cycle was repeated twice. The typical load-displacement curves of CFRP-PS specimens in their pristine state, after the first repair and after the second repair are shown in [Figure A.8](#). Based on the methodology described in [Section 3.1.3.1](#), the load associated with the initiation of failure (L_f) was selected for each load-displacement curve and the corresponding shear (τ^{max}) stresses were calculated.

The shear stresses (τ^{max}) of the CFRP-PS specimens in their pristine state, after the first repair and after the second repair are shown in [Table A.1](#). These failure stresses (τ^{max}) indicate that the CFRP-PS specimens showed 90% and 92.5% strength recovery over the first and second repair cycles respectively. These observations demonstrate the repairability of the CFRP-PS composites.

Furthermore, based on these observations, it can be understood that if an interleaved composite undergoes failure that is localised inside its thermoplastic interleaves, then it could be repaired using the simple technique described here.

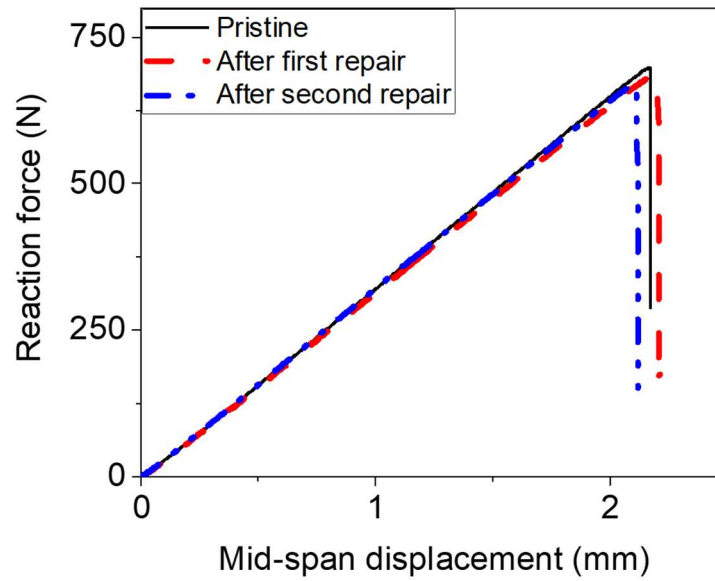


Figure A.8. Typical 3PB load-displacement curves of CFRP-PS specimens in 3PB tests at different damage-repair cycles.

Table A.1. Shear stresses (τ^{max}) and repair efficacy of CFRP-PS specimens in 3PB tests at different damage-repair cycles

Composite state	τ^{max} (GPa)	Strength recovery efficacy ¹
		(%)
Pristine	20.0 ± 2.3	-
After first repair	18.0 ± 1.6	90
After second repair	18.5 ± 3.1	92.4

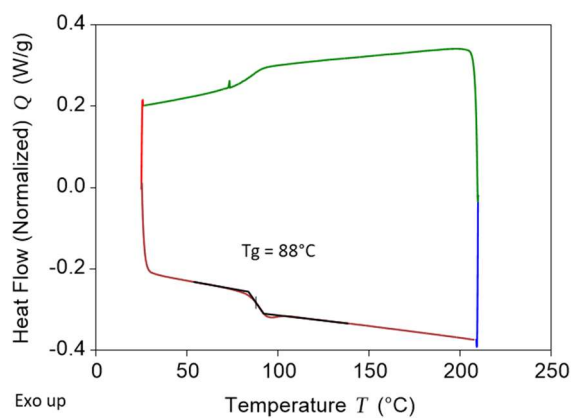
¹ Strength recovery efficacy (%) = $\frac{\text{strength after repair}}{\text{pristine strength}} \times 100$

A.4. Differential scanning calorimetry (DSC) of thermoplastic materials

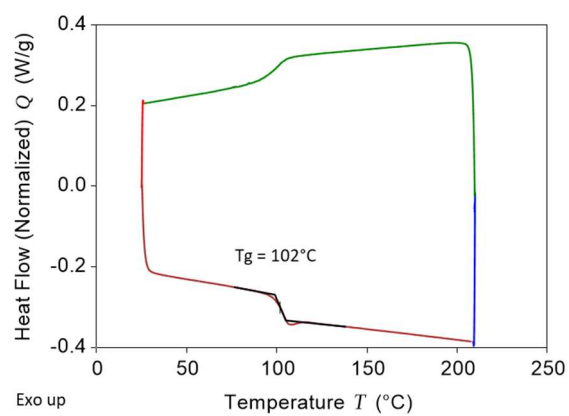
To obtain information on the glass transition temperature (T_g) of the thermoplastic materials used in the layups described in [Chapter 3](#), DSC tests were performed on the TP materials using Discovery DSC (TA Instruments, USA). The tested samples weighed in the range of 6-11 mg. The tests were performed in a nitrogen atmosphere following the steps listed below.

- Step 1. Equilibrate the temperature of samples at 25°C
- Step 2. Heat the samples to 210°C at a heating rate of 10°C/min.
- Step 3. Maintain the samples at 210° for 1 minute.
- Step 4. Cool the samples to 25°C at a cooling rate of -10°C/min.
- Step 5. Maintain the samples at 25° for 1 minute.
- Step 6. Heat the samples to 210°C at a heating rate of 10°C/min.

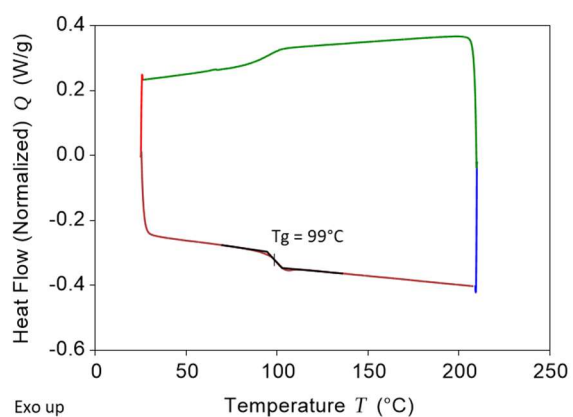
The normalised heat flow vs. temperature chart of each polymer as observed by DSC is given in [Figure A.9](#). From these charts, the glass transition temperature (T_g) of each polymer (see [Table 3.7](#)) is extracted as the midpoint of the non-linear segment of the curve that corresponds to heating the sample during 'Step 6' of the tests, as shown in [Figure A.9](#).



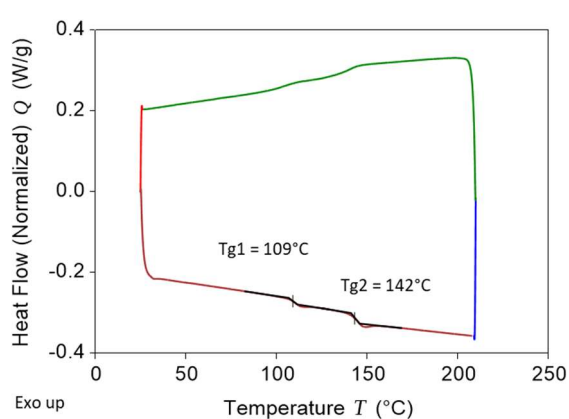
(a) PS



(b) SAN



(c) MABS



(d) ASA+PC

Figure A.9. The heat flow vs. temperature curves of (a) PS, (b) SAN, (c) MABS and (d) ASA+PC obtained from DSC studies

A.5. SBS study of CFRP-PS composites with different layup sequences

Specimens of nominally 15 mm length and 6 mm width were cut from the cured composite panels (listed in Table A.2) that were produced for the studies specified in Sections 3.2 and 3.3, and SBS tests were performed on them using the methodology described in Section 3.2.2.1.

Table A.2. Names and layups of the composite panels
prepared for the studies shown in Section A.5

Composite name ¹	Layup	Nominal thickness of interleaf films used in layup (μm)
CFRP-PS	$[0^\circ_{12}/\text{PS}/0^\circ_{12}]$	70
CFRP-SAN	$[0^\circ_{12}/\text{SAN}/0^\circ_{12}]$	100
CFRP-PS _{174μ}	$[(0^\circ/\text{PS}/\text{PS})_7/0^\circ]$	100
CFRP-SAN _{151μ}	$[(0^\circ/\text{SAN}/\text{SAN})_7/0^\circ]$	100

The typical load-displacement curves obtained from the SBS tests are shown in Figure A.10 (a) and (b). As discussed in Section 3.2.3, in all the cases, the yielding of the thermoplastic interleaves is the cause of the first failure, resulting in a change of slope in the force-displacement curves. Following the methodology described in Section 3.2.3 and Appendix A.2, the shear yield strength (τ_{y-IL}) of the interleaf obtained from the SBS test for all the composites and are shown in Table A.3.

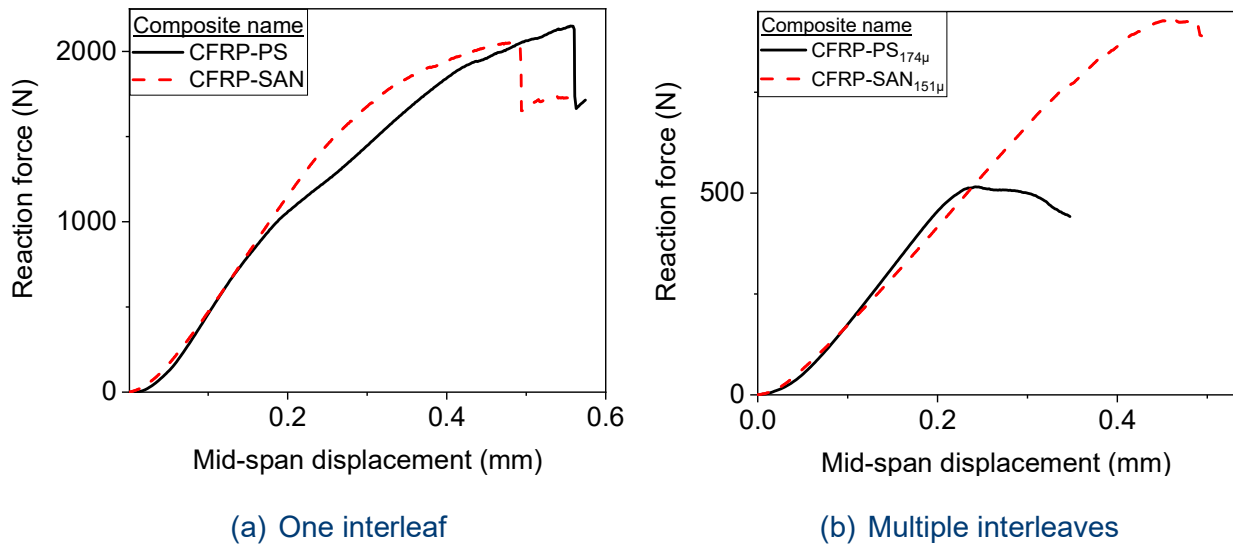


Figure A.10. Typical load-displacement curves of the composites with layup having (a) one thermoplastic interleaf and (b) multiple thermoplastic interleaves in the SBS tests described in Section A.5

On analysing Figure A.10 (b), it can be seen that the yielding of PS and SAN causes a more pronounced change in the slope of the corresponding load-displacement curves in the composites with $[(0^\circ/\text{PS})_7/0^\circ]$ and $[(0^\circ/\text{SAN})_7/0^\circ]$ layups. The yielding of PS and SAN interleaves in these composites results in the formation of a plateau in the load-displacement curves. Hence, for each of these composites, another failure load ($L_{f\text{-ASTM}}$) was selected as the maximum load in the load-displacement curves, as per ASTM D2344M standards. The shear yield strength ($\tau_{y\text{-IL-ASTM}}$) of the interleaf, associated with $L_{f\text{-ASTM}}$ was calculated using the previously described approach and is shown in Table A.3.

This experiment demonstrates how the measured shear yield strength of the thermoplastic interleaves (measured through SBS tests) can vary depending on the layup of the composite, its physical dimension (i.e., span to thickness ratio), and the data processing methodology. Further studies in this regard were not performed as such a task is outside the scope of this research.

Table A.3. Shear yield strength of interleaved composites,
obtained through SBS tests described in Section A.5

Composite name	τ_{y-IL} (MPa)	$\tau_{y-IL-ASTM}$ (MPa)
CFRP-PS	41.0 ± 2.1	-
CFRP-SAN	75.2 ± 3.6	-
CFRP-PS _{174μ}	29.2 ± 0.3	32.2 ± 0.8
CFRP-SAN _{151μ}	58.7 ± 2.8	70.3 ± 1.4

A.6. Behaviour of the 3PB setup while it cools down during the SM tests

The methodology for the SM tests is provided in [Section 3.3.2.3](#). The setup used for these tests is shown in [Figure A.11](#).

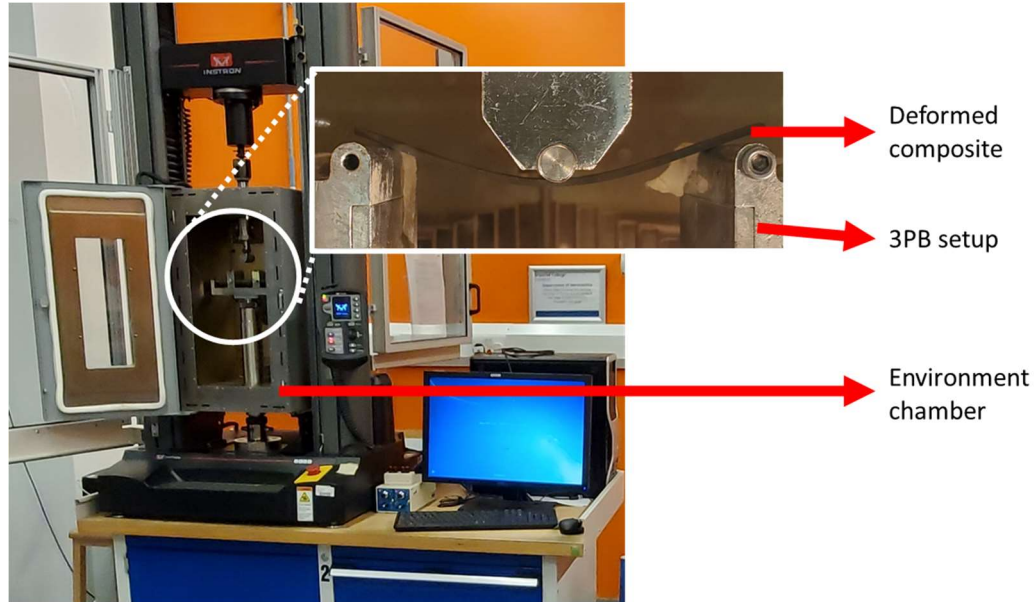


Figure A.11. Experiment setup used for SM tests

The load-displacement curve during the deformation of the CFRP-PS composite with $[(0^\circ/\text{PS})_7/0^\circ]$ layup in the 3PB setup is shown in [Figure A.12](#), which indicates a continuous increase in applied force.

[Figure A.13](#) shows the applied force (plotted against time) recorded by the load cell as the fixtures of the 3PB setup cool down from 120°C to around 50°C . [Note: The temperature indicated here corresponds only to the temperature of the steel fixtures. The deformed composites cool down rapidly due to their lower thermal mass and the ventilation offered by the 3PB setup.]. It can be seen that the applied force continuously decreases over time and effectively becomes zero at around 2000 s of cooling. Such a continuous decrease in the applied force indicates that the composite is being unloaded automatically during the cooling process probably as a result of the thermal contraction of the fixtures.

By optically tracking the rollers of the 3PB setup, the effective mid-span displacement was also observed during this cooling process and is shown in [Figure A.14](#). Here, it is shown that

the effective midspan displacement of the 3PB setup decreases from 18.72 mm to around 18.31 mm as the fixtures of the setup cool down from 120°C to around 50°C.

The continuously changing viscous and elastic properties of the interleaves, along with the continuously changing effective mid-span deformation greatly increase the difficulty of analytically predicting the behaviour of the composites during the cooling process of SM tests.

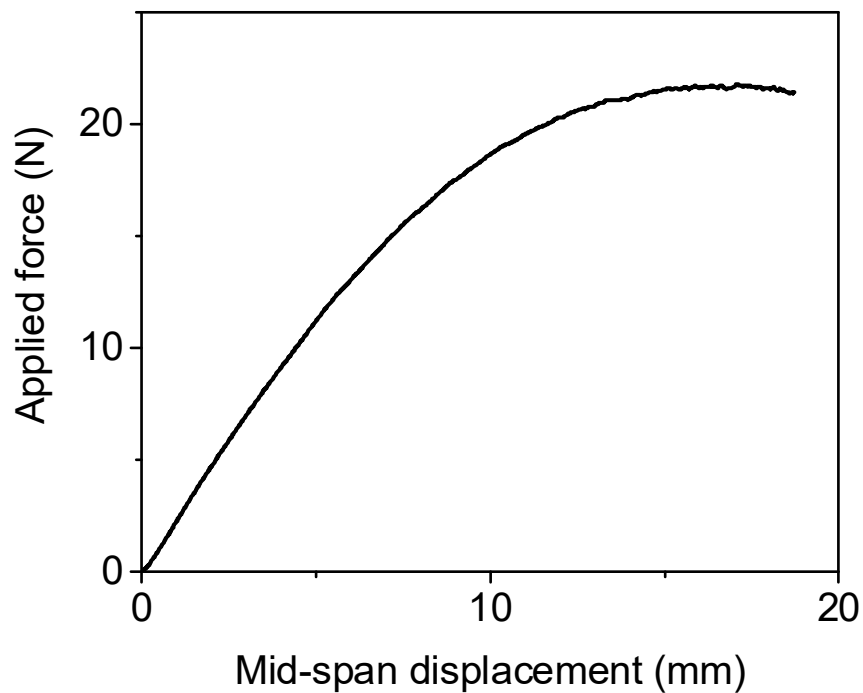


Figure A.12. Load-displacement of a PS-interleaved CFRP composite being deformed in a 3PB setup in an SM test

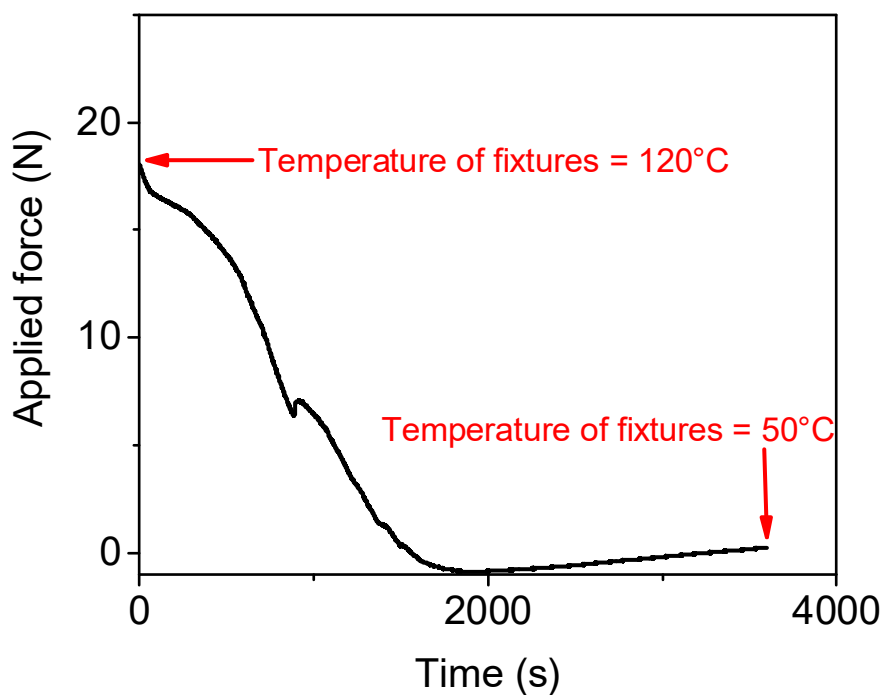


Figure A.13. Applied force of the composite during the cooling process in an SM test

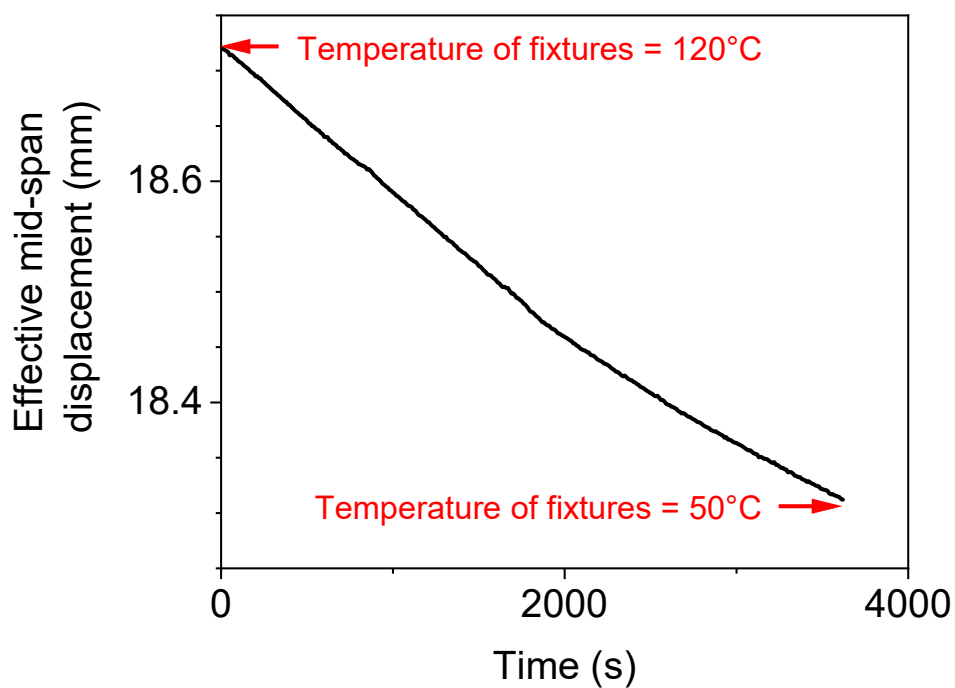


Figure A.14. Change in effective mid-span displacement of the 3PB setup during the cooling process in an SM test

A.7. Comparing the shapes of cross-plyed laminates predicted using analytical and numerical approaches

As an additional validation to the numerical models used in [Chapter 6](#), the shapes of a cross-plyed laminate with a layup of $[0^\circ/90^\circ]$, obtained using analytical methods and numerical methods are discussed here.

A.7.1. Using Timoshenko bimetal curvature equation to predict the shape of a cross-plyed laminate

The temperature-induced curvature of a cross-plyed laminate with a layup of $[0^\circ/90^\circ]$, can be considered comparable to that of a simple bimetal strip. Hence, a curvature of a cross-plyed laminate along its 0° direction (K_{xx-Ti}) can be calculated using [Eq A-2](#), which is modified from the curvature equation proposed by Timoshenko ([Timoshenko, 1925; Angel and Haritos, 2013](#)).

$$K_{xx-Timo} = \frac{2 |\alpha_{11} - \alpha_{22}| \Delta T}{t \left[1 + \frac{(E_{11} + E_{22})^2}{E_{11} E_{22}} \right]} \quad \text{Eq A-2}$$

where,

E_{11} and E_{22} are Young's moduli of CFRP in the 0° and 90° direction respectively (see [Table 6.1](#))

α_{11} and α_{22} are the coefficient of thermal expansion of CFRP in the 0° and 90° direction respectively (see [Table 6.1](#))

t is the thickness of each CFRP ply. Here, it is $125 \mu\text{m}$ ([Ciba-Geigy Plastics, 1989](#))

ΔT is the temperature difference between curing temperature and ambient temperature. Here, ΔT is assumed to be 87°C as the composite is cured at 175°C , and the shape of the composite is expected to stabilise around the glass transition temperature of PS (i.e., 88°C).

A.7.2. Using classical laminate theory (CLT) to predict the shape of a cross-ply laminate

In classical laminate theory, the deformation of a laminate subjected to thermal loading is represented by Eq A-3. To extract the curvature of a cross-ply laminate along its 0° direction (K_{xx}) using classical laminate theory, an unconstrained cross-ply laminate having appropriate thickness and properties of CFRP plies, and thermal boundary conditions (see Section A.7.1) was modelled using an in-house software ‘Laminate Analysis Program’.

$$\begin{bmatrix} \varepsilon^0 \\ K \end{bmatrix} = \begin{bmatrix} [A] & [B] \\ [B] & [D] \end{bmatrix}^{-1} \begin{bmatrix} N^T \\ M^T \end{bmatrix} \quad \text{Eq A-3}$$

where,

ε^0 represents the laminate mid-plane strains,

K represents the laminate mid-plane curvatures,

$\begin{bmatrix} [A] & [B] \\ [B] & [D] \end{bmatrix}^{-1}$ represents the laminate compliance matrix,

N^T represents the laminate mid-plane thermal forces, and

M^T represents the laminate mid-plane thermal moments.

A.7.3. Using numerical modelling to predict the shape of a cross-ply laminate

Following the methodology described in Section 6.2.1., FE analysis was performed on a cross-ply laminate using ABAQUS. The CFRP sub-laminates in the FE model were designed to be 2-dimensional shells having the dimensions as shown in Figure A.15., having a width of 10 mm in the Z-direction. The CFRP shells were assigned a thickness of 125 μm (Ciba-Geigy Plastics, 1989), the material property of CFRP (see Table 6.1), a mesh type of 4-node thermally coupled shell (S4T), and a global mesh size of 1 mm, in line with the convergence studies shown in Section 6.2.1. The parallel CFRP plies were constrained using a ‘Tie’ constraint to represent a primary bond. The entire model was assigned a pre-defined temperature of 175°C (curing temperature of CFRP (Ciba-Geigy Plastics, 1989)) in its initial flat shape and was then modelled to cool to 88°C.

From the shape of the CFRP sub-laminate in the models, after it cools to 88°C, their mid-plane coordinates were extracted along their mid-width. From the deformed shape of laminates (see Figure A.16), their curvature ($K_{xx-ABAQUS}$) was extracted by fitting the data points with a second-order polynomial curve (see Eq A-4 and Figure A.17).

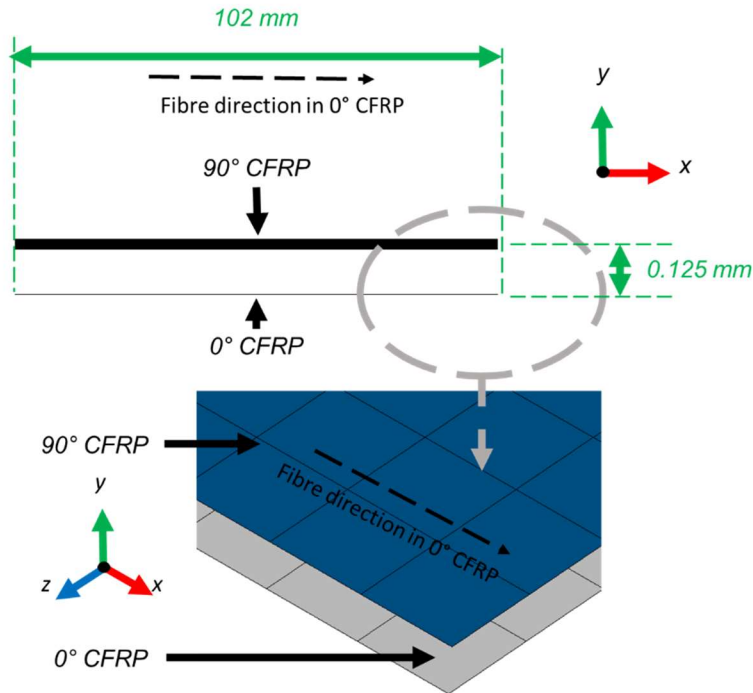


Figure A.15. A schematic of the layup in the FE model to study the shape change of a cross-ply laminate, with its dimensions highlighted

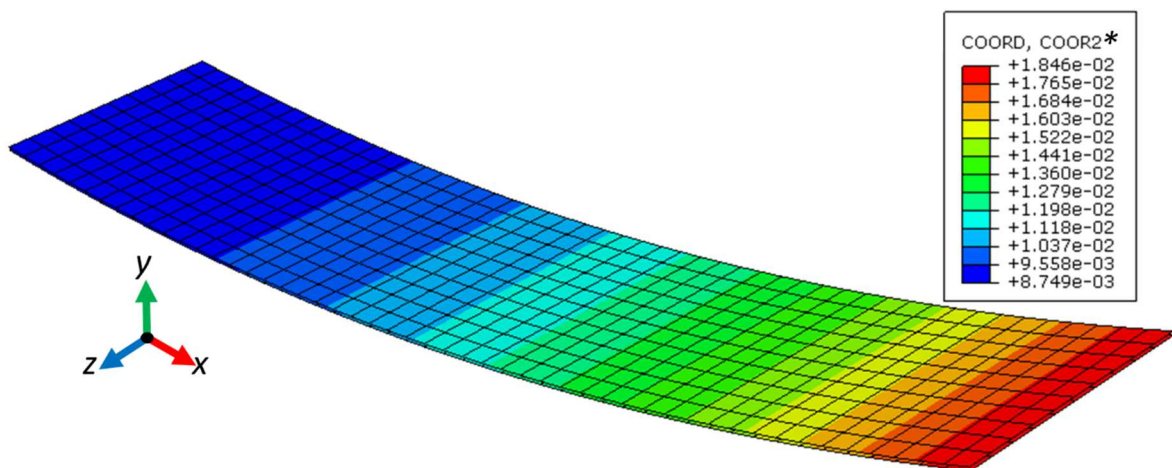


Figure A.16. FE model of a cross-ply laminate after cooling to 88°C

* COOR2 is the y-coordinate of the nodes of the FE model (scale is in metres).

$$y = K_{xx-ABAQUS} \frac{x^2}{2} + C_1 x + C_2 \quad \text{Eq A-4}$$

where C_1 and C_2 are constants

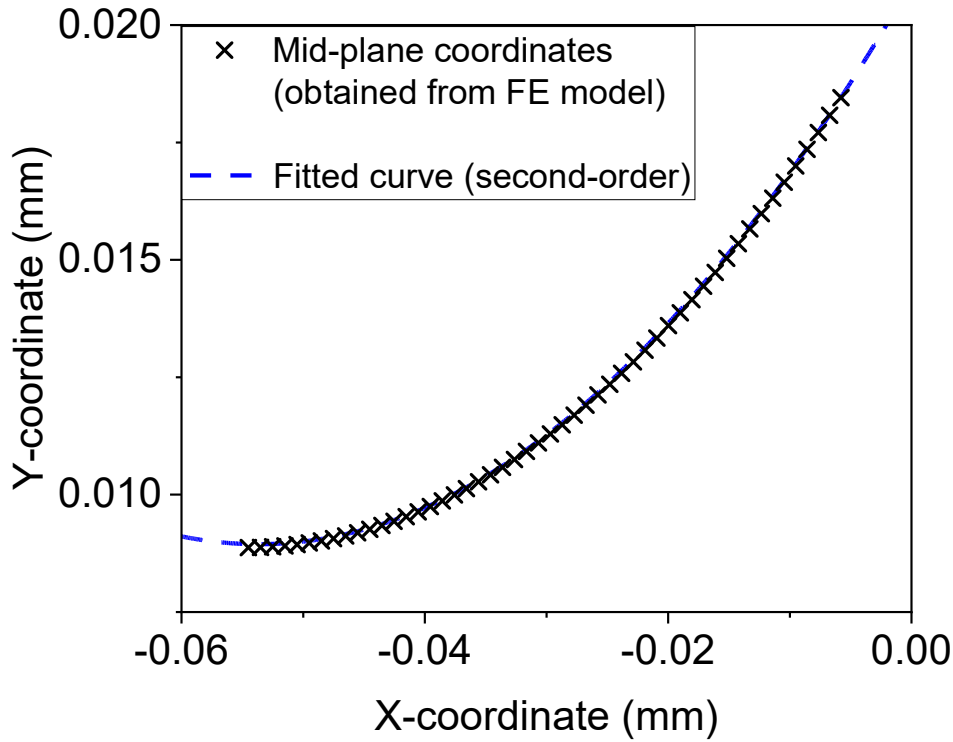


Figure A.17. The shape of the deformed cross-ply laminate obtained through the FE model, and the fitted second-order polynomial curve

A.7.4. Results and discussions

The curvature of a cross-ply laminate obtained through the various methodologies described in Sections A.7.1, A.7.2, and A.7.3 are shown in Table A.4. In the prediction of $K_{xx-Timo}$, the curvature of the cross-ply laminate along its width (Z-direction in Figure A.16) is not considered. Similarly, in the prediction of K_{xx} , the non-linearity of the geometry is not considered. Hence, they vary slightly from the $K_{xx-ABAQUS}^*$.

* Similar $K_{xx-ABAQUS}$ was obtained when the FE model had a global mesh size of 5 mm, 2.5 mm, 0.5 mm and 0.25 mm. Hence, they are not included here.

However, all the models show a significant agreement between their curvatures, as shown in Table A.4. These results provide additional validation to the FE model used in Section 6.2.

Table A.4. Curvature of cross-ply laminates obtained through various analytical and numerical methods

Model	Curvature name	Magnitude of curvature	% deviation from $K_{xx-ABAQUS}$
Analytical			
(Timoshenko bimetal curvature)	$K_{xx-Timo}$	8.43	1.54
Analytical			
(classical laminate theory)	K_{xx-CL}	8.40	1.19
Numerical			
(ABAQUS FE model)	$K_{xx-ABAQUS}$	8.30	-